Università degli Studi di Palermo

Dottorato di Ricerca in Scienze Fisiche e Chimiche
Dipartimento di Fisica e Chimica – Emilio Segrè
Settore Scientifico Disciplinare CHIM/02

Computational Investigation of Model Biomass Compounds Conversion on Isolated and Supported Metal Cluster

IL DOTTORE	IL COORDINATORE
CHIARA NANIA	**MARCO CANNAS**

IL TUTOR	IL CO TUTOR
FRANCESCO FERRANTE	**DARIO DUCA**

CICLO XXXVII
ANNO CONSEGUIMENTO TITOLO 2024

Computational Investigation of Model Biomass Compounds Conversion on Isolated and Supported Metal Cluster

Chiara Nania

December 5, 2024

Contents

Preface

The energy transition is one of the most complex and crucial challenges of the 21st century, representing a fundamental change in the way energy is produced, consumed and integrated into the global economy. With the increasing urgency to mitigate climate change, reduce environmental impacts and promote sustainable development, it becomes essential to adopt cleaner, more efficient and renewable sources of energy. This transformation is not just about moving away from fossil fuels, but requires a complete overhaul of the global energy system. For this reason, the energy transition is often referred to as a "critical transition", an indispensable change to ensure a sustainable and resilient energy future. In this context, the European Union has outlined a series of ambitious policies. The European Green Deal, adopted in 2019, set the goal of making Europe climate-neutral by 2050, with intermediate targets such as a 55% reduction in greenhouse gas emissions by 2030 compared to 1990 levels. Italy has also incorporated these guidelines in its Integrated National Energy and Climate Plan (*PNIEC*), pushing for an expansion of renewable energies and a reduction of emissions. These policy plans emphasise the urgency of a transition to renewable energy sources, including solar, wind, hydro and biomass.

Although technologies such as solar and wind have gained much attention, biomass is often undervalued, despite being a crucial resource in the renewable energy panorama. Unlike intermittent sources such as sun and wind, biomass offers a continuous and reliable energy source. This makes it particularly valuable not only for power generation, but also for reducing dependence on petrochemicals. Biomass stands out for its versatility, as it can be converted into a wide range of energy products, including biofuels, biogas, and biochemical compounds. However, its large-scale application is hindered by the complexity of the conversion processes required to transform it into high-quality liquid fuels. The main challenge lies in optimizing catalytic processes to improve the efficiency of biomass conversion. The

hydrodeoxygenation (HDO) process, which facilitates the removal of oxygen from molecules derived from pyrolyzed biomass, is among the most promising technologies for liquid biofuel production. This process is essential to improve biofuel quality, but to maximize yields and efficiency, a deeper exploration of reaction dynamics and the development of more selective and efficient catalysts are needed.

This is a challenge that requires an interdisciplinary approach, integrating chemistry, materials science and computational modelling, to develop innovative technological solutions in line with the needs of the energy transition. The present PhD project fits within this context and aims to contribute to the understanding of the chemical mechanisms governing biomass conversion into biofuels. Specifically, the focus is on two model compounds of lignocellulosic biomass: guaiacol and isoeugenol, selected to represent the main classes of molecules present in lignocellulosic biomass and for their relevance in bio-oil and biofuel production processes. The study examines the reactions of these compounds catalysed by metal clusters, both isolated and supported on graphene, with the aim of mapping the most significant pathways for their decomposition and hydrodeoxygenation.

Another significant aspect of the project concerns the growth of platinum and nickel metal clusters on defective graphene surfaces, investigated through the implementation of an original algorithm to determine the most stable atomic geometries of particles containing up to 10 metals atoms. The analysis focused on the binding and cohesion energy of these clusters on defective graphene, with particular attention to the effect of the support in improving cluster stability and resistance to deactivation, usually due to coke formation or sintering, phenomena commonly observed in HDO processes. A significant part of the work is devoted to the comparison of the reactivity of Pt_{10}/C and Ni_{10}/C clusters in deoxygenation reactions of biomass-derived compounds, such as guaiacol and 2-methoxycyclohexanol. This study highlights the differences in the catalytic behavior of the two metals and underscores the importance of carefully selecting the most suitable catalyst, depending on the specific characteristics of the reactions involved.

The results of this project aim to enrich the basic knowledge about biomass conversion processes, opening new perspectives for the development of more efficient and selective catalysts, in line with the goals of sustainable chemistry and the European and Italian directives regarding the energy transition.

Chapter 1

Introduction

1.1 Towards a Sustainable Energy Future: Innovations and Strategies for Reducing Fossil Fuel Dependence

Energy is recognized as a crucial factor in achieving the social and economic development goals of nations [1]. It is a vital necessity, as it is essential for the provision of crucial services such as electricity, cooling, heating, and the production of many basic necessities. Improving people's living conditions is closely linked to access to reliable and sustainable energy sources, which support not only daily household activities but also industrial and technological growth, key factors for global socio-economic progress.

In recent decades, the global consumption of fossil fuels for energy production has increased dramatically. This surge has been driven by changes in quality of life, the industrial revolution in developing countries, and world population growth [2]. These dynamics have led to a rapid depletion of fossil fuel reserves and a significant negative impact on the atmosphere. This includes greenhouse gas emissions (*GHGs*), deterioration of air quality due to pollutants such as SO_x, NO_x, and fine particulate matter, and a consequent increase in threats to health, global warming, and climate change [3, 4, 5, 6]. Furthermore, fluctuating fossil fuel prices and their progressive depletion have jeopardized global economic stability.

In response to global energy challenges, researchers around the world are exploring different strategies to reduce or eliminate the use of fossil fuels. Three of

these strategies are particularly relevant:

1. **Improve the efficiency of conventional energy conversion devices and systems through waste heat recovery**. This approach aims to exploit the waste heat generated during energy conversion processes, which would otherwise be lost. For example, in internal combustion engines and thermal power plants, a significant amount of energy is dissipated as heat. Advanced technologies, such as combined cycles and waste heat recovery systems, enable the conversion of this thermal energy into additional electricity or its reuse for industrial and residential heating. Large-scale adoption of these technologies can significantly reduce fossil fuel consumption while improving the overall efficiency of energy systems [7, 8, 9].

2. **Develop environmentally friendly energy conversion devices, such as fuel cells**. These electrochemical devices directly convert the chemical energy of fuels into electricity through redox reactions, with greater efficiency than traditional combustion engines and minimal pollutant emissions. Fuel cells can use various fuels, including hydrogen, methanol, and biogas, making them extremely versatile. Additionally, their use can be integrated into a variety of applications, from electric vehicles to stationary generation systems for homes and industries. Current research focuses on improving fuel cell efficiency, reducing production costs, and increasing operational life, making them an ever more viable solution for the energy transition [10, 11, 12].

3. **Switch to renewable energy sources of natural origins**. The term "renewable" associated with "energy" refers to the ability of a resource to be replenished, reproduced, or recovered. Renewable energy sources, such as solar, wind, hydropower, biomass and geothermal [13], offer significant benefits in terms of sustainability and reduced *GHGs* (see **Fig. 1.1**). Solar energy harnesses solar radiation through photovoltaic panels or solar thermal systems to generate electricity or heat. This energy source is virtually inexhaustible and available in many regions of the world, contributing to the reduction of CO_2 and other pollutants associated with fossil fuels. Wind energy uses wind to drive turbines that generate electricity. This type of energy is particularly effective in areas with constant, strong winds, and, like solar energy, it produces no emissions during operation. The integration of onshore and offshore wind farms can significantly increase the share

of renewable energy in the global energy mix. Hydropower harnesses the power of moving water, such as rivers and waterfalls, to generate electricity. Hydropower plants, especially small-scale ones, offer a stable and continuous source of renewable energy, while also contributing to water resource management and flood mitigation. Biomass energy converts organic materials, such as agricultural residues, wood, and dedicated energy crops, into electricity, heat, or biofuels. This energy source can be carbon-neutral, as the CO_2 released during combustion is offset by the CO_2 absorbed during the growth of the biomass. Additionally, biomass energy contributes to sustainable waste management by reducing the amount of organic material in landfills and decreasing methane emissions, a greenhouse gas. Finally, geothermal energy uses heat from the Earth's interior to generate electricity or heating. This energy source is reliable and can provide continuous production, independent of weather conditions. Geothermal plants are particularly effective in regions with significant geothermal activity, such as volcanic areas [14, 15, 16].

On this basis, renewable energy sources find applications in sustainable systems for large-scale generation [17, 18, 19, 20]. The essential characteristic of a sustainable energy system is its ability to provide the necessary energy without depleting resources. The first step towards this strategy is to improve the efficient use of available resources [21]. Despite the promising characteristics of renewable energy sources, their intermittent nature requires integration with other renewable energy resources and/or adequate energy storage systems. Weather variations, for example, contribute to the intermittent nature of electricity generation from, for example, solar and wind power. On calm days, the generation capacity of wind turbines can be reduced by up to 100%, while on cloudy days, the capacity of solar power plants can decrease by up to 70%. Therefore, the development of renewable energy requires management systems that optimize overall performance using advanced technologies, such as artificial intelligence, as well as effective management of hybrid renewable energy/storage systems to mitigate intermittency [22, 23].

In this context, many international and national institutions are implementing regulatory frameworks to promote renewable energy and diversify energy sources by replacing conventional resources. At the international level, the 2015 Paris Agreement is a key pillar, committing signatory countries to limit the global temperature increase to well below 2℃ above pre-industrial levels, with the aim of limiting the increase to 1.5℃. States must submit updated National Adaptation
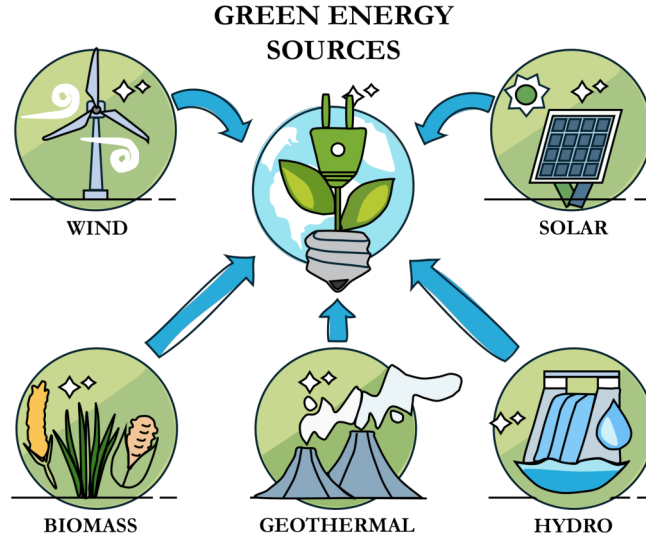
Figure 1.1: Illustration of the main renewable energy sources: wind, solar, hydroelectric, geothermal, and biomass. These sustainable sources are crucial for generating clean energy and preserving the environment.

Plans (*NDCs*) every five years, outlining their strategies for reducing *GHGs*. The agreement also encourages the use of clean technologies and the financing of renewable energy in developing countries through the Green Climate Fund, which aims to mobilize $100 billion per year by 2025. At the European level, the *Green Deal*, launched by the European Commission in 2019, sets out a roadmap to make the European Union climate neutral by 2050. At the heart of this plan is the Renewable Energy Directive 2018/2001/EU, which updates and expands the objectives of the previous *RED I* directive. *RED II* stipulates that by 2030 at least 32% of the EU's final energy consumption will come from renewable sources, with specific support measures for several technologies, including incentives for the production of advanced biofuels and renewable electricity. Additionally, the Regulation on the Governance of the Energy Union and Climate Action (Regulation (EU) 2018/1999) requires Member States to draw up ten-year integrated national energy and climate plans (NECPs), which must be updated every five years. These plans must detail policies and measures to meet energy and climate targets, including those for energy efficiency and emission reductions. In Italy, the *Integrated National Energy* and *Climate Plan* (PNIEC) is the strategic document that aligns national policies with European objectives. The PNIEC 2021-2030 sets the target of a

30% share of energy from renewable sources in gross final energy consumption by 2030, with sector-specific targets: 55.4% in the electricity sector, 33% in the thermal sector, and 21.6% in transport. The transition to a sustainable energy future requires a multidimensional approach, including the implementation of effective policies, the development of advanced technologies, and integrated management of energy resources. In this regard, as highlighted, global and national efforts are directed towards reducing the use of fossil fuels and promoting renewable energy, with the aim of creating a more resilient, efficient, and environmentally friendly energy system.

1.2 The Role of Biomass in Renewable Energy Strategies and Climate Mitigation

The use of renewable energy sources is increasingly prominent in the context of combating climate change. Among these, biomass stands out for its unique characteristics. Biomass is a completely renewable energy resource. The CO_2 emitted during its combustion doesn't contribute to the increase in atmospheric carbon dioxide because it is of biogenic origin, unlike fossil fuels [24, 25, 26, 27, 28, 29]. That is, plants use CO_2 released into the environment during the decomposition of other plants to grow and carry out their metabolic processes [30]. Therefore, the use of biomass only results in a faster transfer of CO_2 to the atmosphere, which is again absorbed by plants to produce more biomass [31] (see **Fig. 1.2**). Any organic matter derived directly or indirectly from photosynthesis can then be considered biomass. More generally, biomass is a combination of natural source materials from plants such as shrubs, trees, algae, and crops, as well as all materials consisting of organic matrix, except for plastics derived from petrochemical and fossil materials [32]. The most relevant biomass sources are agricultural and forestry residues (waste from the wood processing industry, such as chips and sawdust), animal residues (livestock farms), wastewater, algae, and aquatic crops (see **Fig. 1.3**). Municipal solid waste (*MSW*) and waste streams from anthropogenic activities are also counted as biomass, but only if they can't be reused in further production processes [33]. Biomass can be converted into electricity, thermal energy, vehicle fuels and valuable chemicals [34].

Biomass can be transmuted into gaseous fuels such as hydrogen and methane,

liquid fuels like biodiesel, ethanol, and methanol, and solid fuels encompassing biochar and hydrocarbons [27]. Among these, biochar [16, 35] and biodiesel [36, 37] stand out as promising fuels with potential applications across various sectors. Biochar, a carbon-rich solid material derived from biomass pyrolysis, offers diverse uses including soil fertility enhancement, water and nutrient retention, and carbon sequestration, thereby aiding in reducing atmospheric CO_2 levels. Biomass feedstocks for biochar production range from agricultural residues to forestry waste. On the other hand, biodiesel, obtained through the transesterification process of vegetable oils or animal fats, is chemically compatible with conventional diesel, requiring minimal engine modifications for its use. Standard regulations, such as *UNI EN 590:2022* in Europe, allow blending biodiesel with diesel up to 7% (commonly known as B7), facilitating its incorporation into existing fuel infrastructures without major alterations. The introduction of biodiesel blends offers several benefits:

a. **Emission Reduction:** Biodiesel blends yield lower emissions of particulate matter, nitrogen oxides (NO_x), carbon monoxide (CO), and unburned hydrocarbons compared to pure diesel, thereby improving air quality and reducing environmental impact;

b. **Infrastructure Compatibility:** Biodiesel blends can be seamlessly integrated into existing fuel distribution infrastructure, minimizing the need for significant modifications to storage tanks, pumps, and pipelines;

c. **Economic and Environmental Advantages:** Incorporating biodiesel into fuel blends aids in reducing reliance on fossil fuels, supporting the agricultural sector, and fostering sustainable development.

Additionally, the use of this resource is not evenly distributed globally. In some developing countries, biomass accounts for up to 50% of the total energy demand through the combustion of wood, shrubs, and plant and animal residues, while in developed countries, biomass energy production averages 11% of the total energy produced [38].

Biomass has played a crucial role in energy debates promoted by the European Union in recent decades, successfully transforming energy-saving and environmental protection measures into concrete strategic plans [32, 39]. Considering the extensive potential of biomass in producing biofuels for transportation, electricity,
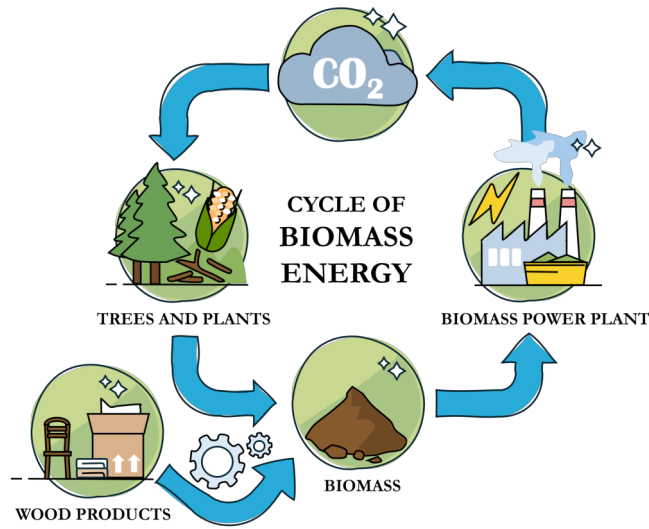
Figure 1.2: Carbon Cycle in Biomass: plants absorb CO_2, converting it into biomass. This biomass is used to produce energy, while organic residues are turned into compost, returning nutrients to the soil.

and heat, it may become even more significant as an energy resource and chemical raw material in the 21st century [40, 41]. In industrialized countries, the economic and political importance of bioenergy is recognized by documents such as the "*Biomass Action Plan*" and the "*Multi-Year Plan*", drafted respectively by the European Commission and the US Department of Energy [38]. The former is part of the European Union's strategy to increase the use of renewable energies and reduce dependence on fossil fuels. This document presents a series of measures and objectives to promote the use of biomass in energy, heating, cooling, and transportation sectors. Additionally, the plan emphasizes the importance of research and innovation, with investments aimed at improving biomass efficiency and reducing associated costs. Special attention is given to sustainability aspects, ensuring that biomass production does not compromise biodiversity and natural resources, with guidelines for sustainable management of agricultural and forestry resources. The latter, on the other hand, is a strategic document that describes a systematic and long-term approach to renewable energy development. The plan sets ambitious goals for carbon emission reduction through increased use of biomass and other renewable sources, in line with *US* international commitments on climate change. A central component of the plan is the funding of research and development to enhance biomass conversion technologies, such as advanced biofuels,
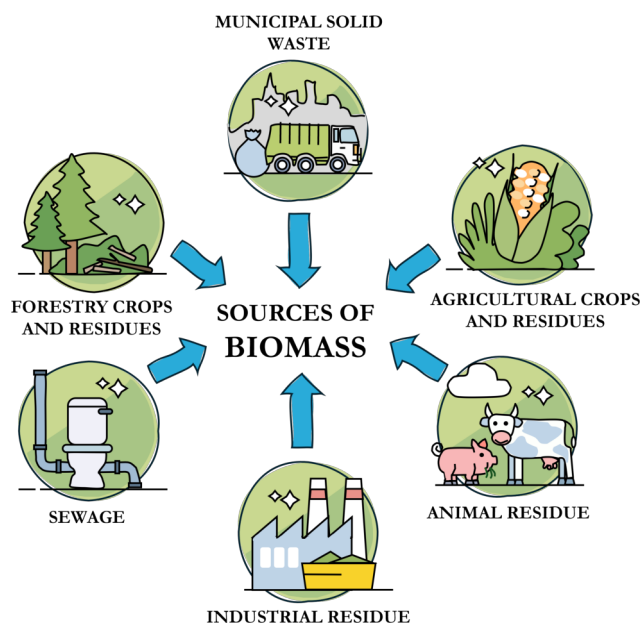
Figure 1.3: The main sources of biomass include forest residues, urban solid waste, energy crops, urban effluents, industrial waste, and agricultural and livestock waste. These resources are used for the production of renewable energy and sustainable materials, contributing to the reduction of carbon emissions and efficient waste management.

bioproducts, and bioenergy. In summary, both documents reflect significant commitment by the respective authorities to promote the sustainable use of biomass as a key component of future energy policies. While the EU's "*Biomass Action Plan*" focuses on incentives, research, and sustainability, the US "*Multi-Year Plan*" places particular emphasis on emission reduction, technological development and infrastructure, highlighting the unique challenges and opportunities of each geographical and political context.

1.3 Biomass Composition

Biomass is a heterogeneous mixture composed mainly of organic substances and a small amount of inorganic substances. A typical dry biomass contains 30–40% oxygen, 30–60% carbon, and 5–6% hydrogen by weight. Elements such as nitrogen, sulfur and chlorine make up about 1% of the biomass. Carbon, derived from

atmospheric CO_2 through photosynthesis, is the main contributor to the heating value of biomass. Hydrogen, integrated into the chemical structures of carbon and phenolic polymers, converts to water during combustion, representing another essential element. These elements form the chemical basis of the three main biomass polymers: cellulose (40-50 % w/w), hemicellulose (15-30 % w/w) and lignin (16-33 % w/w). These elements, combined with N, Ca, K, Si, Mg, Al, S, Fe, P, Cl, Na, Mn and Ti, contribute to a variable extractives and ash content (1-10 % w/w).

Cellulose, hemicellulose and lignin are the main constituents of the plant cell wall[1], each having a specific function (see **Fig. 1.4**). Cellulose, present in both the primary and secondary walls, forms microfibrils that impart strength and structure. Hemicellulose, located between these microfibrils, acts as a matrix that binds them together, providing elasticity to the cell wall. Lignin is mainly found in the secondary wall, especially in woody tissue cells, where it impregnates and strengthens the wall, making it rigid and impermeable. This stiffness is crucial for structural support and water transport within plants. In summary, cellulose imparts structure, hemicellulose acts as a glue, and lignin provides strength and stiffness.

In the following paragraphs, the main components of biomass will be detailed, with emphasis on the main chemical components and their variations among different biomass sources.

1.3.1 Cellulose

Cellulose is a linear polymer and a complex carbohydrate (namely, a polysaccharide) with a high molecular weight, containing up to 10,000 monomeric units of D-glucose linked via β-1,4-glycosidic bonds. The molecular formula of cellulose is $(C_6H_{12}O_6)_n$, where n indicates the degree of polymerization, and its basic structural unit is cellobiose (4-O-β-D-glucopyranosyl-D-glucopyranose) [44]. The $\beta(1-4)$ bond of cellulose prevents ramifications in the linear chain. In addition, if

---

[1]The plant cell wall is composed of a complex matrix of polysaccharides, proteins and lignin, which performs numerous functions, including maintaining cell shape, protecting against pathogens and regulating the flow of substances [42]. It can be divided into several stages: the primary wall (which allows cell growth) is composed mainly of cellulose, hemicellulose, pectin and structural proteins; the secondary wall (which is formed when the cell has reached its final size) contains a high percentage of cellulose and lignin, imparting strength and mechanical resistance [43].
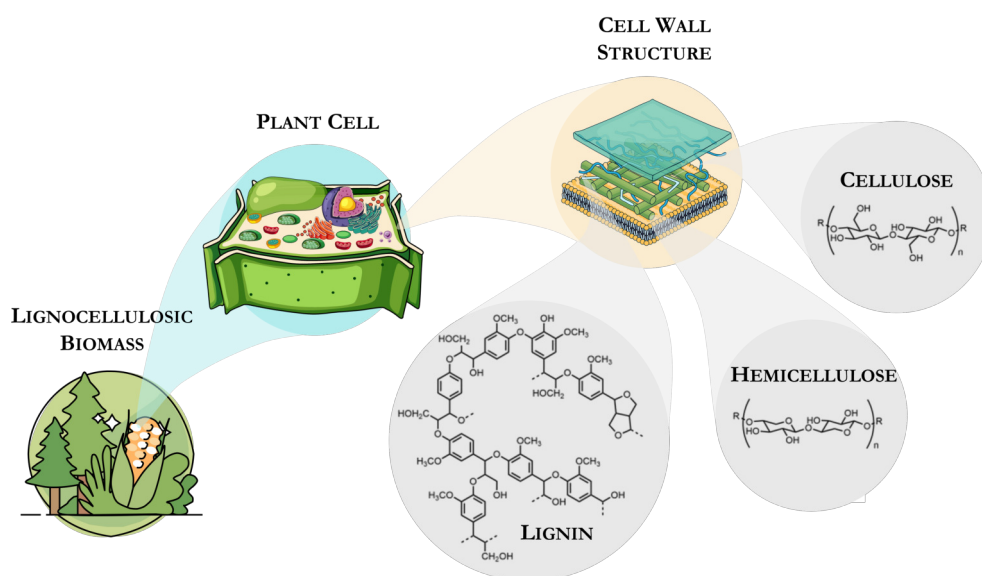
Figure 1.4: Plant cells are composed of three main components: cellulose, a long chain of glucose molecules that provides strength; hemicellulose, a branched polysaccharide that offers flexibility; and lignin, a complex aromatic polymer that ensures rigidity and impermeability. These chemical elements form the robust cell wall of plants.

a on-and-off ring of the glucose molecules are rotated face down, intrachain hydrogen bonds can form between one ring and the next, but also interchain hydrogen bonds laterally. This makes the chains sticky and causes them to aggregate with each other, forming bundles of chains called microfibrils, hydrophilic objects that can bind many water molecules. In nature, however, cellulose is always linked to pectins or lignin and this makes it hydrophobic. Cellulose is the most abundant organic compound in nature, making up 90% of the structure of cotton and 50% of that of wood, playing an essential structural role in plant cell walls.

The reactivity and morphology of cellulose chains are significantly influenced by intermolecular hydrogen bonds between the hydroxyl group of the C3 carbon and the oxygen of the adjacent glycosidic ring. These bonds confer stability and rigidity to the macromolecules. In some cases, the presence of numerous intermolecular bonds can generate ordered crystalline regions; the alternation of crystalline and amorphous regions in cellulose can influence the accessibility of functional groups involved in reactions. Notably, primary hydroxyl groups are more reactive than secondary ones due to lower steric hindrance [45]. The amorphous region is more exposed and thus it is the first to be attacked by the enzyme cellulase, leading to the hydrolysis of the molecule. Complete hydrolysis of cellulose produces D-glucose, while partial hydrolysis forms cellobiose and smaller polysaccharides (with values of n between 3 and 10) [46, 47]. The crystalline part, being hydrophobic, requires mercerization treatments to become hydrophilic, a process devised by the english chemist John Mercer in 1844. Due to its properties, cellulose has become an essential raw material for the paper and chemical fiber industries over the past two centuries. Additionally, it currently plays a significant role in various fields related to environmental protection, such as water remediation for removing hazardous pollutants like hydrocarbons and heavy metals [48, 49, 50, 45].

1.3.2 Hemicellulose

Hemicellulose, an essential component of plant cell walls, distinguishes itself from cellulose through its amorphous, branched structure and shorter chains, with an average molecular weight typically below 30.000 Da [32, 49, 50]. Although its polysaccharide chain resembles that of cellulose, the degree of hemicellulose polymerization varies widely, typically ranging from 50 to 200 units [51]. Monosaccharide units comprising emicellulose primarily include hexoses (glucose, mannose, and galactose) and pentoses (xylose and arabinose), alongside minor sugars such

as rhamnose and fructose. Additionally, emicellulose incorporates uronic acids (4-O-methyl-*D*-glucuronic acid, *D*-glucuronic acid, and *D*-galacturonic acid) and acetyl groups, contributing to its structural complexity [52].

The composition and structure of hemicellulose vary significantly depending on plant species and cell wall type. This structural diversity enables effective interaction with cellulose microfibrils and lignin, forming a matrix that imparts flexibility and strength to the cell wall. Emicellulose plays a crucial role in the structural integrity of plant cell walls, enhancing overall mechanical properties and providing resistance to enzymatic degradation. These interactions are vital for maintaining cell wall architecture and function, allowing plants to adapt to various environmental stresses [53].

Hemicellulose exhibits higher reactivity compared to cellulose due to its diverse structure and the presence of various functional groups. This characteristic enhances its susceptibility to hydrolytic enzymes, a critical property in the bioconversion of biomass for biofuel production. Hydrolysis of hemicellulose is a key step in releasing fermentable sugars necessary for microbial fermentation, yielding bioethanol and other biofuels [54].

In industrial applications, hemicellulose has garnered attention for its potential in biofuel, biochemical, and biomaterial production. Xylose derived from hemicellulose can be fermented to produce xylitol, a low-calorie sweetener, and other high-value products such as furfural, a precursor for various chemicals [55]. Moreover, hemicellulose-based materials have shown promising applications in packaging, adhesives, and films due to their biodegradability and renewable nature [56]. Recent advancements include chemical modifications of hemicellulose to enhance its properties for specific industrial applications, such as bioplastic and advanced composite materials production [57]. In summary, hemicellulose stands as a versatile and pivotal component of plant cell walls, with a structure and composition that dictate its functionality and industrial applications. Ongoing research into its structure, function, and potential uses promises to advance sustainable technologies and products.

1.3.3 Lignin

Lignin is a complex amorphous aromatic polymer, with an elemental composition of approximately 61-65% carbon, 5-6% hydrogen, and the remainder oxygen. This macromolecule forms a three-dimensional network composed of phenylpropane
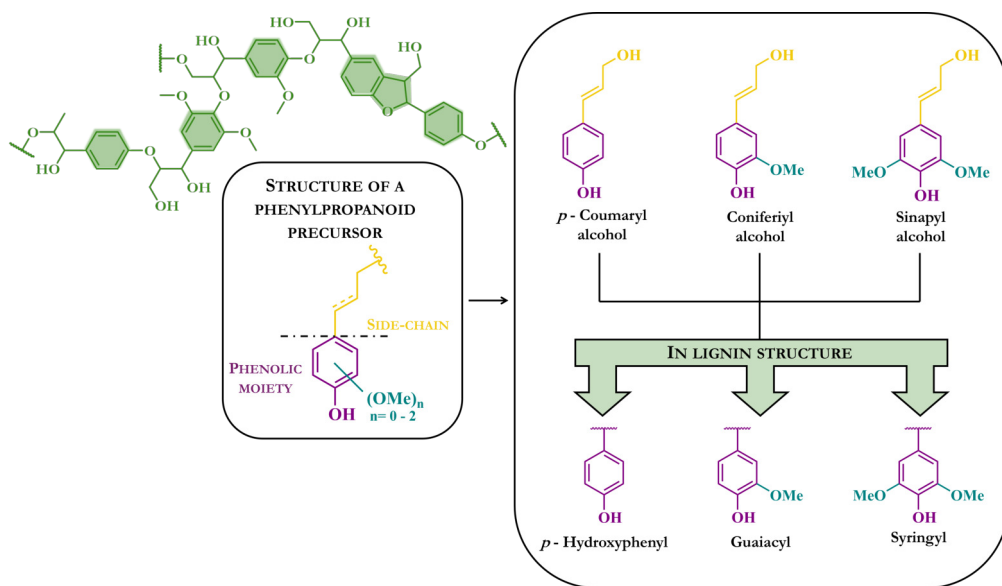
Figure 1.5: Biosynthetic pathway and chemical structure illustration of lignin, a complex biopolymer. The left panel shows the general structure of a phenylpropanoid precursor, which contains a phenolic moiety (highlighted in purple) and a variable side chain (in yellow), with possible methoxy groups (OMe). The right panel depicts three key monolignols – p-coumaryl alcohol, coniferyl alcohol, and sinapyl alcohol – which contribute to the formation of lignin. These alcohols are incorporated into lignin as p-hydroxyphenyl (H), guaiacyl (G), and syringyl (S) units, respectively, forming the polymer backbone.

units linked by various bonds, including oxygen bridges between propyl and phenyl groups, and carbon-carbon bonds. Lignin is synthesized through the oxidative radical polymerization of three hydroxycinnamyl alcohols, which constitute its basic structural monomers: *p*-coumaryl alcohol, coniferyl alcohol, and sinapyl alcohol (see **Figure 1.5**). These compounds differ in their degree of methoxylation.

Lignin contains numerous polar and hydroxyl groups that form strong intramolecular and intermolecular hydrogen bonds, rendering it insoluble in most solvents except alkaline solutions. During condensation reactions, lignin divides into soluble and insoluble fractions, with the latter forming a precipitate. The softening temperature of dry lignin ranges from 127 to 129 °C, but increases with molecular weight. Water within lignin acts as a plasticizer, lowering the softening temperature [47, 44]. Lignification, the infiltration of lignin into the cell wall,

imparts significant mechanical strength to plant structures. Lignified membranes swell less than cellulosic ones because the dipolar -OH groups of cellulose are largely saturated by lignin. With an estimated global availability of around 300 billion tons and an annual increase of approximately 20 billion tons [58], lignin represents a substantial resource. Over the past decade, the pulp and paper industry alone has produced about 50 million tons of extracted lignin, but only 1 million tons have been utilized for value-added products, while the rest has been burned as low-value fuel [59].

The lignin content varies among plant species, ranging from 25-30% in many plants to about 50% in very hard woods like ebony, and around 10-12% in annual plants. Recent research focuses on improving lignin conversion processes to produce high-value-added products such as dispersants for construction, emulsifiers, chemical precursors, and biopolymers. Efficient separation of lignin from lignocellulosic biomass is crucial for enhancing conversion rates to final products [58]. Industrially, lignin is a significant byproduct of pulping and biofuel production processes. Its adhesive and film-forming properties make it a promising candidate to replace petrochemical products. Lignin can be depolymerized into useful aromatic compounds for the production of bioplastics, adhesives, and other high-value materials. The biorefinery approach, integrating biofuels and bioproducts, aims to exploit lignin more efficiently and sustainably.

1.3.4   Extractives and Ash

Extractives are chemical compounds that can be extracted from biomass using organic solvents or water. They include resins, oils, fatty acids, and other organic compounds. Although they represent a small fraction of biomass (about 5–10 %w/w), extractives can significantly influence biomass properties and conversion processes. For example, extractives can contribute to fouling in combustion processes and affect the quality of biofuels produced. Ashes are the inorganic residues that remain after biomass combustion. They include minerals such as calcium, potassium, magnesium and silicon. Ash content varies from 0.5% to 10% by weight and can affect the performance of thermochemical conversion processes, such as combustion and gasification. The presence of ash can cause fouling and corrosion problems in combustion machinery, making their control and management necessary.

1.4   Biomass Classification

Biomass can be divided into two main categories: **lignocellulosic biomass** and **non-lignocellulosic biomass**. Lignocellulosic biomass can be further classified into three groups: **agricultural waste** (corn cobs, straw, rice husks, and wheat straw), **wood residues** (bamboo chips, pine sawdust, and tree bark), and **energy crops** (switchgrass, miscanthus, and rubber trees). Lignocellulosic biomass exhibits various physico-chemical properties, such as water content, particle size, and hydrophobicity, but generally has similar components, namely cellulose, hemicellulose, lignin, water extractives (organic matter), and ash (inorganic matter). Lignocellulosic biomass typically contains negligible amounts of extracts that can affect pyrolysis performance, including fats, tannins, waxes, resins, tea saponins, and sugars. In contrast, non-lignocellulosic biomass consists mainly of **municipal solid waste** (MSW), **sewage sludge**, **animal manure** and **algal biomass**. This type of biomass also contains fatty acids and proteins, while the levels of hemicellulose, cellulose and lignin are much lower than those characterizing lignocellulosic biomass.

Woody biomass generally contains many different components, primarily carbohydrates and lignin. This category includes materials such as tree and root residues, bark, and leaves of woody shrubs, both above and below ground, which can be converted into energy through direct combustion (or gasification) or various conversion processes. Woody biomass is currently the most important source of renewable energy in the world. In 2010, global use of woody biomass resulted in energy production of about 30 EJ, of which 16 EJ were related to domestic firewood and 14 EJ to industrial use of woody biomass.

Energy crops and agricultural by-products constitute herbaceous biomass, derived from plants with non-woody stems that die at the end of the growing season. This includes cereals or seed crops from the food industry and their by-products, such as cereal straw. Energy crops are those exploited solely in the bioenergy sector, while agricultural by-products are residues from food industries, farms, and food. Some of these by-products are collected for various uses, such as animal feed. In any case, these residues aren't fully monitored, and their availability in different regions and potential applications as bioenergy are not entirely clear.

In the realm of non-lignocellulosic biomass, animal waste and MSW include meat, bones, human excrement, animal manure, plastics, food waste, paper, met-

als, and other various components generated by urban activities. In the past, these wastes were collected and sold as fertilizers or simply applied to agricultural land. However, the implementation of various regulations by governments has led to the control of environmental pollution, health, and odor issues, which ultimately play a significant role in waste management. Anaerobic degradation of these wastes is the best technique used so far for converting these types of biomass into useful products. The energy produced from these wastes includes biofuels and biogas, used to generate electricity.

Finally, aquatic biomass includes various types of aquatic plants and microorganisms, such as microalgae and macroalgae. Currently, aquatic biomass is considered an ideal raw material for the production of third-generation biodiesel, as it does not compete with food crops and has the advantage of producing considerably higher biomass yields per hectare compared to terrestrial crops. However, significant economic and technological challenges remain before these biofuels can be effectively commercialized. Moreover, it should be noted that many parameters influence the performance of aquatic biomass, such as irradiation levels, CO_2 and O_2 concentrations, temperature, pH, salinity, and nutrients.

1.5   Biomass Conversion Methods

The lignocellulosic biomass, once collected, stored, and transported, is sent to the plant for conversion to energy through various processes, which can be classified into three categories: physicochemical, biological, and thermochemical. Physicochemical processes are used to transform biomass, such as oil crops, through transesterification into biodiesel and through thermal conversion to generate biofuels and bioenergy. On the other hand, biological processes exploit microorganisms such as bacteria and yeasts to carry out alcoholic fermentation and anaerobic digestion. These processes enable the transformation of different biomasses, including agricultural stocks and organic waste, into biofuels such as biogas and bioethanol, thus contributing to the production of renewable energy and the sustainable treatment of organic waste. Finally, thermochemical processes such as pyrolysis, gasification and direct combustion use heat to decompose biomass into fuel gas or biochar coal. These technologies are crucial for advanced energy applications, offering efficient energy alternatives and reducing environmental impact through the valorization of agricultural and forest residues. In summary, diversifi-

cation and optimization of biomass conversion methods play a key role in achieving environmental sustainability and global energy security goals.

In the following paragraphs, biomass conversion technologies will be described in more detail with a focus on thermochemical and biochemical processes, further outlining the various methodologies and applications.

1.5.1 Thermochemical processes

Combustion

Combustion is a traditional and established technology that consists, thermodynamically, in the conversion of the chemical energy contained in lignocellulosic biomass into thermal energy. Combustion of organic matter essentially occurs through three successive stages: drying, degradation, and combustion. In the initial stage, heat removes residual moisture from the biomass, turning it into water vapor. The evaporation process has an energy cost that burdens the energy yield of the process itself; it follows that the greater the starting moisture, the greater the proportion of process energy used to evaporate the water. The second stage involves thermal degradation of organic materials through the processes of pyrolysis (or pyroscission) and gasification or the processes of thermochemical decomposition, achieved by the application of heat and in the complete absence of oxygen. Under anaerobic conditions, the material undergoes cleavage of the original chemical bonds with formation of simpler molecules. In the last stage, however, there is oxidation of the gases and reduced simple molecules, with energy release.

Depending on the chemical composition of the organic matrix, the achieved temperature, and the amount of oxygen available, different types of residual products can be obtained such as ash, coal (biochar), tar, oils, syngas, as well as emissions of CO, CO_2, H_2O, H_2, CH_4, volatile organic compounds, nitrogen and sulfur oxides, etc. The heat produced by combustion is used to generate steam or hot water, which can be used for direct heating or to power steam turbines for electricity generation. However, combustion exhaust gases contain carbon dioxide (CO_2), water vapor (H_2O), nitrogen oxides (NO_x), sulfur oxides (SO_x) and particulate matter. Before being released into the atmosphere, these gases must be treated to reduce pollutant emissions. Treatments include particulate filtration using bag filters or electrostatic precipitators, reduction of nitrogen oxides through techniques such as selective catalytic reduction (SCR), and reduction of sulfur ox-

ides using wet or dry scrubbers. Ash, on the other hand, can be collected and used as fertilizer or safely discarded.

Pyrolysis

Pyrolysis is a thermochemical conversion process of lignocellulosic biomass with moisture content less than 15 %. This process takes place in a completely oxygen-free environment and at high temperatures (between 200 and 700 ℃), producing bio-oil, biochar and gas. Biochar is a by-product, generally obtained at temperatures of about 450-550 ℃, and can be used to improve the agricultural performance of soils with low productivity. The characteristics of biochar and bio-oil depend strongly on production conditions and the nature of the starting biomass. Crucial factors include the composition of the feedstock (such as carbon and hydrogen content), as well as physical parameters such as particle size and ash content. Removing unwanted elements from the feedstock (such as ash and volatiles) before pyrolysis increases the efficiency of the process.

There are three main types of pyrolysis:

- **Slow pyrolysis**: occurs at temperatures of 300 to 500 ℃ with a long residence time; the main product is charcoal from wood, which accounts for about 30 % of the initial dry matter.

- **Fast pyrolysis**: takes place at temperatures of 500 to 650 ℃, producing mainly gases that account for 80 % of the initial weight.

- **Flash pyrolysis**: occurs at temperatures of 800 to 1000 ℃, with a high heating rate and very short residence time of less than one second; produces 60% liquid products.

Flash pyrolysis is the most promising process, as it transforms biomass into a liquid product called bio-oil or raw tar, with a high energy content, easily transportable and storable for a long time without degradation problems. However, pyrolysis has some disadvantages, such as the poor physicochemical and thermal properties of bio-oil, high oxygen content, high viscosity and low calorific value. To improve bio-oil, it is necessary to reduce the moisture content, acidity and viscosity. Among improvement technologies, integration of catalysts into the pyrolysis reaction is promising, as it reduces additional reactive oxygenated compounds.

Catalytic pyrolysis is a technique that allows these requirements to be achieved, with the subsequent production of bio-oil containing phenolic biochemicals. Ideal catalysts must be highly selective, recyclable, inexpensive and resistant to deactivation. Most catalysts used for bio-oil upgrading are supported by inexpensive materials such as alumina, carbon or silica.

Gasification

Gasification is a physicochemical process that converts a solid fuel, such as wood or plant biomass, into a synthetic gaseous fuel known as syngas. This process involves incomplete oxidation of carbon compounds at high temperatures in an oxygen-deficient environment. There are two main types of gasification: conventional and hydrothermal (HTG). Although both aim to produce syngas, they differ in the composition of the gases produced and the operating conditions.

Conventional gasification converts biomass to hydrogen-rich syngas at temperatures above 800 ℃, using a gasifying agent such as air, steam, CO_2 or their mixtures. This agent facilitates the conversion of heavy hydrocarbons and solid coal to syngas. HTG occurs in the presence of water at temperatures and pressures above the water critical point (temperature > 374 ℃ and pressure > 218 atm). Supercritical water promotes the dissolution of biomass into syngas. Both processes are more efficient than combustion, although the syngas produced has a lower heating value than the starting material.

These processes can be applied to both fossil fuels such as coal and renewable fuels such as woody biomass, producing syngas with varying compositions but similar technical issues. The syngas contains a mixture of carbon monoxide, molecular hydrogen, methane, carbon dioxide, water vapor, molecular nitrogen, trace hydrocarbons (ethylene, ethane) and contaminants (ash, tar, char, oil). Before use, the syngas must be purified through physicochemical, electrostatic and water washing technologies. Once purified, it can be used in endothermic engines, external combustion engines or microturbines. The efficiency of gasifiers for power generation is 30-35%, higher than that of combustion facilities. However, plant complexity and syngas purification issues limit the use of gasification mainly to pilot plants. In Italy, experiments are being conducted with pilot plants that gasify rice husks and wood residues. These experiments offer a promising opportunity for the production of low-cost hydrogen that can be used, for example, in fuel cells.

1.5.2   Biochemical processes

Biochemical (or biological) conversion includes two main processes: anaerobic digestion and fermentation. Anaerobic digestion uses bacteria to convert organic matter into biogas, a mixture of methane and carbon dioxide. This process is cost-effective and widely applied around the world. Fermentation, on the other hand, employs yeasts to convert the sugars in the raw material into ethanol. The resulting product is a dilute alcohol that requires distillation, resulting in lower overall performance and high plant costs.

Both technologies are well known and adapted to different raw materials, environments and purposes globally.

Anaerobic Digestion

Anaerobic digestion is a biochemical process in which biomass is converted into biogas, a mixture of methane and carbon dioxide, by different strains of microorganisms in an anaerobic environment. This process is particularly useful for treating a wide range of organic materials, including agricultural waste, sewage sludge, food waste and animal manure. Anaerobic digestion occurs in a liquid environment and can be schematized into four different stages, in which a particular strain of bacteria operates by producing reaction intermediates as catabolites that act as substrates for the next population in the trophic chain.

The process begins with hydrolysis, during which organic macromolecules such as carbohydrates, proteins, and lipids are broken down into simpler molecules such as sugars, amino acids, and fatty acids. This occurs through the action of hydrolytic enzymes produced by bacteria. Then, in the acidogenesis stage, the hydrolysis products are further degraded by acidogenic bacteria, producing simple organic acids (such as acetic, propionic, and butyric acids), alcohols, carbon dioxide, hydrogen, and ammonia. In the acetogenesis step, organic acids and alcohols are converted to acetic acid, hydrogen and carbon dioxide by acetogenic bacteria. Finally, in methanogenesis, methanogenic bacteria convert acetic acid, hydrogen and carbon dioxide into methane and water. This stage is crucial for the production of biogas, which can be used as a renewable energy source. The biogas generated can be used directly as a fuel for heat and power generation, or purified to obtain biomethane, a fuel equivalent to natural gas. Digestion significantly reduces the volume of organic waste, turning it into a stable residue (digestate)

that can be used as a fertilizer. It also contributes to the reduction of *GHGs*, as the methane produced is captured and used instead of being released into the atmosphere from the natural decomposition of organic waste.

The applications of anaerobic digestion are numerous. In agriculture, anaerobic digestion plants are used to treat animal manure and crop residues, producing biogas and organic fertilizers. Wastewater treatment plants use anaerobic digestion to process sewage sludge, reducing the volume of sludge and generating energy. In urban centers, collected food and organic waste can be treated with anaerobic digestion, reducing waste volume and producing renewable energy.

Fermentation

Alcoholic fermentation of organic materials is a biochemical process in which simple sugars, such as hexoses and pentoses, are converted to ethanol and carbon dioxide under anaerobic conditions by the action of microorganisms, mainly yeasts such as *Saccharomyces Cerevisiae*. This process is essential for the production of bioethanol, the most widely used liquid biofuel in the world [60]. Raw materials for this process fall into three main categories: simple sugars, starch and ligno-cellulosic substrates. Sugars in biomass can be in the form of polymers, such as starch and cellulose, with general structure $(C_6H_{10}O_5)_n$. These can be converted to glucose by hydrolysis processes [61].

The quality and yields of the fermentation process depend on various factors, including feedstock, temperature, pH, inoculum, and fermentation time. The conversion of sugars to ethanol can occur through different metabolic pathways, depending on the starting substrate. Hexoses, such as glucose, are converted mainly through glycolysis or the Embden-Meyerhof (EMP) pathway [62]. Pentoses, on the other hand, are converted through the pentose phosphate pathway (PPP). The conversion reactions of hexoses are generally faster than those of pentoses [63].

In addition to ethanol and CO_2, alcoholic fermentation also produces by-products such as glycerol and carboxylic acids, which may have commercial applications or be further processed. At the end of the fermentation process, ethanol is distilled and dehydrated to obtain concentrated alcohol. The solid residues, known as distillers grains, can be used as fuel in boilers for energy production or as livestock feed [63].

1.6 Bio-oils Upgrading Processes

Among the various fuel products from thermochemical processes, bio-oil is a liquid fuel highly preferred over solid (biochar) and gaseous (syngas) fuels, mainly because of its higher energy density. Bio-oil is a highly viscous black organic liquid with a pH ranging from 3.5 to 4.2, has a typical smoky smell and an energy value ranging from 70 to 95 % of crude oil. Bio-oil contains a wide range of low-carbon organic compounds, such as aldehydes, ketones, carboxylic acids, and aromatic compounds, along with about 20 wt% water. The carbon content in bio-oil is predominant, occupying between 63% and 78%. Oxygen is the second most abundant element, with a concentration ranging from 7% to 26%. In addition, bio-oil contains hydrogen (7.6–11.2%), nitrogen (0.5–7.6%) and sulfur (0.4–1.4%).

Due to the low amount of sulfur in the biomass from which it is originated, bio-oil is considered carbon and *GHG* neutral, with little or no SO_x emissions. This characteristic makes it a more sustainable fuel than traditional fossil ones. Despite its advantages, bio-oil has some inherent limitations arising from its conversion processes. These include its acidic nature, oxidative instability, presence of heteroatoms, and water and oxygen content, which reduce its suitability as a direct use fuel. These undesirable properties limit its use in petroleum refineries for transportation and other industrial applications. Because of the difficulties associated with the invariable composition of bio-oil, it is essential to develop and apply upgrading methods to make it usable. Upgrading strategies focus on reducing viscosity, corrosivity, oxygen, nitrogen, ash and water contents, as well as mitigating phase separation, polymerization, coking and precipitation problems.

Among the bio-oil upgrading processes, the most studied include: **(a)** catalytic cracking, which breaks down complex molecules into lighter, more useful fractions; **(b)** steam reforming, which converts bio-oil into syngas that can be further processed into liquid fuels; **(c)** esterification, which reduces the acidity of bio-oil, improving its fuel properties; and **(d)** catalytic hydrodeoxygenation (HDO), which removes oxygen present in the form of water, improving the stability and energy value of bio-oil. Successful implementation of these technologies can make bio-oil a key component in the energy mix of the future, contributing to the reduction of *GHGs* and global energy sustainability.

1.6.1 Catalytic cracking

Catalytic cracking is a chemical process that breaks down the large and complex molecules in bio-oils into smaller and more useful hydrocarbons. This process not only reduces the oxygen content, improving the stability and heating value of bio-oils, but also makes them more compatible as fuels and chemical feedstocks. Catalysts used in catalytic cracking include zeolites, metal oxides and mesoporous materials, each offering specific advantages [64]. Zeolites, particularly *HZSM-5*, are among the most studied catalysts for catalytic cracking because of their high specific surface area and acidity. These characteristics facilitate the deoxygenation of compounds into bio-oils, producing light hydrocarbons such as alkenes and aromatics, which are key fuel components in the gasoline portfolio. The microporous structure of zeolites allows selection of particle size of the products generated, increasing the efficiency of the process [65].

Metal oxides, such as those containing nickel, cerium and zirconium, are efficient in promoting cracking reactions and reducing the formation of coke, a byproduct that can deactivate catalysts. The design of these catalysts, including the choice of support materials, is crucial to optimizing catalytic activity and stability. Bifunctional catalysts, which combine acid and metal properties, can better balance cracking and hydrogenation reactions by reducing the formation of unsaturated intermediates, which are precursors to coke [66].

The catalytic cracking process typically operates at high temperatures, between 500 and 700°C, to ensure efficient breakdown of bio-oil components. Optimization of operating conditions, such as temperature, pressure and the ratio of catalyst to feed, is essential to maximize the yield of desired products and minimize the formation of undesirable byproducts. The main challenges include catalyst deactivation due to coke deposition and metal sintering. However, the use of catalysts with strong supports and the inclusion of metal promoters can mitigate these problems, improving catalyst durability and efficiency [67].

1.6.2 Steam reforming

Steam reforming is a chemical process in which oxygenated compounds in bio-oils react with steam at high temperatures, converting to carbon monoxide (CO) and hydrogen (H_2) in presence of a catalyst. This process is typically accompanied by two other key reactions: water gas shift (*WGS*) and methanation [68]. During the

water gas shift reaction, carbon monoxide (CO) reacts with water (H_2O) to form carbon dioxide (CO_2) and hydrogen (H_2). On the other hand, in the methanation reaction, carbon monoxide (CO) reacts with hydrogen (H_2) to obtain methane (CH_4) and water (H_2O). While reforming is an endothermic equilibrium process, both methanation and *WGS* are exothermic reactions [69, 70].

The equilibrium of steam reforming is favored by high temperatures and low pressures, while the *WGS* process tends to produce more CO and H_2O at high temperatures. In recent years, research has focused on developing advanced catalytic materials to optimize bio-oil reforming. The aim is to find metals capable of activating oxygenated compounds and facilitating vapor adsorption, as well as developing formulations that reduce coke formation. The latter is a significant problem in bio-oil reforming [68]. In fact, bio-oil components are thermally unstable and undergo a series of decompositions that lead to the formation of coke. In addition to thermal coke, the tendency of oxygenates to produce solid carbon on the catalyst surface is also high. An ideal catalyst should, therefore, not only promote reforming but also suppress reactions that lead to the formation of unsaturated intermediates, precursors to coke [71].

Nickel-based catalysts are widely used because of their relatively low cost and high efficiency. Nickel possesses high activity in breaking C-C bonds and high selectivity in H_2 generation. However, simple nickel catalysts can quickly deactivate due to coke formation and the presence of contaminants such as sulfur. To overcome these problems, they must be modified. In this direction, Yan *et al.* found that nickel-based catalysts with CeO_2 as an additive and ZrO_2 as a support show significantly better performance than commercial nickel catalysts in bio-oil reforming [72]. CeO_2 acts as a stabilizer, improving resistance to coke formation and deactivation, while ZrO_2 increases nickel dispersion and thermal stability of the catalyst. Iriondo *et al.* [73] compared the performance of nickel-based catalysts with various elements (Mg, Zr, Ce, and La) in glycerol reforming, finding that the Zr-containing catalyst had exceptional selectivity and a product gas composition in line with thermodynamic predictions. The presence of ZrO_2 showed improved catalyst stability and reduced coke formation. In addition to nickel-based catalysts, researchers have explored the use of other metals and materials to improve the efficiency of bio-oil reforming. Noble metal-based catalysts such as platinum and rhodium offer high performance, but their high cost limits large-scale application. Recently, the use of catalysts supported on mesoporous materials and nanoparti-

cles has shown promising results in reducing coke formation and increasing catalyst lifetime.

Continued research on catalysts aims to minimize coke formation and maximize process efficiency by exploring new compositions and materials to address operational challenges and improve overall performance.

1.6.3 Esterification

Esterification is a chemical upgrading method widely used to improve undesirable properties of bio-oils, such as high corrosivity, low pH and limited stability. Thus, ester formation enables the reduction of relatively high concentrations of acetic acid and trace of formic and propanoic acids present in bio-oils derived from biomass rapid pyrolysis [74]. Traditionally, esterification is carried out using homogeneous acid catalysts such as sulfuric acid. However, due to the corrosive nature of these chemicals as well as the difficulty of separation, this route is not ideal. In this sense, the use of solid acid catalysts, which possess high acidity and tailored porosity, is more appropriate [75]. Most studies employ acidic ion exchange resins or zeolites since they are readily available. However, other possible catalysts for this application are currently being developed, including metal oxides (such as TiO_2 and ZrO_2) and mesostructured materials (SBA-15) modified with sulfonic groups ($-SO_3H$) to generate acidic centers [76, 77]. These inorganic-organic hybrid materials are very promising for processing feedstocks such as bio-oils, which are rather viscous and contain bulky molecules, because their pore architecture and surface hydrophobicity can be modulated [78]. This last aspect is relevant due to the reversibility of esterification reactions and the high water content of bio-oil. To circumvent this problem, distillation has been applied in combination with esterification [79].

Esterification of organic acids can also occur with alcoholic components intrinsic to bio-oils, particularly phenolic compounds such as guaiacol and cresols and oxygenates such as hydroxyacetone and levoglucosan, or via externally added alcohols such as methanol, ethanol or butanol [61, 80]. The latter are advantageous in terms of carbon neutrality because they can be derived through fermentation of biomass from renewable resources. Since esters' boiling points are lower than their parent acids, upgrading by esterification offers the possibility of reactive distillation to remove water, unreacted alcohols and volatile esters, resulting in light and heavy oil fractions with weaker acidity and higher chemical stability and viscosity

than conventional ones [81].

1.6.4 Catalytic Hydrodeoxygenation

The catalytic hydrodeoxygenation (HDO) reaction represents a promising technique for eliminating oxygen content and enhancing the quality of bio-oil derived from lignin, transforming it into high-quality transportation fuels. However, due to the complex composition of bio-oil, most studies focus on the HDO of model molecules representative of lignocellulosic biomass, such as isoeugenol, guaiacol, phenol, catechol, and cresol. The HDO process utilizes high pressures of molecular hydrogen to remove oxygen atoms from the target molecules, modifying O-C, C-O-H, and C-C bonds to increase the energy density and stability of the fuel. This process, also known as hydro-pyrolysis, hydrocracking, hydrotreating, or hydrogenolysis, includes various reaction pathways such as the breaking of intramolecular bonds through cracking, deoxygenation, hydrogenation of the aromatic ring, and the removal of alkyl and methoxy groups from oxygenated compounds [82, 83, 84] (see **Figure 1.6**).

Similar to hydrodesulfurization (HDS), which removes sulfur atoms from crude oil to form stable fuels, the effectiveness of the HDO process depends on the type of catalyst, hydrogen pressure, temperature, and the quality of the bio-oil. The HDO reaction is currently of great interest, with various pathways proposed in the literature for its application to phenolic compounds to design more efficient catalysts:

1. **Hydrogenation followed by Deoxygenation (HYD)**: this pathway relies on the sequential hydrogenation of the aromatic ring on metallic sites, followed by deoxygenation on the acidic sites of the catalyst. The initial saturation of the aromatic ring helps weaken the $C_{aryl}-O$ bond, facilitating its cleavage through deoxygenation. However, HYD cannot occur with all catalysts, but only with those containing a support with sufficient acidity to catalyze deoxygenation.

1. **Direct Deoxygenation (DDO)**: this involves the cleavage of the $C_{aryl}-O$ bond followed by hydrogenation of the aromatic ring. This pathway requires relatively high activation energy compared to the HYD mechanism and may occur depending on the temperature and catalyst used.
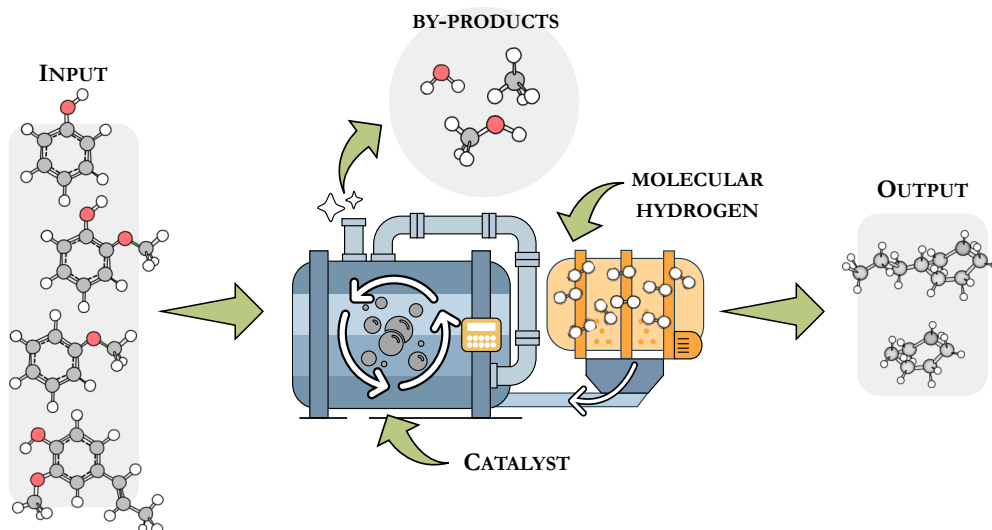
Figure 1.6: Scheme of a typical HDO process in which the reactants, consisting of model compounds of lignocellulosic biomass (phenol, guaiacol, cresol and isoeugenol, respectively from top to bottom), and molecular hydrogen, react in the presence of a catalyst to produce cyclic saturated hydrocarbons and H_2O, CH_3OH and CH_4 as reaction by-products.

3. **Tautomerization-Deoxygenation**: this pathway starts with a rapid and reversible tautomerization leading to the formation of unstable ketonic intermediates. These intermediates undergo secondary hydrogenation, producing partially or fully hydrogenated products. The final step is deoxygenation, which converts the intermediates into arenes or saturated hydrocarbons.

The HDO reaction mechanism is largely determined by the catalyst employed, as well as by temperature, which affects the product selectivity, and by the partial pressure of H_2. Temperature changes alter the stability of intermediates and their subsequent conversion, impacting deoxygenation. Although temperature has a positive effect on kinetics, higher temperatures can also lead to catalyst deactivation through sintering and coke deposition. The partial pressure of H_2 can favor deoxygenation (low partial pressures) rather than hydrogenation (high partial pressures). Therefore, the balance between temperature and H_2 partial pressure primarily determines the HDO pathway. Additional, though less criti-

cal, parameters include contact time, initial substrate concentration, solvent used, substrate-to-solvent ratio, and substrate-to-catalyst ratio. Optimizing all these process parameters is crucial for achieving a high degree of deoxygenation [85].

A wide variety of precious and non-precious metal-based catalysts, including metal oxides, carbides, transition metal sulfides, and phosphides, have been evaluated so far. For their application, a deep understanding of their catalytic nature concerning the oxygenated molecules of bio-oil, as well as their specific ability to withstand low H_2 pressure and high operating temperatures, is necessary. Furthermore, physical characterization, including particle size, active sites, and chemical characteristics such as acidity and basicity, are critical for catalytic activity. Since metallic catalysts possess reducing power to activate hydrogen, their main functions during the HDO process are to promote the hydrogenation of an aromatic ring or unsaturated molecule and initiate the deoxygenation process through direct hydrogenolysis. The characteristics of the catalyst are complemented by those of the potential catalytic supports, which are responsible for dispersing and stabilizing the active metal species. It is believed that the HDO reaction utilizes acidic sites, provided by Lewis and Brønsted acidity, made available by the catalytic supports.

Regarding the selection of metals for use as catalysts, it has been shown that the use of noble metals (e.g., Pt, Ru, and Ir) provides high yields of hydrocarbons as final products. Generally, catalysts containing noble metals as active centers are more active and stable than those created with other metals. Additionally, they do not require a sulfiding agent to keep HDO active, thus avoiding unexpected product contamination during their use. However, the high cost of precious metals and their susceptibility to coking and sintering during the catalytic hydrotreatment process cause significant catalyst deactivation and additional expenses. Consequently, many researchers have begun working with supported non-noble transition metals, which are less expensive, such as Ni, Cu, and Co. Murzin and collaborators, after several studies, argue that Ni-based catalysts can be considered an effective alternative to noble metals due to their low cost and dual functionality towards hydrogenation and hydrogenolysis. Ni-based catalysts have been widely used in HDO reactions with alcohol as a hydrogen donor, thanks to their superior ability to absorb reactants and activate hydrogen in its atomic state. Cu-based catalysts, on the other hand, have demonstrated a natural predisposition for breaking C-O bonds rather than C-C bonds [86].

In addition to metal catalysts, carbides, phosphides, and metal nitrides have attracted particular interest in recent years due to their potent hydrotreating activities. Phosphides, characterized by acidic sites and the ability to activate hydrogen, are used in deoxygenation reactions. Carbides, instead, are studied for their catalytic similarities to noble metals like Pt and Ru, thanks to the alignment of the d-band density of states with the Fermi level, due to the insertion of carbon into the metal lattice. Other widely studied catalysts are zeolites, which act mainly as acidic catalysts and facilitate the removal of oxygen atoms from lignocellulosic biomass molecules. Their porous structure, with well-defined pore sizes and shapes, allows for a uniform distribution of active sites, high selectivity for specific deoxygenation reactions, and a significant reduction in the formation of unwanted byproducts such as coke or light gases. Moreover, surface modifications and/or the introduction of co-catalysts, coupled with high thermal stability, are features that effectively promote HDO reactions. For example, L. Bomont *et al.* [87] synthesized microporous H-Beta-25, H-Beta-150, and H-Beta-300 zeolites modified with Pt and Ir, MCM-41 mesoporous structures, and SiO2 via an evaporation impregnation method. They observed that the most active and selective catalyst was Pt-H-Beta-300, which exhibited the lowest acidity and the largest crystalline size of the zeolite among the Pt and Ir modified Beta zeolites studied. A similar study was conducted by M. E. Martínez-Klimov *et al.* [88], investigating the effects of binder addition, zeolite acidity, and metal location on the hydrodeoxygenation of isoeugenol over a series of bifunctional catalysts consisting of platinum supported on H-Beta-25 or H-Beta-300 zeolite and Bindzil as a binder. It was generally observed that catalysts where Pt was located closer to the acidic sites (deposited only on the zeolite or on both zeolite and binder) showed higher conversion of dihydroeugenol and higher yield of propylcyclohexane, whereas depositing platinum on the binder resulted in lower activity.

Special attention has been paid to catalytic hydrodeoxygenation of biomass model compounds as a method of bio-oil upgrading. This process, which is crucial for improving the properties of bio-oil, is the central theme of this thesis. Through *DFT* calculations, the mechanisms underlying the reaction on different model molecules, catalysts and supports will be explored.

1.7 Catalysis and Green Chemistry

Since the 19th century, chemistry has transformed our lives, shaping society the provision of energy, pharmaceuticals, crop protection, food, and innovative materials. Despite being the science with the greatest impact on our daily lives, the chemical industry suffers from a poor public reputation. Up until the 1980s, it has been accused of producing stoichiometric amounts of waste, leading to significant levels of air and water pollution, and blamed for its inadequate resource management. Over the past 200 years, humanity has improperly and disproportionately utilized natural resources, compromising Nature's recovery capacity [89, 90]. Fortunately, a paradigm shift occurred in the 1990s, transitioning from a "command and control" approach to environmental stewardship. This new, scientifically and economically advantageous approach embraced the concept of sustainability [91]. A sustainable society is defined as one that "meets the needs of the present without compromising the ability of future generations to meet their own needs". Sustainable development, a strategic goal, can be achieved through various approaches, prominently featuring green chemistry as a crucial step [92]. Green chemistry focuses on designing chemical products and processes that generate and utilize reduced (or preferably zero) waste. It is grounded in the 12 principles formulated by Anastas and Warner [91], summarized by the simple concept: "Prevent, not cure". In practice, this involves reengineering chemical pathways to: **(i)** use natural resources more efficiently [93, 94, 95], **(ii)** reduce the volume of hazardous/polluting reagents and solvents [96, 97], and **(iii)** promote the substitution of fossil fuels with renewable alternatives [98, 99, 100, 101]. Achieving these goals necessitates the design of new, efficient catalysts that are active under mild conditions and can be sustainably produced without leading to unacceptably high levels of toxic pollutants [102, 103, 104]. However, before any of these new catalysts can be developed, a fundamental understanding of the properties and currently most environmentally sustainable options must be obtained, enabling the design of their replacements [105, 106, 107, 108, 109]. Catalyst design aims to optimize factors such as stability, turnover number, solubility, and ease of separation from the product. Changes in ligand design or metal selection can yield significant improvements in selectivity, energy consumption, and solvent usage [89]. As Richard Sheldon pointed out, "[...] In fact, as far as chemistry is concerned, catalysis is the key to sustainability [...]" [90]. Catalysts come in various types, ranging from simple protons (H^+),

through Lewis acids, to organometallic and inorganic polymers, and enzymes. For simplicity, catalysis can be categorized into three main types: homogeneous, heterogeneous, and enzymatic. Although the process conditions differ significantly in each, they are based on the same principles. Heterogeneous catalysis, in particular, has revolutionized the chemical industry by enabling the selective conversion of renewable raw materials such as biomass into industrially relevant chemicals, thereby reducing dependence on fossil fuels and mitigating the environmental impact of chemical processes.

1.7.1   Catalysis on metal cluster

Understanding catalysis at the atomic level is a fundamental objective. Supported metal clusters (*SMCs*) have the potential to play a pivotal role in modern chemical industry, and following recent advancements in synthetic methods for metal clusters, they are already considered a distinct subfield of heterogeneous catalysis. Significant efforts have been dedicated to comprehending this phenomenon and designing highly efficient and selective catalytic clusters [110].

More specifically, *SMCs* are a type of heterogeneous catalyst consisting of systems composed by a few metal atoms (clusters) stabilized on solid supports such as metal oxides, silica, carbon-based derivatives, and zeolites. *SMCs* are promising candidates for both basic and applied research due to their unique ability to catalyze reactions that are otherwise difficult to achieve and their relatively straightforward isolation at the end of the process [111]. Despite their high surface-to-volume ratio, SMCs are characterized by metal-metal bonds that are unconventional compared to bulk systems, with specific coordinative unsaturations that result in unique binding modes with the substrate [112]. Given that many important catalytic processes require closely cooperating metal sites for the adsorption, activation, and desorption of reactants, *SMCs* can be utilized in a wide range of catalytic reactions [113].

Furthermore, metal clusters can exhibit structural fluidity during the catalytic process. At high temperatures and under the influence of metal-support and metal-substrate interactions, they can lose their initial rigidity and evolve into fluxional species, generating metastable geometries that can change reactivity [114]. The properties of metal clusters can also be selectively modified by introducing dopant atoms, which alter their electronic structure, relationship with the support, and catalytic activity [115]. The solid support plays a crucial role in cluster catalysis,

imparting unique electronic and geometric characteristics to the metal clusters that are essential for determining efficient processes involving reactive species [113].

Intensive research over the past decades has highlighted that the size and shape of clusters have a significant impact on their reactivity and selectivity [116]. There exists, in particular, a scalable cluster size regime where reactivity changes regularly with cluster size, and a non-scalable size regime for smaller clusters, where reactivity can completely change even with the addition of a single atom. This size-reactivity relationship can be explained in terms of topological changes, resulting electronic variations, and coordinative capacity. Advances in this field have been made possible through approaches in chemical topology and, most notably, quantum mechanical calculations, which are becoming increasingly powerful tools for understanding the processes governing the structure and reactivity of a catalyst [117].

1.7.2 DFT in catalysis

Over the past two decades, computational models have proven to be one of the most efficient and conservative methods for obtaining information on catalysts, becoming an essential component of experimental research [118, 119, 120, 121, 122]. The combined study of experimental and theoretical catalysis has now become a well-established practice, crucial for a fundamental understanding of catalysis at the molecular level [123, 124, 125, 126]. Theoretical calculations have been invaluable for interpreting spectroscopic data, verifying catalytic mechanisms, studying chemical reactivity, and modeling complex reaction pathways. In particular, the application of Density Functional Theory (DFT) to catalysis has provided detailed information on reaction mechanisms at the atomic level. DFT is used to examine the adsorption of reactants on the catalyst surface, the activation of bonds, and the formation of products, providing insights into catalytic active sites, reaction energy barriers, and preferred reaction pathways.

The combination of DFT and experimental studies has enabled many research groups to investigate biomass conversion processes, supporting and guiding the chemical industry towards more environmentally friendly conditions. This translates into reduced energy waste and by-products, as well as increased reaction yields. In the last ten years, numerous studies have applied DFT to understand biomass conversion into fuels, in particular the hydrodeoxygenation (HDO) process. However, since biomass can yield mixtures of several hundred compounds,

the only feasible strategy to better understand the catalytic upgrading process involves mechanistic studies of model compounds representative of lignocellulosic biomass. The simplest models are phenolic monomers such as phenol, anisole, guaiacol, eugenol, and isoeugenol. The *HDO* reactions of these compounds have been extensively studied, as demonstrated by the review by Gollakota and collaborators [86].

For example, in 2015, two computational studies on guaiacol were conducted. The first, by Lu and coworkers, developed a microkinetic model based on parameters obtained from DFT and transition state theory calculations to study the *HDO* of guaiacol on Pt(111) at 573 K, a temperature at which phenolic ring hydrogenation is thermodynamically limited. The model identified two main hydrogenation pathways, with catechol as the primary reaction product, and highlighted that deoxygenation, such as that of phenol or benzene, is significantly slower. They observed that guaiacol deoxygenation proceeds through decarbonylation and possibly phenolic ring hydrogenation followed by C–OH bond cleavage. The model suggests that higher H_2 pressure might facilitate deoxygenation and promote phenolic ring hydrogenation to cycloalkanes, effective only at elevated temperatures. However, this computational study contrasts with some experimental observations, suggesting that the active sites for deoxygenation in Pt catalysts might derive from the support or edge and corner sites of Pt rather than the planar surface of Pt(111) [127].

In the second study, conducted by Lee and coworkers, the reaction mechanism of guaiacol *HDO* to catechol on Pt(111) was investigated using *DFT* calculations combined with linear free energy relationships or Brønsted–Evans–Polanyi (*BEP*) relations. *BEP* relations were proposed for four reaction families: C–H bond cleavage, C–O bond cleavage in C_{ring}–OA/C_{ring}O–CH_x (A=H, x=1,2), O-CH_3 bond cleavage, and O-H bond cleavage. These *BEP* relations were employed to construct a potential energy surface for guaiacol *HDO* on Pt(111), suggesting that guaiacol undergoes methoxy group dehydrogenation rather than direct deoxygenation via dehydroxylation, demethylation, and demethoxylation. The cleavage of the O–CH_x bond, in cases of single or double methyl group dehydrogenation, is followed by hydrogenation of the oxygens attached to the ring. The resulting catechol can then desorb as the main product or undergo further *HDO* to produce phenol. This study suggests that the final step may occur at the Pt/alumina interface, with alumina removing the OH group and Pt performing the necessary

hydrogenation. However, the proposed mechanism does not support the hypothesis of direct demethylation and demethoxylation in the conversion of guaiacol to catechol and phenol [128].

In 2016, a study focused on the catalytic hydrodeoxygenation of phenol on Ru nanoparticles supported on graphene using periodic *DFT* calculations to propose a mechanism for the (*DDO*) pathway. The interaction energies and activation barriers calculated for C–O bond cleavage on bare Ru/C catalyst particles align well with previous studies on the flat Ru(0001) surface and more realistic stepped and terraced Ru surfaces. The results obtained with $Ru_{10}H_x$ particles supported on graphene indicate that a Ru/C catalyst model with explicitly chemisorbed hydrogen on the metal nanoparticle surface (stabilizing Ru–O complexes and creating a barrier separating Ru–O (*DDO*) and Ru–C (*HYD*) intermediates) is essential for a comprehensive understanding of the *DDO* process [129].

Both molecules mentioned have been studied to elucidate the *DDO* reaction mechanism of phenol and guaiacol on Ni_5P_4(001) surfaces using ab initio calculations. Nickel phosphides have shown remarkable catalytic abilities in hydrodeoxygenation reactions and a capacity to preserve product aromaticity. It was found that phenol dissociates immediately with a low activation energy (0.15 eV), whereas guaiacol encounters a higher barrier (1.92 eV). Following the cleavage of O–H and C_{arom}–O bonds, the aromatic fragments of phenol remain oriented perpendicularly/inclined to the Ni_5P_4(001) surface, limiting C=C bond activation in the ring and likely preventing over-hydrogenation, thus maintaining ring aromaticity. Microkinetic modeling highlighted that the overall activation energy decreases with temperature in the range of 500-700 K and that the rate-limiting step of the reaction varies with temperature: for phenol, it is the hydrogenation of the phenyl intermediate to benzene at temperatures below 550 K and C_{arom}–O bond cleavage at higher temperatures, whereas for guaiacol, it is mainly dehydroxylation at temperatures below 600 K and C_{arom}–O bond cleavage at higher temperatures [130].

Finally, for the anisole molecule, two studies can be cited, one conducted in 2018 and another in 2019. In 2018, Zhang and coworkers employed DFT modeling to establish a *HDO* mechanism for phenolic compounds on bifunctional catalysts (metallic and acidic sites). The metals Ni, Co, Mo, and Cu were selected, as the adsorption of anisole on transition metal surfaces showed that these four metals presented the highest adsorption energy values. The results confirmed that

the *HDO* of phenolic compounds, intermediates in the catalytic decomposition of anisole, begins with the protonation of the hydroxyl group and that the presence of metals promotes both the reaction and the dissociation of the hydrogen molecule. Notably, Ni and Mo significantly reduced the energy barriers of *HDO* reactions. Modeling reactions on non-metallic acid catalysts showed that a single methyl group in the *ortho* position of the phenolic compound enhances the $C(sp^2)$–O bond and promotes reactivity, while the presence of methyl groups in both *ortho* positions inhibits the reaction due to steric hindrance. However, the addition of a metallic site compensates for this effect, promoting *HDO*. The excellent activity of metallic/Brønsted sites was consistent with the experimental performance of the corresponding catalysts [131].

In 2019, Agrawal and Kishore conducted a *DFT* study using anisole as a model compound for bio-oil to determine thermochemical parameters for upgrading anisole to platform chemicals. Initially, they conducted a Bond Dissociation Energy (*BDE*) analysis for anisole to determine the energy required to break bonds and initiate the reaction. Subsequently, they proposed three different pathways to produce phenol, benzene, and toluene. Given that the reaction medium is aqueous, a pathway proposing the direct hydrogenation of anisole to produce benzene was also hypothesized as the primary reaction product. The formation of phenol represents the second most energetically demanding reaction, while the formation of toluene is less likely under moderate conditions due to high activation energy. Nonetheless, thermochemical studies indicated that all proposed pathways are spontaneous and technically feasible [132].

Characteristics of bio-oil

Characteristic	Cause	Effect
Low pH	Organic acids from biopolymer degradation.	Corrosion of vessels and pipework.
Viscosity	Chemical composition of bio-oil.	Fairly high and variable with time.
Water content	Pyrolysis reaction and initial water present in feed.	Complex effect on viscosity and stability: increased water lowers heating value, density, stability and increase pH.
Low H/C ratio	Biomass has low H/C ratio.	Upgrading to hydrocarbons is more difficult.
Low miscibility with hydrocarbons	Highly oxygenated nature of bio-oil.	Will not mix with any hydrocarbons so integration into a refinery is more difficult.
Smell or odour	Aldehydes and other volatile organics, many from hemicellulose.	While not toxic, the smell is often objectionable.
Sulphur	Contaminants in biomass seed.	Catalyst poisoning in upgrading.
Char	Incomplete char separation in process.	Aging of bio-oil, sedimentation, filter blockage, catalyst blockage, engine injector blockage, alkali metal poisoning.
Nitrogen	Contaminants in biomass feed, high hydrogen feed such as proteins in wastes.	Unpleasant smell, catalyst poisoning in upgrading NO_x in combustion.
Temperature sensitivity	Incomplete reactions.	Catalyst poisoning in upgrading, irreversible decomposition of liquid into two phases above 100 °C, irreversible viscosity increase above 60 °C.

Table 1.1: Description of the most significant characteristics of bio-oils resulting from biomass conversion, the causes behind them and their effects.

Chapter 2

Methods and Models

2.1 Density Functional Theory

Density Functional Theory (DFT) is one of the most widely used methods for ab initio calculations of the electronic structure of atoms, molecules, crystals, and surfaces. Originally developed to calculate the electronic states of solids, DFT began to find widespread application in quantum chemistry calculations starting in the 1990s. Today, thanks to its high accuracy-to-computational cost ratio, DFT has become the predominant method, employed in more than 80% of all computational chemistry studies [133].

The underlying principle of DFT is the description of an N-electron system by substituting the wave function, which depends on $3N$ spatial variables and N spin variables, with a simpler quantity: the electron density, which depends only on three spatial variables. Despite accounting for correlation energy, DFT does not require prohibitively long computation times, thus representing an ideal compromise between the Hartree-Fock method and heavily correlated calculations.

The validity and applicability of this theory are guaranteed by the first Hohenberg-Kohn (HK) theorem, which states that the ground-state electron density of a system contains all the necessary information (such as the number of electrons, the number, charge, and position of the nuclei) to define the molecular Hamiltonian, and therefore it will also contain all information related to its eigenvalues and eigenfunctions. This implies that any ground-state observable physical quantity, such as total energy, can, in principle, be expressed as a functional of the density. For the total energy functional, a minimization principle is valid, which translates

into the second Hohenberg-Kohn theorem, essentially the variational theorem applied in this context. This theorem asserts that the HK functional, a sum of the kinetic energy and the electron-electron repulsion functionals, achieves the lowest possible energy value if and only if the exact ground-state electron density is introduced into the equation.

While the Hohenberg-Kohn theorems form the theoretical foundation of Density Functional Theory, they are not sufficient on their own, as they do not provide a practical method for calculating the ground-state electronic properties from the exact electron density. The practical implementation of the HK theorems was achieved through the approach introduced by Kohn and Sham in 1965, which solves the variational problem of minimizing the energy functional using Lagrange multipliers.

This approach expresses the ground-state electron density as the sum of the squared moduli of single-electron functions, known as Kohn-Sham orbitals. Similar to the Hartree-Fock method, the Kohn-Sham approach leverages the concept of non-interacting particle systems. Although these systems do not correspond to physical reality, they allow the exact calculation of kinetic energy. Kohn and Sham utilized this non-interacting framework to overcome the longstanding challenge of defining kinetic energy as a functional of the electron density.

The central, albeit unprovable, assumption of the Kohn-Sham scheme is that for any interacting system under a given external potential, there exists a local single-electron potential such that, when applied to a non-interacting system, it reproduces the same electron density as the interacting system.

The problem can be addressed by finding the optimal Kohn-Sham orbitals through a constrained minimization procedure. The resulting equations, known as the Kohn-Sham equations, must be solved iteratively because the Kohn-Sham operator depends on the solutions themselves. In these equations, the contribution of electron correlation to the kinetic energy and the exchange energy are captured by the exchange-correlation functional, whose exact form remains unknown.

Although approximations to this functional are required to satisfy certain physical constraints, it remains unclear whether a systematic procedure exists to approach the exact functional. Consequently, it is crucial to assess the accuracy of a given exchange-correlation functional against appropriate benchmark sets containing experimental data, such as structural parameters, atomization or ionization energies, reaction enthalpies, activation barriers, and more, for a large number of

molecules. For example, one of the first used benchmark set for this purpose was the G2/97 thermochemical database [134], which includes over fifty experimental atomization energies of small molecules composed of main group elements. The number and the quality of benchmark set, however, greatly increase over the years.

It is essential to note that assessing the accuracy of a functional by comparing its results with corresponding experimental data does not provide a definitive measure of its proximity to an exact functional. A more physically accurate evaluation of various functionals would involve a comparative analysis between the modeled exchange-correlation potential and accurate potentials derived from wave function-based calculations. However, such refined potentials are often not available, thus precluding such evaluations [135].

The most common approximations to the exchange-correlation functional can be categorized into four major families: the Local Density Approximation (LDA), the Generalized Gradient Approximation (GGA), the Meta-GGA, and hybrid functionals. The latter, introduced by Becke in 1993, incorporates a fraction of the exact Hartree-Fock exchange term into the exchange-correlation energy formulation, along with semi-empirical parameters that allow for modulation of the various contributions [136].

The most widely used hybrid exchange-correlation functional is B3LYP (Becke, 3-parameter, Lee-Yang-Parr), renowned for its accuracy across a range of chemical applications, including complex systems. Nevertheless, *DFT* also exhibits limitations, one of the most significant being its inability to adequately describe dispersion interactions. As will be discussed in the following section, to enhance this description, empirical corrections have been developed and integrated into functionals, thereby improving their performance while maintaining nearly constant computational time.

2.1.1 *DFT–D* Method

The *DFT-D* method, extensively tested and successfully applied to a variety of systems, was specifically designed as a correction to common hybrid functionals that, while suitable for describing many properties, may not be optimal for non-covalent interactions. Despite integrating the best features of nearly all approaches, it maintains low numerical complexity and provides results that are readily interpretable [137]. This method allows for a more consistent description of dispersion interactions with minimal empirical input—namely, the introduction of a param-

eter associated with each chemical element—while still maintaining an ab initio approach. However, its major drawback is that this correction is independent of the electronic structure and, crucially, does not influence it. Although one might assume that these effects are minor in most practical applications, this limitation ultimately constrains accuracy, particularly in chemically unusual cases [138].

In this doctoral research, the correction proposed by Grimme [138] was selected, as it appears to be, according to the literature, the most promising candidate for permanent integration into all hybrid exchange-correlation functionals.

2.2   Computational Details

All calculations pertaining to the HDO reaction and the decomposition of isoeugenol and guaiacol, discussed in subsequent sections, were performed within the framework of density functional theory (*DFT*) using the Gaussian 16 software package [139]. The DFT computations employed the B3LYP hybrid exchange-correlation functional [140], augmented by Grimme's D3 dispersion correction scheme to account for long-range dispersion interactions [141]. The LanL2DZ basis set of Hay and Wadt [142, 143] was used for all calculations, which incorporates Dunning's D95 basis set [144] for light atoms (H, C, O), while a double-zeta valence basis set, paired with an effective core potential, is applied to platinum atoms. Polarization functions, comprising primitive Gaussian orbitals with angular momenta and exponents as follows – H (s: 0.049, p: 0.587), C (p: 0.0311, d: 0.587), and O (p: 0.0673, d: 0.961) – were added to the D95 basis set. These functions were sourced from the *EMSL* Basis Set Exchange repository [145].

The identification of minima and transition states along reaction pathways was accomplished by calculating and analyzing the harmonic vibrational frequencies. Structures corresponding to minima on the potential energy surfaces (PES) were confirmed to exhibit no imaginary frequencies, while transition state structures were validated by the presence of a single imaginary frequency corresponding to the reaction coordinate. Reaction energetics are reported as zero-point vibrational energy (ZPVE)-corrected values (E_{ZPV}); desorption energies for stable products were corrected for basis set superposition error (*BSSE*) using the counterpoise method of Boys and Bernardi [146]. The *BSSE*, as detailed in the next section, was calculated as the self-consistent field (SCF) energy correction and is presented in parentheses alongside the raw E_{ZPV} energy.

All calculations concerning the growth of M_n clusters (with M = Ni or Pt and n = 1-10) on graphene, as well as the reactions of guaiacol and isoeugenol on supported clusters, were performed under periodic conditions using the *SIESTA* approach as implemented in the homonym code [147]. The Perdew-Burke-Ernzerhof (*PBE*) [148] exchange-correlation functional was employed, alongside a double-zeta polarized (DZP) basis set with a 0.005 Ry energy shift. A mesh cutoff of 450 Ry was applied to define the real-space integration grid, while the reciprocal-space was sampled using a 4×4×1 Monkhorst-Pack grid.

In all calculations, the total electronic spin of the repeating cell was not constrained, allowing the software to determine the optimal spin polarization for each system. Vibrational frequencies were not computed after structural optimization due to the prohibitive computational cost, implying that the identified structures may not represent true energetic minima, but rather other stationary points on the potential energy surface. Consequently, zero-point energy (ZPE) was not included, and the reported final energies correspond solely to the total electronic energy.

The transition state searches for hydrodeoxygenation (HDO) and decomposition reactions on graphene-supported clusters were conducted using the Empathes code [149], which implements the Nudged Elastic Band (*NEB*) method and interfaces with *SIESTA*. Each *NEB* calculation involved six intermediate images generated via the image-dependent pair potential approach, connected by dynamic springs. The elastic band optimization was carried out using the FIRE algorithm, with a convergence threshold of 5×10^{-3} Eh/Å on the norm of the total NEB forces.

2.3   Basis Set Superposition Error

The interaction energy values and the geometrical optimizations of the reference complexes have been corrected for the Basis Set Superposition Error (*BSSE*), which arises due to the formation of an adsorbate/cluster system. This error occurs because the basis set, localized on one reagent, can function as a set of diffuse functions for the electrons of the other reagent, and conversely, leading to a spurious increase in the interaction energy between the two fragments. Since *BSSE* would not be present with a complete basis set, one method to mitigate this issue is to employ progressively larger basis sets. As the basis set is expanded to pro-

vide a more accurate description of the orbitals far from the atomic centers (via increasingly diffuse functions in a traditional calculation), additional basis functions arising from the description of atomic orbitals of another reagent and located in the same long-range region are unnecessary and do not enhance the quality of the calculation. However, using a very large basis set is often computationally prohibitive. Alternatively, the *BSSE* can be estimated using the Boys-Bernardi counterpoise method [142], which approximates *BSSE* as a sum of fragment contributions and can be applied to both mean-field and correlated methods [144].

To obtain the correct interaction energy between two fragments A and B forming an adduct AB, the following four steps are necessary:

1. Calculation of total system energy comprising both fragments, including all electrons and nuclei. This gives the energy of the complex, denoted as W_{AB}.

2. Calculation of the isolated fragment energies A and B in their equilibrium geometries, denoted as W_A and W_B, respectively.

3. Calculation of the energy of each fragment using the geometry which each fragment adopts in the whole aggregate. The energies $W^{\dagger}_A$ and $W^{\dagger}_B$ are thus obtained.

4. Calculation of the energy of each fragment using a modified basis set that includes the basis functions of the other fragment. For example, for fragment A, these additional basis functions are centered on the nuclei of fragment B as positioned in the adduct. However, these calculations do not include the nuclei or electrons of the other fragment. This results in the energies W^{*}_A and W^{*}_B.

The counterpoise correction is then calculated using the expression:

$$\Delta W^{\mathrm{BSSE}} = (W_A{}^{*} - W_A{}^{\dagger}) + (W_B{}^{*} - W_B{}^{\dagger}) \tag{2.1}$$

The interaction energy is the given by

$$\Delta W = W_{AB} - W_A - W_B + \Delta W^{\mathrm{BSSE}} \tag{2.2}$$

2.4 Models

2.4.1 Pt$_{10}$

A platinum cluster composed of ten atoms, featuring tetrahedral symmetry and a spin multiplicity of 9, was selected as a representative catalytic species for subnanometer-sized clusters. Its structure reveals atoms with distinct coordination numbers: the four atoms located at the apex of the cluster exhibit a coordination number of three, while the remaining six atoms have a coordination number of six (see **Figure 2.1**). The Pt$_{10}$ cluster is topologically analogous to a tetracapped octahedron, where six atoms form an octahedral core, and its triangular faces are alternately capped by an additional atom positioned perpendicular to the center of the face. This configuration results from global optimization of platinum clusters containing up to ten atoms, as reported by Demiroglu et al [150]. Among subnanometer clusters, Pt$_{10}$ demonstrates considerable stability, attributable to its valence electron count, which allows it to fill multiple electronic shells (a "magic number") [151]. The optimized structure of Pt$_{10}$ shows an average Pt–Pt bond length of 2.71 Å, and its cohesive energy, calculated as $E_c = (E[Pt_{10}] - 10E[Pt])/10$, is 275.4 kJ mol^{-1}. Previous studies have demonstrated that an H$_2$ molecule, upon chemisorption onto a metal cluster, undergoes bond cleavage, forming hydrogen-metal cluster systems where the hydrogen atoms can diffuse freely. In this case, the model catalyst can be viewed as a hydrogen reservoir, ensuring a continuous supply of hydrogen atoms where needed. This behavior stems from both the ease of hydrogen dissociation on the cluster surface and the hypothesized free diffusion of hydrogen atoms through the catalyst. To support these hypotheses, already validated for most metal systems [128, 152], fragmentation and diffusion tests were carried out on a Pt$_{10}$ cluster with one H$_2$ molecule, referred to as the Pt$_{10}$H$_2$ species. Regarding fragmentation, the chemisorption of the H$_2$ molecule was considered on a platinum atom with a coordination number of three, located at a capping site. The adsorption process, characterized by an energy release of 80.5 kJ mol^{-1}, resulted in the formation of a transient species with a spin multiplicity of 9 (**Figure 2.1(a)**), in which a significant weakening of the H–H bond (lengthened to 0.88 Å from 0.74 Å in the free H$_2$ molecule) was observed. This species quickly evolved into a more stable structure, 32.5 kJ mol^{-1} lower in energy (**Figure 2.1(b)**), exhibiting a septet spin multiplicity and undergoing cluster distortion along with
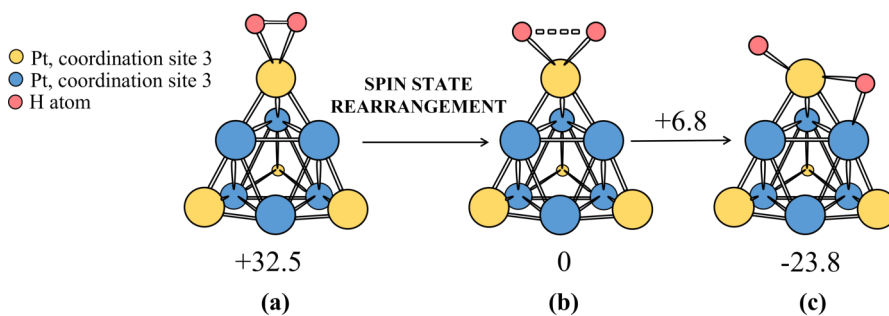
Figure 2.1: Fragmentation of the H_2 molecule on the cluster and relative energies of the involved species (expressed in kJ mol^{-1}). Structure **(a)** represents a transient species in the nonnet state, where a weakening of the bond between the hydrogen atoms is observed. Structure **(b)** is the most stable species, which is in the septet state. Finally, structure **(c)** shows the complete fragmentation of the H_2 molecule, due to the migration of a hydrogen atom from its original position to a cluster edge.

complete H_2 dissociation. During this process, it was observed that a hydrogen atom migrated from the capping position to a bridge position between the same capping atom and a neighboring atom from the octahedral core (**Figure 2.1(b)**), with an activation barrier of only 6.8 kJ mol^{-1}, a negligible energy value.

For the hydrogen diffusion process, five distinct $Pt_{10}H_2$ geometries, characterized by different hydrogen atom arrangements, were considered. Additional evidence supporting the facile diffusion of hydrogen atoms through the cluster was provided by analyzing the two most stable species, labeled as **(a)** and **(c)** in Figure 3, and investigating the migration of a hydrogen atom from one configuration to the other. The estimated activation barrier for this elementary step, 14.3 kJ mol^{-1}, clearly validates the earlier assumptions. Based on these findings, it can be concluded that under the conditions required to overcome the activation barriers in isoeugenol hydrogenation (HDO), which will be discussed later, the barriers governing hydrogen atom diffusion on $Pt_{10}H_2$ clusters are negligible. This implies that hydrogen atoms can adopt any configuration on the cluster. Lastly, it should be noted that, as seen in many metal cluster systems [153, 154, 155], H_2 dissociation results in a reduction of the spin quantum number by one unit in $Pt_{10}H_2$ systems, an occurrence attributed to electron spin coupling phenomena.
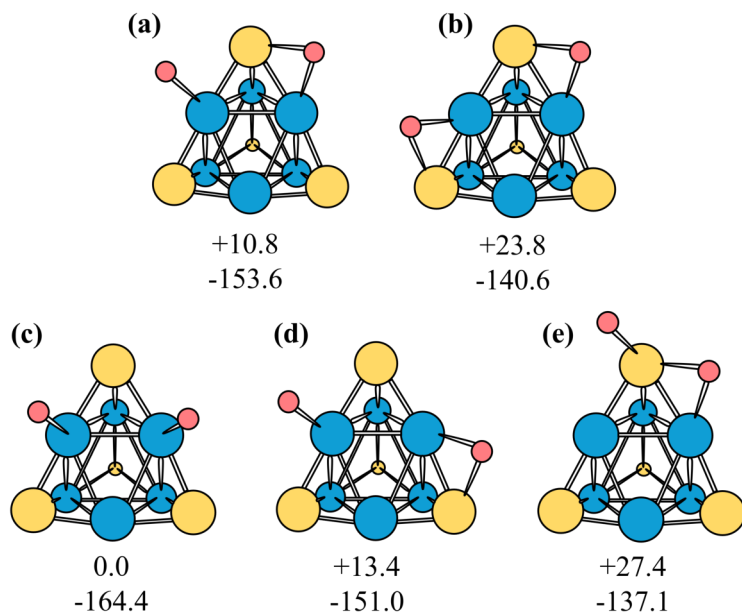
Figure 2.2: The five structures labeled **(a)** to **(e)** differ in the positions of H atoms within the cluster and were used to assess H-diffusion energetics. The values below each figure show the relative energy (in kJ mol^{-1}) compared to the most stable configuration **(c)** (above), and the H_2 chemisorption energy (below), calculated as $E_{ads} = E[Pt_{10} H_2] - (E[Pt_{10}] + E[H_2])$. White, yellow, and light blue spheres represent hydrogen and platinum with coordination numbers three and six, respectively.

2.4.2 Isoeugenol and Guaiacol

Isoeugenol and guaiacol (**Figure 2.3**), containing the key functional groups found in bio-oils derived from lignin, such as hydroxyl, methoxy, and allyl groups, represent particularly suitable molecular models for studying atomistic reactions involved in lignocellulosic biomass conversion. Lignin, a complex polymer abundant in plant cell walls, is composed of phenolic monomers with a variety of functional groups, which can be harnessed to produce bio-oils through thermal or chemical degradation processes. For this reason, isoeugenol and guaiacol are frequently employed in studies aimed at simulating molecular fragmentation and reactivity of lignin-derived compounds.

Isoeugenol, which can be extracted from natural sources such as cloves, nutmeg, and ylang-ylang [156, 157] (where it is the primary component), exists as a mixture of *cis* and *trans* isomers, with the latter typically being predominant. The structural difference between isoeugenol and eugenol, from which it can be obtained via chemical or thermal isomerization, lies in the position of the double bond along the propyl chain [158, 159]. Isoeugenol is widely used in various industrial sectors. In the food industry, it is utilized for its antioxidant properties and as a natural flavoring agent, while in medicine, it is valued for its antiseptic [160], analgesic [161], anti-inflammatory, and anti-arthritic activities [162]. Additionally, it serves as a key precursor in the synthesis of vanillin and vanillic acid [163], compounds with applications in the food, pharmaceutical, and cosmetic industries [164]. Vanillin, in particular, is one of the most widely used flavoring agents globally.

A conformational analysis was conducted on isoeugenol to determine possible structures and their stability. For the *trans* isomer, six conformations were identified by fixing the dihedral angle τ_1 (C5C4C1'C2') at 180°, while angles τ_2 (C2C1OH) and τ_3 (C1C2OC1'') were alternately set to 0° and 180°. An additional three conformations were generated by setting τ_1 at 0° and varying τ_2 and τ_3 at 0° and 180°. The same number of conformations was determined for the *cis* isomer, in which τ_1 was set to 150° to avoid steric repulsion between the CH$_3$ group of the allyl chain and the hydrogen atom on C3 of the aromatic ring. The twelve initial structures identified were then subjected to geometric optimisation. The results show that the most stable conformations for both isomers are those in which an intramolecular hydrogen bond is formed between the hydroxyl hydrogen and methoxy oxygen, i.e. with $\tau_2 = 180°$ and $\tau_3 = 0°$. In these conformations,
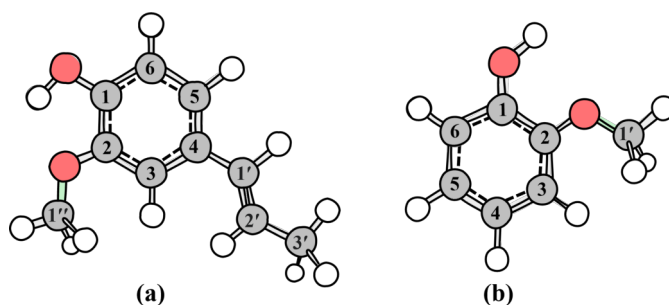
Figure 2.3: Molecular structure of *trans*-isoeugenol **(a)** and guaiacol **(b)** with the IU-PAC numbering of carbon atoms.

the allyl chain orientation is relatively free, with Boltzmann populations of 62.8% ($\tau_1 = 180°$) and 37.1% ($\tau_1 = 0°$) for the *trans* isomer and 55.2% ($\tau_1 = 152°$) and 44.8% ($\tau_1 = -33°$) for the *cis* isomer. Furthermore, it was calculated that the *trans* isomer is approximately 10 kJ mol^{-1} more stable than the *cis* isomer.

Guaiacol (2-methoxyphenol), on the other hand, is a naturally occurring compound found in various plants, including celery seeds, tobacco leaves, orange leaves, and lemon peels [165, 166]. Its chemical structure is characterized by the presence of a methoxy group ($-OCH_3$) positioned *ortho* to the hydroxyl group ($-OH$) on a benzene ring. This arrangement imparts guaiacol with antioxidant and antiseptic properties, making it valuable for numerous industrial applications. It is used in the production of fragrances, as a food additive and preservative, and also serves as a critical intermediate in the synthesis of phenolic resins, dyes, and pharmaceutical products [167].

The same considerations regarding the relative position of the oxygenated groups in isoeugenol also apply to guaiacol, except for the allyl chain.

2.4.3 Graphene

Graphene has been selected as a support for hydrodeoxygenation (HDO) reactions due to its remarkable properties, including high electron mobility, exceptional mechanical strength, and unparalleled chemical and thermal stability. Notably, its thermal conductivity can reach up to 5000 W/m·K, and it boasts a specific surface area of 2630 m^2/g, making it particularly well-suited for hosting nanometric or atomic-scale catalysts, such as nickel or platinum nanoclusters [168, 169, 170].

However, the relatively weak interactions between graphene and metal atoms

often necessitate structural modifications to enhance its chemical reactivity and efficacy as a catalytic support [171]. A widely employed strategy involves the introduction of structural defects. In the present thesis, for example, a single vacancy was created, which generates reactive sites that can increase adsorption energy, stabilizing catalytic species and preventing the aggregation of metal atoms.

In recent years, research on graphene-supported catalysts has experienced rapid growth, particularly in the field of biomass refining. In this context, these catalysts have proven capable of improving both conversion efficiency and selectivity in the production of biofuels [172]. These attributes render graphene a highly promising catalytic support for optimizing various chemical reactions, especially in the pyrolysis and hydrolysis of lignocellulosic biomass, contributing to cost reduction and enhancing the sustainability of industrial production processes [173]. A more extensive discussion on graphene is provided in the **chapter 6**, but is here worth to underline that, from a practical perspective, graphene could be considered too expensive to be used as catalytic support. Nevertheless, the computational study here reported allows to obtain information also on catalytic systems composed by supports that, from a modeling point of view, can be at least in part represented by graphene. This is true, in particular, for some forms of graphene-rich biochar [174], a desiderable support itself produced from biomass.

Chapter 3

HDO reaction of Isoeugenol on Pt$_{10}$ cluster

This chapter provides a comprehensive analysis of the hydrodeoxygenation (HDO) process of isoeugenol, an organic compound of extraordinary relevance to green chemistry and renewable energy applications. HDO represents a central reaction in the context of biomass utilisation, as it enables the transformation of oxygen-rich compounds into more stable, less oxygen-rich hydrocarbons. This transformation is crucial for improving the quality of biofuels and for obtaining high-value chemical materials. After a brief discussion on the chemical characteristics of isoeugenol and its potential as a precursor in the sustainable production of fuels and chemicals, the focus is placed on the role of catalysis in the HDO process, with emphasis on the use of advanced catalysts, such as a subnanometer platinum cluster. The selection of this catalyst is based on its distinctive properties, which enable highly efficient and selective hydrogenation reactions. The discussion proceeds with a thorough analysis of the reaction mechanism, detailing the stages of isoeugenol hydrogenation and the formation of key reactive intermediates. Multiple reaction pathways are explored, highlighting the intricate nature of the elementary steps and their influence on the overall efficiency of the reaction.

Two primary HDO pathways are examined in detail: direct deoxygenation (DDO) and hydrogenation followed by deoxygenation (HYD). For each of these pathways, activation energies and thermodynamic stabilities of the intermediates are analyzed, offering a complete comparison of their energetic and kinetic characteristics. This analysis provides critical insights into the underlying reaction

mechanisms and informs strategies for optimizing reaction conditions to improve both yield and selectivity.

A considerable part of this chapter is dedicated to the application of advanced kinetic models, such as the Simplified Christiansen Method (SCM), which allows the calculation of kinetic rate constants for various reaction pathways. This quantitative approach provides a deeper understanding of reaction dynamics and helps to identify the factors regulating reaction rates. Incidentally, the applicability of the SCM is supported by the assumptions on hydrogen availability on platinum cluster discussed in **Section 2.4.1**. Indeed, these assumption linearize the processes according to the definition of "linear mechanism" given by Murzin [175]. The chapter closes by discussing the broader implications of these results for future research. It proposes potential routes for further investigation, particularly with regard to the role of supports and non-noble metals in the HDO process. Optimisation of catalytic systems and reaction conditions is highlighted as a key area for improving the sustainability and efficiency of chemical production.

3.1   DDO mechanism

The DDO mechanism, as well as the HYD described below, have a common beginning: the hydrogenation of the double on the allyl chain in isoeugenol.

The elementary stages involved in the catalytic hydrogenation of the isoeugenol double bond on the Pt_{10} cluster are shown in **Fig. 3.1**. This reaction is comprised of two main steps: the first step yields a semi-hydrogenated intermediate, $int1/Pt_{10}H^a$, through the transfer of a hydrogen atom from the cluster to the C2 carbon of the allyl group. In the second step, a hydrogen atom migrates from the cluster to the C1 carbon of the chain, leading to the formation of dihydroeugenol/Pt_{10}. In this scenario, as well as in all subsequent cases discussed, the symbol δ enclosed in a circle indicates the diffusion of a hydrogen atom through the cluster toward the reactive center. In this context, the anticipated barrier-free hydrogen diffusion converts $int1/Pt_{10}H^a$ into $int1/Pt_{10}H^b$. Analyzing the activation energies for the two elementary steps suggests that the hydrogenation of the double bond is not a fast reaction, as the energy barriers are slightly greater than those computed for the reaction that converts butene to butane on a subnanometric palladium cluster [154]. The saturation of the double bond results in a system that is 106.3 kJ mol^{-1} less stable than the isoeugenol/$Pt_{10}\,2\,H$ reac-
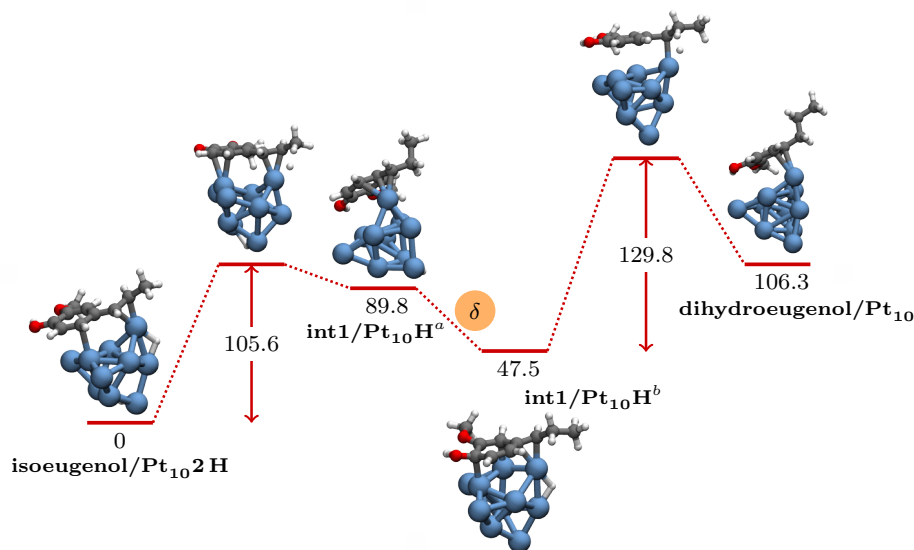
Figure 3.1: The reaction sequence for the catalytic hydrogenation of isoeugenol to dihydroeugenol on the Pt_{10} cluster. The circled δ symbol indicates an elementary step where the hydrogen atom is assumed to diffuse across the cluster to the catalytic site without an associated energy barrier.

tant. This finding is not surprising, as dihydroeugenol interacts with the metal cluster exclusively via the benzene ring. The estimated desorption energy of dihydroeugenol from the cluster is 154.7 kJ mol^{-1} (BSSE = 25.7 kJ mol^{-1}).

The subsequent steps of the reaction involve the direct removal of oxygenated groups. The order and mechanism by which these groups are eliminated give rise to four potential alternative pathways. The selection of the most favorable pathway is determined by multiple factors, such as the stability of reactive intermediates, the energy barriers involved, and the reaction kinetics. These mechanisms (in **Fig. 3.2**) are summarized below:

- **DDO-1**: involves direct removal of the $-OCH_3$ group as methanol with formation of 4-propylphenol from which, by elimination of the $-OH$ group as water, propylbenzene is obtained.

- **DDO-2**: involves first the removal of the $-OH$ group as water with the
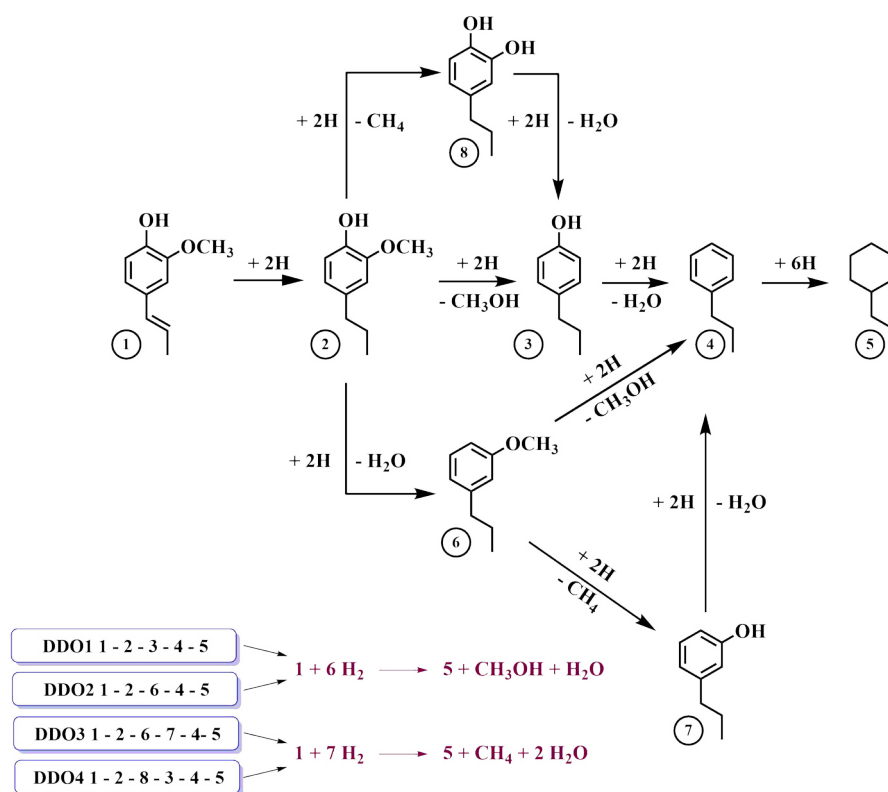
Figure 3.2: Schematic representation of the four DDO mechanisms for the conversion of isoeugenol to propylcyclohexane.

formation of the 1-methoxy-3-propylbenzene species and then the removal of the $-OCH_3$ group as methanol.

- **DDO-3**: in 1-methoxy-3-propylbenzene, obtained by the DDO-2 mechanism through C-OH bond cleavage, methane elimination occurs, leading to the formation of 3-propylphenol. Subsequently, through the elimination of a water molecule, propylbenzene is obtained.

- **DDO-4**: provides the conversion of the $-OCH_3$ group to $-OH$ by elimination of methane resulting in the formation of the 4-propylbenzene-1,2-diol species from which propylbenzene is obtained through removal of two water molecules.

All proposed mechanisms are followed by the conversion of propylbenzene to propylcyclohexane through consecutive hydrogenation of the carbon atoms.

3.1.1 DDO-1

The DDO-1 mechanism involves the breaking of the C2–O bond, with the migration of the OCH_3 fragment towards a platinum atom, which becomes hexa-coordinated in an octahedral environment. This is followed by protonation and subsequent desorption. To induce the C–O bond scission, it was necessary to re-arrange the adsorbed dihydroeugenol on the cluster. In **Fig. 3.3** and throughout the figures, such structural rearrangements are denoted by the symbol ρ inside a circle. The newly rearranged dihydroeugenol/Pt_{10} complex is approximately 25 kJ mol^{-1} less stable than the species formed after the saturation of the allyl group, but positions the methoxy group favorably, aligning it with the edge of the platinum cluster. To assess the feasibility of this rearrangement, the minimum energy path connecting the two adsorption geometries of dihydroeugenol on the cluster was computed using a Nudged Elastic Band (*NEB*) approach [149, 176]. The maximum energy along the path corresponds to a barrier of 34.0 kJ mol^{-1}, indicating considerable mobility of the adsorbed species. This rearrangement facilitates the migration of the OCH_3 fragment towards the cluster with an energy barrier of 107.1 kJ mol^{-1}.

Notably, in the resulting intermediate (int2+CH_3O)/Pt_{10}, the hydrogen bond previously observed in the more stable conformations of isoeugenol and dihydroeugenol – between the hydroxyl hydrogen and the methoxy oxygen – remains intact. In fact, it shortens from 2.13 to 1.63 Å, facilitating the nearly instantaneous formation of methanol via a hydrogen shift from the hydroxyl group, without needing hydrogen activation by the catalyst. The final product (int3+CH_3OH)/Pt_{10} exhibits a stabilizing hydrogen bond of 1.47 Å, which reflects a shared hydrogen atom between the two oxygen atoms. This phenomenon, likely due to the small size and relative flexibility of the Pt_{10} cluster, had not been considered in previous experimental hypotheses related to HDO reactions involving isoeugenol and similar compounds.

This observation is noteworthy as it implicitly highlights that catalytic processes on sub-nanometric clusters do not always adhere to the established rules of heterogeneous catalysis. Instead, they represent a chemistry that must be investigated on a case-by-case basis. To continue the HDO reaction, the methanol molecule was desorbed from the cluster (desorption energy of 100.7 kJ mol^{-1}, BSSE = 11.6 kJ mol^{-1}), and a new H_2 molecule was split on it. The resulting int3/Pt_{10} 2 H complex serves as the starting point for the formation of 4-
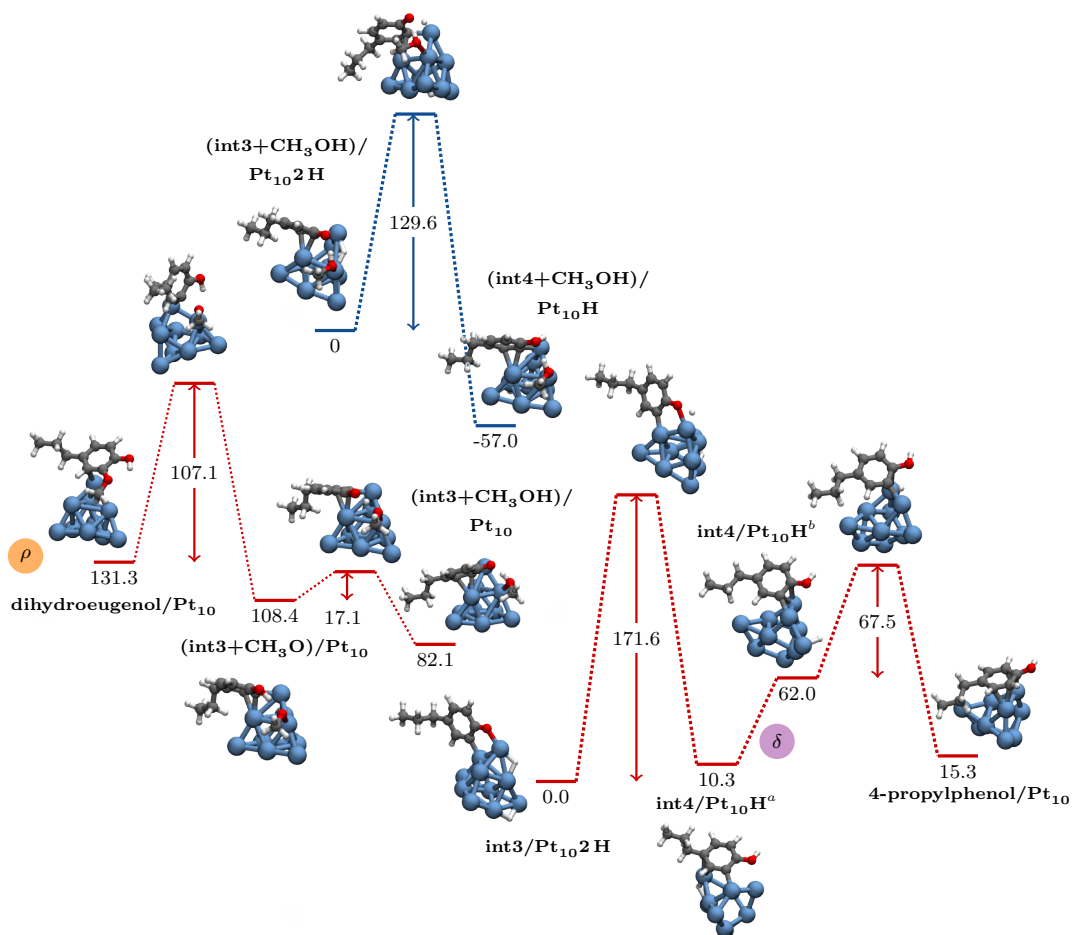
Figure 3.3: Mechanism DDO-1: the cleavage of the C–OCH$_3$ bond in dihydroeugenol results in the formation of the (int3 + CH$_3$O)/Pt$_{10}$ complex. In this step, a hydrogen atom is transferred from the oxygen of the -OH group to the oxygen in the OCH$_3$ fragment. After the CH$_3$OH molecule desorbs, an H$_2$ molecule is dissociated on the cluster to restore the OH group and re-saturate the benzene ring. In the blue profile (above), the hydrogenation of the dangling oxygen in the int3 species is depicted, with CH$_3$OH serving as a spectator molecule.

59

propylphenol adsorbed on the cluster. In the optimized geometry, the int3 species interacts through the dangling oxygen atom and the C2 atom of the benzene ring with the upper edge of the cluster, involving a capping atom and an octahedral atom. As a result, the aromatic ring is positioned almost perpendicular to the cluster and has limited interaction with it, except for the aforementioned carbon atom.

The migration of a hydrogen atom from the cluster to the oxygen atom in int3 (see **Fig. 3.3**) forms the intermediate $int4/Pt_{10}H^a$, which, after hydrogen diffusion, becomes $int4/Pt_{10}H^b$. The second elementary step culminates in the formation of 4-propylphenol/Pt_{10}. The interaction energy between this compound and the platinum cluster is 159.2 kJ mol^{-1} (BSSE = 9.3).

The first elementary step of the reaction reveals that the hydrogenation of the oxygen atom is not a straightforward process due to several stabilizing factors within the reacting system. The oxygen and, more notably, the C2 carbon of the radical form strong bonds with platinum, which must weaken for hydrogenation to occur. In fact, the energy barrier for this elementary event (171.6 kJ mol^{-1}) is the highest in the entire process. This could be the point where significant bifurcations in the mechanism occur: the hydrogen atom may migrate from the cluster to either the oxygen or the carbon atom. In the latter case, the reduction of the benzene ring would begin, with oxygen maintaining its interaction with the cluster. The oxygen hydrogenation could happen later, leading to the formation of 4-propylcyclohexanol.

In this mechanism, it is proposed that the formation of the int4 intermediate could take place before the desorption of CH_3OH. Indeed, the hydrogen bond in (int3+CH_3OH)/Pt_{10} may stabilize the position of the dangling oxygen, preventing its interaction with platinum and making it available for hydrogenation. This is confirmed in **Fig. 3.3**, which shows that the energy barrier for transforming (int3+CH_3OH)/Pt_{10} 2 H into (int4+CH_3OH)/Pt_{10} H is 129.6 kJ mol^{-1}, more than 40 kJ mol^{-1} lower than the barrier for the conversion of int3/Pt_{10} 2 H into int4/Pt_{10} H. Furthermore, the hydrogenation of the oxygen atom in (int3+CH_3OH)/Pt_{10} 2 H releases 57.0 kJ mol^{-1} of energy, compared to the 10.3 kJ mol^{-1} required for the same process in the absence of coadsorbed methanol.

As the hydrogen bond weakens, methanol can desorb more easily from (int4+ CH_3OH)/Pt_{10} H (desorption energy of 76.1 kJ mol^{-1}, BSSE = 9.7 kJ mol^{-1}),
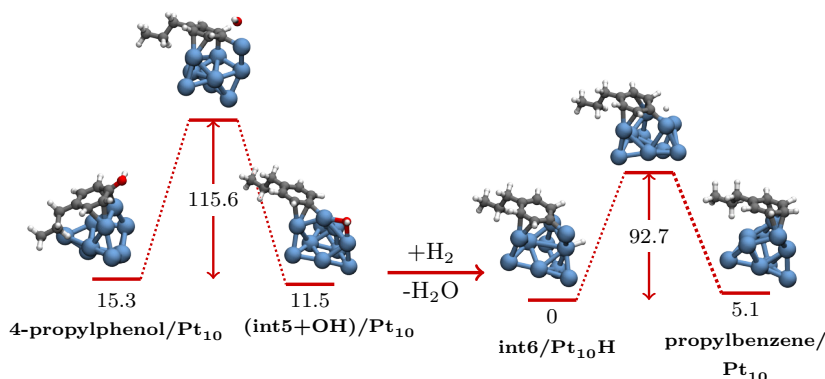
Figure 3.4: DDO-1 mechanism: cleavage of the $C(sp^2)$–OH bond from 4-propylphenol with removal of the -OH group as H_2O and subsequent hydrogenation of the unsaturated C atom to obtain propylbenzene/Pt_{10}.

forming int4/$Pt_{10}H^a$ (after a rearrangement releasing 7 kJ mol^{-1}), which can then be hydrogenated to 4-propylphenol. Notably, the energy barrier for the first hydrogenation step decreases significantly in the presence of coadsorbed methanol, though it remains the highest barrier in the DDO mechanism.

The hydroxyl elimination process from 4-propylphenol occurs in two elementary steps. The first step involves breaking the C1–O bond and adsorbing the OH fragment onto one side of the cluster. In the second step, the OH group is hydrogenated, followed by the desorption of a water molecule from the cluster. As shown in **Fig. 3.4**, the C–O bond cleavage, with an energy barrier of 115.6 kJ mol^{-1}, is nearly as easy as the hydrogenation of the double bond and leads to the formation of a slightly more stable intermediate, labeled (int5+OH)/Pt_{10}. The transfer of a hydrogen atom from the cluster to the -OH group is a low-energy process, with a barrier of 73.3 kJ mol^{-1}. The calculated desorption energy of the resulting water molecule is 97.2 kJ mol^{-1} (BSSE = 18.9). The final elementary step (**Fig. 3.4**) has an energy barrier of 92.7 kJ mol^{-1} and involves transferring a hydrogen atom from the cluster to the phenyl carbon atom, resulting in the formation of stable propylbenzene. The desorption energy of propylbenzene from the cluster is 152.9 kJ mol^{-1} (BSSE = 30.3).

61

3.1.2 DDO-2

In the initial step of the DDO-2 mechanism, the $C(sp^2)$–OH bond in dihydroeugenol is cleaved by overcoming an energy barrier of 109.8 kJ mol^{-1}. This leads to the formation of the (int7 + OH)/Pt$_{10}$ species, which is slightly more stable (-2.9 kJ mol^{-1}) than the reactant species (see **Fig. 3.5**). The splitting of an H$_2$ molecule on the cluster in the (int7 + OH)/Pt$_{10}$ species is required for the formation of water and for the saturation of the benzene ring in int7. To hydrogenate the unsaturated carbon on the ring in int7, an energy barrier of 66.5 kJ mol^{-1} must be overcome, leading to the formation of the stable 1-methoxy-3-propylbenzene/Pt$_{10}$ species, which may desorb from the cluster with an energy of 172.2 kJ mol^{-1} (BSSE=24.9). From the 1-methoxy-3-propylbenzene species, the C–OCH$_3$ bond is broken, forming the (int8 + OCH$_3$)/Pt$_{10}$ species, releasing 38.4 kJ mol^{-1}. The splitting of an H$_2$ molecule then results in the formation of methanol and the saturation of the benzene ring. In this final elementary step, the energy barrier for the hydrogenation of the unsaturated carbon is relatively low (119.4 kJ mol^{-1}), releasing 7 kJ mol^{-1} and forming propylbenzene, which can either desorb as a stable species or evolve into propylcyclohexane through further ring hydrogenation.

3.1.3 DDO-3

The DDO-3 mechanism represents a bifurcation of the DDO-2 mechanism, in which, in the 1-methoxy-3-propylbenzene species, the O–CH$_3$ bond breakage occurs rather than the C–OCH$_3$ bond breakage. This step requires the crossing of a significantly higher energy barrier (181.5 kJ mol^{-1} *vs* 116.2 kJ mol^{-1}) than the alternative elementary step of the DDO-2 mechanism. The species (int9+CH$_3$)/Pt$_{10}$, after fragmentation of an H$_2$ molecule, evolves to 3-propylphenol: the CH$_3$ fragment is hydrogenated to CH$_4$, while int9 undergoes hydrogenation on the unsaturated carbon atom, with an energy barrier of 167.8 kJ mol^{-1} (see **Fig. 3.6**). The calculated desorption energy for 3-propylbenzene is 152.3 kJ mol^{-1}, with a BSSE of 24 kJ mol^{-1}.

In order to obtain a fully deoxygenated and saturated product, 3-propylphenol undergoes C–OH bond breaking, which requires the crossing of an energy barrier of 157.3 kJ mol^{-1}. The OH fragment of the species (int10+OH)/Pt$_{10}$, due to the continuous availability of H atoms in the cluster, desorbs as water. Finally, the adsorbed intermediate evolves to propylbenzene by the transfer of an H atom from
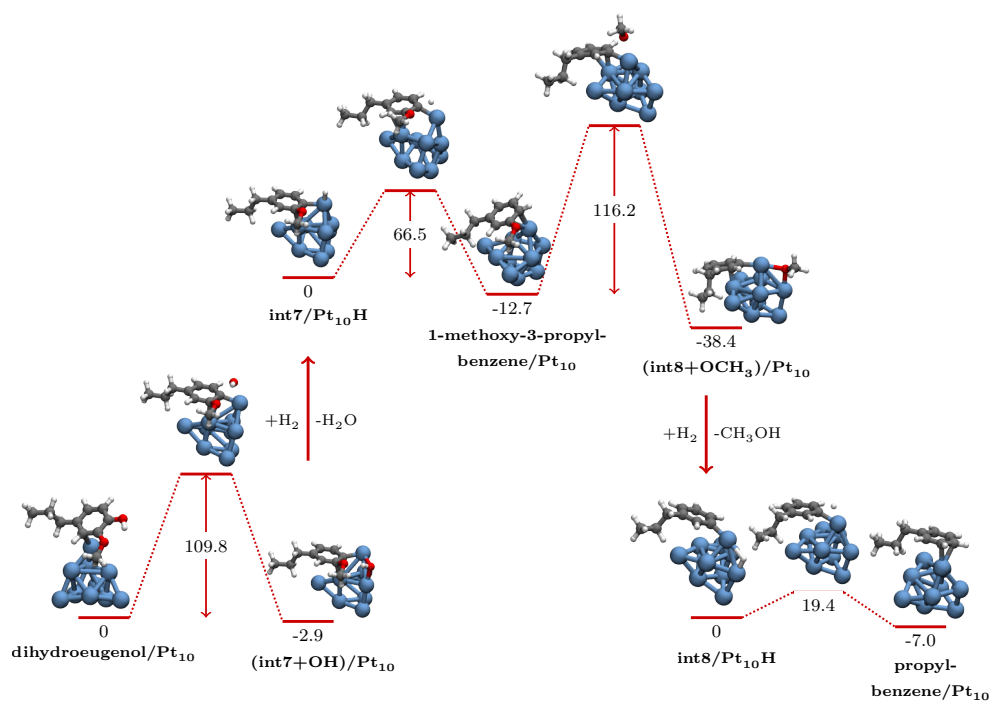
Figure 3.5: Mechanism DDO-2 illustrates the cleavage of the C–OH bond from dihydroeugenol/Pt$_{10}$, leading to the formation of a H$_2$O molecule and 1-methoxy-3-propylbenzene. From this intermediate, propylbenzene is formed through the removal of CH$_3$OH and the hydrogenation of the unsaturated carbon atom.
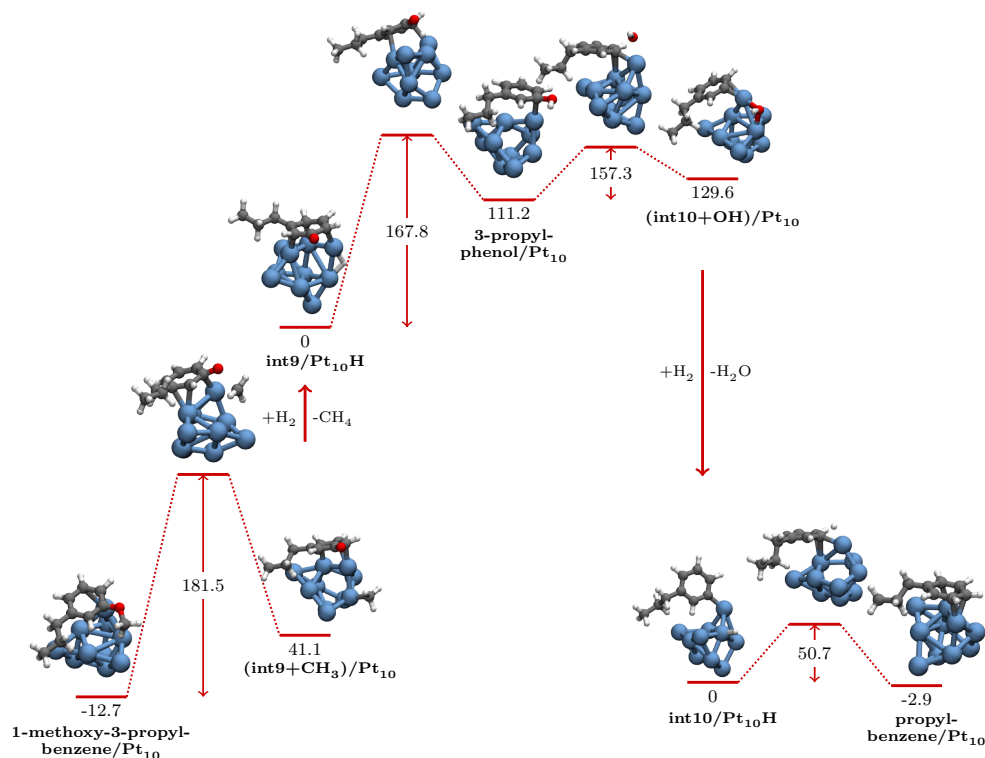
Figure 3.6: Mechanism DDO-3 involves the cleavage of the O–CH$_3$ bond from 1-methoxy-3-propylbenzene/Pt$_{10}$ (formed in the DDO-2 pathway, see **Fig. 3.5**). This bond cleavage, followed by the addition of a H$_2$ molecule, results in the formation of 3-propylphenol and the release of a CH$_4$ molecule. The final step involves the removal of a H$_2$O molecule and the hydrogenation of the unsaturated carbon in the ring, leading to the formation of propyl-benzene.

the cluster to the unsaturated carbon atom of the ring.

3.1.4 DDO-4

In the DDO-4 mechanism, starting from dihydroeugenol adsorbed and rearranged on Pt$_{10}$, the O–CH$_3$ bond breaks, with an energy barrier of 110.3 kJ mol^{-1} (**Fig.3.7**). This is slightly higher than the value calculated for the methoxy group cleavage and leads to the formation of an int2′ intermediate, co-adsorbed with a methyl group. When two hydrogen atoms are introduced into the system, the methyl group, located on a tricoordinated Pt atom, is easily hydrogenated to
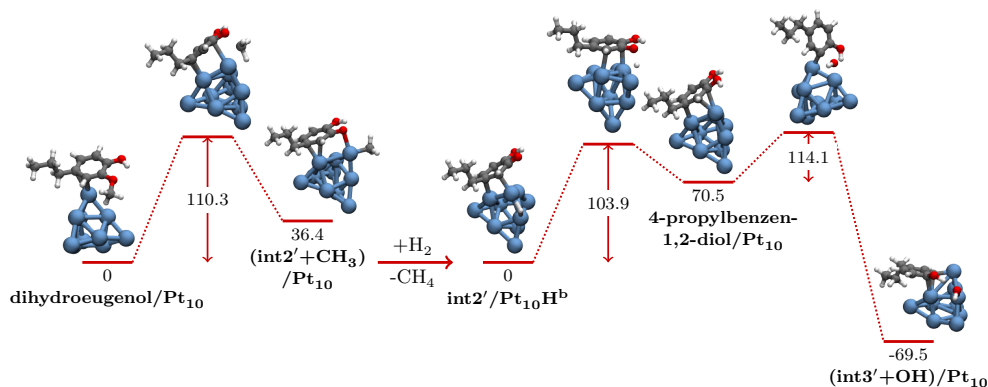
Figure 3.7: DDO-4 mechanism: in dihydroeugenol, the cleavage of the O–CH$_3$ bond occurs, leading to the formation of methane and 4-propylbenzene-1,2-diol through the addition of a H$_2$ molecule. Subsequently, in the 4-propylbenzene-1,2-diol, the C(sp^2)–OH bond is broken, generating the (int3′+OH)/Pt$_{10}$ species. The further addition of a H$_2$ molecule then leads to the formation of 4-propylbenzene and H$_2$O molecule.

methane, which subsequently desorbs. The int2′ intermediate and a hydrogen atom remain on the metal cluster; hydrogen diffusion could facilitate the reaction between these species, forming an O–H bond of a catechol derivative, specifically 4-propylbenzene-1,2-diol. The desorption of this compound requires 133.9 kJ mol^{-1} of energy (BSSE = 27.1 kJ mol^{-1}).

As illustrated in **Fig.3.7**, the cleavage of the OH group from this intermediate occurs with an energy barrier of 114.1 kJ mol^{-1}, which is comparable to that of the methoxy group cleavage (DDO-1 mechanism). The pathway toward 4-propylphenol continues in **Fig. 3.4** after the addition of two more hydrogen atoms: water forms quickly, and following hydrogen diffusion, the int3′ intermediate is converted into the phenolic derivative.

3.1.5 Conversion of propylbenzene to propylcyclohexane

The reduction of aromatic rings has garnered renewed interest within the chemical and petroleum sectors due to its significant role in synthesizing various valuable chemical intermediates [177]. Nevertheless, from an experimental perspective, the challenge remains to develop highly efficient hydrogenation processes under mild, preferably solvent-free conditions. Computational studies have advanced our un-

derstanding of the hydrogenation mechanism of benzene, revealing that it likely follows a Horiuti-Polanyi mechanism [178], characterized by the consecutive addition of hydrogen adatoms. While the existing literature on the hydrogenation of benzene is relatively limited, there is a significant gap in knowledge concerning the hydrogenation of propylbenzene. It is plausible to suggest that the reduction of propylbenzene to propylcyclohexane may proceed via a series of successive hydrogen additions, similar to the mechanism observed for benzene. However, this mechanism requires specific adaptation for the hydrogenation of the phenyl group in propylbenzene when it is adsorbed on platinum surfaces.

Such adaptation presents various challenges, notably the difficulty of accurately predicting which carbon atoms within the aromatic ring will display the highest reactivity based on the electronic effects imparted by the propyl substituent. Additionally, the introduction of hydrogen, often referred to as a "ghost" atom due to its diminutive size, complicates the application of steric hindrance concepts in this context. In the absence of solid theoretical or empirical frameworks, it becomes imperative to consider the hydrogenation process as a series of successive additions, treating each carbon atom in the aromatic ring as a viable reactive site.

The results of my study on the complete hydrogenation of propylbenzene over Pt_{10} cluster are illustrated schematically in **Fig. 3.8**.

Based on the considerations discussed above, I explored the transfer of a hydrogen atom from the Pt_{10} catalyst cluster to four distinct carbon atoms within the propylbenzene ring. These include the carbon atom attached to the propyl group and the carbon atoms located at the *ortho*, *meta* and *para* positions. Accordingly, I examined four elementary steps and calculated the structures of the reactants, products and transition states for each of them. The results reveal that the hydrogen atom preferentially transfers to the carbon at position 2 of the ring. This elementary step shows both kinetic and thermodynamic advantages, with an activation barrier of 94.3 kJ mol^{-1}, leading to the formation of the most stable intermediate.

Therefore, starting with intermediate I, I studied the second elementary step to identify the next most reactive site. This involved sequentially examining the hydrogenation of the remaining unsaturated carbon atoms of the ring. The results indicate that the second hydrogenation step occurs preferentially at the C1 carbon level, driven by factors similar to those in the first step. This step has a significantly lower energy barrier of 41.8 kJ mol^{-1} than the others, resulting in the most stable

66

product.

It is worth noting that the initial catalytic hydrogenation of propylbenzene closely resembles the hydrogenation of a double bond. This process produces a stable compound, specifically 5-propyl-1,3-cyclohexadiene (II), which has a desorption energy of 244.6 kJ mol^{-1} (BSSE = 26.2 kJ mol^{-1}).

The first elementary step of the second catalytic hydrogenation involved all unsaturated carbon atoms of intermediate II. For each potential reactive site, I estimated and optimized the structures of the reagent, product, and transition state, following the same methodology as in the previous steps. The reaction scheme for the second catalytic hydrogenation indicates that the transfer of the first hydrogen atom preferentially occurs at the carbon in position 4. The resulting intermediate III exhibits electron density delocalization over the remaining three carbon atoms in the ring, demonstrating a thermodynamic stability comparable to that of the intermediate formed by adding a hydrogen atom at position 3. However, the latter pathway presents a significantly higher energy barrier that must be overcome.

Beginning with the semi-hydrogenated intermediate III, I investigated the transfer of the second hydrogen atom from the catalyst cluster to the carbon atoms located in positions 1, 2, and 3 of the ring. The energy values associated with the products and the energy barriers for each pathway do not permit a definitive conclusion regarding which of these elementary steps should be favored, whether from a kinetic or thermodynamic perspective. As a result, I considered the carbon atoms in positions 1, 2, and 3 as having equivalent reactivity and proceeded with the third catalytic hydrogenation at each of these sites.

This approach leads to the concurrent formation of two stable products: 3-propylcyclohexene (IV) and 4-propylcyclohexene (VI), which can desorb from the cluster with desorption energies of 196.8 kJ mol^{-1} (BSSE = 9.3 kJ mol^{-1}) and 173.6 kJ mol^{-1} (BSSE = 26.3 kJ mol^{-1}), respectively. In contrast, intermediate V, which is characterized by its diradical nature and displays stability similar to that of IV and VI due to favorable interactions with platinum, is unable to desorb from the cluster.

The first step of the third catalytic hydrogenation, which involves 3-propylcyclo hexene (IV), indicates that the transfer of a hydrogen atom from the catalyst cluster primarily occurs at the C2 position of the ring. The activation barrier associated with this pathway (path 2) is significantly lower than that of the alternative
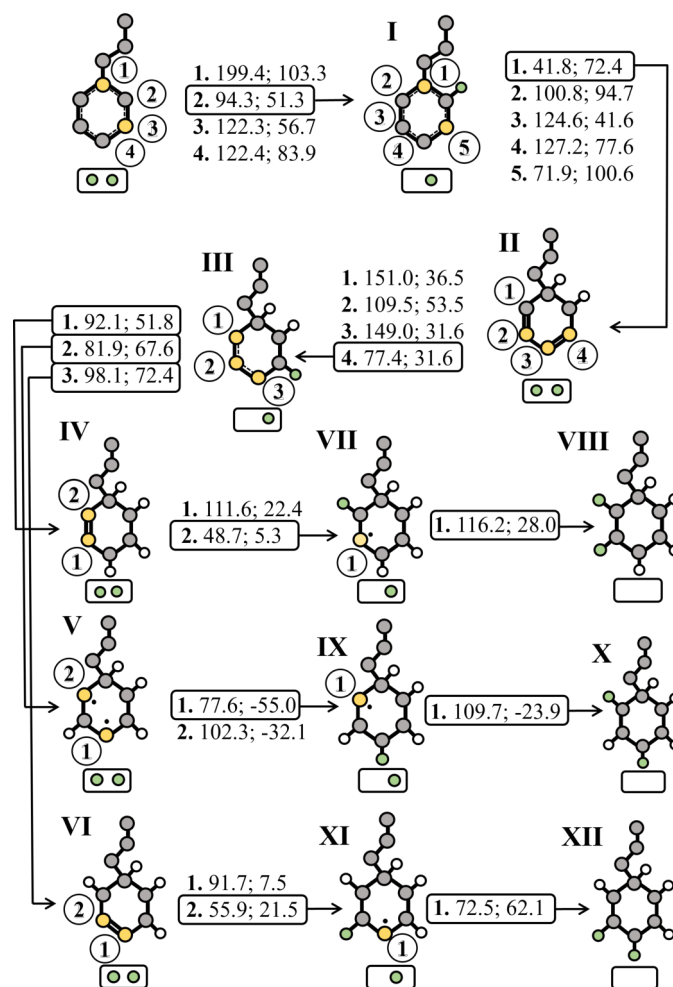
Figure 3.8: Representation of the complete saturation of the benzene ring of propylbenzene on the Pt_{10} cluster. The Pt_{10} cluster is shown as a small rectangle below the molecular species, with the adsorbed hydrogen atoms represented by green circles within the rectangle, while the unadsorbed hydrogen atoms are omitted. The yellow circles indicate the interaction sites between the molecule and the cluster. Each figure shows the location where the catalytic hydrogen attaches, followed by the energy barrier of the transition and the energy of the product, all relative to the starting state (with two hydrogen atoms on Pt_{10}). The energies are expressed in kJ mol^{-1}. The hydrogenation sequence begins with propylbenzene, followed by intermediate species II (5-propyl-1,3-cyclohexadiene), IV, V and VI (various isomers of propylcyclohexene). The values in the inset highlight the energetically preferable pathway, with each intermediate serving as a reagent for the next step.

68

pathway, making it the preferred route. This preference is supported by both kinetic and thermodynamic considerations: the semi-hydrogenated intermediate VII is more stable by 17.1 kJ mol^{-1} compared to the corresponding intermediate derived from path 1.

Consequently, the second hydrogen atom was added to the last unsaturated carbon of intermediate VII, resulting in the formation of propylcyclohexane (VIII) in a chair conformation. The calculated desorption energy for this product from the cluster is 140.4 kJ mol^{-1} (BSSE = 19.6 kJ mol^{-1}).

The first elementary step of the third catalytic hydrogenation, which involves intermediate V, indicates that the formation of the semi-hydrogenated intermediate IX is energetically favorable. This preference arises because its activation barrier is approximately 24.7 kJ mol^{-1} lower than that of the alternative pathway, and IX is also the most thermodynamically stable configuration. As a result, the addition of the second hydrogen atom was directed toward this intermediate, leading to the formation of propylcyclohexane (X) in a distorted boat conformation, recognized as the second most stable form of cyclohexane. The desorption energy for this product is calculated to be 130.7 kJ mol^{-1} (BSSE = 22.4 kJ mol^{-1}).

In comparison, the preferred initial step for 4-propylcyclohexene (VI) in the third catalytic hydrogenation has an energy barrier of 55.9 kJ mol^{-1}, resulting in the creation of intermediate XI. It is important to highlight that the species produced via the alternative pathway is considerably more stable. The hydrogenation of XI leads to a distorted boat conformation of propylcyclohexane (XII), which has a desorption energy of 108.1 kJ mol^{-1} (BSSE = 21.0 kJ mol^{-1}). Furthermore, at the level of theory used in this thesis, the energy difference between the chair and distorted boat conformations of propylcyclohexane is estimated to be 25 kJ mol^{-1}, which is consistent with the literature value of 21 kJ mol^{-1} reported for cyclohexane.

3.2 HYD mechanism

The hydrogenation (HYD) mechanism of isoeugenol involves, after the hydrogenation of the allyl chain's double bond to form dihydroeugenol, a complete hydrogenation of the aromatic ring followed by the removal of oxygenated functional groups. As shown in **Fig. 3.9**, the series of chemical intermediates derived from 4-propyl-2-methoxycyclohexan-1-ol identifies four separate pathways for deoxygena-

tion, ultimately leading to the production of propylcyclohexane. These pathways are summarized as follows:

- **HYD-1**: involves the removal of the $-OCH_3$ group as methanol, followed by the loss of water, starting from 4-propylcyclohexan-1-ol.

- **HYD-2**: begins with the elimination of the $-OH$ group as water, forming 1-methoxy-3-propylcyclohexane, from which methanol is later removed to produce propylcyclohexane.

- **HYD-3**: involves the formation of 3-propylcyclohexan-1-ol by converting the OCH_3 group into OH, through the removal of the $-CH_3$ fragment as methane, followed by the hydrogenation of the residual oxygen.

- **HYD-4**: leads to the formation of 4-propylcyclohexane-1,2-diol, which then undergoes the successive removal of two water molecules to yield propylcyclohexane.

These pathways describe the various chemical routes involved in the removal of oxygen-containing groups during the hydrogenation of isoeugenol.

The ring saturation follows a Horiuti-Polanyi mechanism, characterized by the sequential attachment of hydrogen adatoms [36]. It was noted that, after the initial hydrogen atom is added, subsequent hydrogen atoms consistently bond at the *ortho* position relative to the existing ones, as illustrated in **Fig. 1**. For the first hydrogen atom, all carbon atoms within the ring were evaluated as potential sites for hydrogenation. The calculated energy barriers and the relative stabilities of the intermediates indicate that C3 is the most favorable site for the first hydrogenation event, with an energy barrier of 105.0 kJ mol^{-1} required for this process. Following this observation, the two *ortho* positions adjacent to C3 were identified as the likely locations for the second hydrogen atom addition.

According to **Fig. 3.10**, hydrogenation at the C2 position is strongly favored due to a lower energy barrier (57.0 vs. 127 kJ mol^{-1}) and the higher stability of the resulting intermediate II, identified as the 6-methoxy-4-propylcyclohexa-1,3-dien-1-ol/Pt$_{10}$ species (43.6 vs. 57.0 kJ mol^{-1}). For this intermediate, the desorption energy from the cluster was calculated to be 262.5 kJ mol^{-1} (with a BSSE correction of 31.1 kJ mol^{-1}). In the subsequent hydrogenation step, C1 and C4 were considered as potential reactive sites for the formation of intermediate
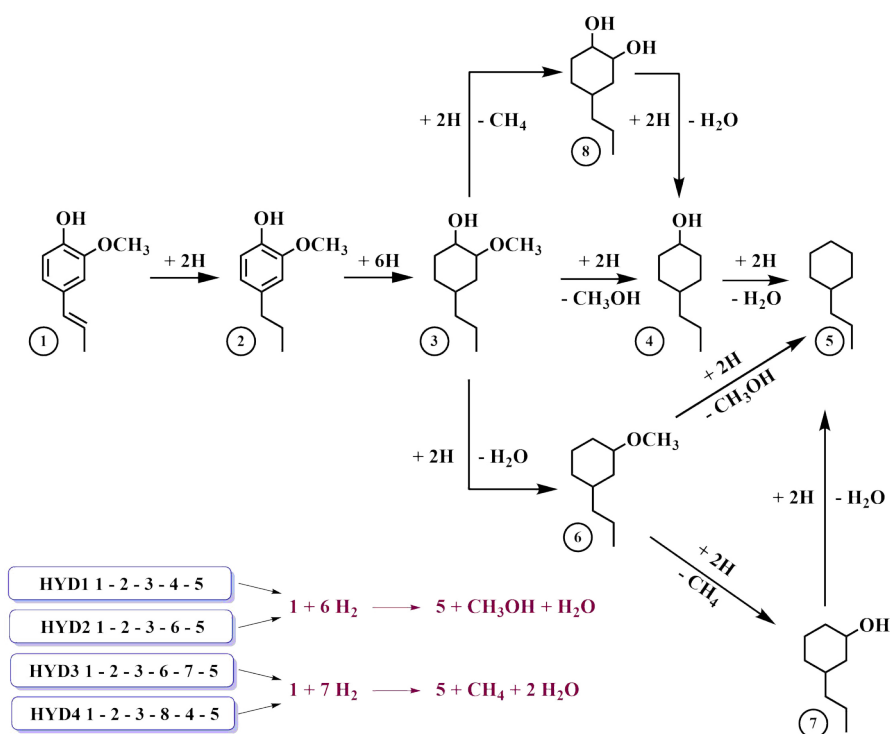
Figure 3.9: Schematic representation of the four reaction routes of isoeugenol conversion to propylcyclohexane via the HYD mechanism.

III. Hydrogenation at C1, however, appeared more favorable due to the greater stability of the resulting intermediate, approximately 48.0 kJ mol^{-1}. The transition to intermediate IV (6-methoxy-4-propylcyclohex-3-en-1-ol/Pt$_{10}$) is governed by an activation energy barrier of 71.9 kJ mol^{-1}. Following this, hydrogenation at C4, with an energy barrier of 45.7 kJ mol^{-1}, leads to the formation of intermediate V. Finally, the addition of the last hydrogen atom to C5 results in the formation of the surface species 2-methoxy-4-propylcyclohexan-1-ol/Pt$_{10}$, positioned at 69.9 kJ mol^{-1} relative to intermediate IV+2H. It is noteworthy that the activation energy required for this final step is 39.3 kJ mol^{-1}, which is significantly lower than the energy barriers calculated for the hydrogenation of other individual carbon atoms in the ring.

In agreement with the known influence of substituents on aromatic reactions, the carbon atoms in the ring that are most susceptible to hydrogenation are those in the *ortho* and *para* positions relative to oxygen-containing substituents. These substituents increase the electron density in the ring, making it more reactive towards hydrogen addition. However, the hydrogenation of dihydroeugenol appears to be less favorable compared to propylbenzene, as discussed in the DDO mechanisms. This could be attributed to stronger interactions between the substrate and the platinum cluster in the presence of oxygenated groups, potentially amplified by the high structural flexibility of the platinum cluster. Additionally, another factor hindering hydrogenation may be that, in isoeugenol, the *ortho* position relative to one oxygenated group corresponds to the *meta* position relative to the other, which reduces the electron-donating effect that enhances reactivity.

3.2.1 HYD-1

The mechanism illustrated in **Fig. 3.11** begins with the elimination of methanol, leading to the formation of 4-propylcyclohexan-1-ol, followed by the release of a water molecule that results in the production of propylcyclohexane. The first elementary step involves the cleavage of the C2–O bond in 2-methoxy-4-propylcyclohexan-1-ol, overcoming an energy barrier of 149.2 kJ mol^{-1}, with the chemisorption of the OCH$_3$ fragment between two metal centers at the cluster's upper edge. In comparison, the methoxy group ($-$OCH$_3$) loss from dihydroeugenol has a significantly higher transition state energy (about 40 kJ mol^{-1} more), although the reaction is considerably more exothermic (again, by roughly 40 kJ mol^{-1}). This discrepancy could be due to the absence of hydrogen bond stabilization in the transition state
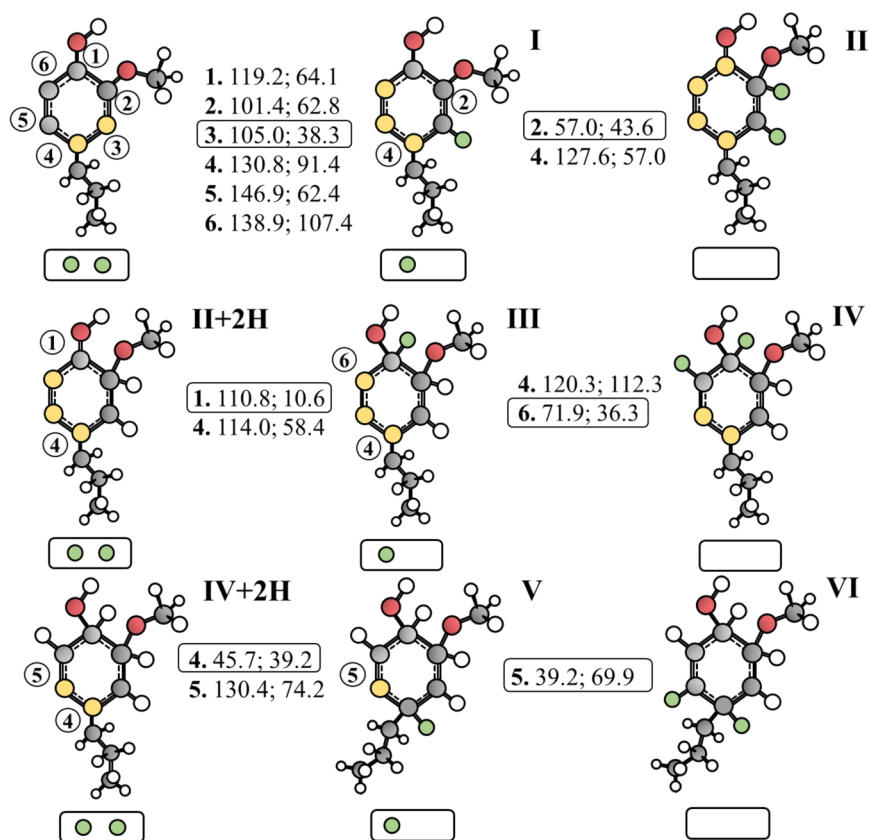
Figure 3.10: A schematic representation illustrates the complete hydrogenation of isoeugenol's phenyl ring on the Pt_{10} cluster. The cluster is shown as a small rectangle beneath the molecular structure, with green circles inside symbolizing adatoms, while non-adsorbed atoms are not depicted. Yellow circles mark the points where the molecule interacts with the cluster. For each step, the first number indicates where hydrogen is added, the second number shows the energy barrier of that step, and the third gives the energy of the resulting product. These energies are measured relative to the reactant's energy, with two hydrogen atoms still adsorbed on Pt_{10}. All energy values are in kJ mol^{-1}. The hydrogenation process starts with dihydroeugenol, followed by **II+2H** (6-methoxy-4-propylcyclohexa-1,3-dien-1-ol/Pt_{10} 2 H), and concludes with **IV+2H** (6-methoxy-4-propylcyclohex-3-en-1-ol/Pt_{10} 2 H), yielding the final product 2-methoxy-4-propylcyclohexan-1-ol/Pt_{10}.

of 2-methoxy-4-propylcyclohexan-1-ol, as the hydroxyl group is coordinated to the metal, while the product is stabilized by the stronger C–Pt interaction replacing the O–Pt bond. The intermediate (int1 + CH_3O)/Pt_{10} is formed with an energy release of 60.5 kJ mol^{-1} and undergoes H_2 fragmentation, a step required for the reaction to proceed. Subsequently, in the second elementary step, hydrogenation of the CH_3O fragment occurs, yielding methanol (CH_3OH) with a calculated desorption energy of 89.7 kJ mol^{-1} (BSSE = 8.9 kJ mol^{-1}).

The int1/Pt_{10} H species facilitates the hydrogenation of the unsaturated C2 carbon, leading to the production of 4-propylcyclohexan-1-ol. The calculated desorption energy for this process is 138.3 kJ mol^{-1} (with a BSSE correction of 20.6 kJ mol^{-1}). This energy is lower than the activation energy required for the subsequent step, which involves C1–OH bond cleavage to form propylcyclohexane. The energy barrier for this step is 178.0 kJ mol^{-1}, implying that only a small proportion of molecules are likely to possess sufficient energy to overcome this threshold and proceed with the reaction.

This 178.0 kJ mol^{-1} barrier is significantly higher than the one observed for the dehydroxylation of propylphenol (115 kJ mol^{-1}). This discrepancy may be attributed to the fact that, in the case of propylphenol, the molecule exhibits strong interactions with the cluster due to the presence of the phenyl group. In contrast, for the current system, the steric hindrance and weaker interactions between the cyclohexane moiety and the cluster – primarily due to the absence of an anchoring group associated with the hydroxyl oxygen – result in the -OH group migrating between two terminal fragments that are nearly isolated from each other.

The resulting (int2+OH)/Pt_{10} species is characterized by the OH fragment positioned between two platinum atoms along the edge of the cluster, with int2 interacting exclusively via the C1 carbon with the apical platinum atom.

The fragmentation of an additional H_2 molecule promotes the desorption of water and leads to the formation of propylcyclohexane. This process involves the addition of a hydrogen atom to the oxygen atom of the hydroxyl fragment, which requires overcoming an energy barrier of 87.7 kJ mol^{-1} and results in an energy release of 12.2 kJ mol^{-1} for the formation of the (int2 + H_2O)/Pt_{10} species.

Subsequently, the H_2O molecule desorbs, a process associated with a calculated energy of 37.8 kJ mol^{-1}, corrected for a BSSE of 5.4 kJ mol^{-1}. Additionally, another adatom facilitates the formation of propylcyclohexane/Pt_{10} by crossing an energy barrier of 47.9 kJ mol^{-1}. The calculated energy for the desorption of
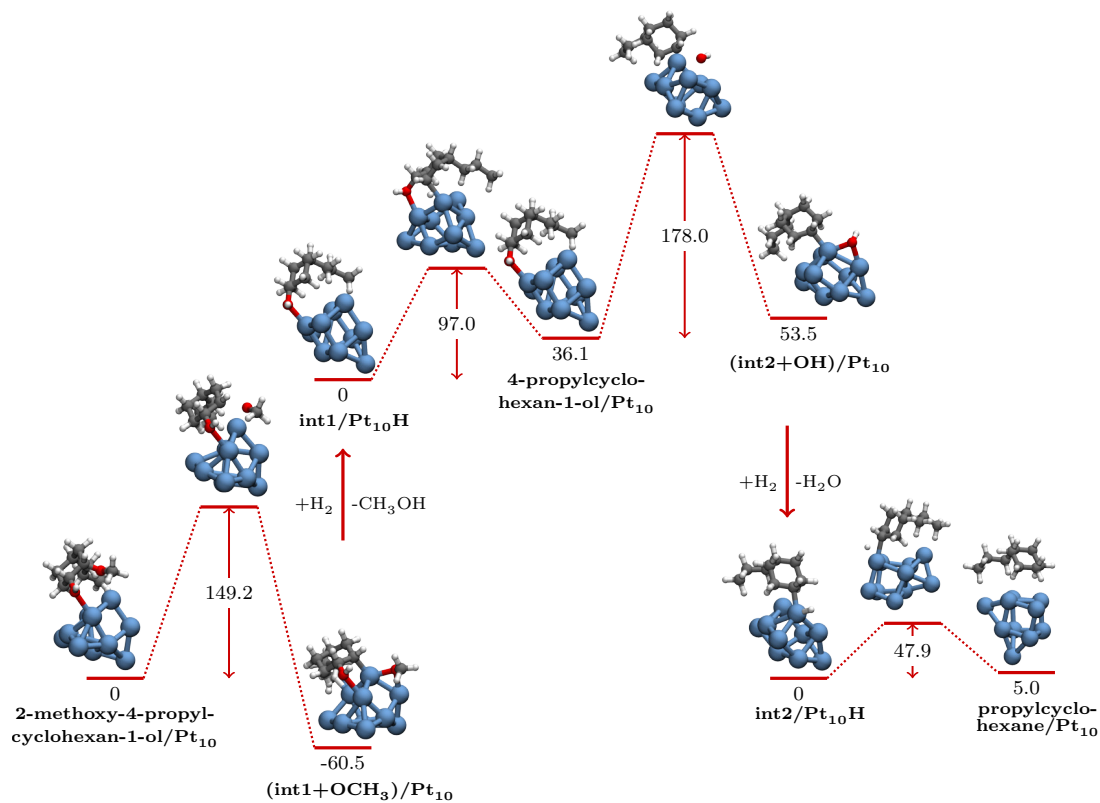
Figure 3.11: The HYD-1 reaction profile shows the cleavage of the $C-OCH_3$ bond, with the OCH_3 fragment attaching to a side edge of the cluster. After adding one H_2 molecule and desorbing methanol, 4-propylcyclohexan-1-ol is formed, followed by the breaking of the $C-OH$ bond. The OH fragment is hydrogenated through the addition of another H_2 molecule and desorbs as H_2O. Finally, hydrogenation of the unsaturated carbon results in the formation of propylcyclohexane.

propylcyclohexane from this species is 97.5 kJ mol^{-1}, with a BSSE adjustment of 21.1 kJ mol^{-1}.

3.2.2 HYD-2

The second reaction pathway entails the removal of the $-$OH group as water, resulting in the formation of 1-methoxy-3-propylcyclohexane, which subsequently undergoes methanol elimination, yielding propylcyclohexane. The initial surface transformation step, with an energy barrier of 164.0 kJ mol^{-1}, involves the cleavage of the C1$-$O bond in 2-methoxy-4-propylcyclohexane-1-ol, releasing 95.2 kJ mol^{-1} of energy and generating the (int3+OH)/Pt$_{10}$ intermediate (**Fig. 3.12**).

On the platinum cluster, the reaction progresses through the dissociation of a H$_2$ molecule. The next step involves the transfer of a hydrogen atom from the cluster to the unsaturated C1 carbon, with an associated energy barrier of 100.8 kJ mol^{-1}, leading to the formation of 1-methoxy-3-propylcyclohexane/Pt$_{10}$. The desorption of this molecular species from the cluster requires overcoming an energy barrier of 139.6 kJ mol^{-1} (with a BSSE correction of 21.9 kJ mol^{-1}).

Starting from 1-methoxy-3-propylcyclohexane/Pt$_{10}$, the elimination of the $-$OCH$_3$ group may lead to the production of methanol or methane, as described in the HYD-3 mechanism, leaving the oxygen atom in a dangling state. In contrast, the HYD-2 mechanism involves the first scenario, wherein the cleavage of the C$-$OCH$_3$ bond occurs with an activation energy of 192.6 kJ mol^{-1}. This reaction results in the formation of the intermediate species (int4+OCH$_3$)/Pt$_{10}$. Subsequently, through the hydrogenation of the OCH$_3$ moiety and the transfer of a hydrogen atom to the unsaturated carbon, propylcyclohexane/Pt$_{10}$ is ultimately obtained (**Fig. 3.12**).

3.2.3 HYD-3

In the HYD-3 mechanism, illustrated in **Fig. 3.13**, 1-methoxy-3-propylcyclohexane/ Pt$_{10}$ undergoes cleavage of the O$-$CH$_3$ bond. This step requires overcoming an energy barrier of 180.5 kJ mol^{-1} and leads to the formation of the intermediate (int5+CH$_3$)/Pt$_{10}$, which is about 52 kJ mol^{-1} less stable than the previous intermediate. Subsequently, methane is removed through hydrogenation of the CH$_3$ fragment, and hydrogenation of the dangling oxygen atom from the int5 intermediate occurs. The next step, with an energy barrier of 118.4 kJ mol^{-1},
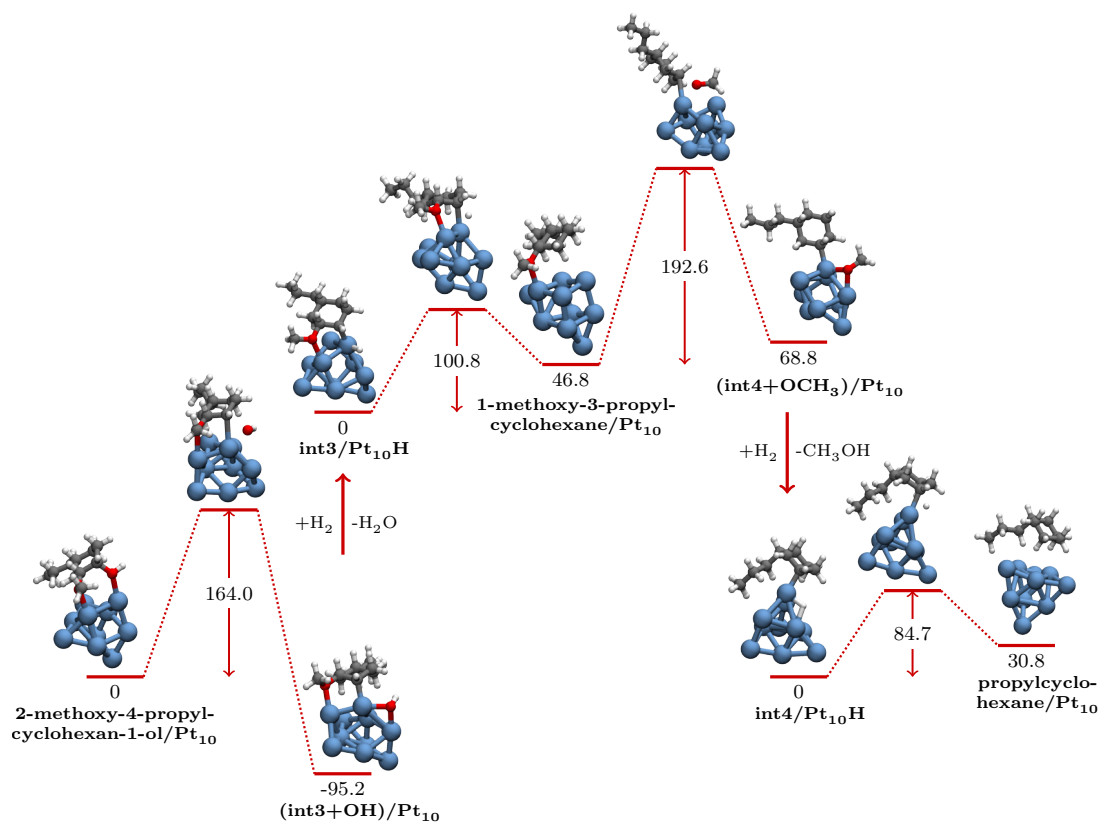
Figure 3.12: The reaction profile for the HYD-2 mechanism involves the cleavage of the C−OH bond, followed by adsorption of the OH fragment. Next, the unsaturated carbon undergoes hydrogenation, leading to the formation of 1-methoxy-3-propylcyclohexane. Subsequently, the C−OCH$_3$ bond is broken, and the unsaturated carbon is further hydrogenated, resulting in propylcyclohexane. These stages require the fragmentation of two H$_2$ molecules.

results in the formation of 3-propylcyclohexan-1-ol/Pt_{10}, which then transforms into chemisorbed propylcyclohexane, resulting in the release of a water molecule and saturation of the C1 position.

3.2.4 HYD-4

The HYD-4 mechanism involves the removal of methane from 2-methoxy-4-propyl-cyclohexane-1-ol, leading to the formation of 4-propylcyclohexane-1,2-diol. This compound is subsequently converted into propylcyclohexane through the elimination of two water molecules. The initial elementary step entails the cleavage of the $O-CH_3$ bond, overcoming an energy barrier of 164.6 kJ mol^{-1} to produce the (int7+CH_3)/Pt_{10} intermediate (**Fig. 3.14**). In this intermediate, the CH_3 fragment is adsorbed on a platinum atom at the apex position, while the int7 species interacts with platinum centers via its two oxygen atoms, which exhibit different coordination modes. Methane is generated after the dissociation of a H_2 molecule on the cluster, involving the transfer of a single hydrogen atom to the carbon atom of the CH_3 fragment. Following the desorption of CH_4, the int7/Pt_{10} H species, characterized by the presence of a dangling oxygen atom, is formed. The subsequent step involves the hydrogenation of the oxygen atom to yield the 4-propylcyclohexane-1,2-diol/Pt_{10} species, which has a calculated desorption energy of 126.2 kJ mol^{-1}, with a BSSE of 24.3 kJ mol^{-1} (refer to **Fig. 3.14**).

The cleavage of the $C-OH$ bond at the *para* position relative to the propyl chain occurs on the 4-propylcyclohexane-1,2-diol/Pt_{10} species, requiring the overcoming of an energy barrier of 161.0 kJ mol^{-1}. The resulting species, denoted as (int1+OH)/Pt_{10} — where int1 refers to the same intermediate seen in the HYD-1 mechanism (**Fig. 3.11**), but coadsorbed with an OH group — is approximately 99 kJ mol^{-1} more stable than the original 4-propylcyclohexane-1,2-diol/Pt_{10}. To facilitate the removal of water, a new H_2 molecule is subsequently dissociated on the cluster, resulting in the formation of propylcyclohexanol.

Following this, after another H_2 molecule fragments on the cluster, a hydrogen atom is transferred to the oxygen atom of the OH fragment, which has an energy barrier of 106.3 kJ mol^{-1}. This leads to the formation of H_2O. Once water desorbs from the cluster, the remaining int1/Pt_{10} H species establishes a connection between the HYD-4 and the previously discussed HYD-1 mechanisms.

78
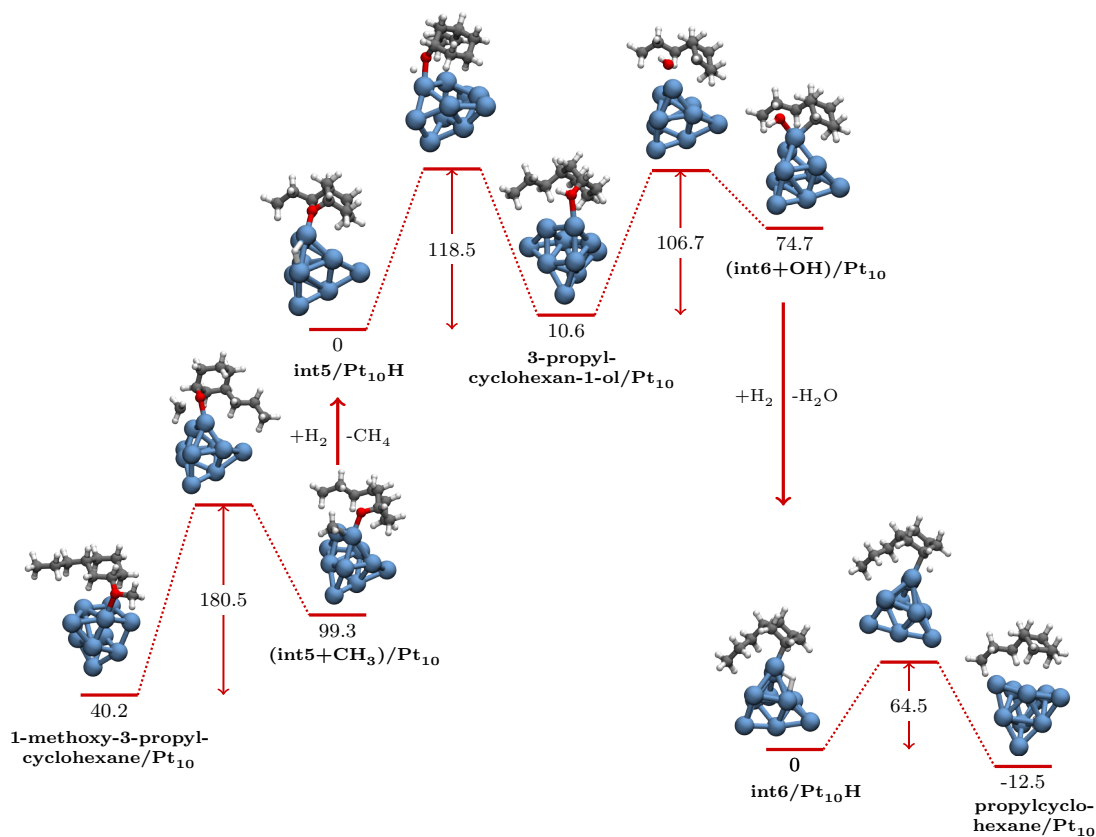
Figure 3.13: The reaction profile for the HYD-3 mechanism describes the cleavage of the $O-CH_3$ bond from 1-methoxy-3-propylcyclohexane/Pt_{10}, followed by hydrogenation of the CH_3 fragment, leading to methane formation. The $-OH$ functionality is then restored, resulting in the formation of 3-propylcyclohexanol/Pt_{10}. Subsequently, after the elimination of a water molecule, propylcyclohexane/Pt_{10} is produced via hydrogenation of the unsaturated carbon atom.
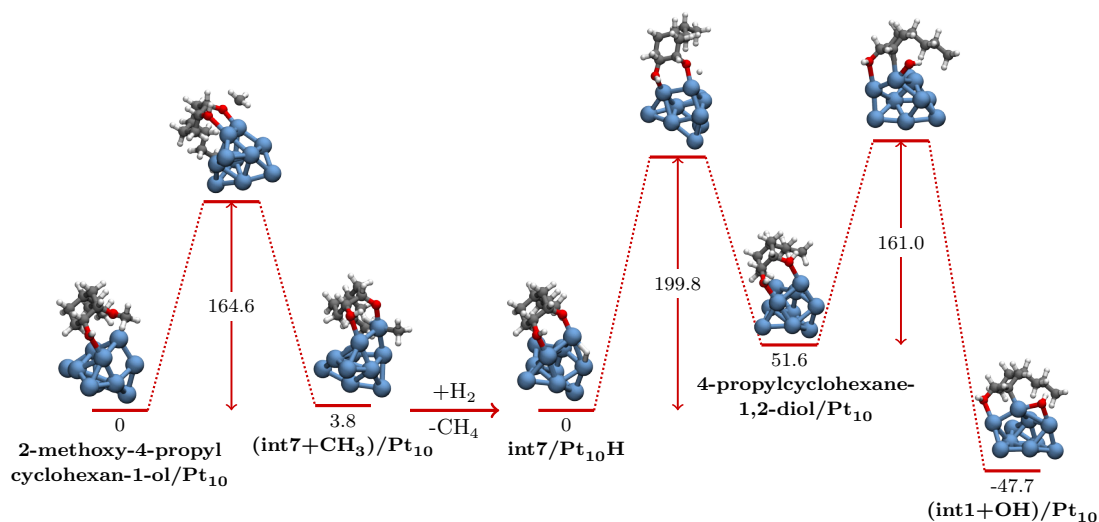
Figure 3.14: The reaction profile corresponding to the HYD-4 mechanism involves the cleavage of the $O-CH_3$ bond in the methoxy group, with adsorption of the CH_3 fragment. After hydrogenation, this fragment desorbs as methane. A second hydrogen atom restores the $-OH$ functionality, resulting in the formation of the 4-propylcyclohexane-1,2-diol/Pt_{10} species, which then converts to 4-propylcyclohexane-1-ol/Pt_{10} due to the breaking of the $C-OH$ bond. As shown in **Figure 3.11**, 4-propylcyclohexane-1-ol/Pt_{10} eventually leads to the formation of propylcyclohexane/Pt_{10}.
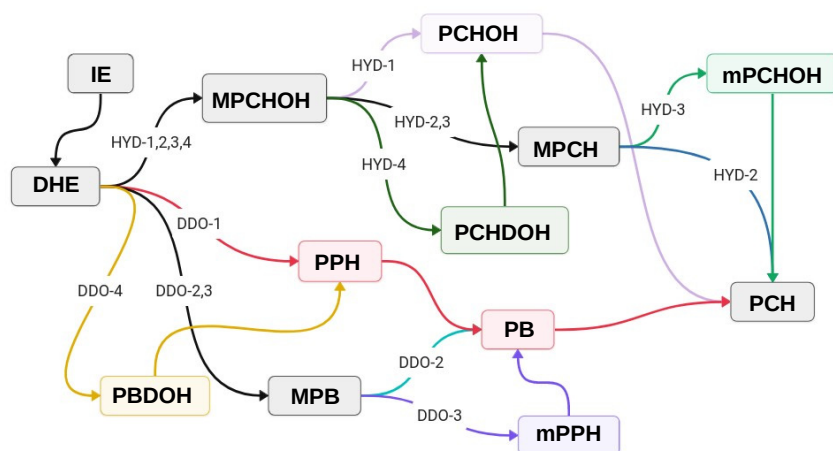
Figure 3.15: A visual overview of the eight main pathways identified for the isoeugenol hydrodeoxygenation reaction on Pt_{10}. Legend: IE = isoeugenol; DHE = dihydroeugenol; MPCHOH = 2-methoxy-4-propylcyclohexan-1-ol; PCHOH = 4-propylcyclohexan-1-ol; MPCH = 1-methoxy-3-propylcyclohexane; PCHDOH = 4-propylcyclohexan-1,2-diol; mPCHOH = 3-propylcyclohexan-1-ol; PCH = 4-propylcyclohexane; PPH = 4-propylphenol; mPPH = 3-propylphenol; PB = 4-propylbenzene; MPB = 1-methoxy-3-propylbenzene; PBDOH = 4-propylbenzen-1,2-diol.

3.3   Kinetic Analysis

The energy profiles for the eight pathways associated with the two alternative mechanisms (DDO and HYD) analyzed in the preceding sections demonstrate that, based solely on the relative energies of the minima and transition states, the hydrogenation of the phenyl ring is kinetically favored in the early stages following the formation of dihydroeugenol. In contrast, it appears more probable that deoxygenation initiates from dihydroeugenol rather than from 4-propyl-2-methoxycyclohexan-1-ol, which is the fully hydrogenated product. Notably, the energy barriers linked to the deoxygenation steps within the HYD mechanism are roughly 40–50 kJ mol^{-1} higher than those associated with the DDO mechanism.

Although these conclusions do not allow us to determine a specific pathway or

identify the overall fastest mechanism, all the data from the *DFT* calculations were employed to perform an equilibrium microkinetic analysis. This analysis was carried out using an innovative approach based on the algebraic system proposed by Christiansen in 1953, known as the Simplified Christiansen Method (*SCM*) [179], which has previously been applied for kinetic analysis of experimental catalytic results [180, 181, 182].

The simple evaluation of energy barriers and energy differences between reaction intermediates can be misleading when trying to distinguish mechanisms in complex, multi-channel processes, as in the case under investigation. The *SCM*, however, allows for the inclusion of all *DFT* data related to the elementary steps that make up the reaction mechanisms and condenses this information into a single parameter. This approach enables the comparison of kinetic constants – expressed as the probability of occurrence of corresponding events per unit of time – for the different pathways that lead from reactants to products (R$\rightleftharpoons$P), identifying the most probable one. Furthermore, it is possible to compare the relative rates of different reactions (R$_i \rightleftharpoons$P$_i$) occurring on the same catalytic system, providing insights into selectivity towards certain processes [183].

Practically, the forward and reverse energy barriers of the elementary steps characterizing each reaction pathway are provided as input to the *SCM*. This method returns the kinetic constants for the different reaction channels over the selected temperature range (473–973 K). To assess the impact of temperature, *SCM* was applied using Gibbs free energy. From the tables summarizing the Gibbs free energy changes for all elementary steps in both the HYD and DDO pathways (**Table 3.1** and **Table 3.2**), it emerges that Gibbs free energy has a more significant influence on the desorption of stable species than on the energy barriers.

According to the simplified Christiansen microkinetic method, the system of equations can be expressed as:

$$\frac{1}{s} \begin{vmatrix} \bar{w}_1 & -w_{-1} & 0 & \cdots & 0 \\ 0 & w_2 & w_{-2} & \cdots & 0 \\ 0 & 0 & w_3 & \cdots & 0 \\ \vdots & \vdots & \vdots & \ddots & \vdots \\ w_{-n} & 0 & 0 & \cdots & w_n \end{vmatrix} \begin{vmatrix} \theta_1 \\ \theta_2 \\ \theta_3 \\ \vdots \\ \theta_n \end{vmatrix} = \begin{vmatrix} 1 \\ 1 \\ 1 \\ \vdots \\ 1 \end{vmatrix} \tag{3.1}$$

The free energy barriers calculated using *DFT*, $\Delta G^{\#}(T)$, are then converted into the overall reaction rate s for a given reaction channel. The kinetic constants,

$w_{\pm j}$, represent the forward and reverse rate constants for the elementary steps $(j \rightleftharpoons j+1)$ at a given temperature T, under quasi-steady-state conditions, and are calculated using the following equations:

$$w_j = \frac{kT}{h} e^{-\Delta G^{\#}(j \to j+1)/RT} \tag{3.2}$$

$$w_{-j} = \frac{kT}{h} e^{-\Delta G^{\#}(j+1 \to j)/RT} \tag{3.3}$$

where θ_j represents the fraction of catalytic sites occupied by species i. The reader could refer to [183] for further details of the procedure and of the possible use of the *SCM*.

The standard free energies at different temperatures, including those for the transition states, were calculated starting from electronic energies and harmonic vibrational frequencies using the Goodvibes code [184], applying Grimme's quasi-harmonic entropy correction [185]. In addition to the corrected energy barriers, the *SCM* analysis also accounted for processes such as molecular rearrangement, hydrogen diffusion, and molecular desorption where necessary. Although these processes were considered relatively simple (with negligible barriers compared to the reactive stages), their effect was evaluated thermodynamically to account for their variability across different reaction pathways.

The *SCM* results, outlined in **Table 3.3**, indicate that the pathways in the DDO mechanism are at least two orders of magnitude faster than those in the HYD mechanism. Notably, the HYD-1 pathway, which involves the formation of propylcyclohexane through the intermediate 4-propylcyclohexan-1-ol, is the fastest within the HYD mechanism. In contrast, the HYD-2 and HYD-3 pathways are closely matched, differing by an order of magnitude except within the temperature range of 673-973 K. The slowest HYD pathway is HYD-4, likely due to the high energy barriers associated with the formation of 4-propylcyclohexane-1,2-diol and the subsequent cleavage of the C−OH bond. Despite this, HYD-4 still proceeds at a faster rate than DDO-3, which is the slowest pathway in the DDO mechanism and overall.

At all the temperatures investigated, and especially at higher ones, the HDO reaction of isoeugenol on Pt_{10} primarily proceeds through the first DDO pathway, which involves deoxygenation via the 4-propylphenol intermediate. According to *SCM* analysis, this pathway is approximately eight orders of magnitude faster than the most efficient HYD mechanism. Among the routes involving the 1-methoxy-

Table 3.1: A summary of the elementary reactions within the HYD mechanism, including their respective standard free energy barriers, $\Delta G^{\#}$, and standard reaction free energies, ΔG, at a temperature of 298.15 K.

	Elementary process[a]	$\Delta G^{\#}$/kJ mol^{-1}	ΔG/kJ mol^{-1}
(1)	DHE/Pt$_{10}$ 2 H $\rightarrow$ I	105.7	41.2
(2)	I $\rightarrow$ II	60.6	-12.6
(3)	II+2H $\rightarrow$ III	109.4	9.9
(4)	III $\rightarrow$ IV	72.0	11.2
(5)	IV+2H $\rightarrow$ V	52.4	40.0
(6)	V $\rightarrow$ VI	35.6	-6.7
(7)	MPCHOH/Pt$_{10}$ $\rightarrow$ (int1+OCH$_3$)/Pt$_{10}$	148.3	-52.8
(8)	int1/Pt$_{10}$ H $\rightarrow$ PCHOH/Pt$_{10}$	99.7	30.3
(9)	PCHOH/Pt$_{10}$ $\rightarrow$ (int2+OH)/Pt$_{10}$	180.3	17.3
(10)	int2/Pt$_{10}$ H $\rightarrow$ PCH/Pt$_{10}$	49.3	7.9
(11)	MPCHOH/Pt$_{10}$ $\rightarrow$ (int3+OH)/Pt$_{10}$	167.5	-91.9
(12)	int3/Pt$_{10}$ H $\rightarrow$ MPCH/Pt$_{10}$	99.0	40.2
(13)	MPCH/Pt$_{10}$ $\rightarrow$ (int4+OCH$_3$)/Pt$_{10}$	191.3	18.1
(14)	int4/Pt$_{10}$ H $\rightarrow$ PCH/Pt$_{10}$	84.7	30.8
(15)	MPCH/Pt$_{10}$ $\rightarrow$ (int5+CH$_3$)/Pt$_{10}$	180.5	59.1
(16)	int5/Pt$_{10}$ H $\rightarrow$ mPCHOH/Pt$_{10}$	114.6	4.6
(17)	mPCHOH/Pt$_{10}$ $\rightarrow$ (int6+OH)/Pt$_{10}$	168.3	65.3
(18)	int6/Pt$_{10}$ H $\rightarrow$ PCH/Pt$_{10}$	65.0	-18.4
(19)	MPCHOH/Pt$_{10}$ $\rightarrow$ (int7+CH$_3$)/Pt$_{10}$	167.3	3.9
(20)	int7/Pt$_{10}$ H $\rightarrow$ PCHDOH/Pt$_{10}$	187.1	43.3
(21)	PCHDOH/Pt$_{10}$ $\rightarrow$ (int1+OH)/Pt$_{10}$	167.3	-4.4

[a] See **Figure 3.15** for the shorthand notation employed for the chemical species.

Table 3.2: A summary of the elementary reactions within the DDO mechanism, including their respective standard free energy barriers, $\Delta G^{\#}$, and standard reaction free energies, ΔG, at a temperature of 298.15 K.

	Elementary process[a]	$\Delta G^{\#}$/kJ mol^{-1}	ΔG/kJ mol^{-1}
(22)	IE/Pt$_{10}$ 2 H $\rightarrow$ int1/Pt$_{10}$ H^{a}	105.9	88.0
(23)	int1/Pt$_{10}$ H^{b} $\rightarrow$ DHE/Pt$_{10}$	119.3	48.6
(24)	DHE/Pt$_{10}$ $\rightarrow$ (int2+OCH$_3$)/Pt$_{10}$	116.9	-16.7
(25)	(int3+CH$_3$OH)/Pt$_{10}$ 2 H $\rightarrow$ (int4+CH$_3$OH)/Pt$_{10}$ H	72.4	-56.6
(26)	int4/Pt$_{10}$ H^{b} $\rightarrow$ PPH/Pt$_{10}$	64.1	21.6
(27)	PPH/Pt$_{10}$ $\rightarrow$ (int5+OH)Pt$_{10}$	108.0	-5.7
(28)	int6/Pt$_{10}$ H $\rightarrow$ PB/Pt$_{10}$	92.7	18.6
(29)	DHE/Pt$_{10}$ $\rightarrow$ (int2$'$+CH$_3$)/Pt$_{10}$	121.6	-32.4
(30)	int2$'$/Pt$_{10}$ H^{b} $\rightarrow$ PBDOH/Pt$_{10}$	101.8	68.7
(31)	PBDOH/Pt$_{10}$ $\rightarrow$ (int3$'$+OH)/Pt$_{10}$	114.4	-66.6
(32)	int3$'$/Pt$_{10}$ H^{b} $\rightarrow$ PPH/Pt$_{10}$	70.4	-14.3
(33)	DHE/Pt$_{10}$ $\rightarrow$ (int7+OH)/Pt$_{10}$	123.1	27.1
(34)	int7/Pt$_{10}$ H $\rightarrow$ MPB/Pt$_{10}$	69.5	-15.3
(35)	MPB/Pt$_{10}$ $\rightarrow$ (int8+OCH$_3$)/Pt$_{10}$	118.9	-20.4
(36)	int8/Pt$_{10}$ H $\rightarrow$ PB/Pt$_{10}$	80.1	-10.8
(37)	MPB/Pt$_{10}$ $\rightarrow$ (int9+CH$_3$)/Pt$_{10}$	198.1	-41.2
(38)	int9/Pt$_{10}$ H $\rightarrow$ mPPH/Pt$_{10}$	164.7	105.8
(39)	mPPH/Pt$_{10}$ $\rightarrow$ (int10+OH)/Pt$_{10}$	156.2	128.0
(40)	int10/Pt$_{10}$ H $\rightarrow$ PB/Pt$_{10}$	53.5	-1.5
(41)	PB/Pt$_{10}$ 2 H $\rightarrow$ I	101.1	53.7
(42)	I $\rightarrow$ II	39.2	-11.6
(43)	II $\rightarrow$ III	84.3	36.0
(44)	III $\rightarrow$ V	82.4	31.3
(45)	V $\rightarrow$ IX	75.6	-54.9
(46)	IX $\rightarrow$ X^{d}	110.7	27.6

[a] See **Figure 3.15** for the shorthand notation employed for the chemical species.

Table 3.3: Rates of the eight isoeugenol hydrodeoxygenation mechanisms based on *SCM* analysis at varying temperatures.

	Reaction rate[a]					
	473[b]	**573**	**673**	**773**	**873**	**973**
HYD-1	1.1(-24)	1.8(-18)	1.9(-14)	2.0(-11)	2.3(-9)	1.5(-7)
HYD-2	6.6(-26)	1.2(-19)	2.5(-15)	3.3(-12)	4.4(-10)	3.3(-8)
HYD-3	7.5(-27)	3.3(-20)	1.1(-15)	1.9(-12)	2.9(-10)	2.4(-8)
HYD-4	4.5(-31)	8.8(-24)	1.1(-18)	4.6(-15)	1.6(-12)	2.6(-10)
DDO-1	8.1(-16)	7.2(-11)	2.0(-7)	6.5(-5)	3.1(-3)	9.6(-2)
DDO-2	1.6(-22)	1.0(-16)	9.9(-13)	7.8(-10)	7.7(-8)	4.2(-6)
DDO-3	5.4(-46)	6.2(-36)	6.3(-29)	8.2(-24)	4.2(-20)	5.1(-17)
DDO-4	1.7(-20)	8.6(-15)	7.4(-11)	4.9(-8)	4.2(-6)	2.1(-4)

[a] Reaction rates are expressed in s^{-1}, with the exponent in scientific notation provided in parentheses. The Gibbs free energies (as a function of temperature at p = 1 atm) have been taken into account for the kinetic analysis.
[b] Temperatures in Kelvin.

3-propylbenzene intermediate, DDO-2 — where the $C-OCH_3$ bond is cleaved as an additional deoxygenation step — is significantly more favorable than DDO-3, which, as previously mentioned, is the slowest pathway. DDO-2 and DDO-4 are fairly competitive with each other.

The *SCM* method offers a streamlined approach for analyzing the kinetics of various mechanisms by simultaneously incorporating all the data obtained from *DFT* calculations of their elementary steps. This approach distills the overall kinetic behavior into a single numerical value. While the accuracy of this value in comparison to experimentally derived kinetic constants depends on the theoretical methods used, the key advantage is that *SCM* allows for the discrimination between mechanisms based on comprehensive, objective data rather than relying solely on energy barrier analysis, which could lead to premature conclusions.

By omitting the fundamental steps common to all DDO-type mechanisms (as illustrated in **Fig. 3.15** and summarized in **Table 3.2**), we can draw several important conclusions. First, DDO-3 can be disregarded due to its exceptionally high energy barriers. However, identifying DDO-1 as the preferred mechanism goes beyond merely having the lowest energy barriers. In fact, the highest barriers

observed in DDO-1, DDO-2, and DDO-4 are relatively similar, with values of 116.9, 123.1, and 121.6 kJ mol^{-1} corresponding to steps 24, 33, and 29 in **Table 3.2**, respectively.

Moreover, the preference for DDO-1 is not solely attributed to a fewer number of elementary steps; in reality, DDO-1 incorporates one additional step compared to DDO-2, encompassing steps 24-28 for DDO-1 and steps 33-36 for DDO-2. It's also noteworthy that DDO-1 does not possess the highest backward barrier, which is found in DDO-3 (239.3 kJ mol^{-1} at step 37) and DDO-2 (181.0 kJ mol^{-1} at step 31), provided DDO-3 is excluded from our consideration.

In contrast, a comprehensive analysis using *SCM* shows that when all forward and backward barriers are evaluated alongside the stability of the intermediates, DDO-1 emerges as the unequivocally fastest mechanism. Following DDO-1, the speed of the mechanisms decreases with DDO-4, DDO-2, and finally DDO-3, which exerts a negligible influence on the overall kinetics of the reaction.

Comparable information to that provided by the *SCM* can be derived by evaluating the differences, Δ_{TEC}, between the total energy content (TEC, defined as the cumulative sum of all energy barriers encountered along the reaction coordinate) for the forward and reverse processes in the DDO mechanisms under investigation. A negative Δ_{TEC} signifies a thermodynamic preference for the forward progression (i.e., from reactants to products) over the reverse pathway, implying that the reaction rate increases as Δ_{TEC} becomes more negative. In fact, it can be rigorously demonstrated that:

$$\Delta_{\mathrm{TEC}} = \mathrm{RT}\ln\left(\frac{\Pi_{\mathrm{B}}}{\Pi_{\mathrm{F}}}\right)$$

where Π_{B} and Π_{F} represent the products of the occurrence probabilities for each elementary step along the reverse and forward reaction pathways, respectively, at a given temperature T, and R is the universal gas constant. Thus, $\Delta_{\mathrm{TEC}} < 0$ when $\Pi_{\mathrm{B}} < \Pi_{\mathrm{F}}$, which is consistent with our assumption, as can be demonstrated from the formal definition of event occurrence probability. Given that Δ_{TEC} is a relative measure, steps common to all four mechanisms were excluded from the analysis. Utilizing the data from **Table 3.2** and **Table 3.1**, the following Δ_{TEC}/kJ mol^{-1} values were obtained: Δ_{TEC}(DDO-1)=−38.8, Δ_{TEC}(DDO-2)=−19.4, Δ_{TEC}(DDO-3)=+202.2, and Δ_{TEC}(DDO-4)=−31.7. These results clearly indicate that DDO-3 is a thermodynamically unviable pathway (as the reverse flux is dominant over the forward flux), while DDO-1 represents the most favorable mechanism, with DDO-2 and DDO-4 ranking in the same order as predicted by the *SCM*.

3.4 Conclusion

This chapter presents a detailed exploration of the hydrodeoxygenation (HDO) process of isoeugenol catalyzed by a subnanometric platinum cluster (Pt_{10}), providing an in-depth mapping of the atomistic mechanisms involved. The deoxygenation-through-hydrogenation pathway was systematically compared with the alternative direct deoxygenation (DDO) mechanism through *DFT* calculations. This comparative approach enabled the determination of the thermodynamic energies and kinetic barriers of key reaction steps, unveiling the preferred reaction pathways.

A Christiansen-type microkinetic analysis, supported by the calculated energy barriers and adsorption/desorption energetics, allowed for the estimation of kinetic constants for the various pathways. The data suggest that, within the temperature range of 473 to 973 K, the DDO mechanism is thermodynamically favored over the hydrogenation-driven deoxygenation route. Under molecular hydrogen flow, the reaction appears to proceed primarily through the formation of a 4-propylphenol intermediate, with the methoxy group being preferentially removed as methanol, ultimately yielding propylcyclohexane as the final product. The hydroxyl group is similarly removed, desorbing as water. Additionally, kinetic data suggest that at higher temperatures, a competitive pathway leading to methane formation could emerge.

The analysis also ruled out alternative pathways, including those that lead to the formation of 1-methoxy-3-propylbenzene as an intermediate. Among the pathways examined, the route involving 3-propylphenol was found to be the slowest.

The implications of this investigation are far-reaching for future research, as it provides an almost comprehensive mapping of the hydrodeoxygenation (HDO) mechanism of isoeugenol on a representative platinum cluster, serving as a valuable reference for further studies. Subsequent chapters will delve into the effects of a support (graphene) and the role of non-noble metals at key points in the reaction. Additionally, it will be crucial to assess whether, under molecular hydrogen conditions, hydrodeoxygenation becomes the preferred pathway over the various decomposition routes typically expected for multifunctional molecules on metal surfaces.

Chapter 4

HDO reaction of Guaiacol on Pt$_{10}$ cluster

In this chapter, I investigate the hydrodeoxygenation (HDO) of guaiacol catalyzed by a sub-nanometric platinum cluster (Pt$_{10}$), emphasizing two principal reaction mechanisms: direct deoxygenation (DDO) and hydrogenation-assisted deoxygenation (HYD). The objective is to elucidate which of these pathways is energetically more favorable. Specifically, the study focuses on whether deoxygenation is more likely to occur via cleavage of the C(sp^2)–OH/OCH$_3$ bond directly from guaiacol (DDO), or through the breaking of the C(sp^3)–OH/OCH$_3$ bond in 2-methoxycyclohexanol (HYD), a hydrogenated intermediate.

Simultaneously, the formation of secondary products that could negatively impact the activity and selectivity of the catalyst, potentially leading to deactivation phenomena, or that may be of interest for other industrial processes, will be evaluated. A comprehensive mapping of the HDO process of guaiacol will also enable a direct comparison with the reactivity of isoeugenol, which has been studied using the same computational approach and catalyst, as discussed in the previous chapter. This comparison will allow for the assessment of whether structurally similar molecules exhibit analogous reaction patterns, thus opening avenues for optimization in processes involving related compounds. While alternative reaction pathways, including those involving intermediates from the dehydrogenation of methyl or hydroxyl groups, may occur, this thesis will focus solely on direct defunctionalization reactions. A detailed examination of the HYD and DDO mechanisms for guaiacol on the Pt$_{10}$ catalyst will be conducted, providing reaction profiles for each

elementary step, supported by an extensive analysis of their energetic and kinetic properties.

4.1 HYD mechanism

The HYD mechanism of guaiacol involves the hydrogenation of the benzene ring, resulting in the formation of 2-methoxycyclohexan-1-ol, followed by the subsequent removal of the oxygenated groups ($-OCH_3$ and $-OH$). From 2-methoxycyclohexan-1-ol, three distinct pathways can emerge, depending on the sequence and chemical form in which the oxygenated components are removed (**Fig. 4.1**): (1) the $-OCH_3$ group is removed as CH_3OH, producing cyclohexanol, which then leads to cyclohexane through the loss of H_2O; (2) the $-OH$ group is removed as water, forming methoxycyclohexane, which subsequently yields cyclohexane through the removal of CH_3OH or CH_4 and water; and (3) the methyl group is removed as CH_4 from the OCH_3 fragment, resulting in the formation of cyclohexane-1,2-diol, which ultimately forms cyclohexane through the elimination of two water molecules.
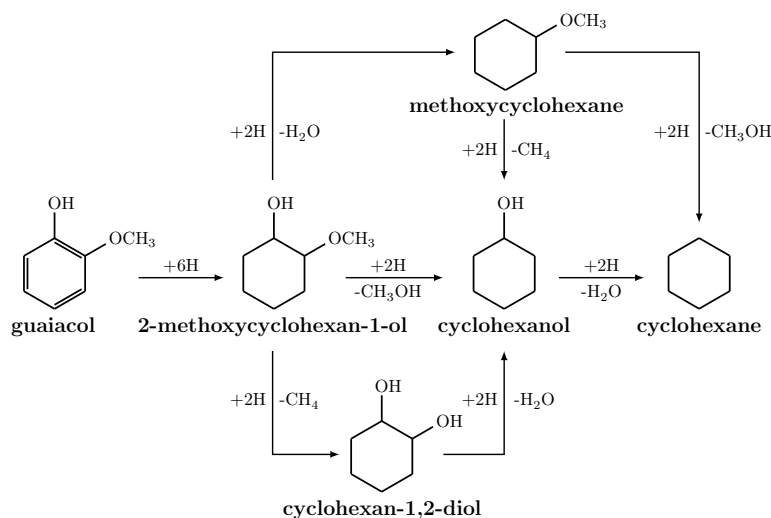

Figure 4.1: Guaiacol conversion to cyclohexane according to HYD mechanism: schematic routes

The hydrogenation of the benzene ring adheres to a *Horiuti-Polanyi*[1] scheme, as described by Saeys et al. [178], which involves the sequential addition of hydrogen

---

[1]A variant of the Langmuir-Hinshelwood mechanism.

adatoms. Due to the electronic effects of substituents and the interactions between the metal catalyst and the substrate, the carbon atoms within the benzene ring exhibit non-equivalence. These effects can result in meta-stable configurations with enhanced reactivity. Consequently, each carbon atom in the ring was initially regarded as a potentially reactive site, especially for the first hydrogen addition.

Kinetic and thermodynamic considerations, specifically a lower activation energy and the greater relative stability of intermediates, indicate that the first hydrogen atom is most likely added to the C6 position (**Fig. 4.2**). For the subsequent hydrogen additions, only the carbon atoms in the *ortho* positions relative to the already hydrogenated sites were considered as potential candidates. Experimental evidence from studies on benzene hydrogenation [178, 186, 187, 188] supports this approach, as these *ortho* carbon atoms are activated by the adjacent hydrogen atoms.

Based on this framework, the second hydrogen atom is likely added to either the C1 or C5 positions, originating from intermediate I. The energetically favored species is 2-methoxycyclohexa-2,4-dien-1-ol (**II**), with an energy barrier of 88.2 kJ mol^{-1} for hydrogenation at C1, and a desorption energy of 273.2 (BSSE=28.0) kJ mol^{-1}. The subsequent addition of a third hydrogen atom to the C5 position leads to the formation of intermediate **III**. The fourth hydrogen atom preferentially attaches to the C2 position due to a lower energy barrier of approximately 16 kJ mol^{-1}, yielding 2-methoxycyclohex-3-en-1-ol (**IV**; desorption energy of 158.2 (BSSE=22.4) kJ mol^{-1}).

Finally, the remaining carbon atoms, C3 and C4, are considered for hydrogenation. Comparative analysis of the energy barriers (26.2 vs. 34.3 kJ mol^{-1}) and the relative stability of the resulting intermediates (-18.5 vs. 24.2 kJ mol^{-1}) indicates that the fifth hydrogen atom is most likely added to the C4 position. The successive addition of the sixth hydrogen atom to C3 culminates in the formation of 2-methoxycyclohexan-1-ol (**VI**). After the benzene ring was fully hydrogenated, the final HYD pathways leading to the complete conversion product were examined.

In the first pathway, cyclohexane is formed through the removal of the $-OCH_3$ group as methanol, followed by the removal of the $-OH$ group as water. The initial step in this route involves the cleavage of the C2-O bond and the adsorption of the OCH_3 fragment onto the upper portion of a side edge of the cluster. This cleavage step has an energy barrier of 137.7 kJ mol^{-1} and results in the formation of the
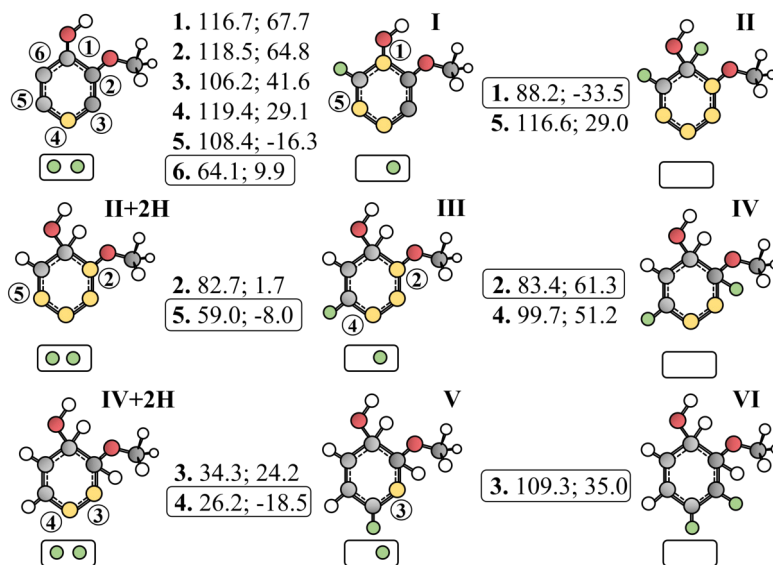
Figure 4.2: The representation shows the complete saturation of the aromatic ring in guaiacol adsorbed on the Pt_{10} cluster. Yellow circles indicate the interaction sites between the molecule and the cluster, which is depicted as a small rectangle containing green circles representing the adsorbed hydrogen atoms. To the right of each species, three numbers are provided: the first denotes the position where the catalytic hydrogen is added, the second indicates the energy barrier, and the third specifies the reaction energy, both relative to the reactant of the elementary step. All energy values are given in kJ mol^{-1}. The catalytic hydrogenation process begins with guaiacol, proceeds with **II+2H** (2-methoxycyclohexa-2,4-dien-1-ol), and concludes with **IV+2H** (2-methoxycyclohex-3-en-1-ol).

(int1+CH_3O)/Pt_{10} species, accompanied by an energy release of 66.5 kJ mol^{-1} (**Fig. 4.3**).

To proceed with the hydrodeoxygenation reaction, a new H_2 molecule was dissociated on the cluster (refer to **Fig. A.1** in Appendix). The resulting (int1+CH_3O)/ Pt_{10} 2 H species was then utilized as a reactant to generate chemisorbed methanol. The desorption energy of this methanol was determined to be 91.9 kJ mol^{-1}, with a BSSE correction of 8.8 kJ mol^{-1}.

Following methanol desorption, an H atom migrates through the cluster to the unsaturated C2 atom of the ring. In the resulting (int1+CH_3O)/Pt_{10} H species, the H atom is transferred to C2 of the ring, which involves overcoming an energy
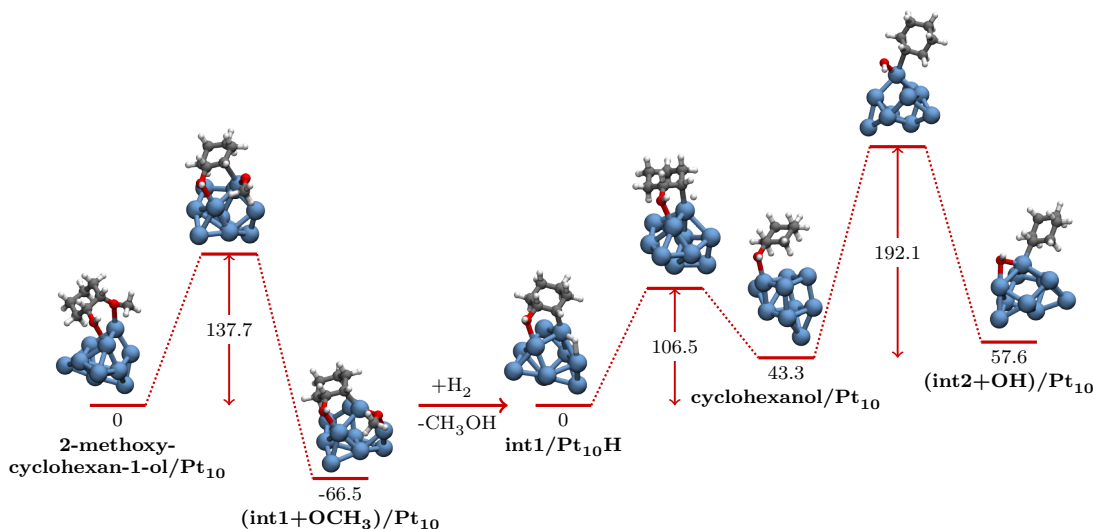
Figure 4.3: The reaction profile illustrates the cleavage of the C2–OCH$_3$ bond, along with the migration of the CH$_3$O fragment to the cluster's edge (HYD pathway 1). Following the addition of a H$_2$ molecule, which dissociates on the cluster, and the desorption of methanol, cyclohexanol is formed, leading to the subsequent cleavage of the C1-OH bond.

barrier of 106.5 kJ mol^{-1} (see **Fig. 4.3**). This transfer leads to the formation of cyclohexanol adsorbed on the cluster, which is 43.3 kJ mol^{-1} less stable than the initial species. Cyclohexanol may desorb from the cluster with an energy of 117.8 kJ mol^{-1} (BSSE = 16.9 kJ mol^{-1}), representing a secondary reaction product.

In the primary reaction pathway, however, cyclohexanol/Pt$_{10}$ undergoes C1–O bond cleavage. This step is characterized by a high energy barrier of 192.1 kJ mol^{-1} and results in the formation of the (int2+OH)/Pt$_{10}$ species, where the OH fragment is adsorbed on the upper part of the cluster edge, between two metal centers.

To remove the OH group as water, a second H$_2$ molecule was dissociated on the cluster. This process produced the species (int2+OH)/Pt$_{10}$ 2 H, which contains one H atom near the OH fragment on the cluster's edge and another H atom positioned further away. The subsequent elementary step involves the transfer of an H atom to the oxygen atom of the adsorbed OH group, with an energy barrier of 89.3 kJ mol^{-1}, leading to the formation of chemisorbed H$_2$O (see **Fig. A.2(a)** in Appendix). To advance the reaction, the H$_2$O molecule must be desorbed from the cluster, which requires an energy input of 66.5 kJ mol^{-1} (BSSE = 5.4 kJ mol^{-1}).

After desorption, the H atom, which was previously adsorbed and shared between two Pt atoms, migrates toward the unsaturated C1 atom. This migration leads to the formation of cyclohexane/Pt_{10}, which is 9.2 kJ mol^{-1} more stable than the starting species, by surmounting a relatively low energy barrier of 54.7 kJ mol^{-1} (see **Fig. A.2(b)** in Appendix). The resulting cyclohexane can then desorb from the cluster with an energy of 89.6 kJ mol^{-1} (BSSE = 16.6 kJ mol^{-1}).

Pathway 2 outlines a process where the $-OH$ group is first eliminated as water, followed by the removal of the remaining oxygenated group, which can either be methanol (if the C2-O bond breaks) or methane (if the O-CH_3 bond cleaves). In the latter scenario, cyclohexane is produced after the removal of two water molecules. Both branches of this pathway share the initial two elementary steps: the cleavage of the C1-O bond and the formation of methoxycyclohexane. Specifically, in the first elementary step (see **Fig. 4.4**), the C1-O bond of 2-methoxycyclohexan-1-ol is broken by overcoming an energy barrier of 157.3 kJ mol^{-1}. This reaction results in significant stabilization of the (int3+OH)/Pt_{10} system, where the OH fragment is adsorbed as a bridge between two metal centers on an upper edge of the cluster. In this state, the int3 species exhibits O-Pt (bond length 2.22 Å) and C1-Pt (bond length 2.06 Å) interactions. After the fragmentation of an H_2 molecule on the cluster, the adsorbed OH can undergo hydrogenation and subsequently desorb as water.

In the second elementary step, the int3/Pt_{10} H species undergoes the transfer of an H atom to the unsaturated C1 atom of the ring, overcoming an energy barrier of 102.7 kJ mol^{-1}. This reaction produces methoxycyclohexane/Pt_{10}, which has a desorption energy of 128.8 kJ mol^{-1} (BSSE = 18.9 kJ mol^{-1}) and is 48.4 kJ mol^{-1} less stable than the preceding intermediate. Methoxycyclohexane/Pt_{10} thus represents the starting point for two alternative pathways leading to the formation of cyclohexane.

According to one pathway (illustrated in blue in **Fig. 4.8**), the first elementary step involves breaking the C2-O bond, which requires overcoming an energy barrier of 185.9 kJ mol^{-1}. This step yields the (int4+CH_3O)/Pt_{10} species, where the OCH_3 fragment is adsorbed on the upper edge of the cluster. After the fragmentation of an additional H_2 molecule on the cluster, the CH_3O group can be hydrogenated to methanol, which then desorbs. The resulting species, related to int2/Pt_{10} H from pathway 1, undergoes hydrogenation at the unsaturated C2 site to form cyclohexane.
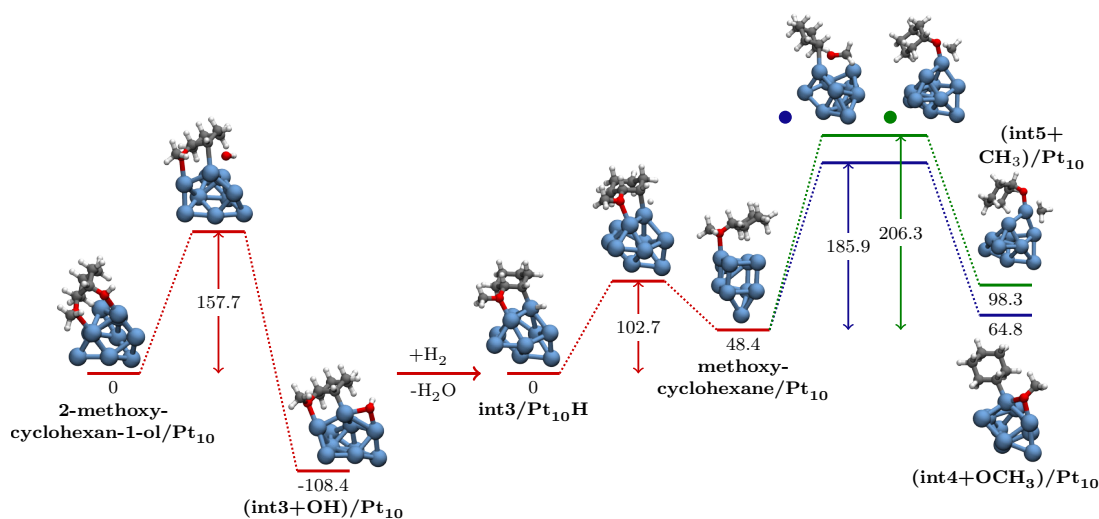
Figure 4.4: The sequence of elementary steps describing the conversion of 2-methoxycyclohexan-1-ol into methoxycyclohexane and the subsequent loss of the OCH_3 group on a platinum cluster (HYD pathway 2) is detailed. Initially, the C1-OH bond is broken. Following the fragmentation of a new H_2 molecule on the cluster and the formation and desorption of water, methoxycyclohexane is produced through hydrogenation at the C1 position. Subsequent steps involve either the cleavage of the C2-OCH_3 bond, resulting in the formation of an adsorbed methanol species (highlighted in blue), or the breaking of the O-CH_3 bond within the methoxy group, leading to methane production (highlighted in green).

Conversely, the alternative pathway (shown in green in **Fig.4.4**) involves breaking the O-CH_3 bond, which encounters a slightly higher energy barrier of 206.3 kJ mol^{-1}. The resulting $(int5+CH_3)/Pt_{10}$ species is approximately 50 kJ mol^{-1} less stable than the methoxycyclohexane/Pt_{10} species. This species features a dangling oxygen atom interacting with a Pt atom at the cluster's apical position (O-Pt bond length of 1.89 Å), along with the adsorbed CH_3 fragment.

The third pathway studied involves the early removal of methane, with a desorption energy of 23.4 kJ mol^{-1} and a BSSE correction of 4.5 kJ mol^{-1}. This process results in the formation of cyclohexane and two water molecules, following the intermediate steps that produce cyclohexane-1,2-diol and cyclohexanol. To achieve this, the O-CH_3 bond in 2-methoxycyclohexan-1-ol must be broken, requiring an energy barrier of 161.0 kJ mol^{-1}. This bond cleavage leads to the

95

formation of the (int6+CH$_3$)/Pt$_{10}$ species (**Fig. 4.5**), where the CH$_3$ fragment is adsorbed onto the Pt atom at the apical position. Additionally, this species is characterized by two interactions involving the oxygen atoms and the adjacent metal centers along the upper edge of the cluster.
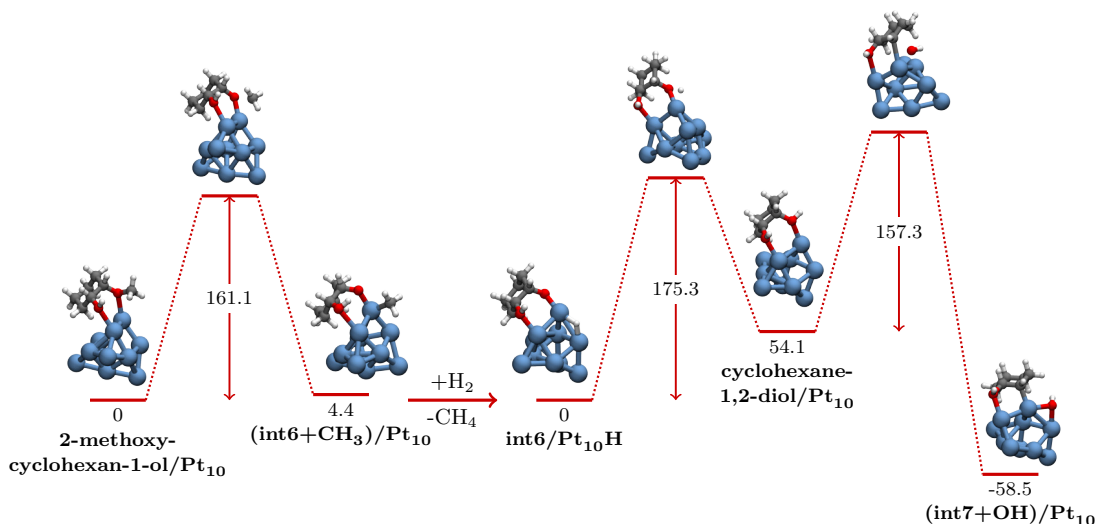

Figure 4.5: The reaction profile for HYD pathway 3: following the breaking of the O-CH$_3$ bond in the methoxy group, the int6 and CH$_3$ species are coadsorbed on Pt$_{10}$, leading to methane desorption after the fragmentation of an H$_2$ molecule. Cyclohexan-1,2-diol/Pt$_{10}$ is then formed through the hydrogenation of the dangling oxygen, followed by the cleavage of the C2-OH bond.

In the subsequent step, the fragmentation of an H$_2$ molecule on the cluster leads to the generation of methane through the transfer of an H atom to the carbon atom in the fragment. After methane desorbs, the hydrogen atom diffuses through the cluster toward the nearby dangling oxygen, forming the int6/Pt$_{10}$ H^b species. This intermediate then transforms into cyclohexane-1,2-diol/Pt$_{10}$. The hydrogenation of the dangling oxygen in this process requires overcoming an energy barrier of 175.0 kJ mol^{-1}, and the desorption energy for cyclohexane-1,2-diol is calculated to be 94.3 kJ mol^{-1} (with a BSSE correction of 19.6 kJ mol^{-1}). Following this, the C2-O bond breaks with an energy barrier of 157.3 kJ mol^{-1}, leading to the stabilization of the (int7+OH)/Pt$_{10}$ species. In this stabilized form, the OH fragment is distributed between two Pt atoms, while int7 interacts via oxygen and the unsaturated C2 with two Pt atoms in different coordination environments. As dis-

cussed in pathway 2, cyclohexane is ultimately formed on Pt_{10} from cyclohexanol through the cleavage of the C1-O bond (energy barrier of 192.1 kJ mol^{-1}), removal of water, and saturation of C1 (energy barrier of 54.7 kJ mol^{-1}, as illustrated in **Fig. A.2** in the Appendix).

4.2 DDO mechanism

The direct deoxygenation (DDO) of guaiacol begins with the removal of its oxygen-containing groups, followed by the hydrogenation of benzene into cyclohexane. The sequence in which the oxygenated groups are removed leads to different possible reaction pathways, as outlined in **Scheme 4.6**. If the hydroxyl group ($-$OH) is removed first, anisole is formed (with a desorption energy of 126.0 kJ mol^{-1} and BSSE = 22.6 kJ mol^{-1}). From anisole, benzene can be produced via two routes: one involves removing the methoxy group (demethoxylation), and the other involves demethanation, which can also generate phenol. On the other hand, if the methoxy group ($-$OCH$_3$) is the first to be removed, phenol is formed directly, which then converts into benzene. Guaiacol can also undergo demethanation to produce catechol, which leads to benzene after the removal of two water molecules. Finally, benzene formed from any of these pathways is hydrogenated to cyclohexane.
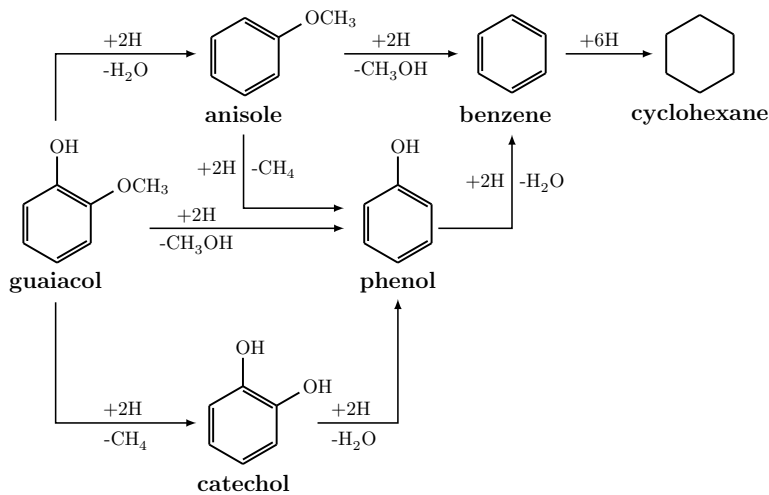

Figure 4.6: Schematic pathways for the conversion of guaiacol to cyclohexane via the DDO mechanism.

The first reaction pathway involves the removal of the $-OCH_3$ group, resulting in phenol, which then forms benzene through the loss of a water molecule. The initial step of this pathway (**Fig. 4.7**) involves breaking the C2-O bond, with an energy barrier of 129.2 kJ mol^{-1}, followed by the migration of the OCH_3 fragment to a platinum atom, where it undergoes hydrogenation and then desorbs. When compared to the demethoxylation energy barrier calculated by Lee *et al.* [128] for guaiacol on Pt(111), it is evident that reducing platinum to subnanometric sizes significantly lowers the energy barrier. This difference, along with other notable variations, can be tentatively explained by the increased flexibility and susceptibility to distortion of a cluster compared to a platinum surface [114].

It is worth noting that in the $(int1'+OCH_3)/Pt_{10}$ species, the hydrogen bond between the hydroxyl hydrogen and methoxyl oxygen is shortened from 2.16 Å (the bond length in guaiacol) to 1.60 Å. This indicates that methanol forms almost instantly by displacing the hydroxyl hydrogen atom, without the involvement of hydrogen activated by the catalyst. Furthermore, the hydrogen bond length of 1.47 Å in the $(int2'+CH_3OH)/Pt_{10}$ product suggests that the hydrogen atom is nearly shared between two oxygen atoms, likely facilitated by the small size of the metal cluster.

Starting with the $(int2'+CH_3OH)/Pt_{10}$ species, after the fragmentation of a H_2 molecule on the cluster, the reaction progresses with the restoration of the $-OH$ group in int2'. To investigate the impact of methanol on this step, the hydrogenation of the dangling oxygen was studied both in the presence and absence of adsorbed methanol. In the presence of methanol, the energy barrier for the transformation from $(int2'+CH_3OH)/Pt_{10}\,2\,H$ to $(int3'+CH_3OH)/Pt_{10}\,H$ is 49.9 kJ mol^{-1}, which is approximately one-third of the 167.1 kJ mol^{-1} required for the conversion from $int2'/Pt_{10}\,2\,H$ to $int3'/Pt_{10}\,H$ in the absence of methanol, as detailed in **Fig. A.3** in Appendix. Additionally, the hydrogenation of the oxygen atom in $(int2'+CH_3OH)/Pt_{10}\,2\,H$ releases 28.4 kJ mol^{-1}, compared to the 11.4 kJ mol^{-1} required for the same process without coadsorbed methanol. These observations suggest that methanol, initially considered a passive spectator, may significantly influence the reaction through local electronic or steric effects.

The subsequent weakening of the hydrogen bond, resulting from the restoration of the $-OH$ group, facilitates the desorption of methanol. The resulting species, $int3'/Pt_{10}\,H$, undergoes hydrogenation at the C2 position, with an energy barrier of 63.3 kJ mol^{-1}, and this step is associated with an energy release of 34.4 kJ mol^{-1}
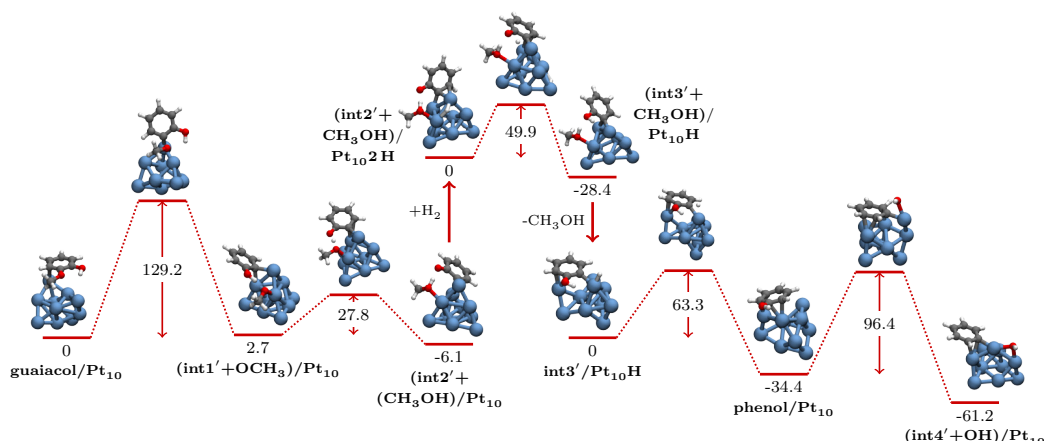
98

Figure 4.7: The reaction profile for DDO pathway 1: initially, the C2-OCH$_3$ bond is cleaved, leading to the formation of the (int1$'$+OCH$_3$)/Pt$_{10}$ species, along with the intramolecular hydrogenation of the OCH$_3$ fragment. This is followed by the hydrogenation of the exposed oxygen in int2$'$, catalyzed by activated hydrogen, in the presence of adsorbed CH$_3$OH. Next, methanol desorbs, restoring aromaticity and producing phenol/Pt$_{10}$. Finally, the cleavage of the C1-OH bond results in the formation of the (int4$'$+OH)/Pt$_{10}$ species.

as phenol/Pt$_{10}$ is formed. The calculated desorption energy for phenol is 132.8 kJ mol^{-1} (BSSE = 24.1). To produce benzene, water must be removed, which necessitates overcoming an activation barrier of 96.4 kJ mol^{-1} for the cleavage of the C1-O bond, leading to the formation of the (int4$'$+OH)/Pt$_{10}$ species. This species is approximately 30 kJ mol^{-1} more stable than phenol. The adsorbed OH fragment is then hydrogenated and removed as water. Meanwhile, the remaining int4 species is converted to benzene following the hydrogenation of the unsaturated C1 carbon, a process that involves a negligible energy barrier of 10.4 kJ mol^{-1} (**Fig. A.4** in Appendix).

The second pathway proposed for the DDO mechanism involves the removal of the $-$OH group, leading to the formation of anisole. From anisole, benzene is generated either through the cleavage of the $-$OCH$_3$ group or the $-$CH$_3$ fragment (in the latter case, via the formation of phenol). Notably, the cleavage of the C-OCH$_3$ bond in anisole is relatively easy, in contrast to the same process occurring on a Pt(111) surface [189]. The flexibility of the subnanometric cluster likely plays a crucial role in this step. In the transition state, the emerging phenyl radical from

bond cleavage is stabilized through strong interactions with the distorted cluster.

Benzene is subsequently converted to cyclohexane by the addition of three catalytically activated hydrogen molecules. The first elementary step in this pathway requires overcoming an energy barrier of 163.9 kJ mol^{-1}, which corresponds to the cleavage of the C1-OH bond. This leads to the formation of the (int5'+OH)/Pt$_{10}$ species, with the OH fragment adsorbed on a three-coordinate metal center of the cluster (**Fig. 4.8**).
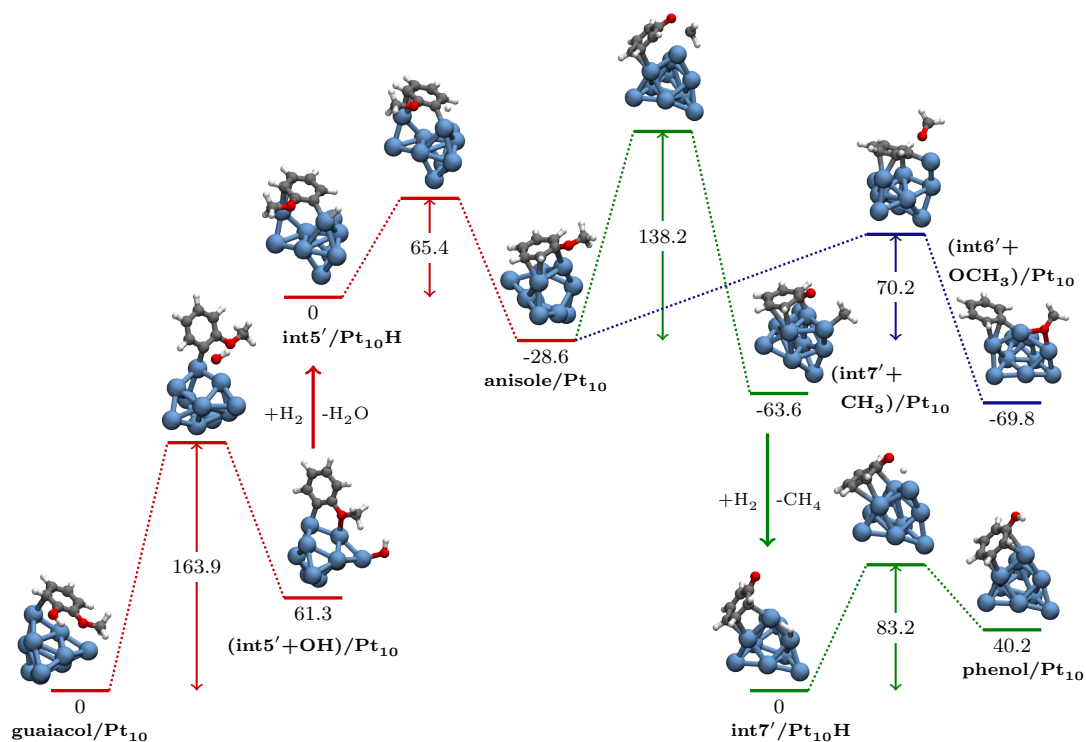
Figure 4.8: Elementary steps of the second DDO pathway: the cleavage of the C1-OH bond in guaiacol/Pt$_{10}$ forms the (int5'+OH)/Pt$_{10}$ species, which, after H$_2$ intervention and water desorption, is converted into anisole/Pt$_{10}$ through the reformation of the phenyl ring. From anisole, two reaction routes are possible: C-OCH$_3$ bond cleavage, yielding methanol and benzene (blue pathway), or OC-CH$_3$ bond cleavage, producing methane, benzene, and water via phenol as an intermediate (green pathway).

The subsequent dissociation of a new H$_2$ molecule initiates the formation and desorption of water, restoring the aromaticity of the system. This occurs in the second elementary step, where the transfer of an H atom to the unsaturated C1 of the

ring, starting from the int5′/Pt$_{10}$ H species, leads to the formation of anisole/Pt$_{10}$. This species is more stable by approximately 29 kJ mol^{-1} compared to the intermediate reactant, and the process requires overcoming a relatively low energy barrier of 65.4 kJ mol^{-1}. From anisole/Pt$_{10}$, two mechanisms can occur.

In the first, cleavage of the C2-O bond, with an energy barrier of 70.2 kJ mol^{-1}, yields the (int6′+OCH$_3$)/Pt$_{10}$ species, which is 41 kJ mol^{-1} more stable than chemisorbed anisole. In this intermediate, the OCH$_3$ fragment is shared between two Pt atoms with different coordination on the upper edge of the cluster. Following H$_2$ dissociation on the cluster, the OCH$_3$ fragment is hydrogenated to CH$_3$OH and desorbs. The resulting species undergoes rapid hydrogenation at the C2 position, yielding a benzene molecule.

Alternatively, cleavage of the O-C bond within the $-$OCH$_3$ group, with an energy barrier of 138.2 kJ mol^{-1}, results in the formation of the (int7′+CH$_3$)/Pt$_{10}$ species. This intermediate is characterized by the CH$_3$ fragment bound to the Pt atom at the apical position, with a dangling oxygen atom interacting only via the ring carbons with the cluster. Upon dissociation of a H$_2$ molecule, the chemisorbed CH$_3$ fragment is hydrogenated to methane, which desorbs, while the second hydrogen atom diffuses to form the int7′/Pt$_{10}$ H species. Subsequently, the transfer of an H atom to the dangling oxygen on the ring (with an energy barrier of 83.2 kJ mol^{-1}) forms chemisorbed phenol, which, following the first proposed pathway, leads to benzene/Pt$_{10}$.

The third proposed pathway involves the early-stage removal of the methyl group as methane, leading to the formation of adsorbed catechol, from which benzene is produced following the loss of two water molecules. The initial elementary step of this pathway involves the cleavage of the O-CH$_3$ bond in guaiacol/Pt$_{10}$, with the methyl fragment adsorbing onto a platinum atom of the cluster, releasing 55.0 kJ mol^{-1} of energy. This is followed by the hydrogenation of the chemisorbed fragment, forming methane, which subsequently desorbs. The diffusion of hydrogen atoms through the cluster enables the hydrogenation of the dangling oxygen atom in the int8′/Pt$_{10}$ H species, a process requiring an energy barrier of 155.8 kJ mol^{-1}, leading to the formation of catechol/Pt$_{10}$, which is 69.1 kJ mol^{-1} less stable than the initial reactant.

For catechol, the desorption energy is calculated at 160.6 kJ mol^{-1} (with BSSE = 23.3 kJ mol^{-1}). The cleavage of the C2–OH bond results in the formation of the (int3′+OH)/Pt$_{10}$ intermediate, where the OH fragment is shared

between two metal centers located at the cluster edge (Fig. 4.5). The subsequent removal of a water molecule generates the int3′/Pt$_{10}$ H species, which leads to the formation of phenol/Pt$_{10}$, and eventually benzene, as described in the first DDO pathway.
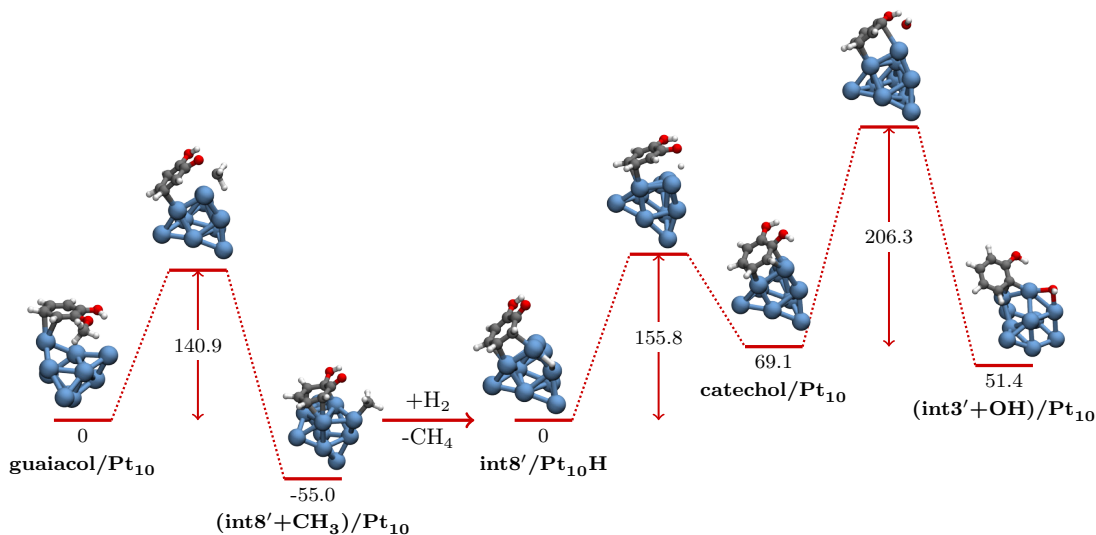
Figure 4.9: DDO pathway 3: formation of methane and catechol from guaiacol. The catechol/Pt$_{10}$ species subsequently undergoes dehydration, leading to the cleavage of the C2–OH bond and its conversion into a phenol precursor.

In the third DDO pathway, the benzene molecule formed (with a calculated desorption energy of 167.5 kJ mol^{-1}, BSSE = 26.4 kJ mol^{-1}) undergoes sequential hydrogenation to yield cyclohexane. Unlike the HYD mechanism, where both electronic effects of substituents and metal/substrate interactions determine the preferred hydrogenation site, in the DDO mechanism, the first hydrogenation step is primarily influenced by metal/substrate interactions. As a result, only carbon atoms in direct interaction with platinum atoms are available for hydrogenation.

Hydrogen addition was evaluated at four carbon atoms in the benzene ring (labeled C1, C2, C5, and C6, see **Fig. 4.10**). Among these, C6 was identified as the most favorable site for initial hydrogenation, exhibiting the lowest energy barrier of 82.4 kJ mol^{-1} and producing the most stable intermediate. For subsequent hydrogenations, carbon atoms in the *ortho*-position relative to the previously hydrogenated site (C6) were considered, specifically C1 and C5. The lower energy barrier (83.6 vs. 103.4 kJ mol^{-1}) indicates that hydrogenation preferentially occurs

at C5, leading to the formation of cyclohexa-1,3-diene, with a desorption energy of 190.9 kJ mol^{-1} (BSSE = 24.1 kJ mol^{-1}).

Following this, a third hydrogen atom adds to C4 with a very low energy barrier of 24.9 kJ mol^{-1}, releasing 22.1 kJ mol^{-1} of energy and resulting in the intermediate species **IIIa**. Subsequent hydrogen transfer to C3 forms a stable cyclohexene species, with a calculated desorption energy of 154.2 kJ mol^{-1} (BSSE = 21.6 kJ mol^{-1}).

Based on the lower activation energy (35.4 vs. 85.9 kJ mol^{-1}) and the higher stability of the intermediate (17.6 vs. 40.1 kJ mol^{-1}), C2 is identified as the preferred site for the addition of the fifth hydrogen atom. Finally, the intermediate **Va** undergoes hydrogenation at C1, resulting in the formation of adsorbed cyclohexane. The desorption energy for cyclohexane is calculated to be 85.0 kJ mol^{-1}, with BSSE = 17.6 kJ mol^{-1}.

4.3   Kinetic Analysis

In the preceding sections, I investigated eight potential pathways for the conversion of guaiacol to cyclohexane using a Pt$_{10}$ cluster, as depicted in **Figures 4.6** and **4.1**. *DFT* calculations provided both the energy barriers and the relative energies of minima on the potential energy surface. Our analysis suggests that, in the initial stages of the reaction, hydrogenation of the aromatic ring is kinetically more favorable than deoxygenation. Notably, deoxygenation is more likely to proceed directly from guaiacol rather than via the fully hydrogenated intermediate, methoxycyclohexanol. To further refine the mechanistic insights and establish the most kinetically favorable pathway, I employed microkinetic modeling rather than solely comparing energy barriers. Specifically, I applied the recently developed Simplified Christiansen Method (*SCM*) as described in previous work (refs. [180] and [183]). Given that cyclohexane desorption is strongly influenced by entropy, which in turn affects the overall reaction rate, *SCM* analysis was performed using Gibbs free energies as a function of temperature. As shown in Appendix **Tables A.3**, **A.5**, and **A.4**, the use of Gibbs free energy (ΔG) in place of zero-point vibrational energy (E$_{ZPV}$) produces negligible changes in the computed energy barriers and intermediate energy differences, but exerts a marked influence on the desorption energies of all stable intermediates.

The *SCM* analysis, presented in **Tables 4.3**, **4.2** and in Appendix **A.2**, **A.4**,
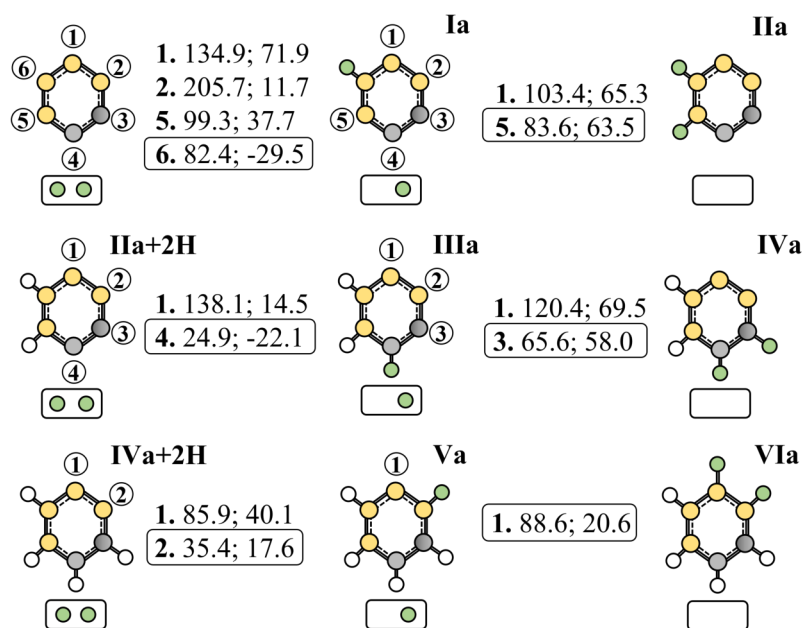
Figure 4.10: A schematic representation of benzene saturation on the Pt_{10} cluster. The yellow circles mark the interaction sites between the benzene molecule and the cluster, which is depicted as a small rectangle containing the adsorbed hydrogen atoms (green circles). To the right of each species, the first number denotes the carbon position where catalytic hydrogen is added, the second indicates the energy barrier of the corresponding elementary reaction step, and the third specifies the product's energy relative to its reactant. All energy values are given in kJ mol^{-1}. The initial hydrogenation starts from benzene, the second proceeds from **IIa+2H** (cyclohexa-1,3-diene), and the final hydrogenation begins with **IVa+2H** (cyclohexene).

demonstrates that DDO pathways are consistently at least two orders of magnitude faster than their HYD counterparts. At lower temperatures, DDO routes leading to anisole and phenol exhibit comparable reaction rates, with benzene hydrogenation identified as the slowest step. As temperature increases, the HDO reaction on Pt_{10} primarily proceeds via the DDO pathway, where phenol is formed as an intermediate following early-stage demethoxylation. Guaiacol, as also experimentally demonstrated by Arvela and co-workers [190], is deoxygenated at high temperatures or at very high pressures at temperatures below 350 °C, resulting in HDO yields between 60-80%. These results can be explained theoretically at

Table 4.1: Summary of the eight most important mechanisms found for the guaiacol hydrodeoxygenation reaction on Pt_{10}, according to the scheme reported in **Figures 4.6** and **4.1**.

mechanism	sequence	other products
HYD-1	G–MOCEO–CEO–CE	CH_3OH, H_2O
HYD-2	G–MOCEO–MOCE–CE	CH_3OH, H_2O
HYD-3	G–MOCEO–MOCE–CEO–CE	CH_4, $2\,H_2O$
HYD-4	G–MOCEO–CEDO–CEO–CE	CH_4, $2\,H_2O$
DDO-1	G–P–B–CE	CH_3OH, H_2O
DDO-2	G–AN–B–CE	CH_3OH, H_2O
DDO-3	G–AN–P–B–CE	CH_4, $2\,H_2O$
DDO-4	G–CA–P–B–CE	CH_4, $2\,H_2O$

the *DFT* level, confirming that the reactivity of phenolic compounds decreases as the number of oxygen atoms increases. Furthermore, from a thermodynamic perspective, the hydroxyl group attached to benzene is more difficult to cleave than a methoxyl group [167, 127, 191, 192, 193] (also in our analysis, the DDO-1 mechanism is favoured over DDO-2). The DDO pathway involving catechol is kinetically hindered by the high energy barrier associated with C–OH bond cleavage. Consequently, the fastest mechanisms are DDO-driven, and due to the slow reduction of benzene, it exhibits the highest surface molar ratio (Θ) over the entire temperature range studied (473–1073 K).

Within the HYD pathways, the route involving methoxycyclohexane, which undergoes direct conversion to cyclohexane, is marginally favored over alternative mechanisms. The analysis suggests that C–OH bond cleavage in 2-methoxycyclohexa-1-ol, a hydrogenated intermediate of guaiacol, is slightly more favorable than the cleavage of the C–OCH_3 bond. In contrast, cleavage of the O–CH_3 bond, leading to methane formation, remains the least favorable process. Nevertheless, all HYD pathways, aside from methane formation, exhibit nearly identical reaction rates.

Based on the calculated energy barriers (reaction rates as a function of E_{ZPV} across temperatures are reported in **Table 4.3**), complete hydrogenation of the phenyl ring in guaiacol proceeds with relative kinetic ease. However, the overall rate of HYD pathways is constrained by the slower C–O bond scission.

Table 4.2: The reaction rates (s^{-1}) of the eight guaiacol hydrodeoxygenation (HDO) mechanisms (M) are reported at various temperatures (K). The exponent of 10 in the scientific notation is indicated in parentheses. Gibbs free energies, as a function of temperature at a pressure of 1 atm, have been taken into account for the kinetic analysis.

T \ M	473	573	673	773	873	973	1073
HYD-1	1.6(-13)	9.3(-9)	1.8(-5)	8.5(-4)	3.2(-3)	4.8(-3)	1.5(-2)
HYD-2	1.9(-12)	5.3(-8)	5.8(-5)	2.0(-3)	5.0(-3)	5.2(-3)	1.3(-2)
HYD-3	6.9(-15)	8.6(-10)	3.0(-6)	8.0(-4)	4.6(-3)	5.0(-3)	1.2(-2)
HYD-4	1.7(-18)	9.8(-13)	9.4(-9)	1.5(-6)	1.4(-5)	4.3(-5)	2.5(-4)
DDO-1	4.9(-9)	3.7(-5)	1.9(-2)	1.7(0)	3.6(+1)	6.2(+2)	1.1(+3)
DDO-2	4.9(-9)	3.7(-5)	1.9(-2)	1.0(0)	3.2(0)	3.1(0)	7.3(0)
DDO-3	4.9(-9)	3.7(-5)	1.8(-2)	6.6(-1)	1.9(0)	1.9(0)	4.5(0)
DDO-4	1.2(-16)	3.2(-11)	2.1(-7)	2.0(-4)	1.0(-2)	4.5(-2)	2.2(-1)

4.4 Conclusions

This chapter has examined the "direct deoxygenation" (DDO) and "deoxygenation-through-hydrogenation" (HYD) mechanisms for the hydrodeoxygenation of guaiacol, catalyzed by a subnanometer platinum cluster, within the broader context of developing renewable and eco-sustainable alternatives. The atomistic-level analysis reveals that, contrary to previous literature which suggests a metal-dependent preference for one mechanism over the other (e.g., noble versus non-noble metals), this generalization doesn't necessarily extend to subnanometer clusters. Such clusters deviate from conventional rules of heterogeneous catalysis, often requiring case-specific evaluations.

Our findings indicate that, while early hydrogenation of the phenyl ring in guaiacol may kinetically favor hydrogenation over $C(sp^2)$–O bond cleavage, the DDO mechanism is nonetheless preferred on Pt_{10}. This preference arises from the lower energy barriers associated with cleaving the $C(sp^2)$–OCH_3 bond in guaiacol and the $C(sp^2)$–OH bond in phenol, compared to the higher barriers for $C(sp^3)$–OCH_3

Table 4.3: The reaction rates (s^{-1}) for the eight guaiacol hydrodeoxygenation (HDO) mechanisms (M) are presented at various temperatures (K). The exponent of 10 in the scientific notation is provided in parentheses. Energy values including the vibrational zero-point energy (ZPE) contribution have been considered for the kinetic analysis.

T / M	473	573	673	773	873	973	1073
HYD-1	4.8(-15)	3.1(-10)	7.3(-7)	2.3(-4)	2.0(-2)	6.9(-1)	1.2(+1)
HYD-2	5.6(-14)	2.2(-9)	3.8(-6)	9.6(-4)	6.9(-2)	2.1(0)	3.3(+1)
HYD-3	3.1(-19)	1.2(-13)	9.9(-10)	8.2(-7)	1.5(-4)	9.1(-3)	2.6(-1)
HYD-4	3.4(-20)	1.8(-14)	1.9(-10)	1.8(-7)	3.6(-5)	2.4(-3)	7.6(-2)
DDO-1	8.1(-13)	2.3(-8)	3.2(-5)	6.9(-3)	4.3(-1)	1.2(+1)	1.7(+2)
DDO-2	8.1(-13)	2.3(-8)	3.2(-5)	6.9(-3)	4.3(-1)	1.2(+1)	1.7(+2)
DDO-3	8.1(-13)	2.3(-8)	3.1(-5)	6.8(-3)	4.3(-1)	1.2(+1)	1.7(+2)
DDO-4	3.9(-18)	9.5(-13)	6.0(-9)	4.0(-6)	6.1(-4)	3.3(-2)	8.7(-1)

bond cleavage in 2-methoxycyclohexan-1-ol and $C(sp^3)$–OH bond scission in cyclohexanol. Furthermore, the energy barrier for $C(sp^2)$–OCH_3 bond cleavage in anisole is lower than that for its fully hydrogenated counterpart in the HYD mechanism. At 0 K, desorption energies for cyclohexanol and methoxycyclohexane are lower than the activation energies for $C(sp^3)$–OH and $C(sp^3)$–OCH_3 bond cleavage, rendering desorption more favorable. In contrast, desorption within the DDO mechanism is less favorable, as the energy required for desorption exceeds that for the subsequent reaction steps. These observations underscore the importance of substrate-cluster interactions: in the DDO mechanism, the aromatic species strongly interact with the Pt cluster via the phenyl ring, facilitating C–O bond scission. Conversely, in the HYD mechanism, hydrogenated intermediates exhibit weak adsorption, limiting the number of molecules capable of surmounting the energy barriers necessary for cyclohexane formation.

At lower temperatures, these conclusions remain consistent when considering Gibbs free energies, although desorption and transformation steps become more competitive within the DDO mechanism. At higher temperatures, desorption is

107

more facile, yet the overall preference for the DDO mechanism persists. Specifically, the most favorable pathway involves elimination of the $-OCH_3$ group as methanol, followed by the removal of the $-OH$ group as water.

Chapter 5

Decomposition of Guaiacol on Pt$_{10}$ cluster

The decomposition of guaiacol on metal catalysts, especially platinum-based catalysts, is a topic of great interest in the context of computational chemistry and hydrodeoxygenation processes. Previous computational studies have provided important insights into the molecular mechanisms underlying guaiacol decomposition, often relying on density functional theory (*DFT*) and kinetic modeling approaches. Notable contributions from Vlachos [194] and Heyden [195] have clarified the key steps in this process, specifically on the Pt(111) surface, and have offered detailed understanding of the activation energies required for elementary reactions such as C−OCH$_3$ bond cleavage and phenyl ring dehydrogenation.

The guaiacol structure, characterized by the presence of a methoxy group (OCH$_3$) and a hydroxyl group (OH), offers several decomposition pathways that vary depending on the nature of the catalyst and the operating conditions. Vlachos and coworkers [194] suggested that the preferential route for the transformation of guaiacol into catechol occurs through a first dehydrogenation of the methoxy group, followed by the cleavage of the O−C bond. In this scenario, direct deoxygenation via C−O bond scission in the aromatic ring is less favorable on platinum surfaces, likely requiring the presence of acidic supports, such as alumina, to be facilitated. Heyden and coworkers [195], extending the analysis with a kinetic approach that takes into account entropic and pressure effects, confirmed these observations, identifying two preferential pathways for the decomposition of guaiacol, both characterized by a first dehydrogenation of the methoxyl or hydroxyl

group.

The morphology of the catalytic surface also plays a crucial role. Investigations by Scollous *et al.* [196], conducted on low-index Pt(100) surfaces, revealed that, contrary to the behavior on the (111) surface, guaiacol does not interact with the benzene ring, probably due to incompatible geometries, and the preferred chemisorbed species arises from the cleavage of the O–H bond. The experimental countepart of the subnanometric cluster used as catalyst model in the present study could be the precise Pt_n (n= 5–13) clusters obtained by Imaoka *et al.* [197] by low-temperature calcination of platinum organothiolates, or those realized by Schmitt and coworkers [198] by using a industrial-appealing continuous-flow method, or still the Pt clusters derived from H_2PtCl_6 by means of solvothermal and deposition-precipitation approches as proposed by Xiang *et al.* [199].

It is not surprising that guaiacol's reactivity, with its multiple functional groups, is highly influenced by the structure of the catalyst, an effect that becomes particularly pronounced in subnanometric metal clusters, where atom coordination numbers vary significantly. In this context, the aim of this chapter is to investigate guaiacol decomposition on a subnanometric platinum cluster using *DFT* simulations. The exploration of novel and not yet documented mechanisms, combined with a Christiansen-type microkinetic approach, will allow to thoroughly evaluate the thermodynamic results and identify the most likely decomposition pathway, if the concurrent reation paths are assumed to be linearly independent.

5.1   Decomposition Mechanism

Four distinct pathways for guaiacol decomposition on Pt_{10} were investigated (see **Fig. 5.1**). Three of these pathways lead to fully deoxygenated products, such as benzene and cyclopentene, and can be considered branches of an initial mechanism (**M1**), which first converts guaiacol into phenol. The fourth pathway, in contrast, results in a partially oxygenated species, 2,4-cyclopentadien-1-one, as the final product, representing a distinct mechanism (**M2**).

These decomposition pathways highlight the versatility of guaiacol reactivity on platinum-based catalysts, with the different mechanisms reflecting variations in bond cleavage and intermediate stability. While the **M1** pathways prioritize complete oxygen removal, leading to full deoxygenation, **M2** provides an alternative route that retains some oxygen, demonstrating the catalyst's ability to facilitate
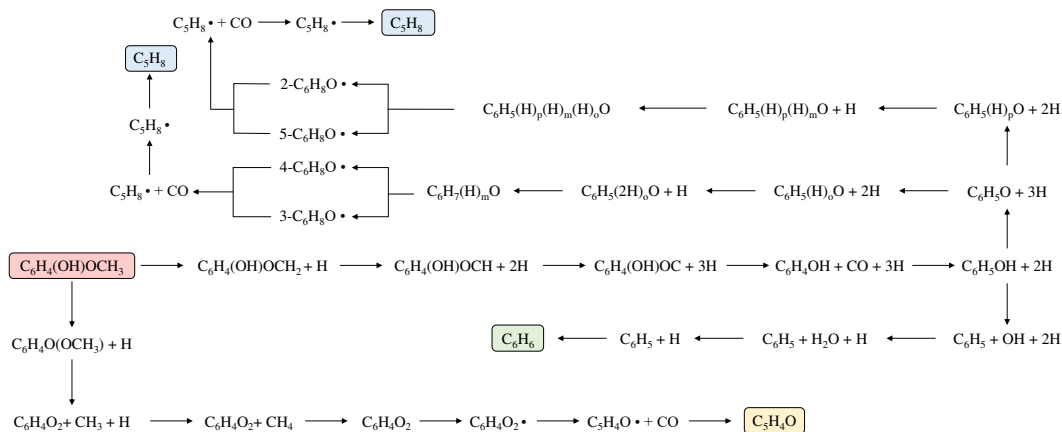
C$_5$H$_8\bullet$ + CO $\longrightarrow$ C$_5$H$_8\bullet$ $\longrightarrow$ [C$_5$H$_8$]

[C$_5$H$_8$]

C$_5$H$_8\bullet$

2-C$_6$H$_8$O$\bullet$ $\leftarrow$

5-C$_6$H$_8$O$\bullet$ $\leftarrow$

C$_6$H$_5$(H)$_p$(H)$_m$(H)$_o$O $\longleftarrow$ C$_6$H$_5$(H)$_p$(H)$_m$O + H $\longleftarrow$ C$_6$H$_5$(H)$_p$O + 2H

4-C$_6$H$_8$O$\bullet$ $\leftarrow$

3-C$_6$H$_8$O$\bullet$ $\leftarrow$

C$_5$H$_8\bullet$ + CO $\leftarrow$

C$_6$H$_7$(H)$_m$O $\longleftarrow$ C$_6$H$_5$(2H)$_o$O + H $\longleftarrow$ C$_6$H$_5$(H)$_o$O + 2H $\longleftarrow$ C$_6$H$_5$O + 3H

C$_6$H$_4$(OH)OCH$_3$ $\longrightarrow$ C$_6$H$_4$(OH)OCH$_2$ + H $\longrightarrow$ C$_6$H$_4$(OH)OCH + 2H $\longrightarrow$ C$_6$H$_4$(OH)OC + 3H $\longrightarrow$ C$_6$H$_4$OH + CO + 3H $\longrightarrow$ C$_6$H$_5$OH + 2H

C$_6$H$_4$O(OCH$_3$) + H

[C$_6$H$_6$] $\longleftarrow$ C$_6$H$_5$ + H $\longleftarrow$ C$_6$H$_5$ + H$_2$O + H $\longleftarrow$ C$_6$H$_5$ + OH + 2H

C$_6$H$_4$O$_2$+ CH$_3$ + H $\longrightarrow$ C$_6$H$_4$O$_2$+ CH$_4$ $\longrightarrow$ C$_6$H$_4$O$_2$ $\longrightarrow$ C$_6$H$_4$O$_2\bullet$ $\longrightarrow$ C$_5$H$_4$O$\bullet$ + CO $\longrightarrow$ [C$_5$H$_4$O]

Figure 5.1: The scheme outlines the pathways explored for the decomposition of guaia-col on the Pt$_{10}$ cluster. The subscripts o, m, and p represent the positions of the added hydrogen atom relative to the oxygen atom, corresponding to *ortho*, *meta*, and *para*, respectively. A black dot ($\bullet$) next to a molecular formula indicates the opening of the phenyl ring. All four reactions begin with a common starting point, the guaiacol molecule C$_6$H$_4$(OH)OCH$_3$ (highlighted in red), and result in either cyclopentene (light blue boxes), benzene (light green box), or 2,4-cyclopentadien-1-one (yellow box).

selective transformations.

5.1.1 M1 mechanism

The first mechanism (named **M1** and illustrated in **Fig. 5.2**) involves a sequen-tial migration of three hydrogen atoms from the $-$OCH$_3$ group to the Pt$_{10}$ cluster, following a process that, once triggered (the first energy barrier is 106.5 kJ mol^{-1}), proceeds relatively smoothly. This three-fold dehydrogenation leads to the forma-tion of the species C$_6$H$_4$(OH)OC/Pt$_{10}$ 3 H. Three different processes (**Fig. 5.3**) have been identified for the subsequent breaking of the C-CO bond. In the pre-viously formed C$_6$H$_4$(OH)OC/Pt$_{10}$ 3 H species, the organic fragment binds to the cluster via the free carbon atom; this interaction appears to be strong enough to reposition the phenyl ring in a position relatively far from the platinum.

- **M1, case a)** Following hydrogen migration from one of the involved Pt center, the carbon atom insert between two Pt, triggering a cluster geome-try reorganization and resulting in a structure which is only 15.8 kJ mol^{-1}
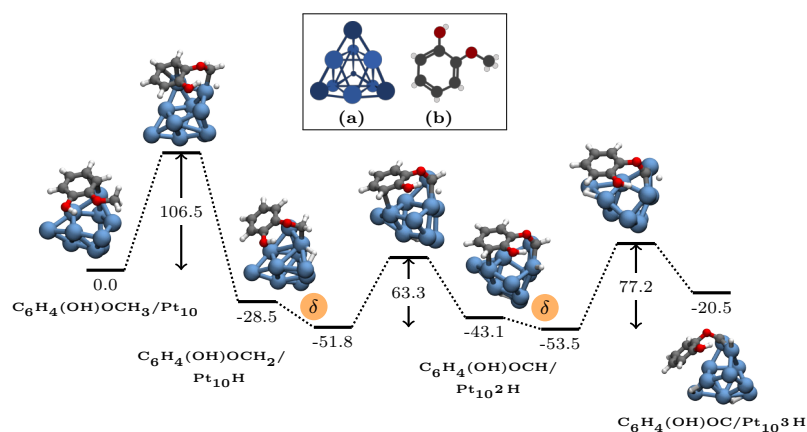
Figure 5.2: M1: The profile depicts the first elementary steps related to the loss of the three hydrogen atoms of the OCH_3 fragment from guaiacol/Pt_{10}: the species $C_6H_4(OH)CO/Pt_{10}\,3\,H$ is thus obtained as a precursor to the loss of carbon monoxide. The greek letter δ within the orange circle denotes the occurrence of a diffusion phenomenon in which the hydrogen atom from its position migrates to a distant location in the cluster. Inside the inset: **(a)** The Pt_{10} cluster selected as the subnanometer catalyst model in the present investigation: the different colors (blue and light blue) indicate the coordination numbers 3 and 6, respectively; **(b)** Guaiacol as a model for the oxygenated compounds contained in lignocellulosic biomass.

less stable. Nevertheless, in this configuration, the C−CO bond breaking is inhibited, since in the transition state structure the phenyl carbon atom involved in the breaking (denoted as C*) cannot benefit of stabilizing interactions with the underlying platinum atoms; the resulting energy barrier should be in this case ca. 290 kJ mol^{-1}.

- **M1, case b)** To achieve a more stable transition state structure, it is essential that the phenyl ring binds to platinum. This could occur if all the C*-CO bonds were to be positioned directly above a single Pt atom. This arrangement could arise in several ways: in the first scenario, the CO moiety would need to leave its position between the platinum atoms and move to sit atop a single platinum atom, prompting a corresponding rearrangement of the entire cluster. From this new configuration, the search for transition states revealed an energy barrier of 135.6 kJ mol^{-1}. Although this elementary step is considerably faster than the previous case (a), the energy gain is somewhat misleading since the rearranged reactant is approximately 75 kJ mol^{-1} less stable than the original $C_6H_4(OH)OC/Pt_{10}\,3\,H$ species. Even if some interactions between phenyl and platinum are restored, this energy difference should not be considered negligible.

- **M1, case c)** However, by examining the qualitative nature of the transition state from case b, it became evident that the stabilizing atop configuration (where the insertion of a platinum atom between C* and OC is facilitated) can be achieved more easily from the $C_6H_4(OH)OC/Pt_{10}\,3\,H$ species. This is accomplished simply by utilizing the missing π-Pt interactions in this species and rotating the entire fragment around the inserted C−O bond. The result is a species with an energy only 12.3 kJ mol^{-1} higher and, importantly, an energy barrier of 73.8 kJ mol^{-1} for the cleavage of the C−CO bond.

After CO desorption, characterised by a high desorption energy ($E des$) of 231.6 kJ mol^{-1} and a BSSE of 21.3 kJ mol^{-1}, a structural rearrangement (denoted by the Greek letter ρ) of the radical species remaining on the cluster occurs. The molecule's aromaticity is restored through the transfer of a hydrogen atom from the platinum to the unsaturated carbon atom of the ring. This elementary step proved to be virtually barrier-free and resulted in a stabilisation of the product of about 60 kJ mol^{-1}. From the species $C_6H_5OH/Pt_{10}\,2\,H$, the phenol could either desorb ($E_{des} = 176.6$ kJ mol^{-1}, with a BSSE of 21.4 kJ mol^{-1}) or, as illustrated in
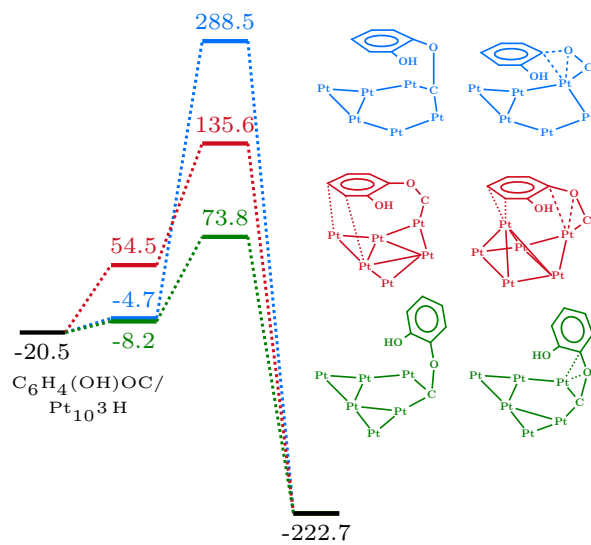
Figure 5.3: Three possible pathways for the breaking of the C–CO bond emerge from the opportunely rearranged $C_6H_4(OH)OC/Pt_{10}\,3\,H$ species in the M1 channel. The energy minima are referred to the guaiacol/Pt_{10} system, while the energy barriers are indicated above the corresponding transition states. Energies are expressed in kJ mol^{-1}. Figures next to the energy diagram (with corresponding colors) schematically show the geometries and the connections of reactants and transition states associated to the three alternative elementary processes. Only the Pt atoms directly involved in the process are shown.

Fig. 5.1, switch to one of the three reaction branches analysed (named **M1–1**). It is worth noting that, from now, the M1 mechanism for the decomposition of guaiacol overlaps with the hydrodeoxygenation reaction of phenol, which could take place at low hydrogen pressure.

M1–1 ramification

In the first ramification of the **M1** mechanism (**M1–1**, **Fig. 5.4**), the loss of a molecule of H_2O could occur through the breaking of the C−OH bond and the hydrogenation of the displaced OH fragment. The first elementary step of this process exhibits a very high energy barrier of 163.7 kJ mol^{-1}, probably due to the fact that, as in the case of C−CO bond cleavage, the cluster must undergo considerable distortion and the adsorbed molecule must rearrange itself in order to use a single Pt atom as a reactive site. The second step, characterised by a lower energy barrier of 95 kJ mol^{-1}, consists of the transfer of an H atom from the cluster to the oxygen atom of the OH fragment, adsorbed by bridging oxygen between two platinum atoms. The C_6H_5/Pt_{10} species, resulting from the desorption of the H_2O molecule thus formed, undergoes hydrogenation on the unsaturated carbon via an elementary step that has an energy barrier of 89.9 kJ mol^{-1}, leading finally to the formation of adsorbed benzene, which is 54 kJ mol^{-1} more stable than the intermediate before it.

M1–2 ramification

The second channel (**M1–2**) examined in this investigation proceeds with the release of the hydrogen atom from the phenol, rather than the breaking of the C−OH bond. The configuration that phenol must assume in order to undergo this process highlights the tendency of molecules to utilise a single platinum atom as an active site for the reaction, as well as platinum's greater affinity for carbon than oxygen, which is possibly not surprising. In fact, the partially unpaired electron resulting from breaking the C−OH bond in the transition state does not locate on the oxygen atom (which would form an Pt−O bond), but prefers to locate on the carbon atom in the *ortho* position, thus facilitating the creation of a partial carbonyl bond, a strong Pt−C bond and the correct local geometry for the reaction. Indeed, it has been hypothesized [200, 201] that the peculiar interaction between platinum and carbon is capable of determining the geometry of small Pt clusters.
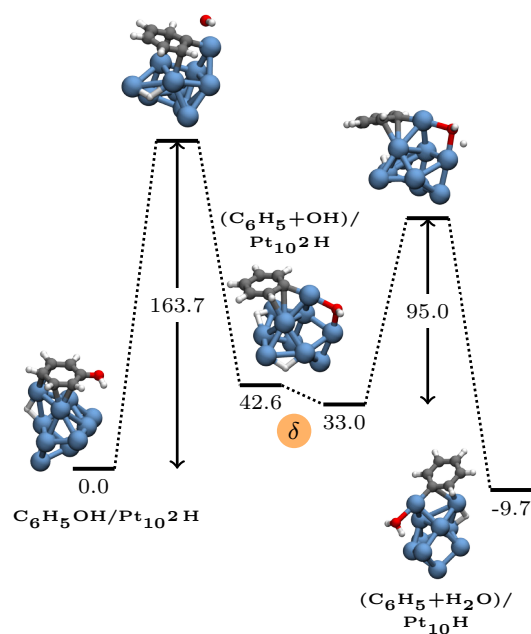
Figure 5.4: The first branch of the **M1** channel: following desorption of carbon monoxide and restoration of system aromaticity, the resulting $C_6H_5OH/Pt_{10}\,2\,H$ species undergoes $C-OH$ bond cleavage. After desorption of the OH fragment as water at expense of the atomic hyrogen in the cluster, the precursor of benzene as final product is formed.
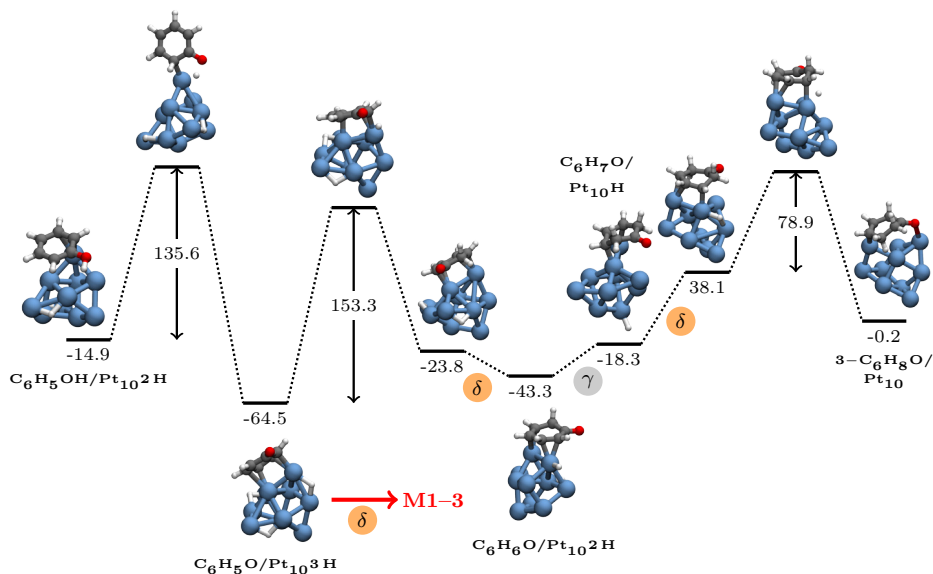
Figure 5.5: The second branch of the **M1** mechanism, after the dehydrogenation of the OH group, involves three consecutive hydrogenations on the ring's carbon atoms, located respectively at the *ortho* and *meta* positions with respect to the oxygen atom. The letter γ on a grey background indicates an elementary stage without energy barriers, while δ, as already explained, represents the diffusion of a hydrogen atom between the cluster sites. The energies of the minima refer to the initial reactant shown in the **Fig. 5.4**.

The $C_6H_5O/Pt_{10}\,3\,H$ species undergoes three consecutive hydrogenation processes. The first occurs on the carbon in *ortho* position with respect to the oxygen atom and requires the overcoming of an energy barrier equal to 153.3 kJ mol^{-1}. Therefore, the species $C_6H_6O/Pt_{10}\,2\,H$, where diffusion of an H atom through the metal sites (δ) occurred, undergoes hydrogenation on the other carbon atom in *ortho* to oxygen with formation of the $C_6H_7O/Pt_{10}\,H$ species. This step is to be considered essentially barrier-free, as indicated by the Greek letter γ within the gray circle in **Fig. 5.5**. Finally, the last H atom on the cluster is added onto the carbon atom in *meta* position. This yields cyclohex-3-en-1-one (3-C_6H_8O/Pt_{10}), whose desorption requires an of energy of 184.9 kJ mol^{-1} (BSSE=19.1 kJ mol^{-1}).

From the 3-C_6H_8O/Pt_{10} species, two different possible reaction pathways can be identified, depicted in orange and blue colors in **Fig. 5.6**, originating from the breaking of the C(1) –C(6) bond rather than the C(1) –C(2) one. Both involve, after cleavage of the C–C bond, the loss of carbon monoxide. The two pathways

appear competitive with each other: if the energy barrier is lower for the formation of the 4-$C_6H_8O\bullet/Pt_{10}$ species (140. 8 vs 170 kJ mol^{-1}), the stabilization of 3-$C_6H_8O\bullet/Pt_{10}$ and, in particular, of the subsequent (3-$C_5H_8\bullet + CO)/Pt_{10}$ species in the alternative channel is significantly greater (-160.1 vs -62.9 kJ mol^{-1}). These differences in energetics makes the identification of the most favorable pathway ambiguous, a matter made worse by the fact that two paths, at the end, converge toward the same C_5H_8/Pt_{10} species, obtained by the formation of a new C–C bond as will be detailed later.

M1–3

The third branch of the M1 mechanism, illustrated in **Fig. 5.8** shares its first elementary step with the second ramification, but differs in the positions where hydrogen atoms are added to the carbon atoms of the ring. In this case, the three hydrogen atoms are consecutively attached to the *para*, *meta*, and *ortho* positions relative to the C=O group. These three hydrogenation steps have comparable energy barriers, around 70-80 kJ mol^{-1}, and lead to the formation of the 2-C_6H_8O/Pt_{10} species (cyclohex-2-en-1-one), with a calculated desorption energy of 170.8 kJ mol^{-1} (BSSE=19.1 kJ mol^{-1}). It is worth noting that the value of the first energy barrier appears lower than the corresponding one (153.3 kJ mol^{-1}) calculated for the first hydrogenation in the **M1** second ramification . However, in this case, the reacting system needs to reorganize into a high-energy state (compared to the strong stabilization that occurs in **M1−2**), making this elementary step particularly challenging. After this initial step, the pathway continues in a lower-energy region. Considering 2-C_6H_8O/Pt_{10} as a reactant, two branches emerge (indicated in **Fig. 5.9** using two different colors) depending on whether the cleavage involves the C(1) –C(2) or the C(1) –C(6) bond. These two situations differ from each other due to varying C⋯Pt interactions and the hybridization nature of the involved carbon atoms. The C(1) –C(6) bond breaking leads to the formation of an α,β-unsaturated radical species, whereas in the other case, a species with the double bond in the terminal position is formed. Among these, the former is energetically more stable, owing to both intrinsic stability from electronic delocalization of the conjugated system and extrinsic stability from molecule-cluster interactions. Conversely, the latter species is less stable due to the absence of resonance and fewer C-Pt interactions. Despite the evidence of higher energy barriers suggesting otherwise, the formation of the α,β-unsaturated radical is presumably
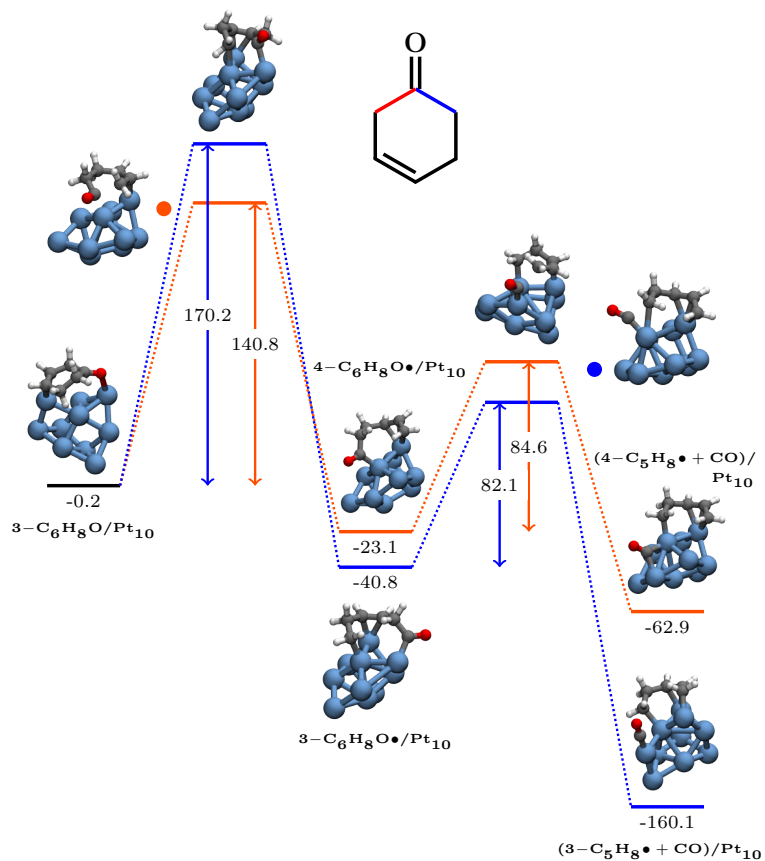
Figure 5.6: Second branch of the **M1** mechanism: starting from cyclohex-3-en-1-one, two possible pathways are identified, involving the cleavage of the C(1)-C(6) or C(1)-C(2) bonds (represented in blue and orange, respectively). Both lead to the formation of the $C_5H_8\bullet/Pt_{10}$ species, which then evolves into C_5H_8/Pt_{10} through the formation of a new C–C bond.
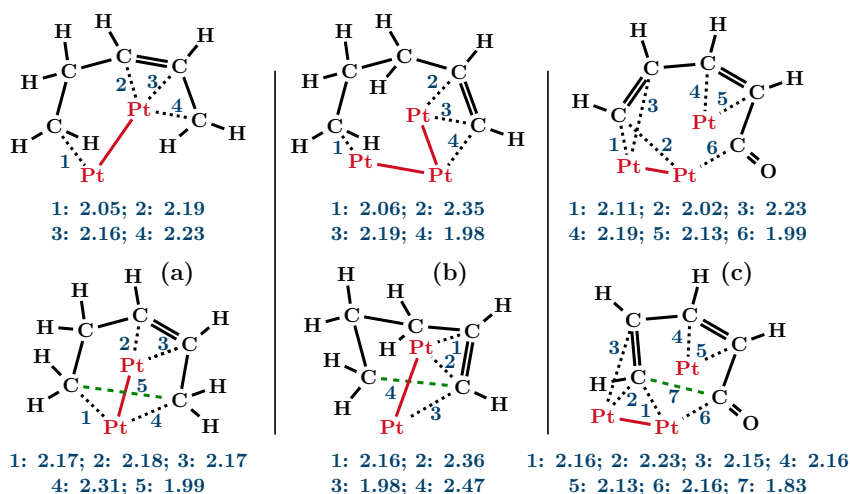
Figure 5.7: Schematic illustration of the structures (reactants and transition states) involved in the ring closure elementary step for the **(a) M1–2, (b) M1–3** and **(c) M2** mechanism. Below each structure the distances in Åcorreponding to the tag numbers are reported. Only the Pt atoms directly involved in the processes are showed here, in red color.

favored. As a matter of fact, the higher energy barrier associated with breaking the $C(1)-C(6)$ bond (158.2 vs. 135.0 kJ mol^{-1}) is significantly offset by the substantial stabilization (approximately 73 kJ mol^{-1} with respect to the competitive intermediate) of the product (see **Fig. 5.9**). In all cases, these species undergo decarboxylation, resulting in the formation of the $C_5H_8\bullet$ species, which subsequently evolves into cyclopentene through ring closure.

The $C_5H_8\bullet/Pt_{10}$ systems formed in both **M1–2** and **M1–2** as precursors of the cyclopentene final product are deeply different, even if them both have diradical character. Let discuss the ring closure elementary step in the two channels with the help of **Fig. 5.7**.

The alkyl radical is present in all scenarios, establishing a bond with platinum while maintaining a tetrahedral geometry in its vicinity. However, the $C_5H_8\bullet/Pt_{10}$ species formed in the **M1–2** pathway exhibits an allylic radical, which interacts with a single platinum center along with the two carbon atoms involved in the double bond. In contrast, the $C_5H_8\bullet/Pt_{10}$ generated in the **M1–3** pathway features a vinyl radical, wherein the double bond engages with two adjacent platinum centers. In this case, the cluster adapts its geometry to accommodate the direc-
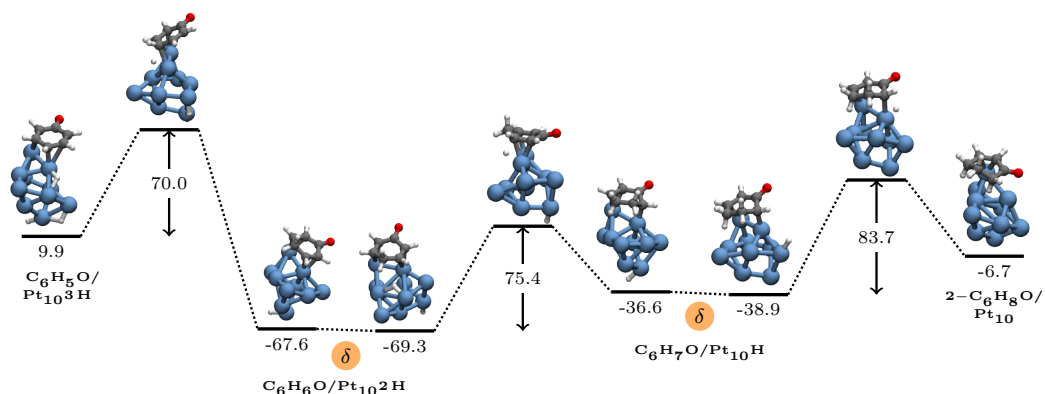
120

Figure 5.8: In the **M1–3** mechanism, following the dehydrogenation of the OH group, the hydrogenation of the ring carbon atoms occurs consecutively at the *para*, *meta*, and *ortho* positions relative to the C=O, leading to the formation of cyclohex-2-en-1-one (2-C_6H_8O/Pt_{10}). The energy values for the minima are based on the initial reactant shown in **Fig. 5.4**.

tional driving force of the radical carbon. The interaction of various radical forms of carbon with platinum cluster is surely an issue that deserves detailed theoretical analysis but in the present work we just say that, even if a carbon ring-closure reaction may seem a simple matter, we have to deal with the overpowering nature of the carbon-platinum interactions. The closed form of cyclopentene on the cluster, C_5H_8/Pt_{10}, displays stability comparable to that of its open form, but energy barriers are as high as 170.6 and 182.4 kJ mol^{-1} for this last elementary step in **M1–2** and **M1–3** pathways, respectively. Although the existence of more stable transition states cannot be excluded, all attempts to identify them indicate that, in order to achieve low-energy barriers, the reactant in the elementary step must reorganize into a conformation that disrupts certain strong Pt–C interactions—whether involving Pt–CH_2, Pt–CH, or Pt–(double bond).

As a matter of fact, the lowest observed energy barrier, which is 31.2 kJ mol^{-1}, was obtained in the **M1–3** pathway for an arrangement of $C_5H_8\bullet/Pt_{10}$ that is 104.5 kJ mol^{-1} higher in energy compared to its most stable form. The microkinetic analysis, which will be discussed in detail later, suggests that a low energy barrier following such an energetic arrangement is essentially the same problem as having a high energy barrier.
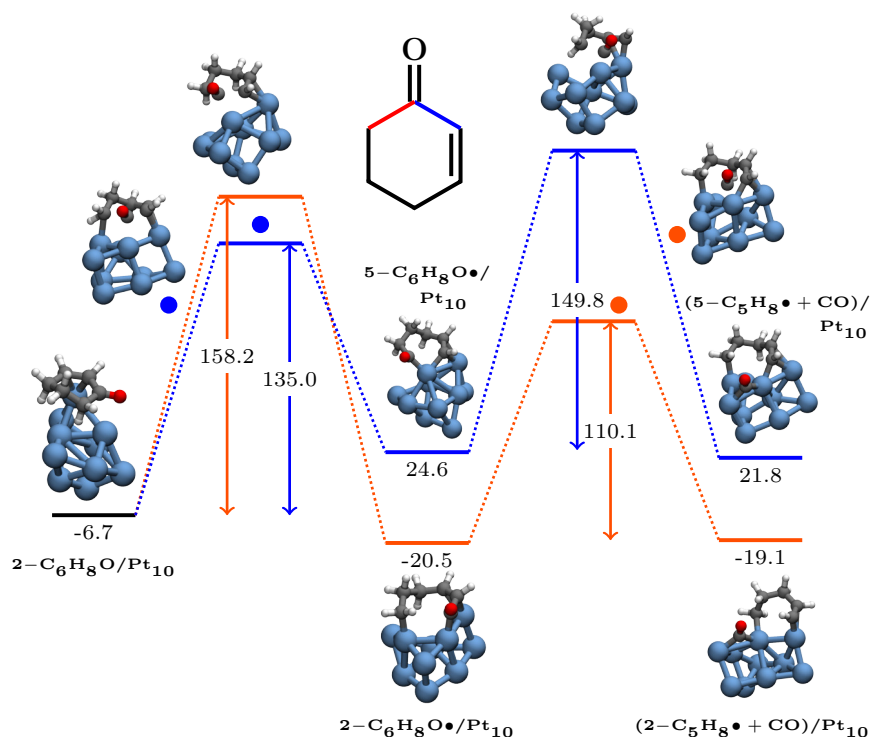
Figure 5.9: M1–3: This profile presents two pathways to form the $C_5H_8\bullet$ species: one through the cleavage of the C(1)–C(6) bond (depicted in orange) and the other via the C(1)–C(2) bond (depicted in blue). After the desorption of carbon monoxide, the $C_5H_8\bullet$ species transitions to C_5H_8 through a ring-closure process. The numbers preceding the molecular formula indicate the carbon atom positions of the double bond.

5.1.2 M2 mechanism

A completely alternative mechanism (**M2**) firstly involves (see **Fig. 5.10(a)**) the transfer of a H atom from the -OH group of the starting $C_6H_4(OH)OCH_3/Pt_{10}$ species to the cluster. This process is relatively easy, involving the rotation of the OH groups toward a platinum atoms already prepared in the right place; it results an energy barrier of 128.4 kJ mol^{-1}. which is not too high if compared to the barrier associated with the breaking of the C–H bond of the methoxy group in guaiacol, at the beginning of the previous mechanisms. This step is followed by the O–CH$_3$ bond breaking occurs and the dislocation of the CH$_3$ moiety on the platinum cluster.

It seems that also in this case, for the process to occur, a rearrangement is necessary that should lead to a transition state in which only one platinum atom represents the active site. This can occur still maintaining the interactions between the cluster and the phenyl ring, but a distortion energy of 75 kJ mol^{-1} is however required, due to the loss of the Pt–O interaction involving the radical oxygen and to the distortion of the cluster. Actually, once this rearrangement occurs, the O–CH$_3$ cleavage is quite easy, being 117.4 kJ mol^{-1} the associated energy barrier. It is true that the resulting *ortho*-quinonic species should have not a great stability, but it must be remembered that the energy behaviour of molecular species interacting with a cluster bearing metallic centers at different coordination numbers may be utterly different from what occurs in vacuum or in solution. As a matter of fact, the $C_6H_4O_2+CH_3/Pt_{10}$ H product is 38 kJ mol^{-1} lower in energy than the starting guaiacol/Pt$_{10}$ system.

Subsequently, this CH$_3$ fragment is subjected to hydrogenation to methane, which was always been an easy process. In the corresponding elementary step occurring in the hydrodeoxygenation of isoeugenol [188], for example, a CH$_3$ on the cluster derived directly from dihydroeugenol, and methane would formed with an energy barrier of 30.9 kJ mol^{-1}. Also in the present case, the CH$_3$/Pt + H/Pt $\longrightarrow$ CH$_4$/Pt reaction proceeds in a fast way: after a hydrogen atom diffusion, which brings H near to CH$_3$ and lowers the energy of the whole system by 24.4 kJ mol^{-1}, a negligible energy barrier of 39.6 kJ mol^{-1} lead to completion of the elementary step. The resulting $(C_6H_4O_2+CH_4)/Pt_{10}$ product shows weak interactions between Pt and methane, but it is only 9.4 kJ mol^{-1} less stable than the reactant of the step, since the strong Pt–CH$_3$ interaction was substitued by the newly formed C–H bond and a better interaction of the $C_6H_4O_2$ fragment

(a)

128.4

46.2

117.4

δ

0.0

$C_6H_4(OH)OCH_3/$
Pt_{10}

-28.8

$C_6H_4O(OCH_3)/$
$Pt_{10}H$

-38.0

$C_6H_4O_2 + CH_3/$
$Pt_{10}H$

(b)

49.1

133.9

0

$C_6H_4O_2/Pt_{10}$

-35.2

$C_6H_4O_2\bullet/$
Pt_{10}

-104.3

$(C_5H_4O\bullet + CO)/$
Pt_{10}
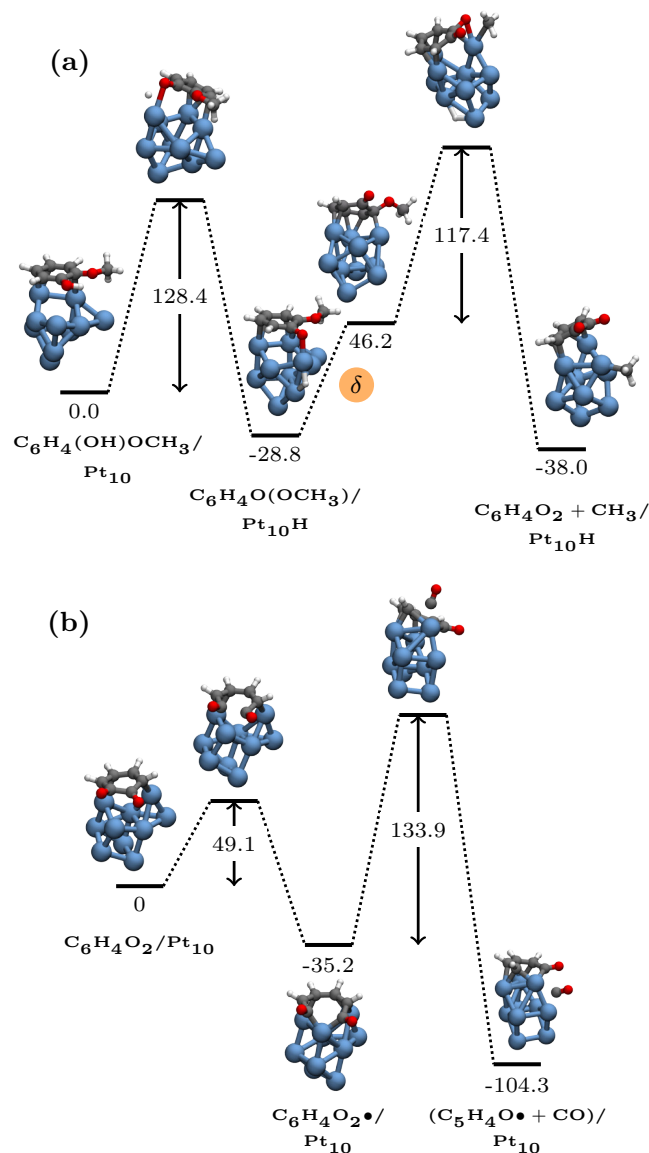
Figure 5.10: (a) The initial elementary stages of the M2 mechanism show the dehydrogenation of the -OH group of guaiacol and the breaking of the $O-CH_3$ bond. The adsorbed CH_3 fragment will be later hydrogenated to methane, which ultimately desorbs leaving the $C_6H_4O_2/Pt_{10}$ species for further reactions. **(b)** The profile depicts the six-term ring opening through the cleavage of the bond between adjacent carbonyl groups. This process is followed by the elimination of a CO molecule, and finally the formation of a new C-C bond resulting in 2,4-cyclopentadien-1-one.

with the cluster, occurring thanks to the elimination of the steric hindrance with the Pt$-$CH$_3$ moiety. Methane can desorb with an amount of energy equal to 23.4 kJ mol^{-1}.

After the CH$_4$ desorption, 1,2-benzoquinone is left on the cluster. This compound could undergo to carbon ring opening, a hereafter investigated process, auspicable to eliminate as much oxygen as possible. Although this species, when bound to Pt$_{10}$, is not as unstable as one might imagine, the OC$-$CO bond breaking occurs extremely easily, with a transition state that closely resembles both the reactant and the product of the elementary step and which is associated with a barrier of 49.1 kJ mol^{-1} (**Fig. 5.10(b)**). The resulting species, C$_6$H$_4$O$_2$●/Pt$_{10}$, which formally displays two carbonyl radicals, shows that the breakage involves an energy gain of 35.2 kJ mol^{-1}. It will transform into a much more stable system, in which the C$_5$H$_4$O● fragment and a newly formed carbon monoxide molecule are coadsorbed onto the cluster as a result of the cleavage of the C$-$CO bond. The energy barrier linked to this process is 133.9 kJ mol^{-1} and, although not prohibitive, is much higher than the lowest barrier identified for decarbonylation in the **M1** mechanism (reported in Fig. 5.3); it is understood, however, that the decarbonylation processes occurring in **M1** and **M2** have actually a pretty different chemical nature.
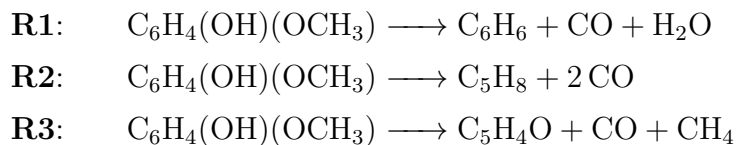
In C$_6$H$_4$O$_2$●/Pt$_{10}$ the two carbonyl radicals are bonded to the same Pt atom and the two adjacent double bonds interact strongly with the cluster. In order for the C$-$CO bond to be broken, the cluster deforms enough to allow a platinum atom to fit between C and CO in the local C=C$-$CO group. Again, therefore, the reaction is aided by the flexibility of the metal cluster and the active site is a single Pt atom. In the product, the CO molecule diffuses away and desorbs, leaving the precursor of a new stable molecule. Indeed, the remaining five-term ring close, forming the 2,4-cyclopentadien-1-one species. In this case, contrary to that relating to the formation of cyclopentene, the ring closure does not require the overcoming of a high barrier (being 127.1 kJ mol^{-1} the calculated one), since as represented in **Fig. 5.7(c)** this process does not have to occur after large cluster distortions or molecular rearrangements, being simply accompanied by a change in the position of the vinylic carbon atom on the same two Pt sites to which it is bonded.

5.2 Kinetic Analysis

In order to avoid drawing hasty conclusions based solely on the energy barriers calculated for the mechanisms studied, a kinetic analysis was performed using the Simplified Christiansen Method (*SCM*) [179]. As discussed in previous chapters, the analysis of energy barriers and energy differences between reaction intermediates alone can be misleading for the discrimination of mechanisms in complex, multi-channel processes, such as those analysed here. *SCM* in fact makes it possible to integrate the results obtained via DFT on the elementary stages of a given mechanism and to express them in a single synthetic value. Therefore, by providing as input the direct and inverse barriers of the elementary stages characterizing each reaction pathway (seen as a sequence of consecutive transformations that starting from $C_6H_4(OH)OCH_3$ ends at C_6H_6 or C_5H_4O or C_5H_8 passing through a number of intermediate species), the *SCM* returns the kinetic constants of the different channels in the selected temperature range (298–800 K). It should be noted that, in performing such analysis, we refererred to standard Gibbs free energies in order to consider the (rather small) influence of temperature on energy barriers and (way more important) on the desorption/absorption processes of surface species.

Other than the proper energy barriers, in the *SCM* analysis processes like molecular rearrangement and hydrogen diffusion on the cluster were taken into account. Excepting the cases explicitly indicated, there processes were considered quite easy (or better, their barriers were supposed negligible with respect to those of reactive steps) but, given their variability in the different reaction paths, it was deemed appropriate to consider their effect at least from a strictly thermodynamic point of view. To accomplish this issue, a rearrangement/diffusion process occurred with $\Delta G < 0$ was considered barrier-less in the forward direction and with a barrier of ΔG in backward one, and viceversa if it occurred with $\Delta G > 0$. On the other hand, the desorption of the molecules produced during the decomposition reactions was taken as having a barrier equal to the calculated desorption standard free energy (reported in **Table 5.1** at given temperature values), while re-adsorption of a desorbed molecule was considered forbidden by inserting an infinite energy barrier in the corresponding expression for w (see eq. 3.2). It is to note that the desorption steps of small molecules (CO, H_2O, CH_4) may have a fundamental role in the whole pathway kinetic, in particular because free energies at increasing

temperature were considered for the *SCM* analysis. Indeed, for a thermodynamic point of view, methane is the only species which desorbs spontaneously at all the considered temperatures, while the desorption of CO is always endoergic. By considering the standard Gibbs free energies associated to the three global processes, *i.e.*

$$\textbf{R1}: \quad C_6H_4(OH)(OCH_3) \longrightarrow C_6H_6 + CO + H_2O$$

$$\textbf{R2}: \quad C_6H_4(OH)(OCH_3) \longrightarrow C_5H_8 + 2\,CO$$

$$\textbf{R3}: \quad C_6H_4(OH)(OCH_3) \longrightarrow C_5H_4O + CO + CH_4$$

reactions reported in the second part of **Table 5.1**, it is to note that only the transformation of guaiacol to benzene is exoergic in the whole 298–300 K temperature range, while the spontaneity of **R2** and **R3** at temperatures higher than 400 K and 500 K, respectively. This likely because **R2** require the desorption of two CO molecules and **R3** the desorption of cyclopentadienone, which due to very strong interactions between the two C=C and one C=O double bonds with platinum, is the species showing the most endoergic desorption at all temperatures.

The calculated values of the kinetic descriptor s appearing in equation in the temperature range 300–800 K are reported in Table 5.2 for six channels. The **M1–1** and **M2** mechanisms were treated independently of each other because they result in different products, C_6H_6 and C_5H_4O, respectively. The **M1–2a/b** and **M1–3a/b** mechanisms, on the other hand, lead to the same product, so a single *SCM* analysis was done for the four of them. Accordingly, the **M1–1** channel is the fastest of the investigated mechanisms at all temperatures. In the high temperature range the M2 mechanism begins to become more competitive, passing from being the slowest of all up to 500 K to the second most fast. The global way to cyclopentene can be analyzed by using the average, $\langle s \rangle$, of the s value associated to the four M1–2 and M1–3 pathways, which is essentially the same as the one corresponding to the fastest of them (M1–3a, having 4-$C_6H_8O\bullet/Pt_{10}$ as an intermediate), and only at high temperatures $\langle s \rangle$ is slightly affected by the negative contributions of the other three slowest branches. It seems that cyclopentene, whose formation is however much slower than that of benzene, is ruled out because in the low end of the temperature range the reaction is endoergic. On the other hand, formation of cyclopentadienone become relatively fast and exergonic at high temperatures.

Table 5.1: The standard desorption Gibbs free energy values as a function of temperature (expressed in kelvin) are reported in the upper part of the table for the possible products associated with the reactions mechanisms investigated in this work. In the lower part the standard Gibbs free energy values for the three whole reactions are collected. All energy values are expressed in kJ mol^{-1}.

	ΔE_{ZPV}[a]	ΔG					
		298	**400**	**500**	**600**	**700**	**800**
G[b]	146.5	80.2	58.3	35.8	13.5	-8.7	-30.9
M1–1							
B	143.6	78.0	55.7	33.7	12.0	-9.4	-30.6
CO	239.5	196.2	179.7	163.6	147.4	131.3	115.2
H$_2$O	139.2	96.4	80.2	64.4	48.9	33.5	18.3
M1–2a[c]							
CO	149.7	105.2	88.3	71.6	55.0	38.41	21.8
M1–2b							
CO	246.9	207.7	184.5	167.5	150.6	133.7	116.9
M1–3a							
CO	202.9	155.0	137.0	111.5	102.1	84.9	67.8
M1–3b							
CO	162.1	116.3	99.0	82.0	65.2	48.6	32.0
common to M1–2 and M1–3							
CPE	163.3	99.0	76.7	54.5	32.5	10.7	-11.0
M2							
CPDEO	348.5	278.1	253.7	229.5	205.7	182.1	158.8
CH$_4$	23.4	-14.7	-28.7	-42.5	-56.2	-70.0	-83.8
CO	183.1	137.1	119.8	103.0	86.2	69.5	52.9
Global reactions							
R1[d]	22.3	-64.2	-96.5	-128.9	-161.2	-193.3	-225.3
R2[e]	125.5	37.1	4.5	-28.0	-60.2	-92.2	-124.0
R3[f]	189.0	97.9	63.6	29.4	-4.8	-38.8	-72.6

[a] Refers to the variation of the SCF energy including the zero-point vibrational contribution. The basis set superposition error (BSSE) was evaluated at SCF level by means of the counterpoise method of Boys and Bernardi [146]. It was found that it is in the range 19–27 kJ mol^{-1} for the desorption of all molecules, except water and methane to which a BSSE of ca. 5 kJ mol^{-1} is associated. This values are in agreement with previous findings [188, 202, 203]. [b] In this table: G = guaiacol, B = benzene, CPE = cyclopentene, CPDEO = cyclopentadienone. [c] In M1–2 and M1–3 mechanisms, the desorption energy of the second CO molecule is reported, being the desorption of the first one in common with M1–1. [d] R1 is the G $\longrightarrow$ B + CO + H$_2$O global reaction. [e] R2 is the G $\longrightarrow$ CPE + 2 CO global reaction. [f] R3 is the G $\longrightarrow$ CPDEO + CH$_4$ + CO global reaction.

Table 5.2: Occurrence probabilities per unit time (in s^{-1}) evaluated for the six most significant mechanisms identified for the decomposition reaction of guaiacol on Pt_{10} at different temperatures (expressed in kelvin). Scientific notation is used, with the power of 10 indicated in parentheses.

	300	400	500	600	700	800
path to benzene						
M1–1	2.6(-22)	2.8(-11)	3.6(-5)	5.8(-2)	8.1(0)	3.3(+2)
paths to cyclopentene						
M1–2a	1.1(-25)	3.6(-16)	1.4(-10)	7.4(-7)	3.2(-4)	3.1(-2)
M1–2b	5.6(-31)	3.9(-20)	8.1(-14)	1.4(-9)	1.4(-6)	2.6(-4)
M1–3a	7.4(-28)	8.0(-18)	5.8(-12)	4.6(-8)	2.8(-5)	3.4(-3)
M1–3b	4.8(-31)	6.0(-20)	1.8(-13)	3.8(-9)	4.4(-6)	8.8(-4)
mean	1.1(-25)	3.7(-16)	1.3(-10)	6.5(-7)	2.7(-4)	2.5(-2)
path to cyclopentadienone						
M2	1.2(-36)	6.3(-21)	1.1(-11)	1.5(-5)	5.8(-2)	4.6(0)

5.3   Conclusion

The *DFT* calculations and the subsequent kinetic analysis performed in this chapter suggest that when guaiacol (and consequently phenol, being an intermediate of the preferred mechanism) decomposes in the absence of hydrogen on a subnanometer platinum cluster, the preferred product is benzene. However, the reaction would become fast only at high temperatures, where the mechanism leading to the formation of cyclopentadienone could be triggered, a still oxygenated product whose desorption is highly energetic and which could therefore poison the catalyst. Based on the calculations, kinetics and thermodynamics would exclude the decomposition of guaiacol to cyclopentene. The reported investigation, however, goes beyond simple prediction, and opens the way to the study of a large number of effects whose understanding would greatly enrich the basic knowledge of cluster catalysis and which are therefore worth exploring in detail.

Indeed, knowing all the possibilities and modalities of the reactive events of a system, even if small like the guaiacol molecule adsorbed on a subnanometer cluster, is an extremely complex matter, especially if one takes into account the fact that the cluster is not an immutable or partially inert component, but it intervenes directly in the process by modifying itself heavily even at the level of

a single atom. In many cases, in fact, the active site for a given elementary step is a single platinum atom, possibly freed a little from the cluster (*i.e.*, a change of coordination number). Still, rearrangements (sometimes energetically favorable, sometimes unfavorable) are very often necessary for the adsorbed molecular species to orient to let a given moiety reach an active site and react. This could be considered the equivalent of the effective collision in gas-phase reactions, but in the cluster case, when the rearrangement of the molecule is difficult (for example because it is a radical whose highly orienting interactions govern the geometry), then the metal particle could intervene by deforming itself. What said above has advantages and disadvantages as well. While the flexibility of metal clusters opens the way to discover new potentials in catalytic processes, it greatly burdens the work to be done to develop a detailed knowledge, which may not be traceable back to general rules and be valid only for one type of metal or even for a cluster with a particular geometry.

As a matter of fact, atomistically accurate computational study of whole cluster-catalysed processes on a system that includes periodic support for the cluster is still prohibitive, if not for the weight of each single calculation, (though it should be not negligible by virtue of the fact that the transition states must be identified through the use of numerical approaches) ultimately for the very high number of calculations to be performed. In this context, the importance of investigations on unsupported clusters comes into play: they will be useful as a reference, in order to acquire knowledge to be used to lighten the more realistic calculations on supported clusters.

Finally, it is worth to underline a remarkable difference between cluster and surface catalysis. In some points of the process one can notice that a certain amount of atomic hydrogen accumulates on the cluster. If the process took place on a metal surface (where hydrogen would diffuse freely) this H atoms could be used to hydrogenate guaiacol molecules other than the one they come from, or other reaction intermediates, potentially giving rise to a partial hydrodeoxygenation reaction and consequently other final products. This is a substantial difference between surface catalysis and catalysis on subnanometer clusters; in the latter case, in fact, the accumulated H cannot easily react with other molecules but only with those that are close to it at that instant on the cluster, unless H cannot diffuse freely on the support. We would conclude that if the support is a metal, HDO can also occur, while if it is for example graphene or an oxide, the diffusion of H between different

clusters should be inhibited, and so would HDO. Further, if the cluster is not in the subnanometer size regime but can contain several adsorbates, HDO without external H could become easy and thus a high number of final products could be obtained.

Chapter 6

Accretion of Pt_n and Ni_n on graphene sheet

This chapter explores the role of graphene as a support for Pt and Ni clusters, focusing on metal accretion processes and an introduction to their catalytic applications. In particular, the behaviour of these metal clusters on defective graphene surfaces, in which carbon vacancies significantly influence the stability and properties of deposited metals, will be analysed. The relevance of graphene as a catalytic support will be illustrated through an in-depth discussion of its physical and chemical properties, and how they promote catalytic efficiency, selectivity and resistance to degradation.

Subsequently, the growth process of metal clusters of Pt and Ni of variable sizes (n=1–10) will be presented, highlighting the optimised cluster geometries and structural changes in the graphene surface. The binding and cohesion energies of the metal clusters will be compared, emphasising how graphene influences the stability of the clusters and their ability to resist surface migration.

The chapter concludes with a preliminary analysis of the catalytic activity of Pt and Ni supported on graphene in deoxygenation reactions, which are crucial for the valorisation of biomass-derived compounds. The differences between the two metals in terms of catalytic efficiency and energy barriers will be discussed, offering insights into how graphene can improve the performance of these catalytic systems.

6.1 Graphene in Heterogeneous Catalysis

Heterogeneous catalysis is a cornerstone of the chemical industry, playing a crucial role in energy conversion, environmental treatment, and materials science. It is estimated that approximately 90% of all industrial chemical processes involve heterogeneous catalysts [204]. Even catalysts designed for homogeneous catalysis are frequently supported on porous materials to enhance their efficiency and stability [205]. Among the various support materials, carbon allotropes, particularly graphene, have received increasing attention due to their large surface area and chemical stability, which enable a high density of active sites and exceptional resistance to degradation in both acidic and basic environments [206, 207, 208]. Moreover, the recovery of active phases, especially for noble metal-based catalysts, is simplified by easy combustion of carbon supports. The synergy between carbon allotropes and heterogeneous catalysis thus emerges as a key factor in improving catalyst selectivity and reducing costs [171, 209]. Among the diverse carbon-based supports, graphene stands out for its appealing properties, making it particularly appropriate as a support for heterogeneous catalysis. This material offers exceptionally high electron mobility at room temperature, a flawless atomic lattice, impressive mechanical strength, and incomparable chemical and thermal stability [168, 169, 170]. With a thermal conductivity reaching up to 5000 W/m·K and a theoretical specific surface area of 2630 m^2/g, graphene holds immense potential across various fields. The general properties of graphene are listed in **Table 6.1**.

In recent years, the number of studies on graphene and its derivatives in heterogeneous catalysis has grown exponentially, with many catalytically active species being successfully immobilized on graphene, demonstrating superior performance in numerous chemical reactions. A particularly significant application is the use of low-cost graphene-supported catalysts in the refining of lignocellulosic biomass [210]. To make biomass-derived fuels economically competitive, it is essential to develop catalysts and processes that substantially improve refining efficiency [211, 173]. In the pyrolysis and hydrolysis of lignocellulosic biomass, the resulting molecules often have high oxygen content and low energy density, making them unsuitable for direct use as fuels. In this context, graphene-supported catalysts play a critical role in enhancing conversion and selectivity while simultaneously reducing production costs [173, 172].

Properties	Values	Reference
Charge Carrier Mobility	$\sim 200\ 000\ \mathrm{cm}^2/\mathrm{V\cdot s}$	[212, 213, 214]
Thermal Conductivity	$\sim 5000\ \mathrm{W/m\cdot K}$	[215, 213, 216]
Trasparency	$\sim 97.4\%$	[217, 218, 219]
Specific Surface Area	$\sim 2630\ \mathrm{m}^2/\mathrm{g}$	[220, 221]
Young's Modulus	$\sim 1\ \mathrm{TPa}$	[222, 223]
Tensile Strenght	$\sim 1100\ \mathrm{GPa}$	[224, 215, 225]
Band gap	Zero	[226, 227, 228]
Electron Mobility	$15\cdot10^{-2}\ \mathrm{cm}^{-2}\ \mathrm{V}^{-2}$	[212, 229, 230, 231]

Table 6.1: Some important properties of graphene.

6.1.1 Graphene as catalytic support

Graphene, when employes as a support, can accomomdate catalysts at the nanoscale or even at the atomic scale. There are three main classes of graphene-supported catalysts: (1) nanoclusters or metal nanoparticles; (2) single metal or non-metal atoms; (3) single atoms or clusters supported on functionalized graphene, such as graphene oxide or reduced graphene oxide [232, 233]. In all cases, graphene must effectively anchor these active species to function as a robust support. The interactions between graphene and metal atoms, particularly transition metals and noble metals, are typically weak, which can lead to atom aggregation and the formation of metal nanoparticles. To improve the anchoring of foreign atoms, graphene must be modified to enhance its chemical reactivity, thereby stabilizing the active species and improving their catalytic performance [234, 235, 236]. One of the most effective approaches to enhance these interactions is the controlled generation of structural or chemical defects in graphene. These defects can be introduced through various techniques, such as ion or electron beam irradiation, plasma exposure, or controlled chemical oxidation. The resulting defects, such as single vacancies (SV) or double vacancies (DV), disrupt the π and σ bonds of surrounding carbon atoms, creating reactive sites that can effectively anchor metal atoms and clusters [237, 238]. For example, vacancies can act as traps for incoming atoms and nanoclusters, improving the adsorption and stability of catalytic species [239, 240, 241, 242]. Theoretical and experimental studies have demonstrated that the presence of these defects can significantly increase adsorption energy and reduce the mobility of adsorbates, thereby preventing aggregation. For instance, gold (Au) and platinum (Pt) nanoclusters anchored on defective graphene exhibit

enhanced stability and reduced diffusion, with binding energies increased by up to 20 times compared to defect-free graphene. This improved stability of adsorbates is accompanied by a significant charge redistribution at the graphene-cluster interface, which can alter the electronic structure of the adsorbates, making them more effective as catalysts [243, 244, 245, 246].

Graphene in the Platinum and Nickel clusters accretion

In view of the particular properties discussed above, in this thesis graphene was selected as the support for platinum and nickel cluster growth in order to investigate some important elementary steps of the HDO and decomposition reactions of isoeugenol and guaiacol on supported metal clusters. The supercell (a=14.78401 Å, b=17.07110 Å, c=20.0000 Å, $\alpha=\beta=\gamma=$ 90°) employed for modeling the pristine graphene comprised 96 carbon atoms (C_{96}), whereas as model of defective graphene, a derived C_{95} system with a carbon monovacancy was considered. This supercell is sufficiently large to minimize the spurious interaction between monovacancies and between the Pt_n or Ni_n clusters. **Fig. 6.1** shows the atomic structure of the optimized graphene monovacancy, in which no significant change in structure beyond the defect site is observed after the removal of a carbon atom from the graphene sheet; however, in the vicinity of the vacancy there occurs a structural distorsion (of, *Jahn–Teller*, type) that breaks the symmetry as a result of local bonding rearrangement. This latter causes the formation of two rings with 5 and 9 atoms, respectively. In addition, no significant out-of-plane atomic displacements were observed in the relaxed structure [247, 248]. The calculated defect formation energy is -7.4 eV, a value in good agreement with literature data (-7.5 eV) [249, 250].

6.2 Platinum Cluster growth on defective Graphene

After monovacancy generation, the growth of Pt_n (with n=1–10) species to defective graphene was studied. The accretion procedure was explained in **Fig. 6.2** and the most stable cluster geometries in **Fig. 6.3**. The first platinum atom, added to the defective system, forms covalent bonds with the undercoordinated carbon atoms at the vacancy by breaking a weak C–C bond (bond lenght 1.9 Å)
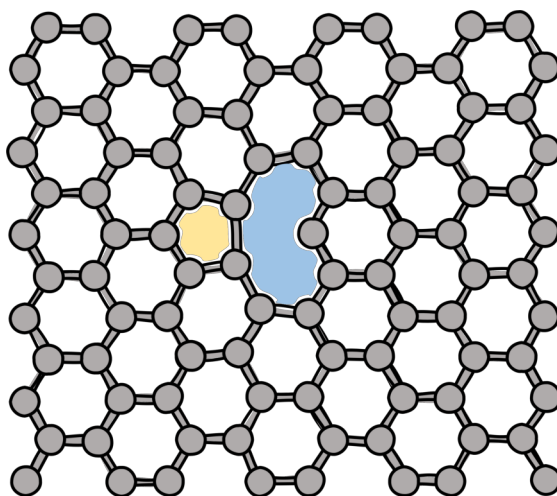
Figure 6.1: Local atomic rearrangement of graphene (C_{96}) following the generation of a vacancy. This results in the formation of a five-term ring (colored yellow) and a nine-term ring (in light blue).

of the five-member ring formed in the local rearrangement of bonds in the C_{95} system. Since the Pt atomic radius is larger than the carbon atom, the Pt atom is displaced outward from the graphene sheet, with an elevation of 1.9 Å. The three C atoms around the vacancy also move out of the graphene plane. The calculated binding energy for a Pt atom on the graphene monovacancy is -8.1 eV, a high value suggesting the inability of platinum atoms migration on the graphene surface. The vacancy-supported Pt_2 results by the binding of a second Pt atom of one of the C atoms around the vacancy and binding the first Pt atom (Pt–Pt bond length equal to 2.6 Å).

Starting with Pt_2/C_{95} system, the addition of the third platinum atom in three different positions was considered: linear bound to Pt(1), linear bound to Pt(2) and between the two atoms to form an almost equilateral triangle with a plane perpendicular to the graphene layer. The most stable system, in singlet state, is the last one. Pt_3 therefore doesn't interact with the carbon atoms, but only with the two platinum atoms (Pt–Pt bond lenghts of about 2.6 Å).

For the addition of the fourth Pt atom on the Pt_3/C_{95} system, four structures were considered in relation to the possibility of forming a tetrahedron or rhombus. In the more stable Pt_4 system, the fourth Pt atom forms the triangular base of the tetrahedron with the other two and therefore interacts with graphene. Due to the complexity in predicting possible geometries with increasing numbers of Pt atoms

to be added, an automated procedure was implemented. It defines around the cluster a grid of points that extends in radius of a given k value connected to the Pt–Pt bonding distance. Each angular point thus constitutes a possible position where the added atom may be located (see section Grid program).

Applying the grid on the Pt_4/C_{95} system, two more stable structures attributable to a square-based pyramid and a trigonal bipyramid that differed by 6.8 $kJ\,mol^{-1}$, were identified among 23 optimized structures. In the square pyramid, the base is placed on a plane perpendicular to the graphene one, while the three Pt atoms on one of the four triangular faces interact with carbon atoms: in particular one Pt atoms interacts bridging with two carbon atoms in a C–C bond. In the trigonal bipyramid only one triangular face interacts with the graphenic plane.

From the two Pt_5 structures selected, by applying the grid, six more stable structures were identified: three from the square-based pyramid and three from the trigonal bipyramid. The Pt_6 structures from the square pyramid, in order of relative stability, have the following geometry: square pyramid with one atom on one side Pt–Pt ($0.0\,kJ\,mol^{-1}$), square pyramid fused with a trigonal pyramid ($11.5\,kJ\,mol^{-1}$) and octahedron ($15.6\,kJ\,mol^{-1}$). In the three Pt_6 structures, however, from the pentagonal bipyramid two show the same geometry as the starting Pt_5 structure but with the seventh atom on one side in one case and with an atom on a triangular face in the other. These have energies of 3.9 and $16.8\,kJ\,mol^{-1}$, respectively. The third structure, less stable than the others ($16.8\,kJ\,mol^{-1}$), is a capped square pyramid.

Applying an energy and geometric sieve, four Pt_7 structures were considered: doubly capped square pyramid ($0.0\,kJ\,mol^{-1}$, trigonal bipyramid fused with a tetrahedron ($2.4\,kJ\,mol^{-1}$), capped octahedron ($5.5\,kJ\,mol^{-1}$) and pentagonal bipyramid ($6.8\,kJ\,mol^{-1}$). From them, therefore, 114 Pt_8 structures were optimized. Only the structures within $20.0\,kJ\,mol^{-1}$ were considered: doubly capped square-based pyramid with an atom on one side of the pyramid ($0.0\,kJ\,mol^{-1}$) and capped pentagonal bipyramid ($19.4\,kJ\,mol^{-1}$) from the doubly capped square pyramid, bicapped octahedron ($18.6\,kJ\,mol^{-1}$) from the capped octahedron, and, finally, trigonal bipyramid with an atom on one side fused with a trigonal bipyramid ($16.7\,kJ\,mol^{-1}$). The same operating scheme, i.e. grid program application and energy sieve, was applied on the four selected Pt_9 structures.

A more stringent energy threshold of $15.0\,kJ\,mol^{-1}$ was considered for the selection of more stable structures with unique geometry for the addition of the
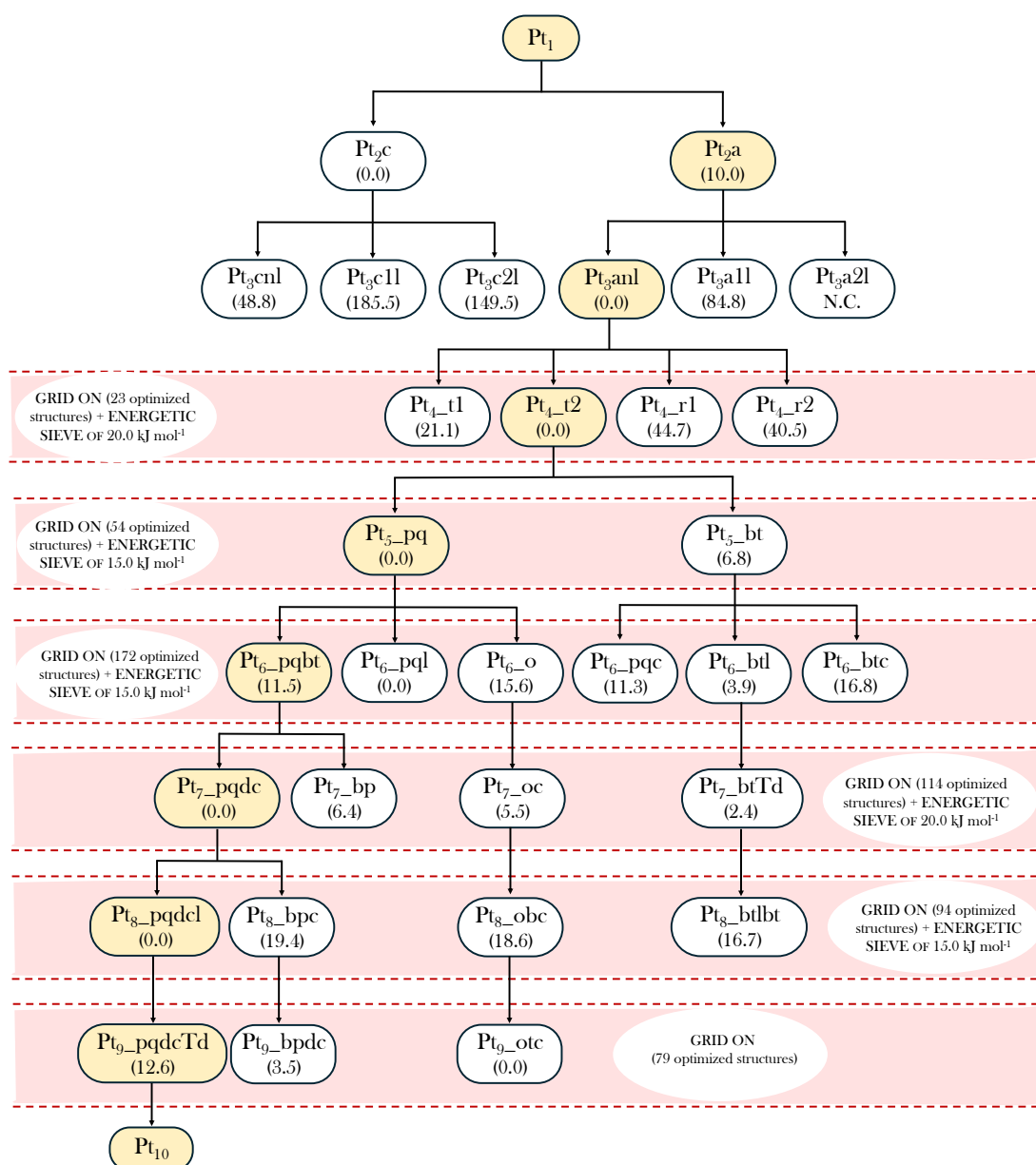
Figure 6.2: Results of the application of the grid program for the accretion of the Pt_n cluster. Highlighted in light red are the steps in which the grid is on with the number of geometries found and optimized, as well as the energy sieve applied.

tenth Pt atom. These are in order of relative stability: triply capped octahedron (0.0 kJ mol^{-1}), doubly capped pentagonal bipyramid (3.5 kJ mol^{-1}) and doubly

capped square pyramid fused with a tetrahedron via one side of the pyramid. Applying the grid program, 79 structures were optimized. However, only 6 structures fell within the energy threshold of 15.0 kJ mol^{-1} and only the most stable one was considered for the adsorption of guaiacol and 2-methoxy-cyclohexan-1-ol and subsequent deoxygenation reactions.
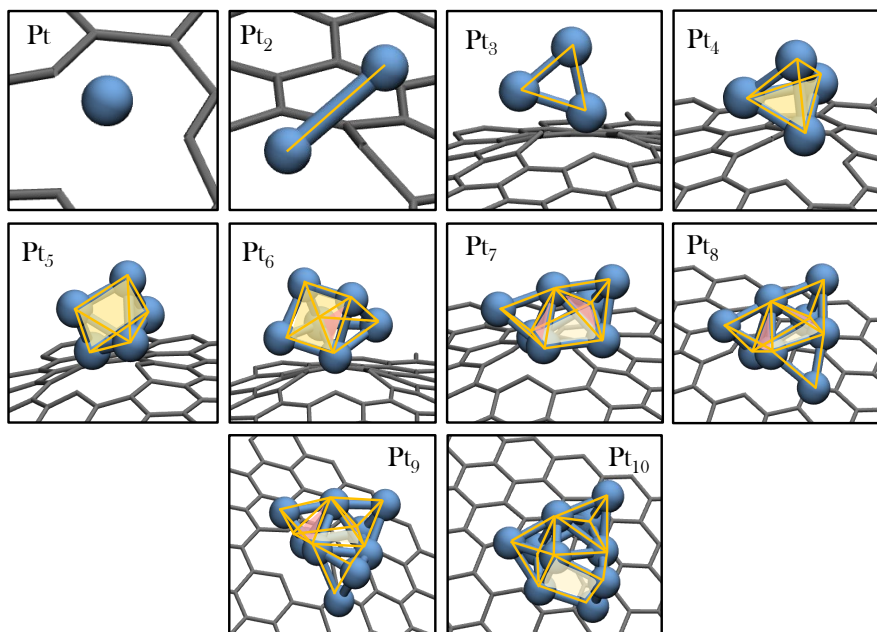

Figure 6.3: Representation of the most stable cluster geometries Pt$_n$ (n=1–10), in which the surfaces in yellow highlight the base of the polyhedron identified by the atomic centers and in light red the polygonal flat faces shared between polyhedra.

6.3 Nickel Cluster Growth on Defective Graphene

Similar to the previous section, the growth of Ni$_n$ clusters (with n=1–10) was also studied on the mono-vacant graphene system C$_{95}$. The accretion procedure

is reported in **Fig. 6.5** and the most stable cluster geometries in **Fig. 6.4**. The first added Ni atom, since its atomic radius is larger than that of carbon, is located outside the graphene plane with an elevation of 1.8 Å causing, therefore, the breaking of a C–C bond of the five–terminal ring. The adsorption energy for a Ni atom on the C_{95} system is 8.5 eV, which is 0.4 eV higher than that calculated for a Pt atom. For the addition of the second Ni atom, two different positions were considered in relation to Ni(1): at the center of a graphene ring and on a surrounding carbon atom. Following the optimization process, however, Ni(2) is positioned in its most stable geometry bridging a C–C bond, thus forming two new C–Ni bonds (bond distance 1.8 Å and 2.0 Å, respectively).

Starting with the most stable Ni_2/C_{95} system, the third Ni atom was added in three different ways: quasi–linear to Ni(1), quasi–linear to Ni(2) and, finally, between the two atoms to form a triangle. The latter is the most stable configuration: the Ni(3) forms with the other two Ni atoms a perfect equilateral triangle with Ni–Ni distances of 2.35 Å. From it, the fourth Ni atom can be arranged above the triangular face to form a tetrahedron and at a certain distance from each of the three sides to form a rhombus. The most stable Ni_4/C_{95} system is in singlet state and has rhombic geometry with average Ni–Ni bond distances of 2.4 Å.

For the addition of the fifth Ni atom, as already described for platinum accretion on graphene, the grid program was applied to explore the possible positions (considering an average Ni–Ni distance of 2.3 Å) at which the atom can be located. Hence, 24 structures were identified and optimized. In the most stable structure, in the singlet state, the fifth Ni atom sits above the rhombic Ni_4 system forming a pyramid with a perfect rhombic base (as shown in **Fig. 6.4)**.

Applying the grid and an energy sieve of 20 kJ mol^{-1} on the Ni_5/C_{95} system, a single structure was selected as the most stable. It, in a quintet state, has the geometry of a rhombic-based pyramid with the fifth atom on one of the faces. Even for the added seventh Ni atom, only one structure among the 24 optimized ones was selected. The Ni_7/C_{95} system, in quintet state, has the geometry of a doubly capped trigonal bipyramid. From this structure, an additional Ni atom was added using the grid program. Applying a slightly wider energy threshold of about 25.0 kJ mol^{-1} by virtue of their unique geometries found, three different structures were considered: a fused trigonal bipyramid with a doubly capped trigonal bipyramid (0. 0 kJ mol^{-1}), a capped pentagonal bipyramid (22.1 kJ mol^{-1}) and a bicapped octahedron (25.3 kJ mol^{-1}). The grid was applied to each of these structures, and
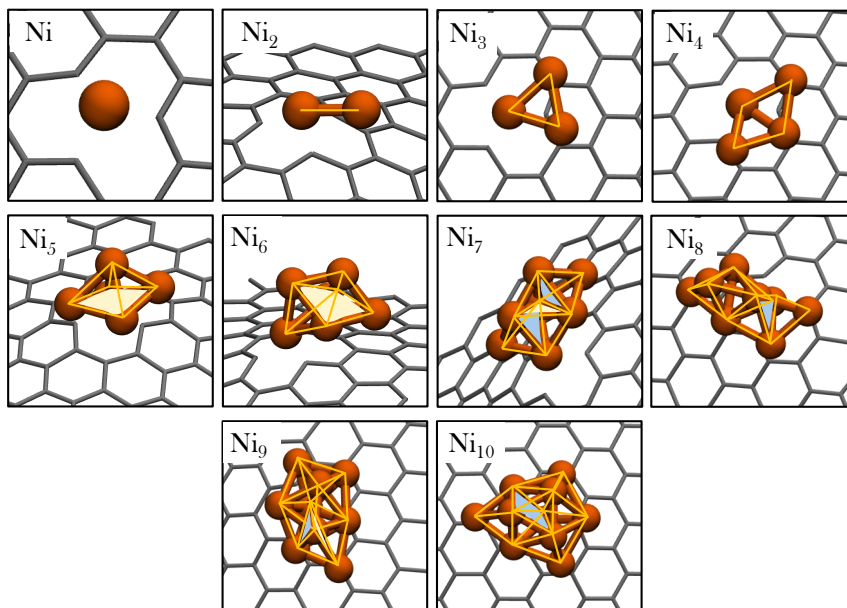
140

Figure 6.4: Representation of cluster geometries Ni$_n$ (n=3–10). Some of them high-light the base (in yellow) of the progenitor polyhedron and the polygonal faces (in light blue) shared between polyhedra, according to the orientation shown.

a total of 74 configurations, corresponding to angular points, were optimized. An energy sieve of 15.0 kJ mol^{-1} was applied, and only two structures, both trace-able as starting geometry to the fused trigonal bipyramid with capped trigonal bipyramid (which was the most stable of the Ni$_8$/C$_{95}$ systems), were considered. These are a pentagonal bipyramid fused with a tetrahedron (0.0 kJ mol^{-1}) and a pentagonal bipyramid fused with a trigonal bipyramid in the nonet and quintet states, respectively. Each of these structures was considered for the addition of the final tenth Ni atom by grid application. Among the 50 optimized Ni$_{10}$/C$_{95}$ structures, only one was considered within an energy range of 20.0 kJ mol^{-1}. This system has the geometry of a pentagonal bipyramid fused with a trigonal capped bipyramid and is in a nonet state.
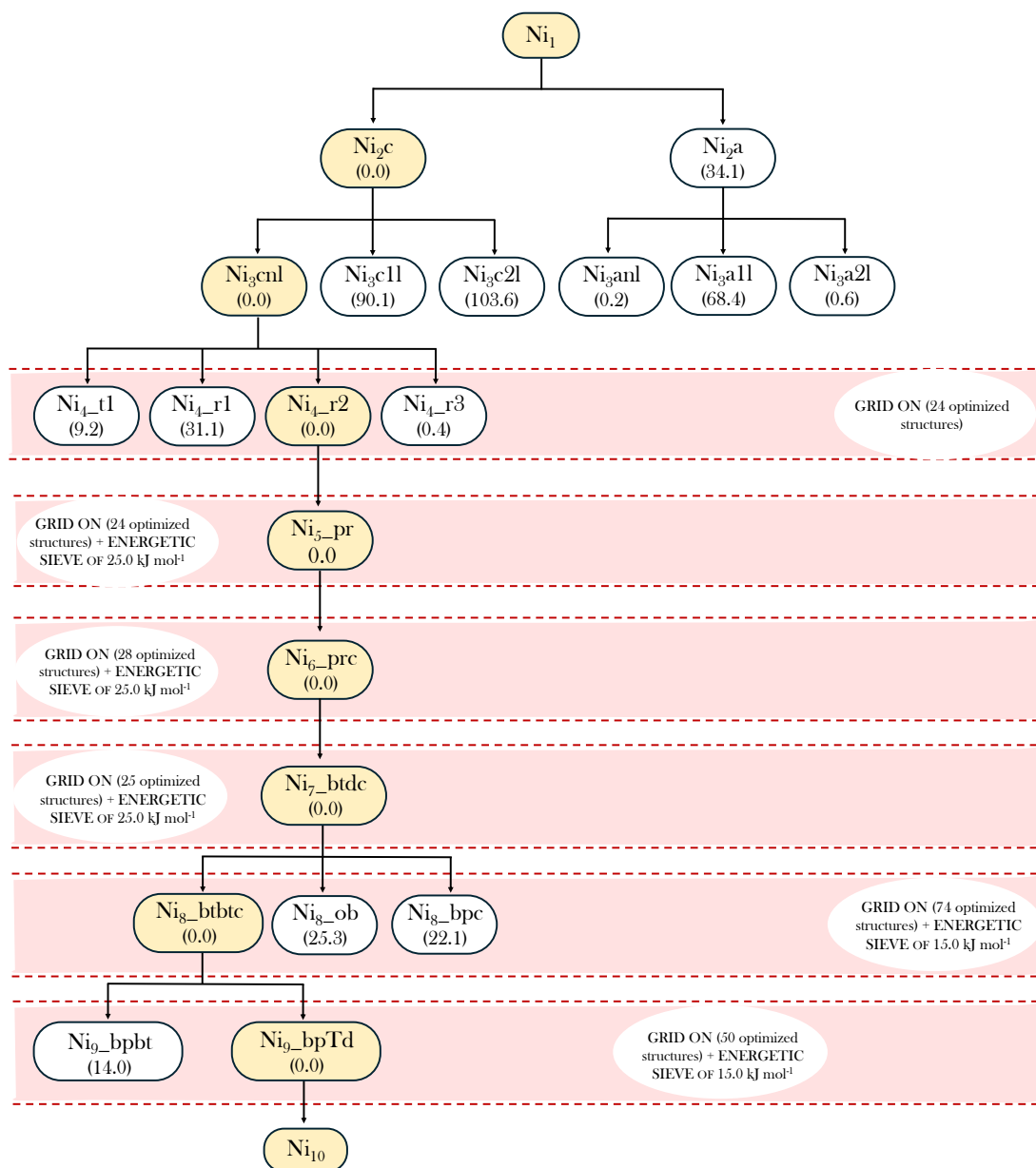
Figure 6.5: Implementation of the grid program in the accretion of the Ni_n cluster. Highlighted in light red are the steps in which the grid is on with the number of geometries found and optimized, as well as the energy sieve applied.

6.4 Binding and Cohesive Energy of Pt_n and Ni_n cluster

The binding energy for Pt_n or Ni_n to the graphene monovacancy was calculated using **eq. 6.1**

$$\Delta E(M_{n/GM}) = E(M_{n/GM}) - E(GM) - E(M_n) \qquad (6.1)$$

where M is the transition metal (Pt or Ni), n is the number of M atoms (n=1–10), GM represents the supporting graphene monovacancy, and E indicates the calculated *DFT* energies. Determining the interaction strength between the M_n clusters and the support is directly related to the mobility of the M_n species on the graphene surface.

Due to the large binding energy (see **Tab. 6.2**), it can be said that the Pt_n stays anchored to the vacancy and doesn't diffuse on the surface, avoiding the possibility of encountering another Pt_n species and forming larger aggregates. In fact, while the Pt_n clusters are known to have a magnetic moment of 2.0 μ_B, upon chemiabsorption of the clusters, this is quenched due to the strong interaction between the clusters and the graphene monovacancy.

In the case of Ni, the evaluation is more complicated due in part to the great variability of its magnetic momentum. It can be seen that the E_b, after decreasing in the range of n=2–4, remains constant in its value of -5.1 eV until the species Ni_{10}. This is consistent with the investigated structures in which there is always less interaction of the added Ni atoms with the support during the accretion phase.

The relative stability of M_n clusters was evaluated by analyzing the cohesive energies, which is the energy required to separate a species into its constituent atoms. Calculations of cohesive energies were performed for both gas-phase and supported clusters, using **eq. 6.2** and **6.3**, respectively.

$$E_c = [E(M_n) - nE(M)]/n \qquad (6.2)$$

$$E_{c/GM} = [E(M_{n/GM}) - E(GM) - nE(M)]/n \qquad (6.3)$$

E_c represents the cohesive energy per atom of clusters in the gas-phase, while $E_{c/GM}$ provides information on the cluster cohesive energy in the presence of the graphene support.

n	Pt			Ni		
	E_b [eV]	E_c [eV]	$E_{c/GM}$ [eV]	E_b [eV]	E_c [eV]	$E_{c/GM}$ [eV]
2	-8.3	-2.1	-6.3	-8.7	-1.8	-6.2
3	-8.4	-2.8	-10.2	-5.6	-2.4	-5.8
4	-8.8	-3.1	-10.2	-5.3	-2.9	-5.5
5	-8.8	-3.4	-10.4	-5.2	-3.3	-5.4
6	-8.7	-3.6	-10.6	-5.1	-3.5	-5.3
7	-9.2	-3.7	-10.7	-5.1	-3.7	-5.2
8	-9.2	-3.9	-10.4	-5.1	-3.9	-5.2
9	-9.6	-4.0	-11.1	-5.1	-3.9	-5.2
10	-9.4	-4.2	-11.2	-5.1	-4.1	-5.2

Table 6.2: Calculated E_b, E_c and E_c/GM values for the Pt_n and Ni_n clusters.

As can be seen in **Tab. 6.2** for Pt and Ni, the cohesive energy per atom of clusters in the gas phase as well as in the presence of graphene increases in absolute value as the number of metal atoms increases. However, this per-atom increase is not constant. Notably, for each n, the $E_{c/GM}$ is consistently higher than the E_c, with a more pronounced difference observed for Pt, where the two energy values differ by approximately 7 eV. This suggests that the intense chemical interaction between the M_n cluster and the graphene monovacancy confers greater stability on the supported clusters than in the gas phase. This stabilization is also consistent with the observed reduction in spin magnetic moment due to the strong hybridization between the M species and the monovacancy.

6.4.1 Grid program

The "grid" program was developed to generate a cylindrical grid around a cluster of metal atoms (M), ensuring that the geometric conditions and bonding distances for the investigated metal (Pt or Ni) are physically realistic.

Initially, the code declares variables to store atomic coordinates, distances, and other relevant geometric parameters, along with critical constants such as the average and maximum bonding distances between M atoms.

The program then reads atomic coordinates from an in *.xyz* format file, representing the initial configuration of the cluster. The coordinates of the M atoms are used to calculate the cluster's centroid, which serves as the reference point for constructing the cylindrical grid. During this process, the atom with the lowest

z-coordinate is identified to correctly position the grid relative to the cluster's height.

Once the centroid is determined, the program calculates the radius of the cylindrical grid and the angular separation between successive points on the circumference, based on the bonding distances and the required number of points. A cylindrical lattice is then created, where each point is initially calculated according to its angular position relative to the centroid.

To ensure that each grid point meets the physical criteria, the program checks whether the distance between each grid point and the nearest atom is within the maximum allowable bonding distance. If this condition is not met, the program solves a quadratic equation to adjust the grid point's position, thereby ensuring compliance with the distance limit. This adjustment ensures that the grid accurately represents the cluster's structure and atomic interactions.

Finally, the grid points' coordinates are written to an *output* file, which serves as the reference for creating the new structures, where each angular point is added to the pre-existing cluster. Each structure is then subjected to geometry optimization.

6.5 Reaction on Pt_{10} and Ni_{10} clusters supported on graphene

The Pt_{10}/C_{95} and Ni_{10}/C_{95} were employed to detail the energetics of two significant elementary processes in guaiacol valorisation: the loss of the oxygenated hydroxyl and methoxyl groups from the unsaturated compound (guaiacol) and the correspondent fully hydrogenated one (2-methoxycyclohexan-1-ol). This enabled us to assess the influence of graphene–metal interactions on the efficiency of the catalytic process and the differences in catalytic performance between the two metals, Pt and Ni.

Optimisations of the reactant and product structures of the elementary steps were performed under periodic conditions using the *SIESTA* approach, while the search for transition states was conducted using the Empathes code, which implements the *NEB* method. The results, reported below, are organised in terms of type of C–O bond breakage and of metal, and display the optimized geometries of the reactant (R), transition state (TS) and product (P). The tables below each
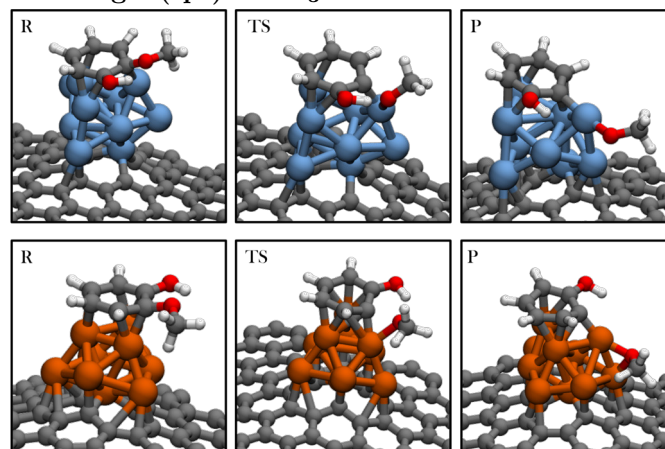
group of figures provide the values, in kJ mol^{-1}, of the energy barrier (E$_b$) and reaction ΔE associated with each elementary step.
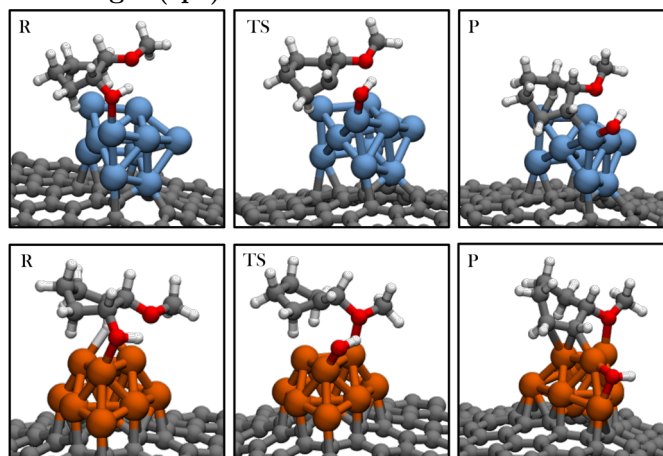
Breaking C(sp^2)–OH
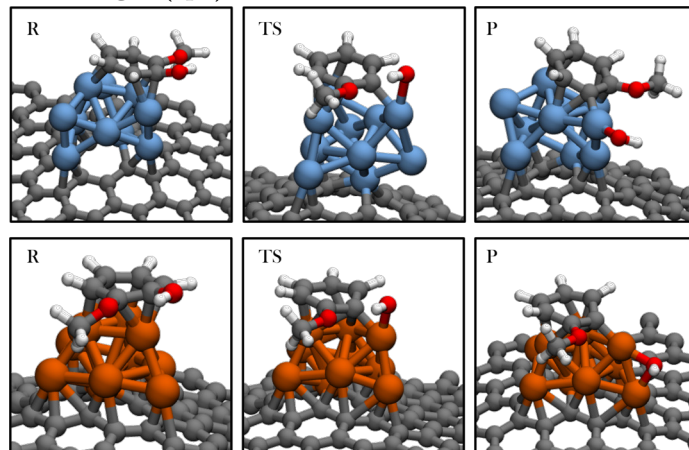
Metal	E$_b$ [kJ mol^{-1}]	ΔE [kJ mol^{-1}]
Pt	182.3	+61.2
Ni	115.1	-69.2

Breaking C(sp^2)–OCH$_3$

Metal	E$_b$ [kJ mol^{-1}]	ΔE [kJ mol^{-1}]
Pt	173.4	+55.0
Ni	172.7	-39.2

Breaking C(sp³)–OH

Metal	E_b [kJ mol^{-1}]	ΔE [kJ mol^{-1}]
Pt	165.0	+51.6
Ni	92.4	-189.4

Breaking C(sp³)–OCH₃
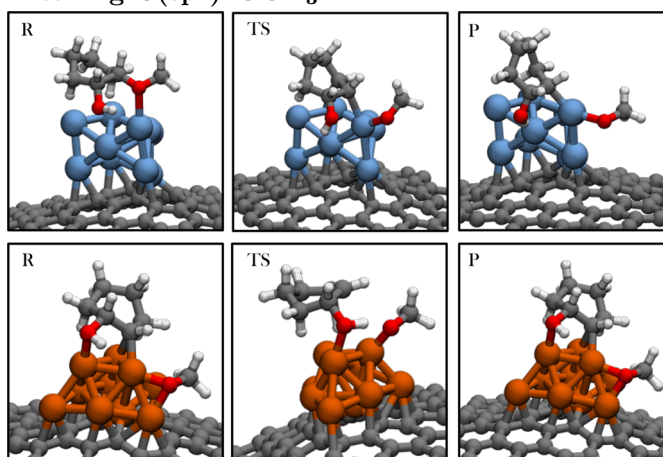
Metal	E_b [kJ mol^{-1}]	ΔE [kJ mol^{-1}]
Pt	148.8	+3.3
Ni	58.5	-151.9

Analyzing the deoxygenation processes on both the Pt_{10}/C_{95} and Ni_{10}/C_{95} systems, it emerges that the cleavage of $C(sp^3)$–O bonds requires overcoming significantly lower energy barriers compared to the cleavage of $C(sp^2)$–O bonds. Specifically, this difference amounts to an average of 20.0 kJ mol^{-1} for platinum and, more notably, 68.0 kJ mol^{-1} for nickel. Comparing the binding energies (E_b) and

ΔE values on supported Ni and Pt clusters, it becomes clear that deoxygenation preferentially occurs on Ni$_{10}$/C$_{95}$,with the cleavage of C(sp^3)–O bonds being the most favorable among all bonds considered.

The ΔE values of the reactions also reveal that nickel interacts more strongly with the oxygen atom (both in $-$OCH$_3$ and in -OH) than platinum, a comprehensible behaviour considering the platinum's nature as a noble metal. This phenomenon is not influenced by π-interactions, as these are either consistently present in unsaturated systems or entirely absent in saturated ones.

6.6   Conclusion

In this chapter, the growth of Pt and Ni clusters on defective graphene surfaces was explored in detail, investigating the chemical and structural properties of the supported metal systems and their catalytic potential. The results revealed the fundamental role of graphene as a support in heterogeneous catalysis, exploiting its excellent physical characteristics, including high thermal and electrical conductivity, large surface area and chemical stability.

One of the most relevant aspects emerging is the importance of graphene's structural defects, such as carbon vacancies, which facilitate the stable anchoring of metal clusters. Metal clusters tend to diffuse and aggregate on non-defect surfaces, reducing the effectiveness of catalysis. However, the presence of defects in the graphene lattice significantly modifies the interactions between the substrate and metals, increasing the adsorption energy and preventing the formation of large metal clusters. This stabilising effect was observed for both metals studied, with platinum showing a higher binding affinity to the vacancy sites than nickel, although both systems were strongly anchored to the substrate.

From a structural point of view, the optimal geometries of Pt and Ni clusters (n=1–10) were identified through the application of the *grid* program and *SIESTA* optimisations, which revealed complex three-dimensional configurations. These exhibit a strong interaction with graphene in the early stages of accretion, with stable geometries such as pyramids and bipyramids evolving into more complex structures as the number of metal atoms increases.

Another important finding concerns bonding and cohesion energies, which show that graphene not only stabilises metal clusters, but also changes their electronic properties. This effect has a direct impact on the catalytic properties of the sup-

148

ported metals. The results indicated that Pt and Ni clusters on graphene exhibit high stability, with cohesion energies increasing with cluster size, confirming that the presence of graphene makes the clusters less prone to surface diffusion and aggregation. This is a crucial aspect for improving catalytic performance, as the stability of metal clusters is closely linked to their ability to remain active during chemical reactions.

Finally, the study of deoxygenation reactions of biomass-derived compounds, such as guaiacol and 2-methoxycyclohexanol, highlighted significant differences between Pt and Ni in terms of reactivity. In particular, nickel showed higher efficiency in breaking $C(sp^3)$–O and $C(sp^2)$–O bonds, with lower energy barriers than platinum. This behaviour can be attributed to the nature of nickel, which interacts more strongly with oxygen atoms, facilitating deoxygenation and making it a promising candidate for deoxygenation processes aimed at biomass upgrading. In contrast, platinum, although exhibiting good stability, showed a lower affinity for oxygen. The differences observed between Pt and Ni underline the importance of choosing carefully the most suitable metal for specific catalytic applications, depending on the nature of the reactions and substrates involved.

In this study, the focus was limited to deoxygenation processes in the absence of hydrogen, aiming to isolate the intrinsic behaviour of the metal catalysts. Future research could explore additional reaction pathways, such as demethylation, to gain a deeper understanding of the deoxygenation mechanisms in complex biomass molecules. Additionally, while nickel has proven to be highly effective for deoxygenation, it is worth investigating whether platinum might exhibit superior performance for hydrogenation processes. Testing this hypothesis in future developments could open new directions for optimizing catalyst functions tailored to specific steps in biomass conversion.

Afterwords

The investigation carried out in this PhD thesis is framed in the crucial context of the contemporary energy transition, a process that is essential to progressively reduce global dependence on fossil fuels and embrace more sustainable, low-impact resources. This transformation is recognised as essential to ensure a sustainable energy future, especially in Europe and Italy, which have set ambitious goals to achieve climate neutrality in the coming decades. In this scenario, biomass emerges as a valuable and versatile resource, capable of generating energy continuously and reliably, in contrast to intermittent sources such as solar and wind power. Biomass, mainly composed of materials such as cellulose, hemicellulose and lignin, offers significant opportunities for the production of valuable fuels, electricity and chemicals. However, its large-scale application is limited by the complexity of the conversion processes required to turn it into high-quality biofuels.

This thesis discusses the conversion of lignocellulosic biomass using model compounds to effectively isolate and represent the complex reactions that occur during the hydrodeoxygenation (HDO) process. In particular, isoeugenol and guaiacol were chosen as representative biomass model molecules, as they contain functional groups and aromatic structures typical of biomass-derived molecules. The deoxygenation of these molecules is crucial to increase the energy density and stability of the produced biofuels, making them more similar in quality and performance to fossil fuels.

The results, obtained from density functional theory and subsequent application of microkinetic analysis, highlight that, in the HDO processes for isoeugenol and guaiacol, the direct deoxygenation is preferred to deoxygenation by hydrogenation (HYD) one. For isoeugenol, analyses show that the removal of the methoxyl group as methanol, followed by desorption of the hydroxyl as water, are the most favoured outcomes, clarifying the kinetic barriers involved. Similarly, in the case of guaiacol, the Pt_{10} cluster shows a particular preference for breaking the $C(sp^2)$–O

bond. This behaviour, in contrast to the typical reactive dynamics of noble metals on the surface, underlines the uniqueness of subnanometer clusters and suggests that catalysis at the atomic level may lead to specific reactivity results, requiring customised approaches for optimisation.

The decomposition of guaiacol on Pt_{10} occurs accornding to reactive pathways leading to fully deoxygenated products such as benzene and cyclo-pentene, passing through phenol as an intermediate and to partially oxygenated products such as 2,4-cyclopentadien-1-one. Also this part of investigation revealed that the structure and size of the metal cluster drastically influence the catalytic reactions, suggesting that further optimisation of the catalyst configuration could make the deoxygenation process more selective and energy-efficient.

A crucial advance in this research concerns the effect of the support on the HDO and decomposition biomass products, hence the analysis of the growth and stabilisation of Pt and Ni metal clusters on defective graphene was performed. According to the results obtained, graphene defects, in particular carbon vacancies, play a key role in stabilising metal clusters, reducing aggregation and sintering phenomena. The presence of graphene not only stabilises the cluster, but also changes its electronic properties, which has a positive impact on catalytic performance. This effect is especially relevant for large-scale catalysis, where stability and resistance to coke formation are essential to maintain reactivity over time. Comparisons between platinum and nickel revealed possibly complementary catalytic characteristics. Nickel has shown greater efficiency in breaking $C(sp^3)$–O and $C(sp^2)$–O bonds than platinum, suggesting that nickel's intrinsic properties make it promising for deoxygenation processes. However, platinum may prove to perform better in hydrogenation reactions, an aspect to be explored in future research to optimise catalysts for specific steps in biomass conversion. The ability of defective graphene to act as an effective support makes this material a promising option for the design of new metal-cluster catalysts for biomass conversion.

The contribution of this thesis is two-fold: on the one hand, it extends the basic knowledge of biomass conversion mechanisms; on the other, it offers concrete direction for the design of optimised catalysts for HDO and decomposition processes. The results showed that metal clusters supported on defective graphene can be particularly effective for biomass deoxygenation, combining stability, high selectivity and resistance to coke formation. Furthermore, the adopted methodologies highlighted the importance of considering the molecular structure of the biomass,

the type of metal and the support chosen, as each of these factors profoundly affects the efficiency of the process.

The results also suggest further research directions, such as exploring other catalytic metals and experimenting with additional defects in graphene, to further optimise the stability and effectiveness of the catalysts. The integration of bi-functional catalysts, capable of combining the properties of various metals, could offer significant advantages for complex reactions, making catalysts adaptable to a wider range of operating conditions and expanding their industrial applicability. These perspectives could contribute significantly to the realisation of sustainable energy processes and the transition to a greener future.

Appendix A

Profiles and Tables

A.1 Table for HDO reaction of Isoeugenol on Pt$_{10}$ cluster

Table A.1: Standard Gibbs free energies of desorption (T = 298.15 K) for the stable intermediates and products involved in the investigated HYD pathways.

compound[a,d] / ΔG_{des}/kJ mol^{-1}			
IE[b]		130.2	
DHE[b]		85.3	
CP[b]		28.8	
HYD		**DDO**	
MPCHDEOH	190.7	PPH	91.1
MPCHEOH	131.9	PB	77.9
MPCHOH	40.4	MPB	105.9
MPCH	70.4	mPPH	80.1
mPCHOH	54.5	PBDOH	60.8
PCHOH	70.4	PCHDE	176.9
PCHDOH	55.8		
CH$_3$OH[c]	42.5	CH$_3$OH	23.6
H$_2$O	1.4	H$_2$O	50.4
CH$_4$	-11.8	CH$_4$	-70.9

[a] See Figure 3.15 for the shorthand notation employed for the chemical species; further, in this table the notation MPCHDEOH = 6-methoxy-4-propylcyclohexa-1,3-dien-1-ol; MPCHEOH = 6-methoxy-4-propylcyclohex-3-en-1-ol; PCHDE = 5-propyl-1,3-cyclohexadiene is used. Each molecule is intended adsorbed on the Pt$_{10}$ cluster. [b] These species are common to all pathways. [c] ΔG_{des} of methanol, water and methane are different for HYD and DDO mechanisms because they desorb leaving different species adsorbed on the platinum cluster. [d] The desorption process of the A species is (A + X)/Pt$_{10}$ $\longrightarrow$ A + X/Pt$_{10}$, being X a different species, if any, left adsorbed on the cluster.

A.2 Profiles for HDO of guaiacol on Pt$_{10}$ cluster
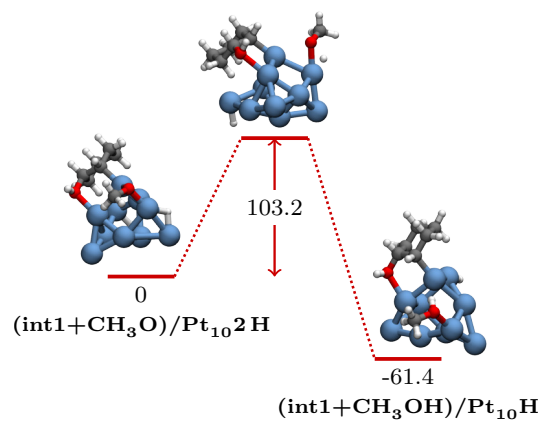
Figure A.1: Hydrogenation of OCH_3, following fragmentation of an H_2 molecule, leads to the formation of chemisorbed methanol.

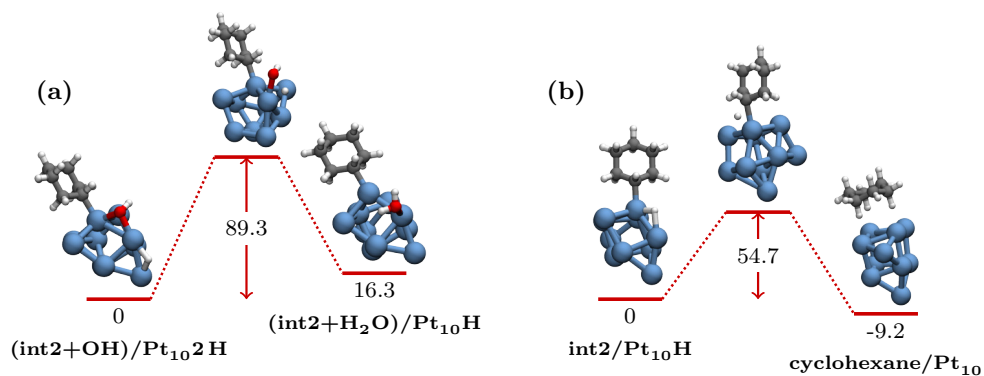## A.3   Tables for HDO of isoeugenol on Pt_{10} cluster

Figure A.2: The reaction profiles illustrate **(a)** the formation of an adsorbed H_2O molecule via the transfer of a hydrogen atom to the OH fragment, followed by the desorption of the H_2O molecule and the diffusion of a hydrogen atom across the cluster, and **(b)** the subsequent generation of cyclohexane.
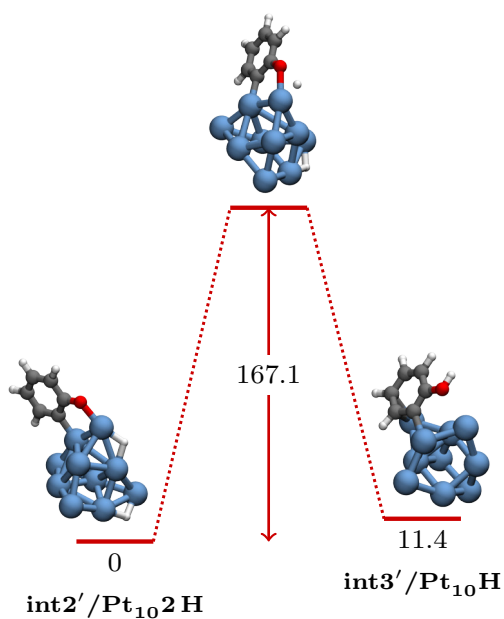
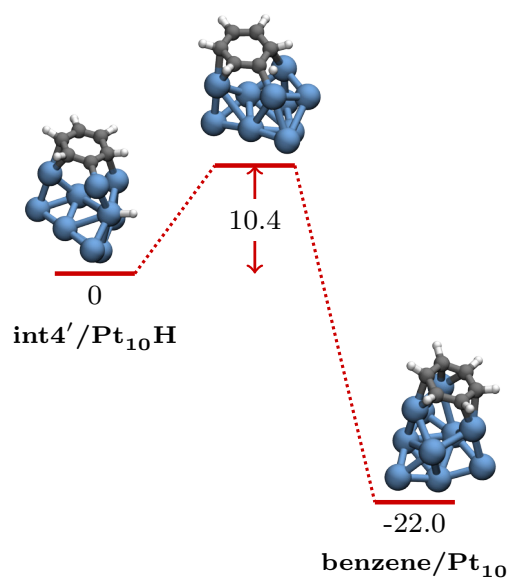**Figure A.3:** Hydrogenation of the dangling O of int2′ in the absence of CH_3OH.

Figure A.4: Hydrogenation of the unsaturated ring to form adsorbed benzene.

Table A.2: The shorthand notation used below for the main species involved in the guaiacol hydrodeoxygenation reaction.

compound	abbreviation
guaiacol	**G**
2-methoxy-cyclohexan-1-ol	**MOCEO**
cyclohexanol	**CEO**
cyclohexane	**CE**
methoxycyclohexane	**MOCE**
cyclohexane-1,2-diol	**CEDO**
phenol	**P**
benzene	**B**
anisole	**AN**
cathecol	**CA**

Table A.3: Gibbs free energies of desorption (T = 298.15 K, p = 1 atm) for the stable intermediates and products involved in the investigated HYD and DDO pathways. Each molecule is considered adsorbed on the Pt_{10} cluster.

compound	ΔG_{des} (kJ mol^{-1})
guaiacol	78.7
2-methoxy-cyclohexan-1-ol	41.4
cyclohexanol	51.0
methoxycyclohexane	59.6
cyclohexane-1,2-diol	27.0
2-methoxycyclohex-2,4-dien-1-ol	199.4
2-methoxycyclohexa-3-en-1-ol	93.3
phenol	63.2
benzene	97.8
anisole	59.7
cathecol	91.8
cyclohexa-1,3-dien	121.8
cyclohexene	87.1
cyclohexane	29.7
methanol	61.9
water	31.3
methane	-12.0

Table A.4: Elementary reaction steps in the HYD mechanism, along with the corresponding free energy barriers and reaction ΔG values, expressed in kJ mol^{-1} (T = 298.15 K, p = 1 atm). The final column indicates the figure number where the elementary process is illustrated.

Elementary process	$\Delta \mathbf{G}^{\#}$	$\Delta \mathbf{G}$	Figure
guaiacol/Pt$_{10}$ → I	64.7	17.0	4.2
I → II	85.3	-35.9	4.2
II+2H → III	57.1	-8.3	4.2
III → IV	85.6	58.3	4.2
IV+2H → V	28.3	-14.0	4.2
V → VI	100.6	25.4	4.2
2-methoxycyclohexan-1-ol/Pt$_{10}$ → (int1+OCH$_3$)/Pt$_{10}$	140.3	-57.0	4.3
(int1+CH$_3$O)/Pt$_{10}$ 2 H → (int1+CH$_3$OH)/Pt$_{10}$ H	99.5	-60.6	S1
int1/Pt$_{10}$ H → cyclohexanol/Pt$_{10}$	106.2	38.1	4.3
cyclohexanol/Pt$_{10}$ → (int2+OH)/Pt$_{10}$	188.2	11.1	4.3
int2/Pt$_{10}$ H → cyclohexane	59.4	-4.4	S2
2-methoxycyclohexan-1-ol/Pt$_{10}$ → (int3+OH)/Pt$_{10}$	151.2	-112.1	4.4
int3/Pt$_{10}$ H → methoxycyclohexane/Pt$_{10}$	101.8	43.3	4.4
methoxycyclohexane/Pt$_{10}$ → (int4+OCH$_3$)/Pt$_{10}$	183.6	11.7	4.4
methoxycyclohexane/Pt$_{10}$ → (int5+CH$_3$)/Pt$_{10}$	204.8	47.5	4.4
2-methoxycyclohexan-1-ol/Pt$_{10}$ → (int6+CH$_3$)/Pt$_{10}$	165.1	6.7	4.5
int6/Pt$_{10}$ H → cyclohexane-1,2-diol/Pt$_{10}$	168.5	47.2	4.5
cyclohexane-1,2-diol/Pt$_{10}$ → (int7+OH)/Pt$_{10}$	161.9	-102.4	4.5

Table A.5: Elementary stage reactions in the DDO mechanism with the corresponding free energy barrier and reaction ΔG expressed in kJ mol^{-1} (T = 298.15 K, p = 1 atm). The last column indicates the figure number where the elementary process is displayed.

Elementary process	$\Delta G^{\#}$	ΔG	Figure
guaiacol/Pt$_{10}$ $\rightarrow$ (int1$'$+OCH$_3$)/Pt$_{10}$	132.4	0.2	4.7
(int1$'$+OCH$_3$)/Pt$_{10}$ $\rightarrow$ (int2$'$+CH$_3$OH)/Pt$_{10}$	26.1	-7.4	4.7
(int2$'$+CH$_3$OH)/Pt$_{10}$ 2 H $\rightarrow$ (int3$'$+CH$_3$OH)/Pt$_{10}$ H	47.9	-28.4	4.7
int3$'$/Pt$_{10}$ H $\rightarrow$ phenol/Pt$_{10}$	61.2	-31.9	4.7
phenol/Pt$_{10}$ $\rightarrow$ (int4$'$+OH)/Pt$_{10}$	103.6	-26.6	4.7
guaiacol/Pt$_{10}$ $\rightarrow$ (int5$'$+OH)/Pt$_{10}$	167.0	59.7	4.8
int5$'$/Pt$_{10}$ H $\rightarrow$ anisole/Pt$_{10}$	62.4	-30.2	4.8
anisole/Pt$_{10}$ $\rightarrow$ (int6$'$+OCH$_3$)/Pt$_{10}$	83.0	-35.1	4.8
anisole/Pt$_{10}$ $\rightarrow$ (int7$'$+CH$_3$)/Pt$_{10}$	145.4	-33.9	4.8
int7$'$/Pt$_{10}$ H $\rightarrow$ phenol/Pt$_{10}$	88.1	42.0	4.8
guaiacol/Pt$_{10}$ $\rightarrow$ (int8$'$+CH$_3$)/Pt$_{10}$	149.3	-43.2	4.9
int8$'$/Pt$_{10}$ H $\rightarrow$ catechol/Pt$_{10}$	151.6	64.6	4.9
catechol/Pt$_{10}$ $\rightarrow$ (int3$'$+OH)/Pt$_{10}$	203.3	-14.6	4.9
benzene/Pt$_{10}$ $\rightarrow$ Ia	89.3	-24.7	4.10
Ia $\rightarrow$ IIa	85.0	61.5	4.10
IIa+2H $\rightarrow$ IIIa	27.0	-24.7	4.10
IIIa $\rightarrow$ IVa	65.2	56.9	4.10
IVa+2H $\rightarrow$ Va	40.8	19.5	4.10
Va $\rightarrow$ cyclohexane/Pt$_{10}$	84.1	13.0	4.10
int2$'$/Pt$_{10}$ 2 H $\rightarrow$ int3$'$/Pt$_{10}$ H	166.2	18.1	S3
int5$'$/Pt$_{10}$ H $\rightarrow$ benzene/Pt$_{10}$	12.7	-20.7	S4

Table A.6: Gibbs free energies of desorption (T = 298.15 K, p = 1 atm) for the stable intermediates and products occurring in the investigated HYD pathway. Each molecule is intended adsorbed on the Pt$_{10}$ cluster.

compound	ΔG_{des} (kJ mol-1)
isoeugenol	-130.2
dihydroeugenol	85.3
6-methoxy-4-propylcyclohexa-1,3-dien-1-ol	190.7
6-methoxy-4-propylcyclohex-3-en-1-ol	131.9
2-methoxy-4-propylcyclohexan-1-ol	40.4
1-methoxy-3-propylcyclohexane	70.4
3-propylcyclohexan-1-ol	54.5
4-propylcyclohexan-1-ol	70.4
4-propylcyclohexan-1,2-diol	55.8
propylcyclohexane	28.8
methanol	42.5
water	1.4
methane	-11.8

Table A.7: Gibbs free energies of desorption (T = 298.15 K, p = 1 atm) for the stable intermediates and products occurring in the investigated DDO pathway. Each molecule is intended adsorbed on the Pt_{10} cluster.

compound	ΔG_{des} (kJ mol−1)
isoeugenol	-130.2
dihydroeugenol	85.3
4-propylphenol	91.1
propylbenzene	77.9
1-methoxy-3-propylbenzene	105.9
3-propylphenol	80.1
4-propylbenzene-1,2-diol	60.8
5-propyl-1,3-cyclohexadiene	176.9
propylcyclohexane	28.8
methanol	23.6
water	50.4
methane	-70.9

Appendix B

Papers
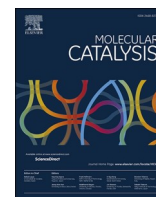
Computational investigation of isoeugenol transformations on a platinum cluster – I: Direct deoxygenation to propylcyclohexane

Francesco Ferrante [*],[a], Chiara Nania [a], Dario Duca [a]

Dipartimento di Fisica e Chimica "E. Segrè" - Università degli Studi di Palermo, Viale delle Scienze Ed. 17, Palermo I-90128, Italy

ABSTRACT

The growing demand for renewable and sustainable fuels, protagonists of an increasingly important research area due to the exhaustion of fossil resources, has oriented our investigation towards the computational mechanistic analysis of the catalytic hydrodeoxygenation (HDO) reaction of isoeugenol. Having the most common functional groups, the isoeugenol molecule is actually considered as an experimental and computational model for typical species of biomass origin. The reported computational investigation outlines the energy barriers and the intermediates along the path for the conversion of isoeugenol to propylcyclohexane through a direct deoxygenation mechanims, catalyzed by a subnanometric metal cluster. For this purpose, the Pt_{10} platinum cluster was chosen as the catalyst model, being this noble metal a reference for hydrogenation reaction. The results obtained rule the formation of the 4-propylphenol intermediate as the rate determining step for the considered branch of the mechanim, and as the pivotal point for further ramifications. The present is the first of a series of studies aimed to a complete mapping of isoeugenol HDO on a Pt cluster, to be used as reference for further, more focused, investigations, such as those regarding the effects of the support and of the metal particle size, as well as the HDO reaction of biomass-derived compounds similar to isoeugenol.

1. Introduction

Pyrolysis of biomass gives rise to the formation of bio-oils, complex mixtures of compounds derived from the rapid and simultaneous depolymerization of cellulose, hemicellulose and lignin, following a rapid increase in temperature. Bio-oils are composed mainly by hydroxyaldehydes, hydroxyketones, sugars, carboxylic acids and phenols [1]. Hydrodeoxygenation reaction (HDO) of lignin-derived bio-oils is currently an important research area due to the depletion of fossil fuel resources, and is devoted to satisfy the increasingly pressing demand for renewable and sustainable alternatives for the production of fuels, chemicals and energy. Bio-oils as such are not suitable as fuels due to their acidity and high oxygen content, as well as their instability [2,3]. Being a mixture of oxygenated components, they do not have the physico-chemical properties to compete, as a transport fuel, with petroleum distillates. However, their liquid form facilitates further processing, making the refining and upgrading of biofuel into liquid hydrocarbons an important process [4]. Various catalytic pathways for hydrogenation and deoxygenation of bio-oils have been extensively studied, but among these HDO is considered the most effective method

[5]. Although there are some studies on the HDO of bio-oils, in order to facilitate the elucidation of the HDO reaction mechanism, it is preferred to replace more complex species with simpler models, consisting of monomeric lignin compounds. Due to its molecular structure, which contains the most common functional groups in bio-oils derived from lignin (i.e. hydroxyl, methoxy and allyl groups), isoeugenol can be considered as an appropriate and representative molecular candidate model.

Understanding catalytic processes at the atomic level is a fundamental goal of chemistry, and catalysis on supported metal cluster (SMC) systems play a role that is becoming more and more important in the modern chemical industry [6]. Indeed, following the recent developments of the synthetic methods aimed at obtaining small metal cluster systems, the related catalysis approaches have rapidly become a subfield of heterogeneous catalysis and much effort is at present dedicated to the creation of specifically tailored SMC catalysts showing high efficiency and selectivity [7–11]. Stabilized on solid supports, such as metal oxides, silica, various forms of carbon, zeolites, and others [12–15] SMCs are promising catalytic systems both for academic and industrial applications, being either able to catalyze reactions otherwise

---

difficult to occur or to be separated quite easily at the end of the process [16].

Besides that, SMCs possess high surface/volume ratio, another very important feature is the presence of metal-to-metal bonds, that is, of nearby metal sites that offer greater possibilities for binding with the substrate [17]. Since many important catalytic processes require tightly cooperating metal sites for reactant adsorption, activation and product desorption, SMCs can be used in a wide variety of catalytic reactions [16,18,19]. SMCs, moreover, can show a certain structural fluidity during the catalytic process. At high temperatures and under the influence of metal-support and/or metal-substrate interactions, SMCs can actually lose their initial stiffness and evolve into fluxional species, generating metastable geometries that can increase reactivity [20]. The properties of metal clusters can also be selectively modified by introducing dopant atoms, which change their electronic structure, their relationship with the support and their catalytic activity as well [21].

Intensive research in recent years has shown that clusters size has a very large impact on their reactivity, as well as on the efficiency and selectivity of the catalytic processes in which they are involved [22]. There is a scalable regime, in which reactivity changes constantly with cluster size, and a non-scalable size regime for small clusters, in which reactivity could completely change even after adding a single atom [23]. This size-reactivity relationship can be explained in terms of the change in surface morphologies. Advances in this area have benefited from the development of accurate quantum-mechanical calculations, which became an increasingly powerful tools for understanding the processes that rule the structure of the catalyst and, ultimately, its catalytic performance.

It has been suggested [24–26] that HDO reaction of phenolics may occur with two limiting mechanisms depending on nature of the metal catalyst: deoxygenation-through-hydrogenation, HYD, according to which the first steps involved concern the hydrogenation of the benzene ring, and direct deoxygenation mechanism, DDO, meaning that the saturation of benzene ring occurs after removal of oxigen-containing groups. The present work is the first of a series aimed to elucidating, by means of an atomistic approach based on density functional theory, the whole mechanism of HDO of phenolics on noble and non-noble subnanometric metal clusters, in order to reveal how the reduced size of the catalyst may affect the outcomes of the reaction. Here the HDO reaction of isoeugenol catalyzed by a small platinum cluster is presented. Isoeugenol and platinum are, in fact, considered as models for compounds of biomass origin and for hydrogenation catalyst [27,28], respectively. Among the many foreseeable pathways, it was decided to follow the DDO mechanims on a platinum cluster in order to create a reference for future investigations with other, possibly non-noble, catalytic systems and to find key points for possible branches of the mechanism which could lead to significant differences in catalytic activity and selectivity between noble and non-noble metals. Further, a reference mechanism reported for an unsupported cluster can be used to identify the effects that various kind of supports could have on important stages of the hydrodeoxygenation process.

After a short section concerning the preliminary study on H_2 fragmentation and H diffusion on the platinum cluster, the computational data collected on the elementary processes characterizing the surface species involved in the hydrogenation are reported and analyzed to detail one of the possible mechanisms for the reaction that converts isoeugenol into propylcyclohexane.

2. Computational details and models

All the calculations were performed in the framework of density functional theory (DFT), using the Gaussian 16 package [29]. The B3LYP hybrid exchange-correlation functional [30] was used and the D3 correction scheme developed by Grimme (GD3), which allows one to take into account dispersion interactions [31], was added to the functional. For the conformational study of isoeugenol, the correlation

consistent polarized valence double zeta (cc-pVDZ) basis set by Dunning and coworkers [32] was used. The study of isoeugenol HDO reaction on the platinum cluster was instead carried out with the LANL2DZ basis set [33,34]; this, developed by Hay and Wadt, uses Dunning's basis set (D95) [35] for light atoms (H, C, O) and, for platinum, a double-zeta valence basis set associated to an effective core potential. Polarization functions consisting of primitive Gaussians having angular momentum and exponents in accordance with the following scheme have been added to the D95 set: H (s: 0.049, p: 0.587), C (p: 0.0311, d: 0.587), O (p: 0.0673, d: 0.961). These functions were retrieved from the EMSL Basis Set Exchange website [36]. Minima and transition state (TS) species on the reaction paths were revealed by inspection of the harmonic vibrational frequencies, checking that imaginary frequencies were not present in the structures corresponding to potential energy surface minima and only one imaginary frequency (corresponding to the one related to the eigenmode transforming reactant to the product) was present in the TS structures. In one case, due to the difficulty of finding the transition state for a whole molecule rearrangement (see Section 3.4), the nudged elastic band approach was used, as implemented in the Empathes code [37,38].

The energetics of the reaction paths will be given in terms of vibrational zero-point corrected energies (E_{ZPV}); the desorption energies of intermediates and final product has been corrected for the basis set superposition error (BSSE) by using the counterpoise method of Boys and Bernardi [39]. Since BSSE was calculated as correction to the SCF energy, it will be reported in parenthesis along with the uncorrected E_{ZPV} energies.

A magic number [40] corresponding to a regular tetracapped octahedron [41] platinum cluster shaped by ten atoms, having T_d symmetry and spin multiplicity equal to 9, was chosen as the subnanometric catalytic model [42]. Its structure shows the presence of atoms with different coordination. The four cap atoms have actually coordination three, while the remaining six atoms have coordination number six. These determine the octahedron cage, on whose triangular faces the cap atoms are arranged. In particular, two platinum cap atoms with coordination three are found in the upper portion of the octahedron, while the other two in the lower portion, arranged on a plane perpendicular to that where the first two lie. The geometry of Pt_{10} cluster is represented in Fig. 1, along with the numbering used throughout for the carbon atom centers in the isoeugenol molecule and all its derivatives up to propylbenzene.

3. Results and discussion

The simultaneous presence, in the isoeugenol molecule, of some of the most common functional groups characteristic of bio-oils opens up several possibilities for the HDO reaction study. In this first work, the HDO mechanism on a platinum cluster was investigated according to the four consecutive stages
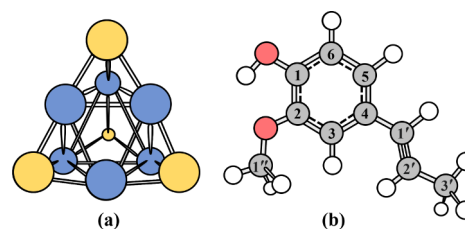

Fig. 1. (a) Pt_{10} cluster, model of the subnanometric catalyst; the Pt atoms with different coordination numbers are distiguished by different colors (yellow and light blue for coordination number three and six, respectively). (b) Molecular structure of *trans*-isoeugenol with the IUPAC numbering of carbon atoms. (For interpretation of the references to color in this figure legend, the reader is referred to the web version of this article.)

1. saturation of allyl double bond;
2. removal of metoxy group;
3. removal of hydroxy group;
4. saturation of benzene ring.

which, apart from the first process, represent a typical DDO mechanism. This follows one of the experimental hypotheses put forth by the research group of D.-Yu. Murzin, which, in the aim to employ low cost catalysts, conducted their experiments using nickel [2,43]. The computational results obtained will be reported in the next sections, starting from the preliminary investigation on the H_2 fragmentation and H diffusion on the Pt_{10} cluster and the interaction of isoeugenol with the catalytic system.

3.1. Fragmentation of H_2 on Pt_{10}

As evidenced by other studies [42], the Pt_{10} cluster has nonect spin multiplicity and tetrahedral geometry. The Pt-Pt bond lengths in the optimized structure are in the range 2.60–2.82 Å, with an average value of 2.71 Å. The longest linear dimension of the cluster is therefore slightly less than 6 Å. The binding energy of the cluster with respect to ten isolated Pt atoms in the d^9s^1 electronic configuration is equal to 2754.0kJ mol^{-1}; therefore the cohesive energy, calculated as $E_c = (E[Pt_{10}] - 10E[Pt])/10$, is equal to 275.4 kJ mol^{-1}.

It has been already claimed that H_2 molecule, once chemisorbed on a given metal cluster, undergoes bond cleavage leading to the formation of hydrogen-species/metal-cluster systems in which the hydrogen atoms diffuse freely. In this case, the model catalyst, therefore, can be considered as a reservoir of hydrogen, ensuring a continuous availability of H atoms where necessary. This because, in addition to the ease of hydrogen fragmentation on the cluster, free diffusion of the hydrogen atoms through the catalyst could be hypothesized. To corroborate these inferences, demonstrated for most of metal systems [44,45], fragmentation and diffusion tests were carried out considering one H_2 molecule on the Pt_{10} cluster, in the following represented as $Pt_{10}H_2$ species.

As far as fragmentation is concerned, the chemisorption of the H_2 molecule on the platinum cap atom, showing coordination three, was considered. Adsorption, characterized by an energy release equal to 80.5 kJ mol^{-1}, led to the formation of a transient species with multiplicity of spin 9 (Fig. 2a), in which a considerable weakening of the H···H bond (length of 0.88 Å against 0.74 Å in the free H_2 molecule) is observed. The latter rapidly evolves into a species of 32.5 kJ mol^{-1} more stable (Fig. 2b), in a septet spin multiplicity state, that undergoes transformation by cluster distortion, paralleled by the total fragmentation of H_2. In this species, it has been found that the migration of a hydrogen atom from the top position on a cap site to a bridge
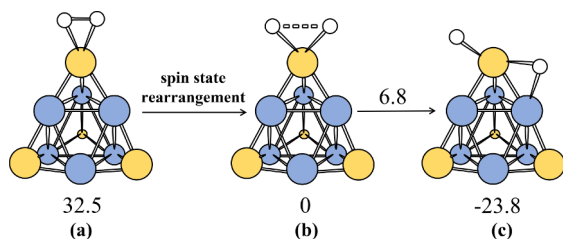
arrangement involving the same cap atom and one neighboring atom belonging to the octahedron cage (Fig. 2c) has an activation barrier equal to 6.8 kJ mol^{-1}, i.e. an almost negligible low energy value.

For the diffusion process, the geometries of five $Pt_{10}2H$ arrangements, characterized by different hydrogen constellations were considered. A further verification in support of the easy diffusion of the hydrogen atoms through the cluster was performed by considering the two most stable species, indicated in Fig. 3 with the letters (a) and (c), and the process of H atom migration converting one into the other. The estimated activation barrier of this elementary event, equal to 14.3 kJ mol^{-1}, clearly demonstrates the validity of the assumptions made above.

In view of these results, it can be stated that in the conditions needed to overcome the activation barriers occurring in the isoeugenol HDO, which will be discussed later, the barriers characterizing the hydrogen atom diffusion on the $Pt_{10}2H$ fragments are negligible. This implies that the hydrogen atoms can be arranged in any configuration on the cluster. It is finally to be underlined that, as it happens in the case of a large number of metal clusters [44,46,47], the fragmentation of H_2 is the cause of the decrease of one unit of the spin quantum number observed in the $Pt_{10}2H$ systems, being this occurrence correlated to electron spin coupling phenomena.

3.2. Adsorption of isoeugenol on $Pt_{10}2H$

There are six conformations for the *trans* isomer of isoeugenol, three of which are obtained by keeping the dihedral angle τ_1(C5C4C1$'$C2$'$) fixed at 180° and fixing, alternatively, the value of the τ_2(C2C1OH) and τ_3(C1C2OC1$''$) angles to 0° and 180°; the other three conformations can be obtained by keeping the dihedral angle τ_1 fixed at 0° and imposing, alternatively, the values 0° and 180° for the τ_2 and τ_3 angles. An equal number of conformations obviousy exist for the *cis* isomer. In it, however, the dihedral angle τ_1 has been set to 150°, because of the steric repulsion between the CH_3 group of the allyl chain (outside the plane identified by the aromatic ring) and the hydrogen atom of the C3 of the ring.

The twelve starting structures thus generated were subjected to geometry optimization. Not surprisingly, the most stable conformations for both stereoisomers are those where an intramolecular hydrogen bond occurs between the hydroxyl hydrogen and the metoxy oxygen, i.e. $\tau_2 = 180°$ and $\tau_3 = 0°$. In these conformations there is flexibililty as regard

Fig. 2. Fragmentation of the H_2 molecule on the Pt_{10} cluster and relative energies of the species involved (in kJ mol^{-1}). Structure (a) is a transient species in nonect state in which there is a weakening of the H···H bond, (b) is the most stable species, with septet spin multiplicity and (c) is the final structure (always a septet) in which the total fragmentation of the H_2 molecule occurs, through the migration of one hydrogen atom from its initial top position towards a bridge arrangement on the cluster. White, yellow and light blue balls identify hydrogen and platinum with coordination number three and six, respectively. (For interpretation of the references to color in this figure legend, the reader is referred to the web version of this article.)
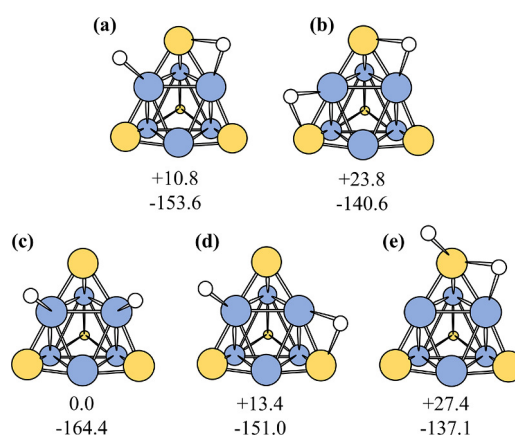

Fig. 3. $Pt_{10}2H$ fragments: The five structures, labeled with the letters (a)-(e), differ from each other for the positions of the H atoms in the cluster; they were used to evaluate the H-diffusion energetics. The values below each figure indicate the relative energy (in kJ mol^{-1}) with respect to the most stable (c) configuration (up), and the H_2 chemisorption energy (down), calculated as $E_{ads} = E[Pt_{10}H_2] - (E[Pt_{10}] + E[H_2])$. White, yellow and light blue balls identify hydrogen and platinum with coordination number three and six, respectively. (For interpretation of the references to color in this figure legend, the reader is referred to the web version of this article.)

the rotation of the allyl chain, resulting in Boltzmann populations of 62.8% ($\tau_1 = 180°$) and 37.1% ($\tau_1 = 0°$) for the *trans* isomer, and of 55.2% ($\tau_1 = 152°$) and 44.8% ($\tau_1 = -33°$) for the *cis* isomer. The *trans* stereoisomer of isoeugenol was calculated to be ca. 10 kJ mol^{-1} more stable than the *cis* one.

The adsorption of the most stable conformation of *trans*-isoeugenol on the lowest energy configuration of $Pt_{10}2H$ was therefore investigated. The various tests performed to find the adsorption geometry of isoeugenol on the cluster allowed to conclude that, in the most stable structure, the compound interacts with a cap platinum by means of the carbon atoms, C1′ and C2′, of the allyl chain as well as through the benzene ring with the lower portion of a cluster edge, involving a site of the octahedron cage. The adsorption of isoeugenol does not affect the spin multiplicity of the system, which remains in the septet state, but causes the two H atoms to shift from top to edge positions in the cluster, likely due to electron donation from the benzene ring to the metal centers [48]: the H − Pt bond length increases (from 1.54 to 1.64 Å) and the H atoms do interact also with another metal center (at distance equal to 1.82 Å), thus stabilizing configurations like the one showed in Fig. 3 (b). The adsorption energy of isoeugenol is equal to -237.7 (BSSE = 28.3) kJ mol^{-1}. This value, which is quite high if one looks at adsorption studies of simple alkenes on metal clusters [49], is indeed justified by the presence of the aromatic component which strongly interacts with the cluster. By calculating, with the same computational methods, the adsorption energy of propene on $Pt_{10}2H$, it was possible to roughly estimate that the energetic contribution of the aromatic portion to the adsorption of isoeugenol is about 140 kJ mol^{-1}, thus representing more than half of the total interaction energy.

In the optimized *trans*-isoeugenol/$Pt_{10}2H$ system a hydrogen atom is neighboring to the site where the first catalytic hydrogenation could take place, corresponding to the saturation of the allyl chain.

3.3. Hydrogenation of allyl group

The elementary steps involved in the catalytic hydrogenation of the isoeugenol double bond on the Pt_{10} cluster are reported in Fig. 4. The process is formed by two elementary steps: the first one leads to the formation of a semi-hydrogenated intermediate, int1/$Pt_{10}H^a$, by transferring the H atom from the cluster to the C2′ carbon atom of the allyl group; in the second one the migration of one H atom from the cluster to the C1′ atom of the chain with the formation of dihydroeugenol/Pt_{10} is conversely involved. In this and in all the other cases discussed below, the letter δ inside a circle indicates the diffusion of a hydrogen atom

through the cluster towards the reactive center; here the already supposed barrier-free H-diffusion transforms int1/$Pt_{10}H^a$ into int1/$Pt_{10}H^b$. On the basis of the activation energies of the two elementary steps, it can be noticed that the hydrogenation of the double bond should not be a fast process: energies barriers are indeed slightly higher than those calculated for the reaction converting butene to butane on a subnanometric palladium cluster [45].

The double bond saturation leads to a system, which is 106.3 kJ mol^{-1} less stable than the isoeugenol/$Pt_{10}2H$ reactant. This is not unexpected, since the dihydroeugenol interacts with the metal cluster only by means of the benzene ring. The desorption energy of dihydroeugenol from the cluster is calculated as 154.7 (BSSE = 25.7) kJ mol^{-1}.

3.4. Formation of 4-propylphenol

The next stage of the reaction should be the removal of the OCH$_3$ group from the adsorbed dihydroeugenol and the subsequent formation of 4-propylphenol. To investigate this reaction, two major channels can be hypotesized: (i) the direct cleavage of the methoxy group, with the final formation of methanol and 4-propylphenol, or (ii) the cleavage of the methyl group, giving rise to methane, water and 4-propylphenol as products and a cathecol derivative as intermediate. One or two hydrogen molecules are needed for the first and second case, respectively. It has been reported that the route involving the production of methane is the one actually preferred when platinum or even non noble metals are used as catalysts for the HDO reaction of phenolics [50–52]; nonetheless, since details of cluster catalysis still have to be discovered, both the hypotesized mechanisms were taken into consideration hence investigated.

Following the methanol channel it must be considered that, according to preliminary calculations, the H atom residing on the platinum cluster is not able to protonate the oxygen atom of the methoxy group, meaning that this mechanism should involve the breaking of the C2-O bond with the migration of the OCH$_3$ fragment toward a platinum atom (that, as a consequence, become hexacoordinated in an octahedral environment), its protonation and subsequent desorption. In order to trigger the C-O bond breaking it was necessary to rearrange the dihydroeugenol adsorbed on the cluster; in Fig. 5 and in the following a structural rearrangement is indicated by the symbol ρ inside a circle. The new form of dihydroeugenol/Pt_{10} is ca. 25 kJ mol^{-1} less stable than the one produced by the allyl group saturation, but it shows the methoxy group correctly aligned with a platinum cluster edge. In order to verify the ease with which this rearrangement takes place, the minimum
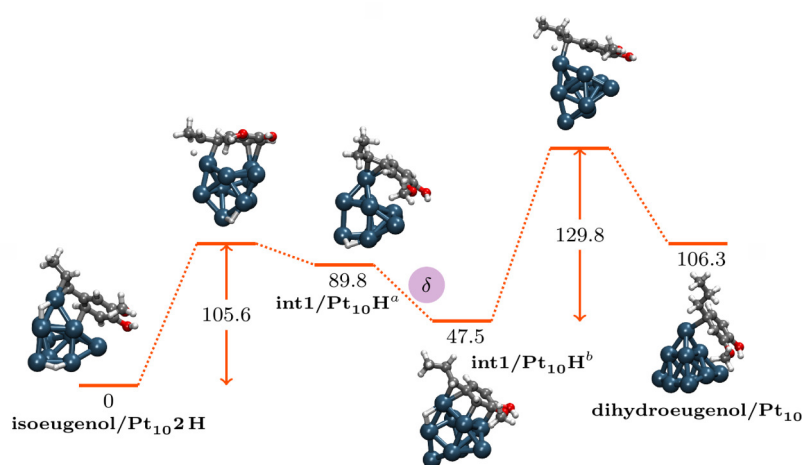

Fig. 4. Reaction profile of the steps involved in the isoeugenol catalytic hydrogenation to dihydroeugenol on the Pt_{10} cluster. The δ symbol inside a circle indicates an elementary step characterized by an assumed barrier-less diffusion of the H atom across the cluster toward the catalytic site.
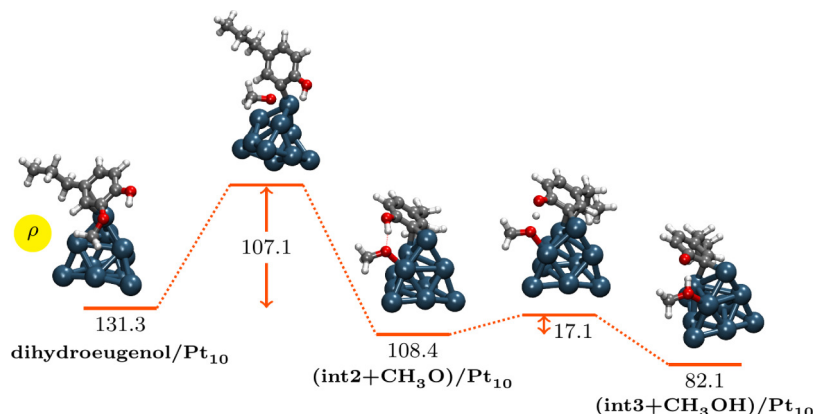
Fig. 5. Reaction profile related to the C 2-O bond cleavage and the subsequent formation of CH_3OH on the Pt_{10} cluster. The whole process takes place on the same potential energy surface of the first catalytic hydrogenation, implying that the energies of the intermediates refer to the isoeugenol/$Pt_{10}H_2$ system. The Greek letter ρ inside the circle indicates a structural rearrangement of dihydroeugenol on the cluster.

energy path connecting the two adsorption geometries of dihydroeugenol on the cluster was searched by using a nudged elastic band approach. The maximum along the path revealed an energy barrier of 34 kJ mol^{-1}, a value suggesting a good mobility of the adsorbed species. The rearrangement of dihydroeugenol prompts the shift of the OCH_3 moiety toward the cluster, with an energy barrier of 107.1 kJ mol^{-1}. It is interesting to note that in the resulting (int2+CH_3O)/Pt_{10} intermediate, the hydrogen bond, already observed in the most stable conformations of isoeugenol and dihydroeugenol and taking place between the hydroxyl H and the methoxy O centers, does not break. On the contrary, it is shortened from 2.13 to 1.63 Å. This allows the formation of methanol to occur almost instantly by H-shift from the hydroxyl group, without the intervention of catalyst activated hydrogen. Finally, a stabilizing H-bond (with length 1.47 Å) is present in the (int3+CH_3OH)/Pt_{10} product. As usual, this highlights a sharing of the H atom between the two oxygen atoms connected. The phenomen, presumably originated by the limited size of the Pt_{10} cluster and connected to its relatively high flexibility, was not taken into account before by experimental hypotheses, related to HDO reactions involving either isoeugenol or related compounds [53, 54]. This remark deserves to be underlined since implicitly emphasizes how catalytic processes on subnanometric clusters do not always follow the established rules of heterogeneous catalysis and conversely do represent a case by case chemistry to be investigated.

In order to proceed with the HDO reaction, the methanol molecule was desorbed from the cluster (desorption energy equal to 100.7 kJ mol^{-1}, with BSSE = 11.6 kJ mol^{-1}) and a new H_2 molecule was fragmented on it; the int3/Pt_{10}2H system so originated was used as starting point for the formation of an adsorbed 4-propylphenol species. In the optimized geometry, the int3 species interacts through the dangling O atom and the C2 of the benzene ring with the upper portion of one edge of the cluster, including one cap and one octahedron cage atom; therefore the aromatic portion, placed almost perpendicular to the cluster, does not interact significantly with it except for the single carbon atom indicated above. The migration of a H atom from the cluster to the oxygen atom of int3 (see Fig. 6) leads to the int4/$Pt_{10}H^a$ intermediate, which, after hydrogen diffusion, forms int4/$Pt_{10}H^b$. In the second elementary step, 4-propylphenol/Pt_{10} is finally formed. The interaction energy of this compound with the platinum cluster is 159.2 (BSSE = 9.3) kJ mol^{-1}.

The first elementary step of the reaction highlights that the hydrogenation of the oxygen atom is not a simple process because various factors, connected to each other, concur to the stabilization of the reacting system. Oxygen and, in particular, the radical C2 carbon atom give rise to strong bonds with platinum that have to be weakened for hydrogenation to take place. In fact, the energy barrier (171.6 kJ mol^{-1}) for this elementary event would be the highest of the whole process. This
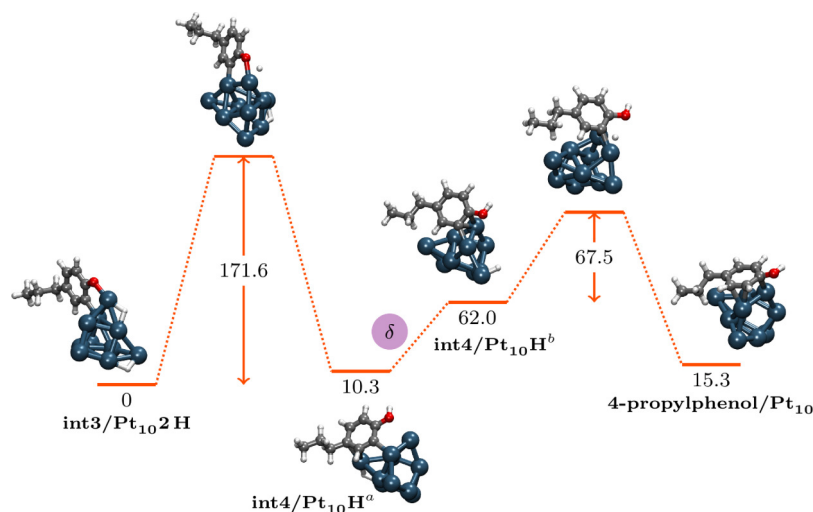

Fig. 6. Reaction profile showing the restoration of the -OH fragment and the formation of the adsorbed 4-propylphenol species. Energies of the reaction intermediates refer to the catalytic hydrogenation system obtained following the desorption of methanol and the placement of two new H atoms on the cluster. The letter δ indicates the rapid diffusion of one H atom through the cluster.

indeed seems to be the point in which significant bifurcations of the mechanism could occur: the hydrogen atom could migrate from the cluster towards the oxygen or the carbon atom. In the second case, the reduction of the benzene ring would be triggered, with oxygen maintaining the interaction of the fragment with the cluster. The hydrogenation of oxygen could take place subsequently, with the formation of 4-propylcyclohexanol. The investigation of this mechanism, along with possible parasite reactions and undesired products, will be the subject of future investigations.

In the present work, the purpose of which, as already said, is to detail the "direct" deoxygenation of isoeugenol, it was considered that the formation of the int4 intermediate could actually occur before the desorption of CH_3OH. Indeed, the hydrogen bond in $(int3+CH_3OH)/Pt_{10}$ could maintain the position of the dangling oxygen atom, inhibiting its interaction with platinum and making it available for hydrogenation. This is actually the case, since as can be seen from Fig. 7, the energy barrier to trasform $(int3+CH_3OH)/Pt_{10}2H$ to $(int4+CH_3OH)/Pt_{10}H$ is 129.6 kJ mol^{-1}, i.e. more than 40 kJ mol^{-1} lower than that occurring in the int3/$Pt_{10}2H$ to int4/$Pt_{10}H$ conversion. Moreover, the hydrogenation of the oxygen atom in $(int3+CH_3OH)/Pt_{10}2H$ occurs with an energy release of 57 kJ mol^{-1}, to be compared to the 10.3 kJ mol^{-1} of energy required for the same process in the absence of coadsorbed methanol. Since the hydrogen bond is weakened, methanol could desorb more easily from $(int4+CH_3OH)/Pt_{10}H$ (desorption energy of 76.1 kJ mol^{-1}, with BSSE equal to 9.7 kJ mol^{-1}), giving rise to int4/$Pt_{10}H^a$ (after a rearrangement releasing 7 kJ mol^{-1} of energy), which in turn can be hydrogenated to 4-propylphenol following the same path already depicted in Fig. 6. It is worth to note that the energy barrier for the first hydrogenation step sensibly decreases, due to the presence of coadsorbed methanol, but it still shows the highest barrier that was found along the DDO mechanism.

Let's now take into consideration the second channel for the formation of 4-propylphenol, the one resulting in the production of methane. Starting again from adsorbed and rearranged dihydroeugenol on Pt_{10}, the $O-CH_3$ bond breaking involves a energy barrier of 123.4 mol^{-1} (Fig. 8a), which is slightly higher than the one calculated for the methoxy group cleavage and gives a int2' intermediate coadsorbed with a methyl group. When two H atoms are inserted in the system, the methyl group, located atop a three-coordinated Pt atom, is easily hydrogenated to methane (Fig. 8b), which in turn easily desorbs. The int2' intermediate and one hydrogen atom are therefore left on the metal cluster; H-diffusion could let the two species react to form the O-H bond of a cathecol derivative, the 4-propylbenzene-1,2-diol, whose desorption would require 133.9 kJ mol^{-1} (BSSE = 27.1 kJ mol^{-1}) of energy. As reported in Fig. 8c, the cleavage of the OH group from this intermediate

occur by overcoming an energy barrier of 114.1 mol^{-1}, which is roughly the same as the one for the methoxy counterpart. The road to 4-propylphenol continues in Fig. 9, after that two further hydrogen atoms were added: water is promptly formed and, following H diffusion, the int3' intermediate is saturated to the phenol derivative.

Based on the energy barriers involved, it can be concluded that the two reaction paths leading from dihydroeugenol to 4-propylphenol on the Pt_{10} cluster can be considered essentialy competitive. However it must be taken into account that one more hydrogen molecule is consumed in the methane path, where the formation of $CH_4 + H_2O$ instead of CH_3OH occurs.

3.5. Formation of propylbenzene

The hydroxyl elimination process from 4-propylphenol consists of two elementary steps: the first involves the cleavage of the C1-O bond and the adsorption of the OH fragment on one face of the cluster; the second step is the hydrogenation of the OH and the desorption of a water molecule from the cluster. The reaction profile reported in Fig. 10a shows that the breaking of the C-O bond, with an energy barrier of 115.6 kJ mol^{-1}, is almost as easy as the hydrogenation reaction of the double bond, and that it leads to the formation of a slightly more stable system, here labelled as $(int5+OH)Pt_{10}$. On the other hand, from Fig. 10b it is evident that the passage of the H atom from the cluster to the OH is an easy process, being its energy barrier equal to 73.3 kJ mol^{-1}. The water molecule thus formed has a calculated desorption energy equal to 97.2 (BSSE = 18.9) kJ mol^{-1}. The last elementary process (Fig. 10c), showing an energy barrier of 92.7 kJ mol^{-1}, is the transfer of one H atom from the cluster to the phenyl C atom, which leads to the formation of the stable propylbenzene. The desorption energy of this species from the cluster is 152.9 (BSSE = 30.3) kJ mol^{-1}.

3.6. Total reduction of propylbenzene to propylcyclohexane

The reduction of the aromatic ring has attracted renewed attention in the chemical and petroleum industries, thanks to its application in the synthesis of a variety of useful chemical intermediates [55]. However, from an experimental point of view the development of highly efficient hydrogenation processes under mild and, hopefully, solvent-free conditions is still a challenge. From the computational side, however, a number of studies have made it possible to obtain a detailed description of the hydrogenation mechanism of benzene; the results have shown that it likely follows a Horiuti-Polanyi scheme [56], which involves the consecutive addition of hydrogen adatoms. Although there is a modest literature on benzene hydrogenation, nothing seems to be reported for propylbenzene; it can be easily argued, however, that its reduction to propylcyclohexane could occur through simple successive additions of hydrogen atoms, similarly to the benzene case. As a matter of fact, this mechanism must, in fact, be adapted to the specific hydrogenation process of phenyl, belonging to the propylbenzene adsorbed on Pt_{10}. This presents some difficulties, associated with various factors, the most evident of which is the impossibility of being able to discriminate, *a priori*, the most reactive carbon atoms of the ring on the basis of the electronic effects of the substituent (propyl chain). Furthermore, the addition of hydrogen, which can be defined as a "ghost" atom due to its size, does not allow one to confidently exploit the information that could be acquired by considering things in terms of steric hindrance. Therefore, not having firm theoretical or practical support, it was necessary to proceed with consecutive hydrogenations, taking into consideration every single carbon atom of the ring as a potential reactive site.

The results of our analysis regarding the total hydrogenation of propylbenzene on Pt_{10} are collected schematically in Scheme 1. In reading this scheme it must be noted that (i) the H atoms of propylbenzene are not showed; (ii) the circled numbers near a figure refer to the position of benzene ring where catalytic hydrogen will attach; (iii)
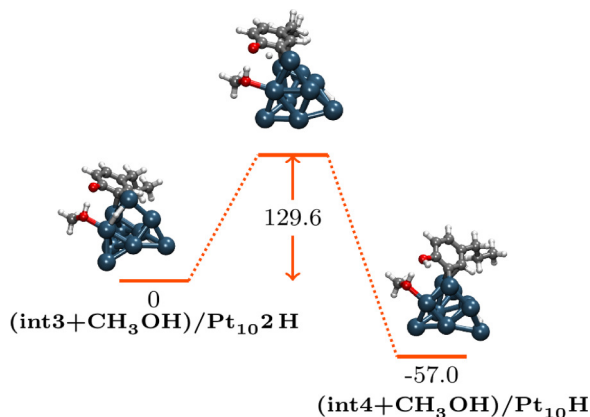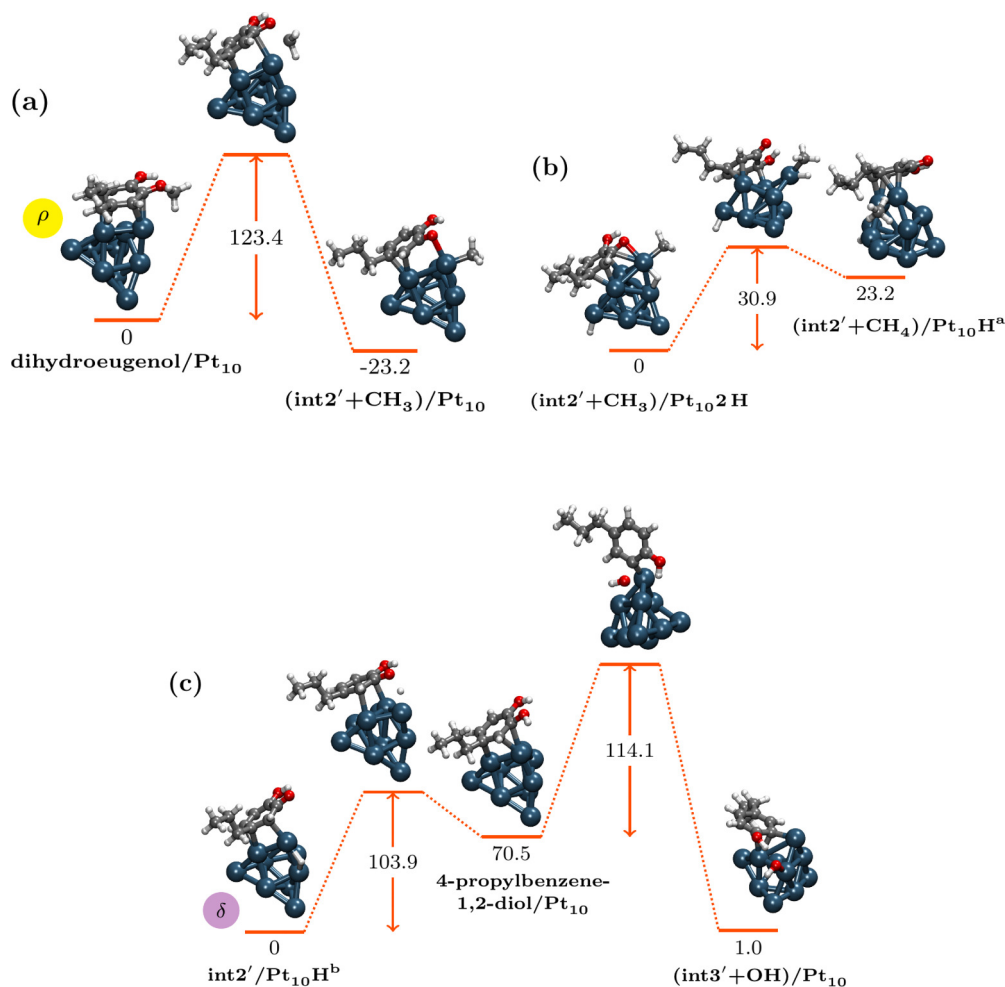

Fig. 7. The direct formation of the int4 intermediate from $(int3+CH_3OH)/Pt_{10}2H$ occurring by an elementary step where two hydrogen atoms are inserted in the cluster before methanol desorbs.

Fig. 8. DFT calculated reaction profile related to the $O - CH_3$ bond cleavage (a) and the formation of CH_4 (b) on the Pt_{10} cluster. The C2-O bond breaking occurs after the formation of a cathecol derivative as intermediate (c).

yellow circles represent carbon site directly interacting with the platinum atoms of the cluster; (iv) on the right of each figure the energy barrier and the energy of the product (relative to the reactant of the corresponding elementary step, the former, and to the starting reactant, the latter) are reported, separated by a semicolon; (v) two new H atoms are inserted in the system when needed for consecutive hydrogenations; (vi) the energetics of what is considered the kinetically and thermodinamically preferred hydrogenation path is reported inside a box and the corresponding structure is the reactant of the subsequent elementary step.

On the basis of the considerations above, for the first catalytic hydrogenation the passage of one H atom from the cluster to four chemically different C atoms of the propylbenzene ring was investigated, i.e. the carbon bearing the propyl group and the carbon atoms in *ortho-*, *meta-* and *para-* position to it. Therefore, four elementary steps were considered, and for each of them the structures of reagent, product and transition state were calculated. The results obtained show that the passage of the H atom from the cluster to the C of the ring occurs preferentially in position 2. This elementary step is favored, with respect to the other three, both at the kinetic and thermodynamic level since its activation barrier is equal to 94.3 kJ mol^{-1} and the intermediate obtained is the most stable. Then we proceeded, starting from intermediate **I**, with the second elementary step. In order to identify the second most reactive site, the hydrogenation of the residual unsaturated carbon atoms of the ring was investigated one at a time. It can be observed that the second elementary hydrogenation, for the same reasons as the previous one, takes place preferentially on C1. It has an energy barrier of

41.8 kJ mol^{-1}, much lower than the others obtained and it leads to the most stable product. It can be noted that the first catalytic hydrogenation on propylbenzene occurs in a similar way to hydrogenation of a double bond. It leads to the formation of a stable species, the 5-propyl-1,3-cyclohexadiene (**II**), whose desorption energy is 244.6 (BSSE = 26.2) kJ mol^{-1}.

The first elementary step of the second catalytic hydrogenation involved all the unsaturated carbon atoms of **II**. For each hypothetical reactive site, similarly to what was done previously, the reagent, product and transition state were estimated and optimized. The reaction scheme for the second catalytic hydrogenation highlights that the transfer of the first H atom preferentially takes place on the carbon in position 4. The resulting intermediate **III**, in which the electron density is delocalized on the remaining three carbon atoms of the ring, shows a thermodynamic stability similar to that found for the intermediate obtained by attaching one H atom in position 3; for the latter, however, there is a much higher energy barrier to overcome.

Starting from the semi-hydrogenated intermediate **III**, the passage of the second H atom from the cluster to carbon atoms 1, 2 and 3 of the ring, respectively, was investigated. The energies of the products and the energy barriers for each stage, however, do not allow us to discriminate which of the three elementary steps should occur preferentially, in either kinetic or thermodynamic terms. For this reason, the carbon atoms in position 1, 2 and 3 were considered equally reactive sites and, therefore, it was considered appropriate to continue with the third catalytic hydrogenation on each of them. This leads to the competing formation of two stable products, 3-propylcyclohexene **IV** and 4-
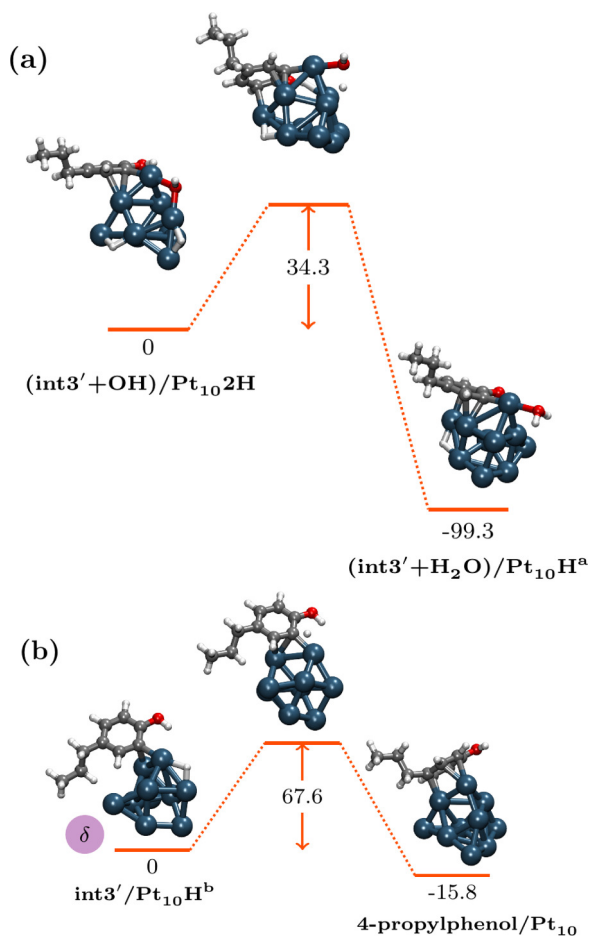
Fig. 9. The easy formation of the water molecule (a) and the saturation of int3′ to 4-propylphenol in the methane channel.

propylcyclohexene **VI**, which can desorb from the cluster with 196.8 (BSSE = 9.3) and 173.6 (BSSE = 26.3) kJ mol^{-1}, respectively. On the other hand, the intermediate **V**, which due to its diradicalic character has a stability comparable to that of **IV** and **VI**, evidently due to favorable interactions with platinum, cannot desorb from the cluster.

The first step of the third catalytic hydrogenation, involving 3-propylcyclohexene **IV**, shows that the transfer of the atom H from the cluster occurs preferentially on the C2 site of the ring. The activation barrier of path 2 is much lower than that of the alternative path; this allows us to indicate this as the favored path not only on a kinetic level, because the corresponding barrier is the lowest, but also from a thermodynamic point of view. The semi-hydrogenated intermediate **VII**, in fact, is more stable, by 17.1 kJ mol^{-1}, than the equivalent intermediate derived from path 1. The second H atom was therefore added on the last unsaturated carbon atom of intermediate **VII**, thus leading to the formation of propylcyclohexane **VIII** in the chair conformation. Its desorption energy from the cluster is 140.4 (BSSE = 19.6) kJ mol^{-1}.

The first elementary step of the third catalytic hydrogenation, involving intermediate **V** shows that the semi-hydrogenated intermediate **IX**, not only should form more rapidly because it has an activation barrier of about 24.7 kJ mol^{-1} lower than that pinpointed along the formation of the semi-hydrogenated intermediate resulting from the other path but it is also the most thermodynamically stable. Therefore, it was considered just the transfer of the second hydrogen atom on this intermediate. In this way propylcyclohexane **X** was obtained in a distorted boat conformation, the second more stable form of cyclohexane (desorption energy equal to 130.7 kJ mol^{-1} with BSSE = 22.4 kJ mol^{-1}).

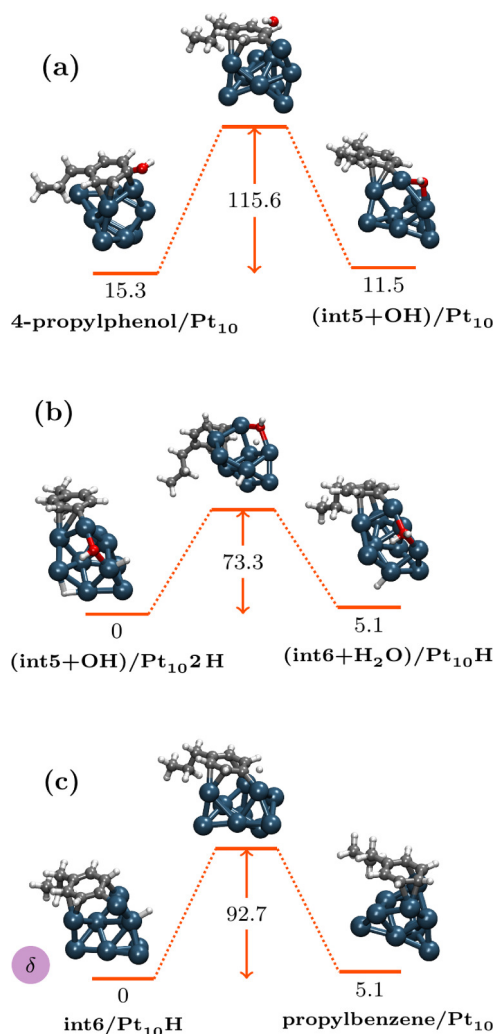Finally, as regards 4-propylcyclohexene **VI**, the preferred first

Fig. 10. Reaction profiles related to (a) the cleavage of the C1-OH bond, (b) the hydrogenation of the OH fragment adsorbed on one face of the cluster and (c) the passage of a H atom from the cluster to C1. In (c) the highlighted δ indicates the diffusion, following the desorption of the H$_2$O molecule, of the H atom through the cluster.

elementary step of the third catalytic hydrogenation has an energy barrier of 55.9 kJ mol^{-1} and gives the intermediate **XI**, even if it must be noticed that the species resulting from the other path is certainly more stable. The hydrogenation of **XI** create a distorted boat conformation of propylcyclohexane **XII**, whose desorption energy from the cluster is 108.1 (BSSE = 21.0) kJ mol^{-1}. Incidentally, at the level of theory used in this work, the chair and distorted boat conformations of propylcyclohexane differ by 25 kJ mol^{-1}, a value in agreement with the 21 kJ mol^{-1} reported in the literature for cyclohexane [57].

4. Conclusions and future directions

The present investigation, which is part of a more ambitious project, does not aim at rigorously compare theoretical and experimental data but to elucidate the HDO reaction mechanism on a standard metal, namely platinum, cluster (Pt$_{10}$) in order to identify the elementary steps and intermediate reaction routes, hence to outline the possible ramifications and parallel processes of greatest interst.

The investigated sequence of steps for isoeugenol HDO was the one experimental hypotesized for non-noble catalysts, according to which the first molecular fragment that undergoes catalytic hydrogenation is the double bond on the allyl chain, leading to dihydroeugenol, then the
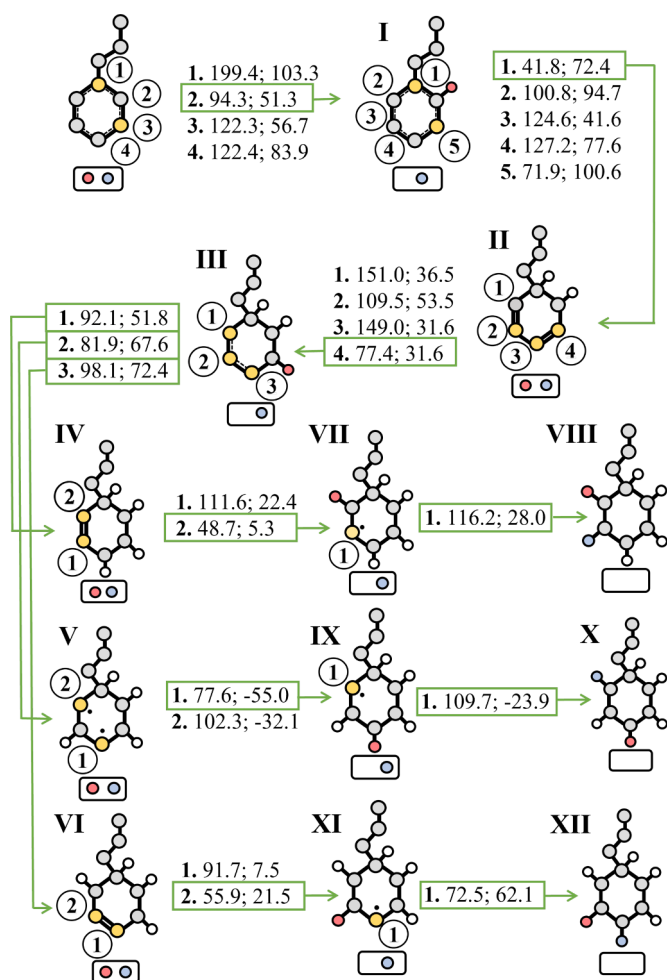
Scheme 1. Representation of the whole saturation of the benzene ring present in propylbenzene on the Pt_{10} cluster. The latter is represented by the small rectangle under the sketched molecular species; adsorbed hydrogen atoms are depicted as red and blue circles inside the rectangle, the not adsorbed ones are conversely not shown; yellow circles represent the interaction sites of the molecule with the cluster. In each entry, the first number is the position where catalytic hydrogen attaches, the second is the energy barrier of the corresponding elementary step, the third is the energy of the product, always referred to the reactant with two H atoms still on Pt_{10}. All energy values are expressed in kJ mol^{-1}. The first catalytic hydrogenation starts from propylbenzene, the second one from **II** (5-propyl-1,3-cyclohexadiene), the last one from **IV** (3-propylcyclohexene), **V** and **VI** (4-propylcyclohexene).

reaction proceeds through a direct deoxygenation mechanism. According to the reported results based on DFT calculations, the removal of the OCH$_3$ moiety following the route leading to the formation of methanol (which resulted essentially competitive to the one producing methane and water) would not take place by simple transfer of one hydrogen atom from the cluster to the methoxy group, but by cleavage of the C–O bond and subsequent hydrogenation of the chemisorbed fragment by the hydroxy group of the same substrate molecule. This would generate an intermediate where a dangling oxygen atom is stabilized by a very strong hydrogen bond with the coadsorbed methanol. If atomic hydrogen is available at this stage on the cluster, the hydrogenation of the intermediate above would first restore the hydroxyl group and subsequently form 4-propylphenol. On the contrary, if methanol desorbs before the hydrogenation of the dangling oxygen atom occurs, the intermediate would rearrange on the cluster to give a geometry where the interactions with the cluster would hamper the formation of 4-propylphenol, due to a very high energy barrier along the path. This point of the mechanism seems therefore to be crucial for the whole HDO to

propylcyclohexane and could constitute one of the step where the most significant bifurcations of the mechanism occur. Once formed, 4-propylphenol loses the OH group by cleavage of the C–OH bond and the subsequent hydrogenation of the fragment, which desorbs as water. When the aromaticity of the system is restored by transferring one hydrogen atom from the cluster to the unsaturated carbon, propylbenzene is formed. This, after three consecutive catalytic hydrogenations, leads finally to propylcyclohexane, in its distorted boat conformation. The whole process producing propylcyclohexane starting from isoeugenol:

$$C_{10}H_{12}O_2 + 6H_2 \rightarrow C_9H_{18} + CH_3OH + H_2O$$ is finally characterized by a calculated Gibbs free energy difference equal to -309.6 kJ mol^{-1}.

The present work can be considered as the starting point to investigate the possible different reaction paths characterizing HDO reactions on different metal clusters, in order to provide experimental chemists with useful tools (such as the identification of the largest number of secondary and/or parasitic products) for the optimization of the process conducted on a large scale.

Future perspectives are precisely (i) investigating the HYD channel for isoeugenol conversion to propylcyclohexane, (ii) investigating reaction paths potentially involved that lead to other products, such as propylcyclohexanol or benzene and cyclohexene derivatives originating by disproportionation of cyclohexadiene derivatives, as well as (iii) conducting the same reaction using non-noble and inexpensive metal catalysts, such as nickel, in order to determine their activity and selectivity with respect to those shown by the platinum clusters.

CRediT authorship contribution statement

Francesco Ferrante: Conceptualization, Methodology, Investigation, Data curation, Writing – review & editing, Supervision. **Chiara Nania:** Conceptualization, Data curation, Writing – review & editing, Project administration. **Dario Duca:** Investigation, Data curation, Writing – original draft, Visualization.

Declaration of Competing Interest

The authors declare that they have no known competing financial interests or personal relationships that could have appeared to influence the work reported in this paper.

Acknowledgments

References

[1] D. Mohan, C.U. Pittman, P.H. Steele, Pyrolysis of wood-biomass for bio-oil: a critical review, Energy Fuels 20 (2006) 848–889, https://doi.org/10.1021/ef0502397.

[2] S. Tieuli, P. Mäki-Arvela, M. Peurla, K. Eränen, J. Wärnà, G. Cruciani, F. Menegazzo, D.Y. Murzin, M. Signoretto, Hydrodeoxygenation of isoeugenol over Ni-SBA-15: kinetics and modelling, Appl. Catal. A 580 (2019) 1–10, https://doi.org/10.1016/j.apcata.2019.04.028.

[3] P. Mäki-Arvela, D. Murzin, Hydrodeoxygenation of lignin-derived phenols: from fundamental studies towards industrial applications, Catalysts 7 (2017) 265, https://doi.org/10.3390/catal7090265.

[4] D.C. Elliott, Transportation Fuels from Biomass via Fast Pyrolysis and Hydroprocessing, in: Advances in Bioenergy, John Wiley & Sons,Ltd., 2016, https://doi.org/10.1002/9781118957844.ch6.65–72.

[5] J. Feng, C.-Y. Hse, Z. Yang, K. Wang, J. Jiang, J. Xu, Liquid phase in situ hydrodeoxygenation of biomass-derived phenolic compounds to hydrocarbons over bifunctional catalysts, Appl. Catal. A 542 (2017) 163–173, https://doi.org/10.1016/j.apcata.2017.05.022.

[6] U. Heiz, E.L. Bullock, Fundamental aspects of catalysis on supported metal clusters, J. Mater. Chem. 14 (2004) 564–577, https://doi.org/10.1039/B313560H.

[7] G. Ertl, H.J. Freund, Catalysis and surface science, Phys. Today 52 (2008) 32, https://doi.org/10.1063/1.882569.

[8] G.A. Somorjai, The flexible surface: new techniques for molecular level studies of time dependent changes in metal surface structure and adsorbate structure during

catalytic reactions, J. Mol. Catal. A 107 (1996) 39–53, https://doi.org/10.1016/1381-1169(95)00227-8.

[9] F. Arena, F. Ferrante, R.D. Chio, G. Bonura, F. Frusteri, L. Frusteri, A. Prestianni, S. Morandi, G. Martra, D. Duca, DFT And kinetic evidences of the preferential CO oxidation pattern of manganese dioxide catalysts in hydrogen stream (PROX), Appl. Catal. B 300 (2022) 120715, https://doi.org/10.1016/j.apcatb.2021.120715.

[10] L. Gueci, F. Ferrante, A. Prestianni, F. Arena, D. Duca, Benzyl alcohol to benzaldehyde oxidation on MnO^x clusters: un- raveling atomistic features, Mol. Catal. 513 (2021) 111735, https://doi.org/10.1016/j.mcat.2021.111735.

[11] L. Gueci, F. Ferrante, A. Prestianni, R.D. Chio, T. Patti, D. Duca, F. Arena, DFT insights into the oxygen-assisted selective oxidation of benzyl alcohol on manganese dioxide catalysts, Inorg. Chim. Acta 511 (2020) 119812, https://doi.org/10.1016/j.ica.2020.119812.

[12] A. Prestianni, R. Cortese, F. Ferrante, R. Schimmenti, D. Duca, S. Hermans, D.Y. Murzin, α-d-glucopyranose adsorption on a pd$_{30}$ cluster supported on boron nitride nanotube, Top. Catal. 59 (2016) 1178–1184, https://doi.org/10.1007/s11244-016-0638-3.

[13] F. Ferrante, A. Prestianni, R. Cortese, R. Schimmenti, D. Duca, Density functional theory investigation on the nucleation of homo- and heteronuclear metal clusters on defective graphene, J. Phys. Chem. C 120 (2016) 12022–12031, https://doi.org/10.1021/acs.jpcc.6b02833.

[14] R. Schimmenti, R. Cortese, F. Ferrante, A. Prestianni, D. Duca, Growth of sub-nanometric palladium clusters on boron nitride nanotubes: a DFT study, Phys. Chem. Chem. Phys. 18 (2016) 17450–11757.

[15] A. Prestianni, F. Ferrante, E.M. Sulman, D. Duca, Density functional theory investigation on the nucleation and growth of small palladium clusters on a hyper-cross-linked poly-styrene matrix, J. Phys. Chem. C 118 (2014) 21006–21013, https://doi.org/10.1021/jp506320z.

[16] C. Dong, Y. Li, D. Cheng, M. Zhang, J. Liu, Y.-G. Wang, D. Xiao, D. Ma, Supported metal clusters: fabrication and application in heterogeneous catalysis, ACS Catal. 10 (2020) 11011–11045, https://doi.org/10.1021/acscatal.0c02818.

[17] B.J. Holliday, Surface and interfacial organometallic chemistry and catalysis. Topics in organometallic chemistry, J. Am. Chem. Soc. 129 (2007) 3772–3773, https://doi.org/10.1021/ja0697065.

[18] K. Koichumanova, A.K.K. Vikla, R. Cortese, F. Ferrante, K. Seshan, D. Duca, L. Lefferts, In situ ATR-IR studies in aqueous phase reforming of hydroxyacetone on Pt/ZrO$_2$ and pt/AlO(OH) catalysts: the role of aldol condensation, Appl. Catal. B 232 (2018) 454–463, https://doi.org/10.1016/j.apcatb.2018.03.090.

[19] R. Cortese, R. Schimmenti, F. Ferrante, A. Prestianni, D. Decarolis, D. Duca, Graph-based analysis of ethylene glycol decomposition on a palladium cluster, J. Phys. Chem. C 121 (2017) 13606–13616, https://doi.org/10.1021/acs.jpcc.7b00850.

[20] H. Zhai, A.N. Alexandrova, Fluxionality of catalytic clusters: when it matters and how to address it, ACS Catal. 7 (2017) 1905–1911, https://doi.org/10.1021/acscatal.6b03243.

[21] H. Häkkinen, S. Abbet, A. Sanchez, U. Heiz, U. Landman, Structural, electronic, and impurity-doping effects in nanoscale chemistry: supported gold nanoclusters, Angew. Chem. Int. Ed. Eng. 42 (2003) 1297–1300, https://doi.org/10.1002/anie.200390334.

[22] S.M. Lang, T.M. Bernhardt, Gas phase metal cluster model systems for heterogeneous catalysis, Phys. Chem. Chem. Phys. 14 (2012) 9255–9269, https://doi.org/10.1039/C2CP40660H.

[23] O. Hübner, H.J. Himmel, Metal cluster models for heterogeneous catalysis: a matrix-isolation perspective, Chem. Eur. J. 24 (2018) 8941–8961, https://doi.org/10.1002/chem.201706097.

[24] M. Hellinger, H.W.P. Carvalho, S. Baier, D. Wang, W. Kleist, J.D. Grunwaldt, Catalytic hydrodeoxygenation of guaiacol over platinum supported on metal oxides and zeolites, Appl. Catal. A 490 (2015) 181–192, https://doi.org/10.1016/j.apcata.2014.10.043.

[25] H. Lee, H. Kim, M.J. Yu, C.H. Ko, J.K. Jeon, J. Jae, S.H. Park, S.C. Jung, Y.K. Park, Catalytic hydrodeoxygenation of bio-oil model compounds over Pt/HY catalyst, Sci. Rep. 6 (2016) 28765, https://doi.org/10.1038/srep28765.

[26] A. Bielić, M. Grilc, B. Likozar, Catalytic hydrogenation and hydrodeoxygenation of lignin-derived model compound eugenol over Ru/C: intrinsic microkinetics and transport phenomena, Chem. Eng. J. 333 (2018) 240–2659, https://doi.org/10.1016/j.cej.2017.09.135.

[27] D. Duca, F. Frusteri, A. Parmaliana, G. Deganello, Selective hydrogenation of acetylene in ethylene feedstocks on Pd catalysts, Appl. Catal. A 146 (1996) 269–284, https://doi.org/10.1016/S0926-860X(96)00145-7.

[28] R. Schimmenti, R. Cortese, L. Godina, A. Prestianni, F. Ferrante, D. Duca, D.Y. Murzin, A combined theoretical and experimental approach for platinum catalyzed 1,2-propanediol aqueous phase reforming, J. Phys. Chem. C 121 (2017) 14636–14648, https://doi.org/10.1021/acs.jpcc.7b03716.

[29] M.J. Frisch, G.W. Trucks, H.B. Schlegel, G.E. Scuseria, M.A. Robb, J.R. Cheeseman, G. Scalmani, V. Barone, G.A. Petersson, H. Nakatsuji, X. Li, M. Caricato, A. V. Marenich, J. Bloino, B.G. Janesko, R. Gomperts, B. Mennucci, H.P. Hratchian, J. V. Ortiz, A.F. Izmaylov, J.L. Sonnenberg, D. Williams-Young, F. Ding, F. Lipparini, F. Egidi, J. Goings, B. Peng, A. Petrone, T. Henderson, D. Ranasinghe, V. G. Zakrzewski, J. Gao, N. Rega, G. Zheng, W. Liang, M. Hada, M. Ehara, K. Toyota, R. Fukuda, J. Hasegawa, M. Ishida, T. Nakajima, Y. Honda, O. Kitao, H. Nakai, T. Vreven, K. Throssell, J.A. Montgomery Jr., J.E. Peralta, F. Ogliaro, M. J. Bearpark, J.J. Heyd, E.N. Brothers, K.N. Kudin, V.N. Staroverov, T.A. Keith, R. Kobayashi, J. Normand, K. Raghavachari, A.P. Rendell, J.C. Burant, S.S. Iyengar, J. Tomasi, M. Cossi, J.M. Millam, M. Klene, C. Adamo, R. Cammi, J.W. Ochterski, R.L. Martin, K. Morokuma, O. Farkas, J.B. Foresman, D.J. Fox, Gaussian, Revision C.01 16 (2016).

[30] A.D. Becke, A new mixing of Hartree-Fock and local density functional theories, J. Chem. Phys. 98 (1993) 1372–1377, https://doi.org/10.1063/1.464304.

[31] S. Grimme, J. Antony, S. Ehrlich, H. Krieg, A consistent and accurate ab initio parametrization of density functional dispersion correction (DFT-D) for the 94 elements H-Pu, J. Chem. Phys. 132 (2010) 154104, https://doi.org/10.1063/1.3382344.

[32] T.H. Dunning, Gaussian basis sets for use in correlated molecular calculations. I: the atoms boron through neon and hydrogen, J. Chem. Phys. 90 (1989) 1007–1023, https://doi.org/10.1063/1.456153.

[33] P.J. Hay, W.R. Wadt, Ab initio effective core potentials for molecular calculations. potentials for K to Au including the outermost core orbitals, J. Chem. Phys. 82 (1985) 299–310, https://doi.org/10.1063/1.448975.

[34] P.J. Hay, W.R. Wadt, Ab initio effective core potentials for molecular calculations, potentials for the transition metal atoms Sc to Hg, J. Chem. Phys. 82 (1985) 270–283, https://doi.org/10.1063/1.448799.

[35] T.H. Dunning, P.J. Hay, Gaussian basis sets for molecular calculations, in: H. F. Schaefer (Ed.), Methods of Electronic Structure Theory, Modern Theoretical Chemistry pp. 1–27., Springer US, 1977.

[36] B.P. Pritchard, D. Altarawy, B. Didier, T.D. Gibson, T.L. Windus, New basis set exchange: an open, up-to-date resource for the molecular sciences community, J. Chem. Inf. Model. 59 (2019) 4814–4820, https://doi.org/10.1021/acs.jcim.9b00725.

[37] M. Bertini, F. Ferrante, D. Duca, Empathes: a general code for nudged elastic band transition states search, Comp. Phys. Commun. 271 (2022) 108224, https://doi.org/10.1016/j.cpc.2021.108224.

[38] G. Henkelman, B.P. Uberuaga, H. Jonsson, A Climbing Image Nudged Elastic Band Method for Finding Saddle Points and Minimum Energy Paths, J. Chem. Phys. 113 (2000) 9901, https://doi.org/10.1063/1.1329672.

[39] S.F. Boys, F. Bernardi, The calculation of small molecular interactions by the differences of separate total energies. Some procedures with reduced errors, Mol. Phys. 19 (1970) 553–566, https://doi.org/10.1080/00268977000101561.

[40] M. Brack, Metal clusters and magic numbers, in: Scientific American 277, publisher: Scientific American, a division of Nature America, Inc, 1997, pp. 50–55. http://www.jstor.org/stable/24996042.

[41] R.B. King, Applications of Graph Theory and Topology in Inorganic Cluster and Coordination Chemistry, CRC Press, 1992.Ch. 6.4.E, p. 94

[42] I. Demiroglu, K. Yao, H.A. Hussein, R.L. Johnston, DFT global optimization of gas-phase subnanometer Ru-Pt clusters, J. Phys. Chem. C 121 (2017) 10773–10780, https://doi.org/10.1021/acs.jpcc.6b11329.

[43] C. Lindfors, P. Mki-Arvela, P. Paturi, A. Aho, K. Eränen, J. Hemming, M. Peurla, D. Kubiäka, I.L. Simakova, D.Y. Murzin, Hydrodeoxygenation of isoeugenol over Ni- and Co-supported catalysts, ACS Sustain. Chem. Eng. 7 (2019) 14545–14560, https://doi.org/10.1021/acssuschemeng.9b02108.

[44] F. Ferrante, A. Prestianni, M. Bertini, D. Duca, H$_2$ Transformations on graphene supported palladium cluster: DFT-MD simulations and NEB calculations, Catalysts 10 (2020) 1306, https://doi.org/10.3390/catal10111306.

[45] V. D'Anna, D. Duca, F. Ferrante, G. La Manna, DFT Studies on catalytic properties of isolated and carbon nanotube supported Pd$_9$ cluster: part II. hydro-isomerization of butene isomers, Phys. Chem. Chem. Phys. 12 (2010) 1323–1330, https://doi.org/10.1039/b920949m.

[46] V. DAnna, D. Duca, F. Ferrante, G.L. Manna, DFT studies on catalytic properties of isolated and carbon nanotube supported Pd9 cluster - I: adsorption, fragmentation and diffusion of hydrogen, Phys. Chem. Chem. Phys. 11 (2009) 4077–4083, https://doi.org/10.1039/b820707k.

[47] G. Barone, D. Duca, F. Ferrante, G.L. Manna, CASSCF/CASPT2 analysis of the fragmentation of H$_2$ on a Pd$_4$ cluster, Int. J. Quant. Chem. 110 (2010) 558–562, https://doi.org/10.1002/qua.22119.

[48] M.T. de M. Cruz, J.W. de M. Carneiro, D.A.G. Aranda, M. Bühl, Density functional theory study of benzene adsorption on small pd and pt clusters, J. Phys. Chem. C 111 (2007) 11068–11076, https://doi.org/10.1021/jp072572c.

[49] F. Mittendorfer, C. Thomazeau, P. Raybaud, H. Toulhoat, Adsorption of unsaturated hydrocarbons on Pd(111) and Pt(111): a DFT study, J. Phys. Chem. B 107 (2003) 12287–12295, https://doi.org/10.1021/jp035660f.

[50] R. Shu, R. Li, B. Lin, C. Wang, Z. Cheng, Y. Chen, A review on the catalytic hydrodeoxygenation of lignin-derived phenolic compounds and the conversion of raw lignin to hydrocarbon liquid fuels, Biomass Bioenergy 132 (2020) 105432, https://doi.org/10.1016/j.biombioe.2019.105432.

[51] D. Gao, Y. Xiao, A. Varma, Guaiacol hydrodeoxygenation over platinum catalyst: reaction pathways and kinetics, Ind. Eng. Chem. Res. 54 (2015) 10638–10644, https://doi.org/10.1021/acs.iecr.5b02940.

[52] T. Nimmanwudipong, C. Aydin, J. Lu, R.C. Runnebaum, K.C. Brodwater, N. D. Browning, D.E. Block, B.C. Gates, Selective hydrodeoxygenation of guaiacol catalyzed by platinum supported on magnesium oxide, Catal. Lett. 142 (2012) 1190–1196, https://doi.org/10.1007/s10562-012-0884-3.

[53] M. Alda-Onggar, P. Mäki-Arvela, K. Eränen, A. Aho, J. Hemming, P. Paturi, M. Peurla, M. Lindblad, I.L. Simakova, D.Y. Murzin, Hydrodeoxygenation of isoeugenol over alumina-supported Ir, Pt, and Re catalysts, ACS Sustain. Chem. Eng. 6 (2018) 16205–16218, https://doi.org/10.1021/acssuschemeng.8b03035.

[54] L. Bomont, M. Alda-onggar, V. Fedorov, A. Aho, J. Peltonen, K. Eränen, M. Peurla, N. Kumar, J. Wärna, V. Russo, P. Mäkiarvela, H. Grnman, M. Lindblad, D. Y. Murzin, Production of cycloalkanes in hydrodeoxygenation of isoeugenol over Pt- and Ir-modified bifunctional catalysts, Eur. J. Inorg. Chem. 2018 (2018) 2841–2854, https://doi.org/10.1002/ejic.201800391.

[55] H. Liu, R. Fang, Z. Li, Y. Li, Solventless hydrogenation of benzene to cyclohexane over a heterogeneous Ru-Pt bimetallic catalyst, Chem. Eng. Sci. 122 (2015) 350–359, https://doi.org/10.1016/j.ces.2014.09.050.

[56] M. Saeys, M.-F. Reyniers, M. Neurock, G.B. Marin, Ab initio reaction path analysis of benzene hydrogenation to cyclohexane on Pt(111), J. Phys. Chem. B 109 (2005) 2064–2073, https://doi.org/10.1021/jp049421j.

[57] J. Clayden, N. Greeves, S. Warren, Organic Chemistry, OUP Oxford, 2012.

Chiara Nania
Dipartimento di Fisica e Chimica "E. Segrè"
Università degli Studi di Palermo
chiara.nania@unipa.it

HDO DELL'ISOEUGENOLO SU CLUSTER DI PLATINO

L'attività di ricerca legata al "Premio Pier Luigi Nordio 2022" della Divisione di Chimica Teorica e Computazionale della Società Chimica Italiana ha riguardato lo studio meccanicistico - con i metodi della chimica computazionale supportati da analisi cinetiche - della reazione di idrodeossigenazione, HDO, dell'isoeugenolo su cluster di platino. Il processo HDO è attualmente una delle vie più promettenti per l'ottenimento di biocarburanti.
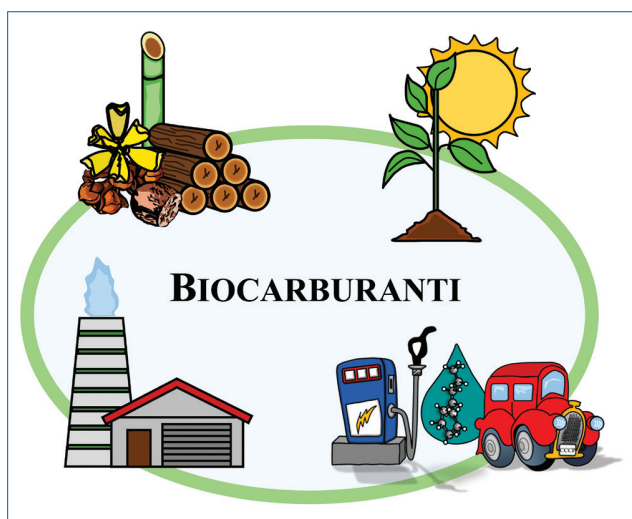
Ciclo di vita, produzione ed utilizzo, di un biocarburante

La ricerca per la quale ho ricevuto il "Premio Pier Luigi Nordio 2022" riguarda la conversione catalitica della biomassa in idrocarburi saturi, composti aventi caratteristiche termodinamiche idonee a sostituire i combustibili convenzionali derivanti da fonti fossili. Il mio lavoro si è focalizzato sull'investigazione, mediante un approccio atomistico basato sulla teoria del funzionale della densità, DFT, del meccanismo della reazione di idrodeossigenazione, HDO, dell'isoeugenolo - composto presente nella biomassa lignocellulosica - su un cluster subnanometrico di platino. Tale studio è stato oggetto della mia tesi di laurea magistrale, che ho svolto presso il Centro di Chimica Computazionale dell'Università degli Studi di Palermo,

CCCP, sotto la supervisione dei proff. Francesco Ferrante e Dario Duca, da decenni impegnati nello studio di processi catalitici con approcci teorico computazionali.

La reazione HDO di bio-oli è centrale nell'attuale panorama globale segnato dalla crisi energetica, che ha determinato un aumento della domanda di alternative rinnovabili e sostenibili nella produzione di prodotti chimici ed energia. Sebbene l'energia solare, idroelettrica, eolica e geotermica siano fonti di energia rinnovabile, la biomassa costituisce l'unica fonte rinnovabile che sia simultaneamente di facile accesso e ricca di derivati del carbonio e che, in ultima analisi, sia quindi in grado di offrire una facile e graduale transizione nell'impiego delle attuali tecnologie energetiche, basate sull'utilizzo di derivati carboniosi. Negli ultimi anni l'utilizzo della biomassa e dei biocombustibili - questi ultimi identificabili quali vettori di energia ottenuti dalla trasformazione delle biomasse - ha avuto un riscontro considerevole a livello ambientale, portando ad una significativa riduzione dell'emissione di gas serra, prodotti dallo sfruttamento massivo e prolungato dei combustibili fossili e/o di loro derivati.

Le biomasse, analogamente alle fonti fossili, producono energia grazie alla loro combustione, ma l'anidride carbonica che emettono è quella catturata in atmosfera dalle piante, usate nella produzione della biomassa, e successivamente trasformata dalle stesse, mediante il processo di fotosintesi clorofilliana, nella materia organica di cui si compongono. Ciò significa che nella fase di

combustione si emette tanta CO_2 quanta è stata assorbita dalle piante nella fase di crescita e il bilancio emissivo netto è potenzialmente pari a zero, *Carbon Neutrality*.

Le strutture polimeriche che costituiscono la biomassa però devono essere degradate e scomposte, depolimerizzate, per essere successivamente lavorate e usate come prodotti chimici e combustibili. A questo scopo, si effettua la pirolisi della biomassa che conduce alla formazione dei bio-oli, che però non possono essere usati direttamente come combustibili; ciò, a causa della loro acidità, dell'elevato contenuto di ossigeno e di un'intrinseca instabilità che li caratterizza. L'elevato contenuto di ossigeno, in particolare, li penalizza rispetto ai distillati del petrolio quali carburanti d'uso per i mezzi di trasporto. Tuttavia, la loro naturale forma liquida (in condizioni SATP) ne facilita l'ulteriore lavorazione, rendendo la raffinazione del biopetrolio in idrocarburi liquidi un processo importante da realizzare. Negli ultimi decenni sono stati ampiamente studiati diversi percorsi catalitici di idrogenazione e deossigenazione dei bio-oli, ma tra questi i processi HDO sono considerati gli approcci più efficaci per la conversione di biopetrolio in biocarburante.

Sebbene esistano molti studi su HDO di bio-oli, al fine di facilitare l'analisi del meccanismo di reazione, si preferisce, in genere, sostituire i bio-oli, estremamente complessi, con modelli più semplici, costituiti da composti lignici monomerici. Tra questi, un composto di rilievo è l'isoeugenolo (Fig. 1b), componente base dell'olio essenziale dei chiodi di garofano, della noce moscata e dello ylang-ylang. La scelta di tale modello come substrato per la reazione è stata suggerita dal fatto che i suoi gruppi funzionali sono quelli più comuni nei bio-oli derivati dalla lignina. È stato inoltre dimostrato che l'uso di metalli, in particolare di metalli del gruppo del Pt, in reazioni HDO di composti fenolici fornisce alte rese in idrocarburi. Per tale ragione, ho scelto come modello di catalizzatore un cluster di platino (Fig. 1a), nell'intento di unire le qualità riconosciute di standard in processi di idrogenazione del Pt con la forma molecolare di cluster subnanometrico, auspicabilmente di elevata efficienza catalitica.

Uno degli aspetti più rilevanti nello studio della reazione HDO riguarda l'ordine in cui avvengono le
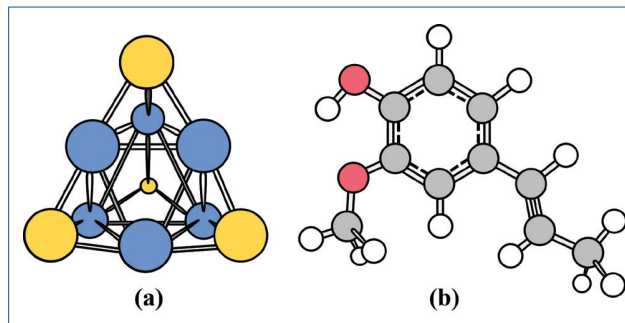

Fig. 1 - a) Cluster Pt10, modello di catalizzatore subnanometrico. La struttura evidenzia la presenza di atomi di platino con differente numero di coordinazione: i quattro atomi (in giallo) ai vertici del tetraedro hanno numero di coordinazione tre, i restanti sei atomi (in blu) hanno numero di coordinazione sei; b) struttura molecolare della conformazione più stabile del *trans*-isoeugenolo. Adattato da F. Ferrante *et al.*, *Mol. Catal.*, 2022, **529**, 112541, DOI: **https://doi.org/10.1016/j.mcat.2022.112541**

fasi di idrogenazione e deossigenazione. Entrambe sono necessarie per ottenere biocarburanti, ma la deossigenazione assume un ruolo primario. Essa comporta la rimozione dei gruppi ossigenati, -OH, $-OCH_3$, nell'isoeugenolo che sono responsabili dell'instabilità dei bio-oli. Sono stati proposti due percorsi per i meccanismi di idrodeossigenazione: a) idrogenazione-attraverso-deossigenazione (*Hydrodeoxygenation through Deoxygenation*, HYD), in cui avviene dapprima l'idrogenazione dell'anello aromatico e poi la rimozione dei componenti ossigenati mediante scissione dei legami C-O dall'anello idrocarburico saturo; b) deossigenazione diretta (*Direct Deoxygenation*, DDO) che comporta la scissione del legame Ar-O tramite idrogenolisi senza saturazione del gruppo arilico, Ar.

Diversi studi sperimentali e computazionali suggeriscono la predominanza di un meccanismo piuttosto che un altro a seconda del metallo considerato. Indipendentemente da questa variabile, l'uso di cluster introduce ulteriori potenziali modifiche nell'attività catalitica in quanto i processi su cluster non sempre si allineano ai corrispondenti processi catalitici su superficie estesa e, al contrario, presentano una chimica da indagare caso per caso, nell'ambito di un dato metallo. Per questo motivo, è stata effettuata una mappatura di entrambi i meccanismi per la reazione HDO dell'isoeugenolo su Pt_{10}. In ciascun meccanismo, come illustrato dalla Fig. 2, la presenza di due gruppi ossigenati e l'ordine, così come la forma chimica, con cui la loro
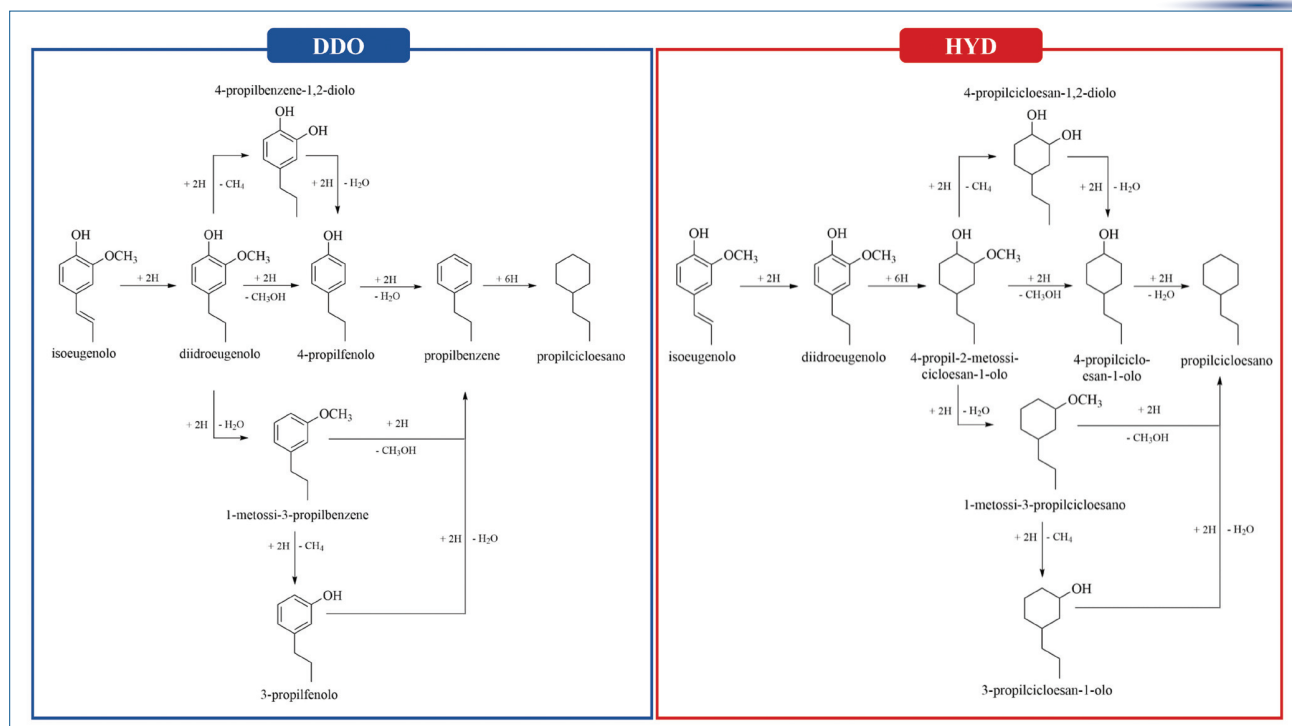
Fig. 2 - Meccanismo DDO e HYD per la conversione catalitica dell'isoeugenolo a propilcicloesano

rimozione dall'anello saturo (meccanismo HYD) o insaturo (meccanismo DDO) avviene, suggeriscono differenti percorsi di reazione per l'ottenimento del propilcicloesano. L'energetica dei quattro percorsi nei due meccanismi alternativi suggerisce, sulla base esclusiva delle barriere energetiche, che nei primi stadi elementari, in seguito alla formazione del diidroeugenolo, non vi è alcuna predominanza di un meccanismo rispetto all'altro. Tuttavia, nel meccanismo HYD gli stadi di deossigenazione sembrerebbero più difficili, in quanto presentano barriere energetiche più elevate di circa 40-50 kJ mol^{-1} rispetto ai corrispettivi stadi del meccanismo DDO. L'informazione DFT è stata usata per un'analisi microcinetica all'equilibrio che impiegava un nuovo approccio, *Simplified Christiansen Method* (SCM), ispirato allo schema algebrico di Christiansen, già applicato per analisi cinetiche di risultati catalitici sperimentali, e sviluppato dal gruppo CCCP dell'Università di Palermo. Usando come *input* i valori DFT delle barriere energetiche dirette ed inverse caratterizzanti la formazione delle diverse specie di superficie e l'energia di adsorbimento e desorbimento di reagenti e prodotti, l'approccio SCM ha restituito le costanti cinetiche dei diversi percorsi alle temperature selezionate. L'analisi ha quindi rivelato che le quattro vie di reazione nel meccanismo DDO sono significativamente più veloci delle corrispettive nel meccanismo HYD in

un range di temperatura 477-873 K. In particolare, all'interno del meccanismo DDO, il percorso che conduce al propilcicloesano attraverso il 4-propilfenolo è quello favorito. L'analisi SCM ha così permesso di concretizzare le preliminari indicazioni, ricavabili sulla base della valutazione dell'energetica dei processi di superficie, che identificavano il DDO come meccanismo più probabile per la reazione HDO dell'isoeugenolo su Pt$_{10}$.

Ringraziamenti

HDO of Isoeugenol on Platinum Cluster
The research activity related to the "Pier Luigi Nordio 2022 Prize" of the Theoretical and Computational Chemistry Division of the Italian Chemical Society involved the mechanistic investigation - using the methods of computational chemistry supported by kinetic analysis - of the isoeugenol hydrodeoxygenation, HDO, reaction on a platinum cluster, which is currently one of the most promising routes for obtaining biofuels.

PAPER

Check for updates

DFT insights into competing mechanisms of guaiacol hydrodeoxygenation on a platinum cluster†

Chiara Nania, Marco Bertini, [ID] Laura Gueci, [ID] Francesco Ferrante [ID] * and Dario Duca

In a scenario of declining fossil resources and increasing demand for renewable and sustainable alternatives, biomass is the only source able to offer an easy and gradual transition in the use of current energy technologies based on the exploitation of carbon derivatives. Its conversion to liquid fuels has oriented our study towards the computational mechanistic analysis of the guaiacol catalytic hydrodeoxygenation, which is currently considered one of the most challenging routes for upgrading biomass-derived bio-oils. For this purpose, a subnanometric Pt_{10} platinum cluster was chosen as the catalyst model, with Pt as a computational reference element for catalytic hydrogenation, and guaiacol as a model compound of bio-oils. DFT calculations revealed that the energy barriers related to the cleavage of $C(sp^2)$–O bonds in the direct deoxygenation mechanism are significantly lower (by an average of 60 kJ mol^{-1}) than those in the deoxygenation-through-hydrogenation mechanism in which $C(sp^3)$–O bond breaking from a saturated ring occurs. Even if the ring hydrogenation is easier in the oxygenated compound, the analysis reveals that the direct deoxygenation mechanism is favoured at all temperatures. Furthermore, the results obtained highlight that, from a thermodynamic perspective, the removal of oxygen groups preferentially occurs by the elimination of the $-OCH_3$ fragment as methanol and then of the $-OH$ fragment as a water molecule.

1 Introduction

Currently, fossil fuels are the main source of energy because of their good anti-knocking properties, and high calorific and heating values; however, reserves are limited.[1,2] In this scenario, renewable energy sources offer great potential to complement the depleting energy reserves and to significantly decrease the anthropogenic greenhouse gas (GHG) emissions into the atmosphere.[1,3] Among alternative energy sources, lignocellulosic biomass (LC) has received amplified attention during the last decade because it represents the most abundant reservoir of renewable carbon that is easily accessible on earth.[4] It could provide a viable means of reducing the GHG impact of fossil fuels in the transportation sector.[1,5] Fast pyrolysis is a promising method to convert solid biomass into liquid bio-oils

in the absence of oxygen.[6,7] However, the bio-oils produced by pyrolysis are a complex mixture of oxygenated components and, as such, have neither the chemical nor physical properties to compete with petroleum distillates as a transportation fuel.[8] However, their liquid form facilitates further processing making bio-oils key intermediates in the conversion of biomass to hydrocarbon products. Although these exhibit mainly cyclic structures, rather than linear chains as in petroleum, their use should not be limited by this characteristic.[9]

In this context, catalytic hydrodeoxygenation (HDO) is considered to be one of the most challenging processes for upgrading LC biomass-derived bio-oils.[10] Although a number of bio-oil HDO processes have been studied,[5,11] bio-oils derived from different feedstocks typically consist of more than 400 different organic compounds, which significantly complicates the study of catalytic activities and reaction pathways of the involved processes. Hence, it is important to select model compounds that represent the raw bio-oils for providing basic insight into the HDO process.

One of the most relevant aspects in the study of HDO concerns the order in which the hydrogenation and deoxygenation steps occur. Both of them are necessary to obtain biofuels, but deoxygenation has a primary role, actually involving the

Dipartimento di Fisica e Chimica, Università degli Studi di Palermo, Viale delle Scienze Ed. 17, 90128 Palermo, Italy. E-mail: francesco.ferrante@unipa.it; Fax: +39 091 590015; Tel: +39 091 23897979

† Electronic supplementary information (ESI) available: Additional figures reporting elementary steps for HYD and DDO mechanisms (S1–S4). Gibbs free energy variations for all elementary steps; and Gibbs free energy variations for molecule desorption. Detailed results from the application of a modified Christiansen method. See DOI: https://doi.org/10.1039/d2cp06077a

10460 | *Phys. Chem. Chem. Phys.*, 2023, **25**, 10460–10471

This journal is © the Owner Societies 2023

removal of oxygenated groups (such as –OH and –OCH$_3$) which are responsible for the instability of the bio-oils. Generally, two paths have been proposed for the hydrodeoxygenation mechanisms: (a) deoxygenation-through-hydrogenation (HYD) in which aromatic ring hydrogenation occurs first, followed by the removal of oxygen *via* C–O hydrogenolysis from the saturated hydrocarbon ring; (b) direct deoxygenation (DDO) which involves cleavage of the Ar–O bond *via* hydrogenolysis before ring saturation.[12–15]

Several catalysts have been applied for HDO of phenolic compounds,[16–18] *e.g.* metals supported on carbon nanostructures, zeolites, carbides, oxides, and even bifunctional catalysts[19–23] in which the synergic effect between the metal and acid sites seems to have a crucial role.

Regarding metal selection, it has been shown that the use of noble metals (*e.g.* Pt, Ru, and Ir) provides high yields of hydrocarbons. However, owing to their high cost, there is growing interest in non-noble metals, such as Ni and Co.[12,14,24–26] Murzin and coworkers actually claim that Ni-based catalysts can be considered an effective alternative to noble metals due to their low cost and dual functionality towards hydrogenation and hydrogenolysis.[27–30] Many studies suggest that the reaction pathway over noble metals is different from those occurring on other transition metal catalysts, and propose a HYD mechanism as the predominant reaction pathway rather than DDO.[13,31]

Cluster catalysis, performed through metal or metal-containing systems with a definite number of atoms, is a research area that requires high synergy between experimental and computational approaches.[23,32,33] The great variety of possible cluster structures, and their fluxionality, can be exploited to design new systems with tunable catalytic properties, defined by the appropriate choice of their sizes, shapes and dispersion degrees on a support.[19,21,34,35] In this broad context, the present work aims to study both the HYD and DDO mechanisms proposed for the hydrodeoxygenation of guaiacol on a subnanometric ten-atom platinum cluster. This was in order to create a reference study for these kinds of catalyzed reactions, showing data and descriptors that can be employed to evaluate the effects of customizing the catalytic model, for example changing either the metal or the shape of the cluster, or fixing the latter on a given support.

2 Models and computational details

2.1 Models

A cluster of platinum with ten atoms, with tetrahedral symmetry and a spin multiplicity of 9,[36,37] was chosen as a representative of catalytic species consisting of subnanometer-sized clusters. Its structure, represented in Fig. 1, shows the presence of atoms with different coordination: the four atoms at the top of the cluster have coordination number three, the remaining six atoms have coordination number six. Pt$_{10}$ is topologically relatable to a tetracapped octahedron: six atoms form an octahedron whose triangular faces alternately show a cap, *i.e.* they have an additional atom arranged perpendicular to the
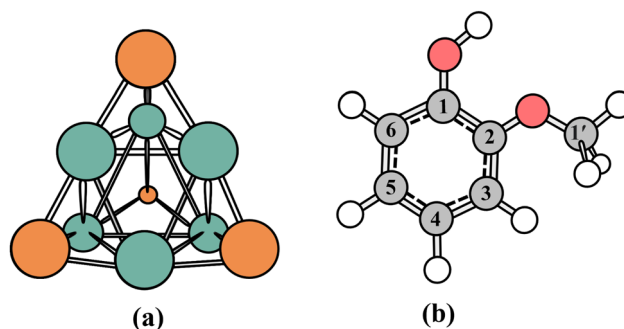

Fig. 1 (a) The Pt$_{10}$ cluster used as a subnanometric catalyst model; (b) the guaiacol molecule, whose atoms are numbered according to IUPAC rules. In the cluster, the orange and aquamarine colors indicate the coordination sites 3 and 6, respectively.

center of the face itself. This geometry is the result of global optimization of Pt clusters up to ten atoms, as reported by Demiroglu *et al.*[37] Among the subnanometer clusters, Pt$_{10}$ exhibits large stability due to the number of its valence electrons that allow it to be filled with multiple electronic shells (magic number).[38] In its optimized structure Pt$_{10}$ has average Pt–Pt bond lengths of 2.71 Å and a cohesive energy of 275.4 kJ mol^{-1}. The hypotheses that both the hydrogen molecule fragmentation and H-atom diffusion among the catalyst sites are very easy processes were already tested in other investigations.[20,34,39] As a matter of fact, DFT calculations revealed that hydrogen atoms can reach any configuration in the cluster and that the diffusion phenomena have to be considered essentially barrier-free when compared with the activation barriers typical of the HDO reaction.[40]

Guaiacol (2-methoxyphenol), a component of celery seed, tobacco leaf, orange leaf and lemon peel essential oils, was chosen as a catalytic substrate.[41] It is an interesting compound for HDO mechanism studies since the –OH and –OCH$_3$ groups are representative of a large number of oxygen-containing components in lignin-derived bio-oils, such as eugenol and vanillin.[42–45]

2.2 Computational details

All calculations were performed in the framework of DFT, using the Gaussian 16 package.[46] DFT calculations were carried out using the B3LYP hybrid exchange correlation functional,[47] to which the D3 correction scheme, developed by Grimme, was added to account for dispersion interactions.[48] The lanl2dz basis set of Hay and Wadt[49,50] was used for each calculation. It employs Dunning's basis set (D95)[51] for light atoms (H, C, and O) and, for platinum, a double-zeta valence basis set associated to a pseudopotential. Polarization functions consisting of primitive Gaussians having angular momentum and exponents in accordance with the following scheme were added to the D95 basis set: H (s: 0.049, p: 0.587), C (p: 0.0311, d: 0.587), and O (p: 0.0673, d: 0.961). These functions were retrieved from the EMSL Basis Set Exchange website.[52]

The nature of minima and transition states on the reaction paths was revealed by inspection of the harmonic vibrational frequencies, checking that no imaginary frequencies are

This journal is © the Owner Societies 2023

Phys. Chem. Chem. Phys., 2023, **25**, 10460–10471 | **10461**

present in structures corresponding to minima in the potential energy surfaces, and only one imaginary frequency is present in transition state structures. The energetics of the reaction will be given in terms of vibrational zero-point corrected energy (E_{ZPV}); the desorption energies of stable products have been corrected for the basis set superposition error (BSSE) by using the counterpoise method of Boys and Bernardi.[53] Since BSSE was calculated as a correction to the SCF energy, it will be reported in parenthesis along with the uncorrected E_{ZPV}.

3 Results and discussion

In the present investigation both the proposed mechanisms for the guaiacol HDO process were studied in order to evaluate whether deoxygenation occurs more readily from guaiacol, by breaking a $C(sp^2)$–OH/OCH$_3$ bond (DDO), or from 2-methoxycyclohexanol, through the cleavage of a $C(sp^3)$–OH/OCH$_3$ bond (HYD). In addition, it was aimed at investigating the formation of secondary products, which might deactivate the catalyst by consequently reducing its activity and selectivity, or whose formation could be considered of special interest in other production processes. Ultimately, the mapping of the HDO process of guaiacol allows us to compare the same process on the isoeugenol species, which was studied at the same computational level and with the same catalyst, in order to understand whether structurally similar molecules may have correspondingly similar reactive patterns.[40]

It is worth noting that other pathways could connect guaiacol to cyclohexane, including those where intermediates originating from dehydrogenation reactions (of the methyl or hydroxyl group) are involved.[54] To these could be added the high number of transformations a molecule such as guaiacol can undergo.[12,55] Here we actually considered only the direct defunctionalization reactions, from both the guaiacol (fully unsaturated phenyl ring) and 2-methoxycyclohexan-1-ol (fully saturated ring) molecules.

The selected HYD and DDO mechanisms of guaiacol on Pt$_{10}$ will be discussed in detail below, presenting the reaction profiles of the elementary stages and providing the energetics associated with each process (such as energy barriers and desorption energies).

3.1 HYD mechanism

The HYD mechanism of guaiacol involves hydrogenation of the benzene ring with the formation of 2-methoxycyclohexan-1-ol and the subsequent removal of the oxygenated groups (–OCH$_3$ and –OH); from 2-methoxycyclohexan-1-ol, depending on the order and chemical form whereby the oxygenated components are removed, three different pathways arise (Scheme 1): (1) removal of the –OCH$_3$ group as CH$_3$OH, leading to cyclohexanol, whence cyclohexane is obtained by loss of H$_2$O; (2) removal of the –OH group as water and subsequent formation of methoxycyclohexane from which, by removal of CH$_3$OH or CH$_4$ and water, the cyclohexane is obtained; and (3) removal of the methyl group as CH$_4$ from the OCH$_3$ fragment with the
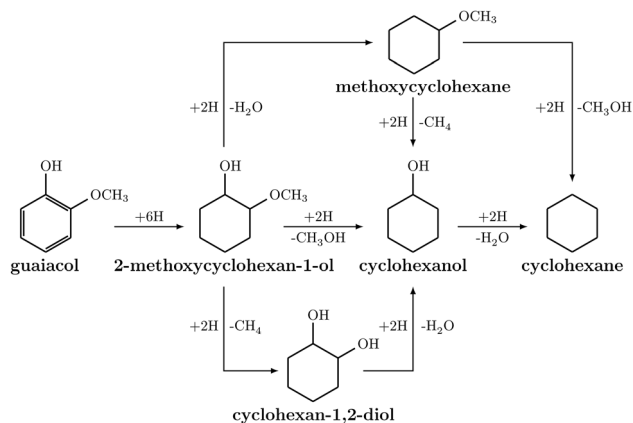
Scheme 1 Guaiacol conversion to cyclohexane according to the HYD mechanism: schematic routes.

formation of cyclohexane-1,2-diol, finally yielding cyclohexane through the elimination of two water molecules.

Hydrogenation of the benzene ring follows a Horiuti–Polanyi[56] scheme involving the consecutive addition of hydrogen adatoms. Since the carbon atoms of the ring are not equivalent due to electronic effects of substituents and metal/substrate interactions that sometimes generate metastable geometries with increased reactivity, each carbon atom of the ring was considered, at least for the addition of the first hydrogen atom, to be a potentially reactive hence hydrogenable site. Based on kinetic and thermodynamic criteria, respectively governed by a lower energy barrier and higher relative stability of the intermediate in the involved stage, the first hydrogen atom was shown to be preferentially added on C6 (Fig. 2). For the addition of subsequent hydrogen atoms, we considered as potential sites for hydrogen attachment only the carbon atoms in *ortho* to the progressively added hydrogen atoms. As a matter of fact, as evidenced in experimental studies conducted on the hydrogenation of benzene[56–58] and in our previous computational work,[40] these carbon atoms appear to be activated by the vicinal presence of a hydrogen atom. On this basis, from intermediate I, the addition of a second H atom on the C1 and C5 centers was considered. The species preferentially obtained is 2-methoxycyclohexa-2,4-dien-1-ol (II; energy barrier of 88.2 kJ mol^{-1} for hydrogenation of C1 and desorption energy of 273.2 kJ mol^{-1} with BSSE = 28.0 kJ mol^{-1}), which, by addition of a third H atom to C5 of the ring, leads to intermediate III. By virtue of a lower energy barrier of about 16 kJ mol^{-1}, addition of the fourth hydrogen atom occurs preferentially on C2 leading to the 2-methoxycyclohex-3-en-1-ol (IV; desorption energy of 158.2 (BSSE = 22.4) kJ mol^{-1}). From this one, the last carbon atoms of the ring (C3 and C4) were considered as potential sites available for hydrogenation. Both the energy barrier (26.2 *vs.* 34.3 kJ mol^{-1}) and the relative stability of the resulting intermediate (−18.5 *vs.* 24.2 kJ mol^{-1}) suggest that the addition of the fifth hydrogen occurs preferentially on C4 leading, by successive addition of the last H atom to C3, to the 2-methoxycyclohexan-1-ol species (VI), whose desorption energy is 102.3 (BSSE = 19.0) kJ mol^{-1}.
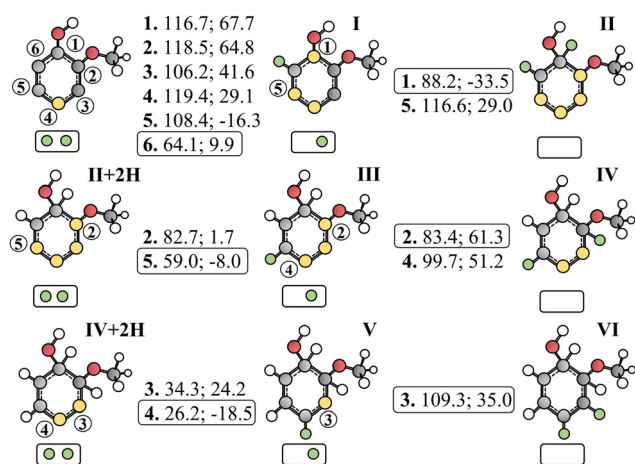
10462 | *Phys. Chem. Chem. Phys.*, 2023, **25**, 10460–10471

This journal is © the Owner Societies 2023

Fig. 2 Representation of the complete saturation of the aromatic ring of the guaiacol species adsorbed on the Pt_{10} cluster. In the molecular species, the yellow circles indicate the interaction sites of the molecule itself with the cluster, which is instead represented by a small rectangle containing the adsorbed hydrogen atoms (green circles). To the right of each species, the first number indicates the position where the catalytic hydrogen is added, the second is the energy barrier and the third is the reaction energy, both referring to the reactant of the elementary step. All energy values are expressed in kJ mol^{-1}. The first catalytic hydrogenation starts from guaiacol, the second from II + 2H (2-methoxycyclohexa-2,4-dien-1-ol), and the last from IV + 2H (2-methoxycycloes-3-en-1-ol).

Once the benzene ring was fully hydrogenated, the investigation of the final HYD paths, in order to get the whole conversion product, could be taken into account.

The first route (pathway 1) involves the formation of cyclohexane through the removal of –OCH$_3$ as methanol and the subsequent removal of –OH as water. Therefore, the first elementary step entails cleavage of the C2–O bond and adsorption of the OCH$_3$ fragment on the upper portion of a side edge of the cluster. The cleavage is characterized by an energy barrier

of 137.7 kJ mol^{-1} and leads to the (int1 + CH$_3$O)/Pt$_{10}$ species with an energy release of 66.5 kJ mol^{-1} (Fig. 3).

In order to proceed with the HDO reaction, a new H$_2$ molecule was fragmented on the cluster (Fig. S1 of the ESI†); thus the resulting (int1 + CH$_3$O)/Pt$_{10}$2H species was used as a reactant for the formation of chemisorbed methanol, whose desorption energy was calculated to be equal to 91.9 kJ mol^{-1}, with BSSE = 8.8 kJ mol^{-1}. Following the desorption of methanol, there is the diffusion of an H atom through the cluster sites towards the unsaturated C2 atom of the ring. From the resulting species, (int1 + CH$_3$O)/Pt$_{10}$H, there is a shift of an H atom to C2 of the ring (energy barrier of 106.5 kJ mol^{-1}) with the formation of the adsorbed cyclohexanol, which is less stable than the reactant species of 43.3 kJ mol^{-1}. Cyclohexanol could desorb from the cluster with an energy of 117.8 (BSSE = 16.9) kJ mol^{-1}, representing a secondary reaction product. In the main reaction pathway, however, cyclohexanol/Pt$_{10}$ undergoes C1–O bond cleavage. The elementary stage involved is characterized by a very high energy barrier of 192.1 kJ mol^{-1} and leads to a species, (int2 + OH)/Pt$_{10}$, in which the OH fragment is adsorbed on the upper portion and between the two metal centers of a cluster edge.

For the removal of the OH species as water, a second H$_2$ molecule was fragmented on the cluster. The resulting species, (int2 + OH)/Pt$_{10}$2H, is characterized by the presence of an H atom on an edge adjacent to the OH fragment and a second H atom on a far site of the cluster. The elementary stage in which this species becomes the reactant involves the transfer of an H atom to the O atom of the adsorbed fragment (energy barrier of 89.3 kJ mol^{-1}) with the formation of chemisorbed H$_2$O (Fig. S2a of ESI†). In order to proceed with the reaction, the H$_2$O molecule was desorbed from the cluster – desorption energy of 66.5 (BSSE = 5.4) kJ mol^{-1} – and the H atom, adsorbed and shared between two Pt atoms, diffused near the unsaturated
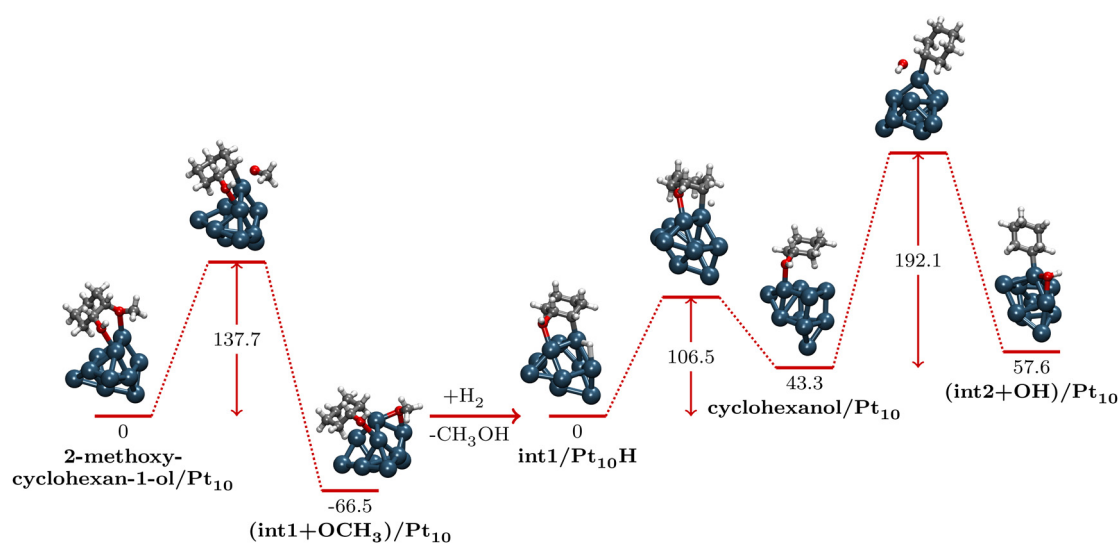
Fig. 3 Reaction profile showing C2–OCH$_3$ bond cleavage together with the shift of the CH$_3$O fragment on an edge of the cluster (HYD pathway 1). After addiction of the H$_2$ molecule (which fragments on the cluster) and desorption of the methanol molecule, the formation of cyclohexanol with subsequent cleavage of the C1–OH bond occur.
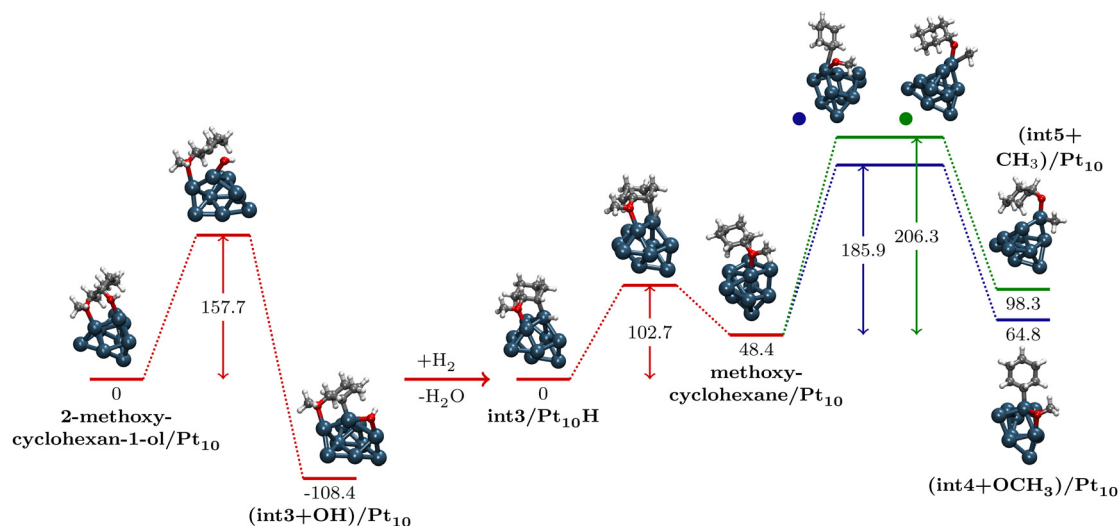
This journal is © the Owner Societies 2023

Phys. Chem. Chem. Phys., 2023, 25, 10460–10471 | 10463

Fig. 4   Elementary steps related to the transformation on the platinum cluster of 2-methoxycyclohexan-1-ol to methoxycyclohexane and the OCH_3 loss from the latter (HYD pathway 2). The first step illustrates the breaking of the C1–OH bond. After fragmentation of a new H_2 molecule on the cluster and the formation and desorption of water, the formation of methoxycyclohexane occurs through hydrogenation on C1. In the following steps the breaking of the C2–OCH_3 bond with the subsequent formation of methanol adsorbate (shown in blue), or the cleavage of the O–CH_3 bond in the methoxyl group to obtain methane (in green), is shown.

C1. From the int2/Pt_{10}H intermediate so obtained, the cyclohexane/Pt_{10} species forms (9.2 kJ mol^{-1} more stable than its reactant) through the crossing of a low energy barrier, equal to 54.7 kJ mol^{-1} (Fig. S2b of the ESI†). The resulting cyclohexane can desorb from the cluster with an energy of 89.6 (BSSE = 16.6) kJ mol^{-1}.

Pathway 2 suggests firstly the elimination of the –OH group as water and then the removal of the remaining oxygenated group as methanol, if C2–O bond breaking occurs, or methane, if O–CH_3 bond cleavage happens instead. In the latter case cyclohexane is obtained by the removal of two water molecules. The early two elementary stages common to both bifurcations involve C1–O bond cleavage and methoxycyclohexane formation, respectively. Particularly, in the first elementary stage (Fig. 4), there is, through the overcoming of an energy barrier of 157.7 kJ mol^{-1}, the breaking of the C1–O bond from 2-methoxycyclohexan-1-ol leading to a remarkable stabilization of the (int3 + OH)/Pt_{10} system; the latter is characterized by the OH fragment adsorbed as a bridge between two metal centers on an upper edge of the cluster, and the int3 showing O–Pt (bond length 2.22 Å) and C1–Pt (bond length 2.06 Å) interactions. The adsorbed OH, after fragmentation of an H_2 molecule on the cluster, can undergo hydrogenation hence desorption as water.

In the second elementary step, from the int3/Pt_{10}H species, there is the transfer, characterized by an energy barrier of 102.7 kJ mol^{-1}, of an H atom to the unsaturated C1 of the ring with the formation of methoxycyclohexane/Pt_{10}, with a desorption energy of 128.8 (BSSE = 18.9) kJ mol^{-1}, which is less stable than the intermediate that preceeds it by 48.4 kJ mol^{-1}. Methoxycyclohexane/Pt_{10} represents the species from which two alternative paths leading to cyclohexane are branched. According to one ramification (depicted in blue in Fig. 4), the first

elementary step includes, by crossing an energy barrier of 185.9 kJ mol^{-1}, the breakage of the C2–O bond with formation of the (int4 + CH_3O)/Pt_{10} species, featuring the OCH_3 fragment adsorbed on the upper portion of the cluster edge. Following fragmentation of a new H_2 molecule on the cluster, the CH_3O could be hydrogenated to methanol and desorb. The resulting species, traceable to int2/Pt_{10}H from pathway 1, is hydrogenated on the unsaturated C2, giving cyclohexane. In the alternative bifurcation (shown in green in Fig. 4), on the other hand, a slightly higher energy barrier (206.3 kJ mol^{-1}) is in the way for the O–CH_3 bond breaking. The (int5 + CH_3)/Pt_{10} species, less stable by ca. 50 kJ mol^{-1} than the methoxycyclohexane/Pt_{10} species, exhibits a dangling oxygen atom interacting with the Pt atom at the apical position (O–Pt bond length of 1.89 Å) of the cluster and the adsorbed CH_3 fragment.

The last investigated route (pathway 3) involves the early elimination of methane (desorption energy equal to 23.4 kJ mol^{-1} with BSSE = 4.5 kJ mol^{-1}), which would lead to cyclohexane and two water molecules through the following formation of cyclohexane-1,2-diol and cyclohexanol. Overcoming an energy barrier of 161.0 kJ mol^{-1}, from the 2-methoxycyclohexan-1-ol there is an O–CH_3 bond scission leading to the (int6 + CH_3)/Pt_{10} species (Fig. 5). The latter, in addition to the CH_3 fragment being adsorbed on the Pt atom at the apical position, is characterized by two interactions, at the level of the oxygen atoms, with the adjacent metal centers of the upper portion of the cluster edge.

In the next elementary stage, due to fragmentation of an H_2 molecule on the cluster, methane generation occurs by transfer of an H atom to the C of the fragment. The subsequent desorption of methane and diffusion of the hydrogen atom through the cluster in the closeness of the dangling oxygen leads to the int6/Pt_{10}H^b species, from which there is the
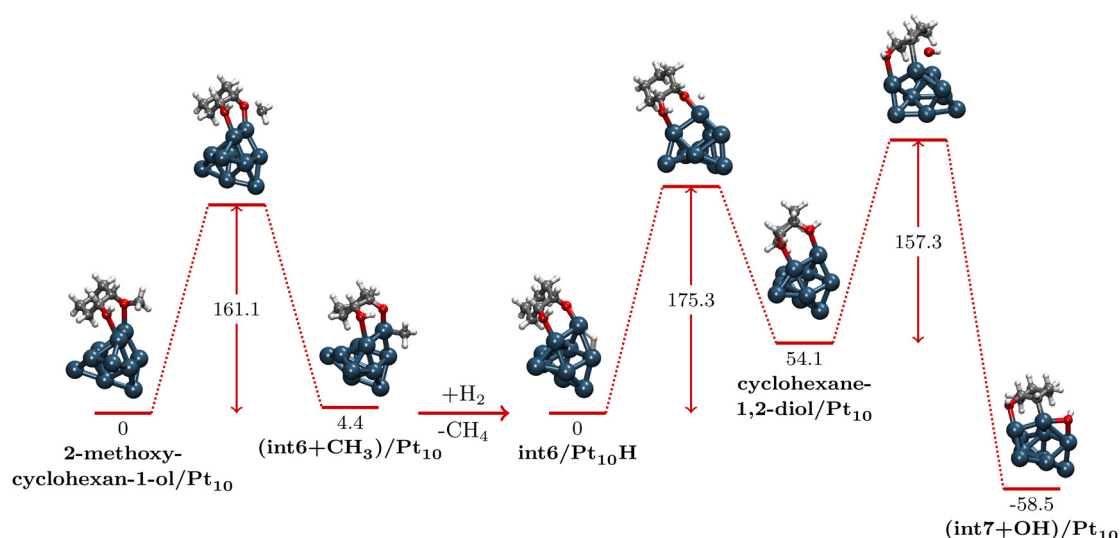
Fig. 5 The reaction profile according to the HYD pathway 3: after the O−CH$_3$ bond breaking in the methoxyl group, with the formation of the int6 and CH$_3$ species coadsorbed on Pt$_{10}$, methane desorbs following a H$_2$ molecule fragmentation. The formation of cyclohexan-1,2-diol/Pt$_{10}$ occurs by hydrogenation of the dangling oxygen and is followed by cleavage of the C2−OH bond.

formation of cyclohexane-1,2-diol/Pt$_{10}$. For this process, which requires oxygen atom hydrogenation, an energy barrier of 175.0 kJ mol^{-1} and a desorption energy of 94.3 (BSSE = 19.6) kJ mol^{-1} for cyclohexane-1,2-diol was calculated. From this, there is C2–O bond breakage (energy barrier 157.3 kJ mol^{-1}) with a considerable stabilization of the resulting species, (int7 + OH)/Pt$_{10}$, in which the OH fragment is shared between two Pt atoms, and int7 interacts *via* O and the unsaturated C2 with two differently coordinated Pt atoms. As discussed for pathway 2, through the breaking of the C1–O bond (energy barrier: 192.1 kJ mol^{-1}), the removal of water and the saturation of C1 (energy barrier: 54.7 kJ mol^{-1} in Fig. S2, ESI†), cyclohexane is formed on Pt$_{10}$ from cyclohexanol.

3.2 DDO mechanism

The direct deoxygenation (DDO) mechanism of guaiacol involves firstly the removal of the oxygenated groups and then the hydrogenation of benzene to cyclohexane. Regarding deoxygenation, the order in which group removal can occur opens up different pathways, reported schematically in Scheme 2. If the first removed group is the –OH one the formation of anisole occurs (desorption energy 126.0 kJ mol^{-1}, with BSSE = 22.6 kJ mol^{-1}), from which two ramifications branch off to form benzene: one involves demethoxylation and the other a process of demethanation; in the latter case phenol can be formed. On the other hand, if the first group removed from guaiacol is the –OCH$_3$, phenol forms directly, which evolves to benzene. Alternatively, guaiacol could undergo demethanation to form catechol, which through the removal of two water molecules leads to the formation of benzene. The latter, generated from either one or more of the three proposed pathways, is subsequently hydrogenated to cyclohexane.

The first reaction pathway involves the elimination of the –OCH$_3$ group to obtain phenol which, through the removal of a
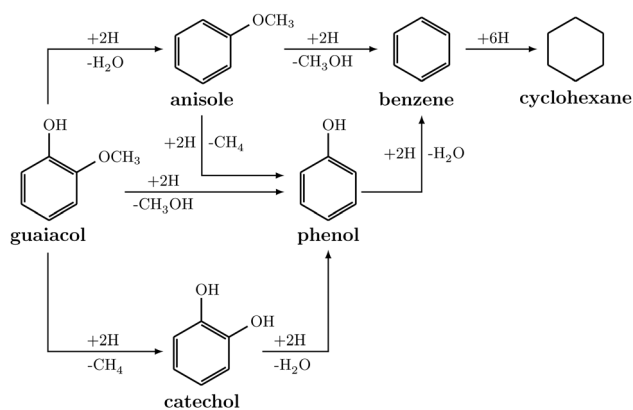
Scheme 2 Guaiacol conversion to cyclohexane according to the DDO mechanism: schematic routes.

water molecule, gives benzene. The initial elementary step of this channel (Fig. 6) involves cleavage of the C2–O bond (energy barrier of 129.2 kJ mol^{-1}) along with the migration of the OCH$_3$ fragment to a platinum atom, its hydrogenation and subsequent desorption. If a comparison is done with the demethoxylation energy barrier calculated by Lee *et al.*[59] for guaiacol on Pt(111), it turns out that when the platinum is reduced to subnanometric size the involved energy barrier can be sensibly lower. This occurrence, as well as other significant differences, can tentatively be explained taking into account the higher susceptibility to distortion of a cluster[60] with respect to the platinum surface.

It is now interesting to note that in the (int1′ + OCH$_3$)/Pt$_{10}$ species, the hydrogen bond, which is established between the hydroxyl H and methoxyl O centers, is reduced from 2.16 Å, (the length of the hydrogen bond in the guaiacol), to 1.60 Å. This means that methanol formation occurs almost instantaneously by displacement of the hydroxyl H atom and without the
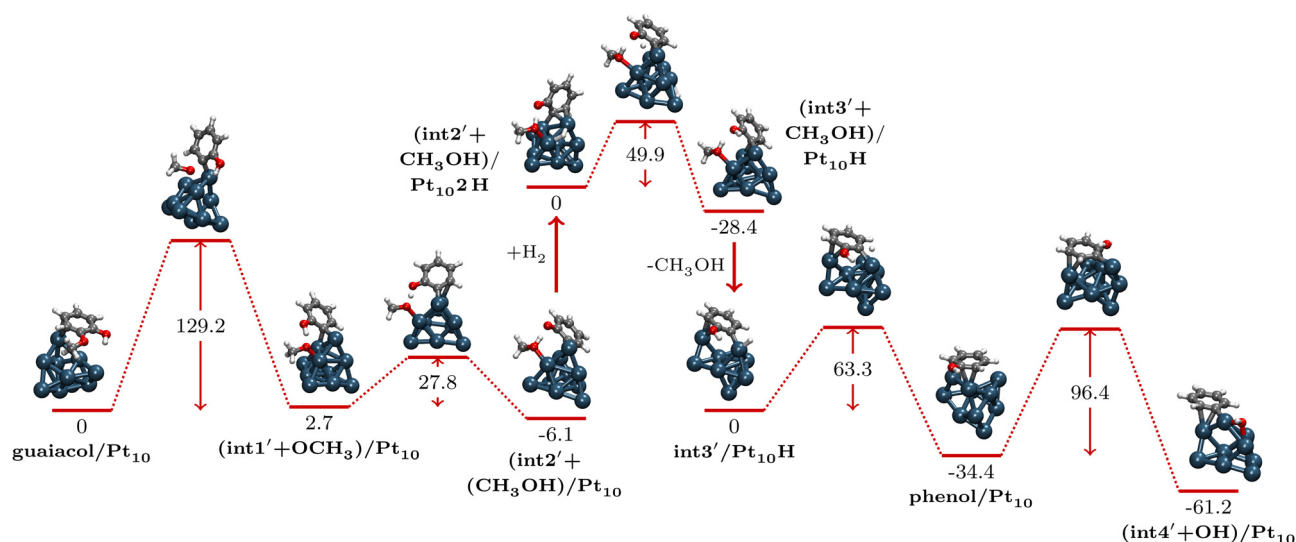
Fig. 6 The reaction profile corresponding to the DDO pathway 1: at first the cleavage of the C2–OCH$_3$ bond with the formation of the (int1′ + OCH$_3$)/ Pt$_{10}$ species occurs along with intramolecular hydrogenation of the OCH$_3$ fragment. The hydrogenation, by catalyst-activated hydrogen, of the dangling O of int2′ in the presence of adsorbed CH$_3$OH follows. Afterwards, the desorption of methanol with the restoration of aromaticity gives phenol/Pt$_{10}$, while the subsequent cleavage of the C1–OH bond results in the (int4′ + OH)/Pt$_{10}$ species formation.

intervention of hydrogen activated by the catalyst. In addition, the hydrogen bond length of 1.47 Å in the (int2′ + CH$_3$OH)/Pt$_{10}$ product suggests a near-sharing of the hydrogen atom between two oxygen atoms, probably favored by the small size of the metal cluster.

Starting from the (int2′ + CH$_3$OH)/Pt$_{10}$ species, after fragmentation of a H$_2$ molecule on the cluster, the reaction continues with the restoration of the –OH group in the int2′. In order to deepen this aspect, it was decided to test to what extent the presence of methanol is able to influence this elementary stage by investigating the hydrogenation of dangling oxygen both with and without adsorbed methanol. In the former case, the energy barrier required for the conversion of (int2′ + CH$_3$OH)/Pt$_{10}$2H to (int3′ + CH$_3$OH)/Pt$_{10}$H is 49.9 kJ mol^{-1}, which is three times lower than that needed for the conversion of int2′/Pt$_{10}$2H to int3′/Pt$_{10}$H (167.1 kJ mol^{-1}), as illustrated in Fig. S3 of the ESI.† Furthermore, the hydrogenation of the O atom in (int2′ + CH$_3$OH)/Pt$_{10}$2H occurs with an energy release of 28.4 kJ mol^{-1}, to be compared with the 11.4 kJ mol^{-1} energy required for the same process in the absence of coadsorbed methanol. It is interesting here to observe the upshots related to the presence of the adsorbed methanol which apparently could be, at first glance, thought of as a spectator species and which instead might locally act either electronically or sterically by inductive or proximity effects, respectively. The following hydrogen bond weakening, due to the restoration of the –OH group, facilitates methanol desorption. The resulting species, int3′/Pt$_{10}$H, undergoes hydrogenation on C2 (energy barrier of 63.3 kJ mol^{-1}) and the process is characterized by an energy release of 34.4 kJ mol^{-1} related to phenol/Pt$_{10}$ formation. The calculated energy for phenol desorption is 132.8 (BSSE = 24.1) kJ mol^{-1}. However, for benzene to form, water must be removed. This requires overcoming an activation

barrier of 96.4 kJ mol^{-1} for cleavage of the C1–O bond and obtaining the (int4′ + OH)/Pt$_{10}$ species that is more stable than phenol by about 30 kJ mol^{-1}. The adsorbed OH fragment is subsequently hydrogenated and removed as water; the adsorbed int4 species, on the other hand, is converted to benzene following hydrogenation of the unsaturated C1 carbon, a process characterized by a negligible energy barrier of 10.4 kJ mol^{-1} (Fig. S4 of the ESI†).

The second pathway proposed for the DDO mechanism involves the removal of the –OH group with the formation of anisole from which, either by loss of the –OCH$_3$ or of the –CH$_3$ fragment (in this case passing through phenol), benzene is obtained. We note here that the C–OCH$_3$ bond cleavage in anisole would be, again, a relatively easy step, opposite to the same process as it would occur for anisole in the Pt(111) surface.[54] It also seems that in this case the flexibility of the subnanometric cluster plays a fundamental role. In the transition state of this elementary process it can indeed be argued that the incipient phenyl radical which originates from the cleavage is stabilized by strong interactions with a distorted cluster. From benzene, by the addition of three catalytically activated hydrogen molecules, cyclohexane is achieved. The first elementary stage of this pathway occurs by crossing an energy barrier of 163.9 kJ mol^{-1}, which is actually needed to break the C1–OH bond and thus obtain the (int5′ + OH)/Pt$_{10}$ species with the OH fragment adsorbed on a three-coordinate metal center of the cluster (Fig. 7).

The subsequent fragmentation of a new H$_2$ molecule triggers the formation and desorption of water, as well as the restoration of the system aromaticity. This process takes place in the second elementary stage in which, starting with the int5′/Pt$_{10}$H species, there is the transfer of an H atom to the unsaturated C1 of the ring with the formation of anisole/Pt$_{10}$, which is more stable by
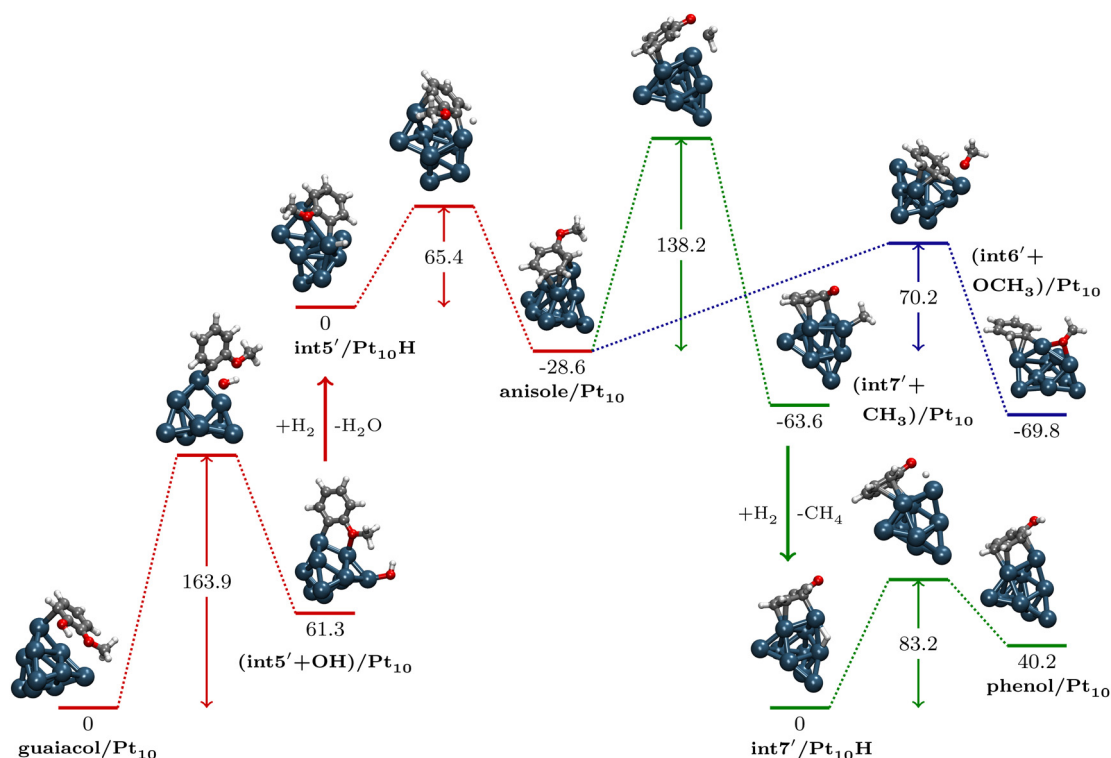
Fig. 7 Elementary steps for the second DDO pathway: the cleavage of the C1–OH bond from guaiacol/Pt$_{10}$ gives the (int5′ + OH)/Pt$_{10}$ species that, after a H$_2$ molecule intervention and water desorption, is transformed to anisole/Pt$_{10}$ through the restoration of the phenyl ring. The latter can follow two paths: the C–OCH$_3$ bond breaking, which ultimately results in methanol and benzene (blue lines) or OC–CH$_3$ bond breaking, which instead produces methane, benzene and water (green lines), through phenol as the intermediate species.

about 29 kJ mol^{-1} than the intermediate reactant and for which overcoming a relatively low energy barrier of 65.4 kJ mol^{-1} is required. Starting from the anisole/Pt$_{10}$ species two mechanisms can take place. The C2–O bond breaking, characterized by an energy barrier of 70.2 kJ mol^{-1}, results in the formation of the (int6′ + OCH$_3$)/Pt$_{10}$ species. This, which is more stable than the chemisorbed anisole by 41 kJ mol^{-1}, has the OCH$_3$ fragment shared between two differently coordinated Pt atoms in the upper portion of an edge of the cluster. The fragment, following the dissociation of a H$_2$ molecule on the cluster, is hydrogenated to CH$_3$OH and desorbs. The resulting species, as already stated, readily undergoes hydrogenation on C2 giving a benzene molecule. Alternatively, there is the cleavage of the O–C bond in the –OCH$_3$ group, for which an energy barrier of 138.2 kJ mol^{-1} must be overcome; the obtained (int7′ + CH$_3$)/Pt$_{10}$ species is characterized by the CH$_3$ fragment on the Pt atom at the apical position and the presence of a dangling oxygen atom of the intermediate that interacts only *via* the ring carbons with the cluster. A hydrogen molecule dissociated on the cluster and hydrogenates the chemisorbed fragment to methane. This, following the desorption of the latter and the diffusion of the second H atom, leads to the int7′/Pt$_{10}$H species. From the latter, by the transfer of one H atom to the dangling O of the ring (energy barrier of 83.2 kJ mol^{-1}), chemisorbed phenol is formed, which, reconnecting with the first proposed pathway, leads to benzene/Pt$_{10}$.

The third pathway, finally, includes the removal of the methyl group as methane at the early stage with formation of the adsorbed catechol, from which by leakage of two water molecules benzene is obtained. The first elementary step of this proposed pathway involves cleavage of the O–CH$_3$ bond in the guaiacol/Pt$_{10}$ with adsorption of the methyl fragment on a Pt atom of the cluster. For this species there is an energy release of 55.0 kJ mol^{-1}. This step is followed by hydrogenation of the chemisorbed fragment with the formation of methane and its subsequent desorption. As a result of H atom diffusion through the cluster, there is hydrogenation of the dangling O atom in the int8′/Pt$_{10}$H (energy barrier of 155.8 kJ mol^{-1}) with the formation of catechol/Pt$_{10}$, which is 69.1 kJ mol^{-1} less stable than the reactant. From the catechol (whose desorption energy is 160.6 kJ mol^{-1}, with BSSE = 23.3 kJ mol^{-1}) there is cleavage of the C2–OH bond with the formation of the (int3′ + OH)/Pt$_{10}$ intermediate, where the –OH fragment is shared between two metal centers of a cluster edge (Fig. 8). Subsequent removal of H$_2$O leads to the int3′/Pt$_{10}$H species, which leads to phenol/Pt$_{10}$, hence to benzene, as already discussed in the case of the first DDO pathway.

The benzene molecule obtained in the three DDO pathways (which could desorb with an energy of 167.5 kJ mol^{-1}, BSSE = 26.4 kJ mol^{-1}) must be transformed, by consecutive hydrogenations, to cyclohexane. Whereas in the HYD mechanism there is the combination of two factors (the electronic
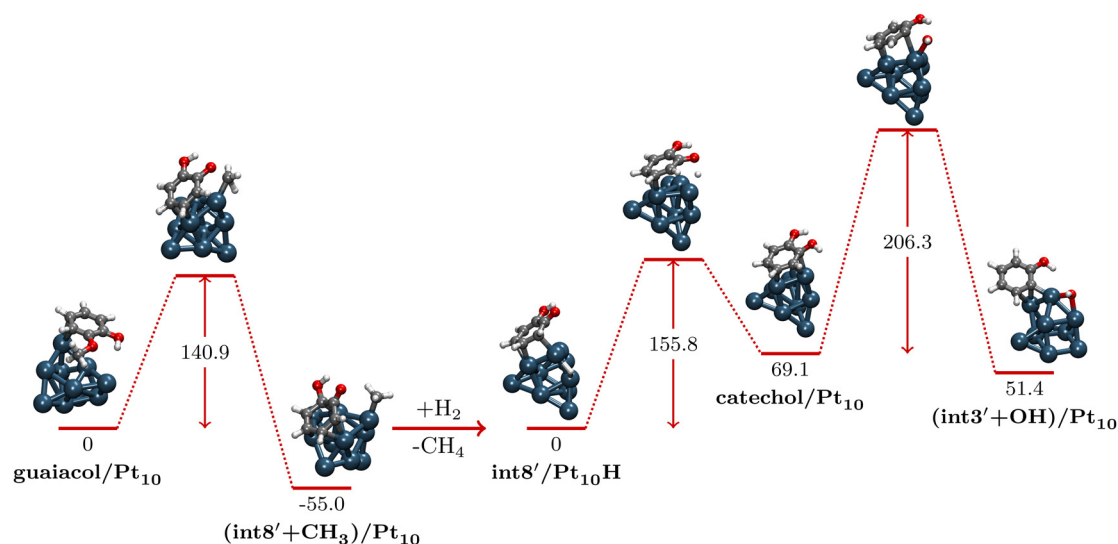
Fig. 8 DDO pathway 3: methane and catechol formation from guaiacol. Catechol/Pt$_{10}$ will then lose water and transform to a phenol precursor through C2−OH bond cleavage.

effects of substituents and the metal/substrate interactions) complicating the choice of the favorite site for hydrogenation, in this case the addition of the first hydrogen atom is governed only by the presence of the metal/substrate interactions. On this basis, the only carbon atoms available to hydrogenation are those for which interaction with Pt atoms in the cluster occurs. In view of this, the addition of the first hydrogen atom was only considered on four carbon atoms of the ring, numbered 1, 2, 5 and 6 in Fig. 9. C6 is the carbon atom that preferentially undergoes hydrogenation by virtue of its lower energy barrier

Fig. 9 Representation of the complete saturation of benzene on the Pt$_{10}$ cluster. The yellow circles indicate the interaction sites of the molecule with the cluster, which is instead represented by a small rectangle containing the adsorbed hydrogen atoms (green circles). To the right of each species, the first number indicates the position where the catalytic hydrogen is added, the second is the energy barrier of the corresponding elementary step, and the third is the energy of the product referred to its reactant. All energy values are expressed in kJ mol^{-1}. The first catalytic hydrogenation starts from benzene, the second from **IIa** + **2H** (cyclohexa-1,3-diene), the last from **IVa** + **2H** (cyclohexene).

(82.4 kJ mol^{-1}) with respect to the alternative sites and the higher stability of the obtained intermediate. For subsequent hydrogenations, as mentioned above, carbon atoms in the *ortho*-position with respect to the pre-existing H atom(s) are identified as potential sites for hydrogenation. The carbon atoms, *ortho* to C6, on which the addition of the second H atom was considered are thus 1 and 5. The lower energy barrier (83.6 *vs.* 103.4 kJ mol^{-1}) suggests that hydrogenation takes place preferentially on C5, leading to cyclohexa-1,3-diene (desorption energy of 190.9 kJ mol^{-1} with BSSE = 24.1 kJ mol^{-1}). From it, the addition of a third H atom to C4 (very low energy barrier of 24.9 kJ mol^{-1}) results in an energy release of 22.1 kJ mol^{-1} due to the formation of the intermediate species **IIIa**. Then, following the transfer of an H atom to C3, there is the formation of a stable cyclohexene species, for which a desorption energy of 154.2 kJ mol^{-1} with BSSE = 21.6 kJ mol^{-1} was calculated. On the basis of a lower activation energy (35.4 *vs.* 85.9 kJ mol^{-1}) and higher relative stability of the intermediate involved (17.6 *vs.* 40.1 kJ mol^{-1}), the C2 is considered the favored site for the addition of the fifth H atom and, finally, the **Va** intermediate undergoes hydrogenation on C1 leading to the formation of the adsorbed cyclohexane. The calculated desorption energy for cyclohexane was finally equal to 85.0 kJ mol^{-1} with BSSE = 17.6 kJ mol^{-1}.
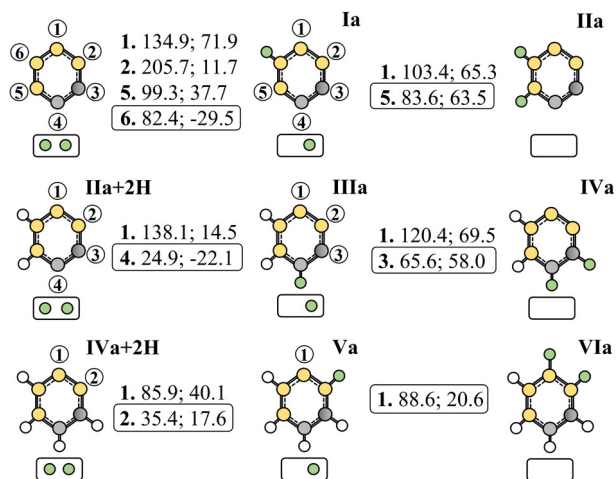
3.3 Kinetic analysis

In the previous sections we discussed eight possible mechanisms for the conversion of guaiacol to cyclohexane on the Pt$_{10}$ cluster, which are summarized in Schemes 1 and 2. The results of DFT calculations comprise energy barriers and relative energies of minima on the potential energy surface. These results would indicate that, in the early stage of the reaction, the hydrogenation of the phenyl ring would be kinetically favored with respect to deoxygenation, but this latter would have a higher probability of occuring just from guaiacol instead

of the full hydrogenated product, methoxycyclohexanol. In order to better discriminate the fastest mechanism we used microkinetic analysis instead of basing our conclusions on the inspection of energy barriers. In particular, the Simplified Christiansen Method (SCM) recently developed and described in ref. 23 and 61 was employed. Since the desorption of the final product, cyclohexane, is significantly affected by entropy variation and, in turn, affects the rate of the whole reaction, SCM analysis was performed in terms of Gibbs free energies as a function of the temperature. It can be concluded from Tables S1–S3 of the ESI,† that the use of ΔG instead of E_{ZPV} has a negligible effect on the barriers and intermediate energy differences, but has a major influence on the desorption energies of all stable intermediates.

The results of the SCM analysis, whose details are reported in Tables S4–S7 of ESI,† indicated that the DDO channels are always at least two orders of magnitude faster than those present in the HYD pathways. In particular, the DDO routes involving the formation of anisole and phenol share the same reaction rate in the lowest part of the temperature range, with the benzene hydrogenation being the slowest process. At higher temperatures the HDO reaction on Pt_{10} seems to proceed essentially through the first DDO pathway, the one involving the formation of intermediate phenol originating from early demethoxylation. The DDO channel passing through catechol has lower reaction rates since it involves the high reaction barrier corresponding to the C–OH bond cleavage. Since the fastest mechanisms are of DDO type and benzene reduction is slow, the benzene molecule is the one showing the higher surface molar ratio Θ at all the considered temperatures (from 473 to 1073 K).

The HYD channel passing through methoxycyclohexane, which directly transforms to cyclohexane, is slightly preferred over the other HYD pathways. The analysis indicated that the C–OH cleavage in 2-methoxycyclohexa-1-ol (product of the phenyl ring hydrogenation of guaiacol) is slightly favored with respect to the C–OCH$_3$ one and that, conversely, the O–CH$_3$ bond breaking, to ultimately form methane, is always the less favored process. However, all HYD routes but the one involving methane production have essentially the same reaction rate. According to what was anticipated on the basis of energy barriers (for the sake of comparison, the SCM-calculated reaction rates at various temperatures in terms of E_{ZPV} are reported in Table S7, ESI†), the full reduction of the phenyl ring in guaiacol is a kinetically easy process, but the rate of the HYD mechanisms are negatively affected by the slow process corresponding to the C–O cleavage.

4 Conclusions

The present investigation, framed in the context of the constant demand for renewable and eco-sustainable alternatives, aims to provide an atomistic-level analysis of the "direct deoxygenation" (DDO) and "deoxygenation-through-hydrogenation" (HYD) mechanisms for the hydrodeoxygenation reaction of guaiacol catalyzed by a subnanometric platinum cluster. Although

several experimental and computational studies suggest the predominance of one mechanism rather than another depending on the metal used (as an example, noble or non-noble), this may not be true in the investigated catalytic model since processes on subnanometer clusters do not necessarily follow the established rules of heterogeneous catalysis and, conversely, represent a chemistry to be investigated case by case. For this reason, both mechanisms have been studied and the observations deduced from the DFT calculations and the SCM analysis of the results are summarized below.

Even if the early hydrogenation of the phenyl ring in guaiacol would be faster than the homolytic cleavage of C(sp^2)–O bonds, on Pt_{10} the DDO mechanism is favored with respect to the HYD one. This is because the energy barriers for the breaking of both the C(sp^2)–OCH$_3$ bond from guaiacol and the C(sp^2)–OH bond from phenol results are substantially lower than for the breaking of the C(sp^3)–OCH$_3$ bonds in 2-methoxycyclohexan-1-ol and C(sp^3)–OH bonds in cyclohexanol. In addition, the energy barrier related to the cleavage of the C(sp^2)–OCH$_3$ bond of anisole is lower than the corresponding barrier in the fully hydrogenated equivalent occurring in the HYD mechanism. At 0 K, the desorption energies related to the molecular species cyclohexanol and methoxycyclohexane are lower than the amount of energy required to overcome the energy barriers for the elementary stages of C(sp^3)–OH and C(sp^3)–OCH$_3$ bond cleavage, which are necessary for the reaction to proceed. In contrast, in the DDO mechanism the desorption of molecular species is more difficult; the amount of energy calculated for the species desorption is always greater than the energy barrier for the following elementary stage of the reaction. This evidence can be attributed to the interaction of the substrate with Pt: in the DDO mechanism, the aromatic species shows considerable interactions with the cluster through the phenyl ring, which makes it easier to break the C–O bonds. In the HYD mechanism, on the other hand, the hydrogenated species are weakly adsorbed. Consequently, it can be inferred that in the HYD mechanism only a negligible percentage of molecules will be able to cross the energy barriers necessary for the reaction progress and thus only a very small fraction of it will succeed in yielding the desired cyclohexane as a final product. For the HYD channels the same conclusions hold true at low temperatures if the reaction energetic is formulated in terms of Gibbs free energies, while in the DDO cases desorptions and transformations become competitive. At higher temperatures desorption phenomena occur more easily but, according to the microkinetic analysis, the net effect is always a preference for the DDO mechanism. In particular, in the preferred pathway the elimination of the –OCH$_3$ group as methanol is followed by the elimination of the –OH group as water.

Author contributions

Chiara Nania: investigation, data curation, writing – original draft; Marco Bertini: investigation, data curation, methodology;

This journal is © the Owner Societies 2023

Phys. Chem. Chem. Phys., 2023, **25**, 10460–10471 | **10469**

Laura Gueci: investigation, data curation; Francesco Ferrante: conceptualization, methodology, data curation, writing, supervision; Dario Duca: supervision, project administration.

Conflicts of interest

There are no conflicts to declare.

References

1 D. C. Elliott, *Advances in Bioenergy*, John Wiley & Sons, Ltd, 2016, pp. 65–72.

2 R. Ahorsu, F. Medina and M. Constantí, *Energies*, 2018, **11**, 1–19.

3 M. N. Uddin, K. Techato, J. Taweekun, M. M. Rahman, M. G. Rasul, T. M. I. Mahlia and S. M. Ashrafur, *Energies*, 2018, **11**, 3115.

4 A. Bjelic, M. Grilc, M. Hus and B. Likozar, *Chem. Eng. J.*, 2019, **359**, 305–320.

5 A. Bridgwater, *Biomass Bioenergy*, 2012, **38**, 68–94.

6 G. Boyle, *Renewable Energy: Power for a Sustainable Future*, Oxford University Press, Oxford *in association with The Open University, Milton Keynes*, 3rd edn, 2012.

7 A. Bridgwater, *Chem. Eng. J.*, 2003, **91**, 87–102.

8 D. C. Elliott, *Curr. Opin. Chem. Eng.*, 2015, **9**, 59–65.

9 M. Bertero, G. de la Puente and U. Sedran, *Fuel*, 2012, **95**, 263–271.

10 J. Feng, C.-y Hse, Z. Yang, K. Wang, J. Jiang and J. Xu, *Appl. Catal., A*, 2017, **542**, 163–173.

11 D. Mohan, C. U. Pittman and P. H. Steele, *Energy Fuels*, 2006, **20**, 848–889.

12 D. Gao, Y. Xiao and A. Varma, *Ind. Eng. Chem. Res.*, 2015, **54**, 10638–10644.

13 F. E. Massoth, P. Politzer, M. C. Concha, J. S. Murray, J. Jakowski and J. Simons, *J. Phys. Chem. B*, 2006, **110**, 14283–14291.

14 L. Bomont, M. Alda-Onggar, V. Fedorov, A. Aho, J. Peltonen, K. Eränen, M. Peurla, N. Kumar, J. WärnÅ, V. Russo, P. Mäki-Arvela, H. Grénman, M. Lindblad and D. Y. Murzin, *Eur. J. Inorg. Chem.*, 2018, 2841–2854.

15 L. Nie and D. E. Resasco, *J. Catal.*, 2014, **317**, 22–29.

16 M. Hellinger, H. W. Carvalho, S. Baier, D. Wang, W. Kleist and J.-D. Grunwaldt, *Appl. Catal., A*, 2015, **490**, 181–192.

17 H. Lee, H. Kim, M. Yu, C. H. Ko, J.-K. Jeon, J. Jae, S. Park, S.-C. Jung and Y.-K. Park, *Sci. Rep.*, 2016, **6**, 28765.

18 A. Bjelić, M. Grilc and B. Likozar, *Chem. Eng. J.*, 2018, **333**, 240–259.

19 A. Prestianni, F. Ferrante, E. M. Sulman and D. Duca, *J. Phys. Chem. C*, 2014, **118**, 21006–21013.

20 F. Ferrante, A. Prestianni, M. Bertini and D. Duca, *Catalysts*, 2020, **10**, 1306.

21 F. Ferrante, A. Prestianni, R. Cortese, R. Schimmenti and D. Duca, *J. Phys. Chem. C*, 2016, **120**, 12022–12031.

22 K. Koichumanova, A. K. K. Vikla, R. Cortese, F. Ferrante, K. Seshan, D. Duca and L. Lefferts, *Appl. Catal., B*, 2018, **232**, 454–463.

23 L. Gueci, F. Ferrante, A. Prestianni, F. Arena and D. Duca, *Mol. Catal.*, 2021, **513**, 111735.

24 C. González, P. Marín, F. V. Díez and S. Ordóñez, *Ind. Eng. Chem. Res.*, 2016, **55**, 2319–2327.

25 C. Liu, H. Tao, C. Lian and H. Liu, *J. Phys. Chem. C*, 2022, **126**, 9724–9735.

26 S. Tieuli, P. Mäki-Arvela, M. Peurla, K. Eränen, J. Wärnà, G. Cruciani, F. Menegazzo, D. Y. Murzin and M. Signoretto, *Appl. Catal., A*, 2019, **580**, 1–10.

27 P. Mäki-Arvela and D. Y. Murzin, *Catalysts*, 2017, **7**, 265.

28 C. Lindfors, P. Mäki-Arvela, P. Paturi, A. Aho, K. Eränen, J. Hemming, M. Peurla, D. Kubička, I. L. Simakova and D. Y. Murzin, *ACS Sustainable Chem. Eng.*, 2019, **7**, 14545–14560.

29 M. Alda-Onggar, P. Mäki-Arvela, K. Eränen, A. Aho, J. Hemming, P. Paturi, M. Peurla, M. Lindblad, I. L. Simakova and D. Y. Murzin, *ACS Sustainable Chem. Eng.*, 2018, **6**, 16205–16218.

30 M. Alda-Onggar, P. Mäki-Arvela, A. Aho, I. Simakova and D. Murzin, *React. Kinet., Mech. Catal.*, 2019, **126**, 737–759.

31 C. Zhao, S. Kasakov, J. He and J. A. Lercher, *J. Catal.*, 2012, **296**, 12–23.

32 L. Gueci, F. Ferrante, A. Prestianni, R. Di Chio, A. F. Patti, D. Duca and F. Arena, *Inorg. Chim. Acta*, 2020, **511**, 119812.

33 F. Arena, F. Ferrante, R. Di Chio, G. Bonura, F. Frusteri, L. Frusteri, A. Prestianni, S. Morandi, G. Martra and D. Duca, *Appl. Catal., B*, 2022, **300**, 120715.

34 V. D'Anna, D. Duca, F. Ferrante and G. La Manna, *Phys. Chem. Chem. Phys.*, 2010, **12**, 1323–1330.

35 R. Schimmenti, R. Cortese, F. Ferrante, A. Prestianni and D. Duca, *Phys. Chem. Chem. Phys.*, 2016, **18**, 1750–1757.

36 R. B. King, *Applications of graph theory and topology in inorganic cluster and coordination chemistry*, CRC Press, 1993.

37 I. Demiroglu, K. Yao, H. A. Hussein and R. L. Johnston, *J. Phys. Chem. C*, 2017, **121**, 10773–10780.

38 M. Brack, *Sci. Am.*, 1997, **277**, 50–55.

39 G. Barone, D. Duca, F. Ferrante and G. La Manna, *Int. J. Quantum Chem.*, 2010, **110**, 558–562.

40 F. Ferrante, C. Nania and D. Duca, *Mol. Catal.*, 2022, **529**, 112541.

41 J. A. Maga and I. Katz, *Crit. Rev. Food Sci. Nutr.*, 1978, **10**, 323–372.

42 A. M. Verma and N. Kishore, *R. Soc. Open Sci.*, 2017, **4**, 170650.

43 J. Lu, S. Behtash, O. Mamun and A. Heyden, *ACS Catal.*, 2015, **5**, 2423–2435.

44 K. Lee, G. H. Gu, C. A. Mullen, A. A. Boateng and D. G. Vlachos, *ChemSusChem*, 2015, **8**, 315–322.

45 D. Gao, C. Schweitzer, H. T. Hwang and A. Varma, *Ind. Eng. Chem. Res.*, 2014, **53**, 18658–18667.

46 M. J. Frisch, G. W. Trucks, H. B. Schlegel, G. E. Scuseria, M. A. Robb, J. R. Cheeseman, G. Scalmani, V. Barone, G. A. Petersson, H. Nakatsuji, X. Li, M. Caricato, A. V. Marenich, J. Bloino, B. G. Janesko, R. Gomperts, B. Mennucci, H. P. Hratchian, J. V. Ortiz, A. F. Izmaylov, J. L. Sonnenberg, D. Williams-Young, F. Ding, F. Lipparini, F. Egidi, J. Goings, B. Peng, A. Petrone, T. Henderson,

10470 | *Phys. Chem. Chem. Phys.*, 2023, **25**, 10460–10471

This journal is © the Owner Societies 2023

D. Ranasinghe, V. G. Zakrzewski, J. Gao, N. Rega, G. Zheng, W. Liang, M. Hada, M. Ehara, K. Toyota, R. Fukuda, J. Hasegawa, M. Ishida, T. Nakajima, Y. Honda, O. Kitao, H. Nakai, T. Vreven, K. Throssell, J. A. Montgomery, Jr., J. E. Peralta, F. Ogliaro, M. J. Bearpark, J. J. Heyd, E. N. Brothers, K. N. Kudin, V. N. Staroverov, T. A. Keith, R. Kobayashi, J. Normand, K. Raghavachari, A. P. Rendell, J. C. Burant, S. S. Iyengar, J. Tomasi, M. Cossi, J. M. Millam, M. Klene, C. Adamo, R. Cammi, J. W. Ochterski, R. L. Martin, K. Morokuma, O. Farkas, J. B. Foresman and D. J. Fox, *Gaussian 16, Revision C.01*, 2016.

47 A. D. Becke, *J. Chem. Phys.*, 1993, **98**, 1372–1377.

48 S. Grimme, J. Antony, S. Ehrlich and H. Krieg, *J. Chem. Phys.*, 2010, **132**, 154104.

49 P. J. Hay and W. R. Wadt, *J. Chem. Phys.*, 1985, **82**, 270–283.

50 P. J. Hay and W. R. Wadt, *J. Chem. Phys.*, 1985, **82**, 299–310.

51 T. H. Dunning and P. J. Hay, in *Methods of Electronic Structure Theory*, ed. H. F. Schaefer, Springer, US, 1977, pp. 1–27.

52 B. P. Pritchard, D. Altarawy, B. Didier, T. D. Gibson and T. L. Windus, *J. Chem. Inf. Model.*, 2019, **59**, 4814–4820.

53 S. F. Boys and F. Bernardi, *Mol. Phys.*, 1970, **19**, 553–566.

54 R. Réocreux, C. A. Ould Hamou, C. Michel, J. B. Giorgi and P. Sautet, *ACS Catal.*, 2016, **6**, 8166–8178.

55 A. M. Verma and N. Kishore, *Chem. Select*, 2016, **1**, 6196–6205.

56 M. Saeys, M.-F. Reyniers, M. Neurock and G. B. Marin, *J. Phys. Chem. B*, 2005, **109**, 2064–2073.

57 T. Bera, J. W. Thybaut and G. B. Marin, *Ind. Eng. Chem. Res.*, 2011, **50**, 12933–12945.

58 L. Lozano, G. B. Marin and J. W. Thybaut, *Ind. Eng. Chem. Res.*, 2017, **56**, 12953–12962.

59 K. Lee, G. H. Gu, C. A. Mullen, A. A. Boateng and D. G. Vlachos, *ChemSusChem*, 2015, **8**, 315–322.

60 H. Zhai and A. N. Alexandrova, *ACS Catal.*, 2017, **7**, 1905–1911.

61 L. Gueci, F. Ferrante, A. Prestianni, F. Arena and D. Duca, *Data Brief*, 2021, **38**, 107369.
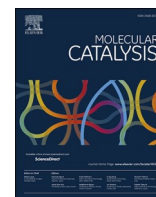
This journal is © the Owner Societies 2023

Phys. Chem. Chem. Phys., 2023, **25**, 10460–10471 | **10471**

Computational investigation of isoeugenol transformations on a platinum cluster—II: Deoxygenation through hydrogenation to propylcyclohexane

Chiara Nania , Francesco Ferrante [*] , Marco Bertini , Laura Gueci , Dario Duca

Dipartimento di Fisica e Chimica "Emilio Segrè" - Università degli Studi di Palermo, Viale delle Scienze Ed. 17, I-90128 Palermo, Italy

ARTICLE INFO

ABSTRACT

The debate on climate change and the future of our Planet has brought to general attention the problem of fossil fuels (coal, oil and natural gas), among the main causes of pollution on Earth. At the same time, the necessity to encourage research and development of alternative and renewable energy resources has become increasingly relevant. In this context, biomass is an attractive option to produce biofuels and chemicals currently derived from petroleum. The hydrodeoxygenation process of bio-oils, produced by the rapid pyrolysis of biomass, is the most effective strategy for obtaining biofuels, hence the reason for the investigation of its mechanism on model biomass compounds. Having investigated the direct deoxygenation (DDO) mechanims in the first paper of this series, the present work aims to illustrate the deoxygenation-through-hydrogenation (HYD) mechanism, by which isoeugenol, a compound chosen as a model of bio-oils, is converted into propylcyclohexane on a ten-atom platinum cluster. DFT calculations highlight, from kinetic and thermodynamic perspectives, how the formation of propylcyclohexane takes place through 4-propyl-2-methoxycyclohexane-1-ol, the removal of $-OCH_3$ as methanol and then of the $-OH$ group as water. Microkinetic analysis, performed by joining findings on both DDO and HYD routes, reveals that the isoeugenol DDO mechanism is favored at any selected temperatures.

1. Introduction

The impending depletion of fossil fuels, joined to the growing concerns for environmental protection, increases the global demand for renewable energy [1,2]. Lignocellulosic biomass has been identified as an attractive feedstock for the production of biofuels and chemicals because the involved energy can be harnessed directly by combustion or indirectly by conversion to gas or liquid fuel [3,4]. Among the several biomass conversion technologies, rapid pyrolysis followed by hydro-deoxygenation (HDO) has received the most attention because it is capable of transforming the solid and low-density biomass into a vehicle fuel that is CO_2-neutral and not affected by SO_x emissions, in virtue of its negligible sulfur content [5,6]. Through pyrolysis, essentially any biomass source can be converted into bio-oil. Although remarkably more energy dense than the original biomass, bio-oils have a low calorific value compared to crude oils and a low shelf life; moreover, being viscous and polar they are unsuitable as motor fuels [7,8]. These characteristics are associated with their high water and oxygen content. However, since bio-oils have a higher volumetric energy density and are easier to handle than biomass, they would be more suitable for transportation and further processing [9,10]. The purpose of upgrading bio-oils is therefore to remove oxygenated groups so as to increase thermal and chemical stability, heating value and volatility [11–13]. Among the suitable methods to achieve these goals, the HDO process, which involves the challenging C–O bond cleavage reaction, is considered the most efficient technology [14–16]. Since the mixtures of several hundred compounds can be extracted from biomass, the only possible strategy to better understand the catalytic upgrading process involves mechanistic investigation of model compounds representative of ligno-cellulosic biomass. The simplest of such models are phenolic monomers, like phenol, anisole, guaiacol, eugenol and isoeugenol. Their HDO reactions have all been extensively studied, as demonstrated by the comprehensive review work conducted by Gollakota and coworkers [17], both from the experimental and modeling perspective [5,18–21]. For example, the hydrodeoxygenation mechanism of anisole was recently investigated on clean and H-covered Ni(111) surfaces by using computational techniques [22]. Based on calculated energies, a microkinetic modeling was built, which approximately simulated the real catalytic system under different conditions of temperature and H_2 pressure. It predicted outcome distributions with phenol and

* Corresponding author.
  E-mail address: francesco.ferrante@unipa.it (F. Ferrante).

methylcyclohexane as the main products for the clean and hydrogenated surfaces, respectively, providing a mechanistic understanding for anisole conversion under different experimental conditions. Saleheen et al. [23] investigated the solvent effect on the hydrodeoxygenation mechanism of guaiacol catalyzed by Pt terrace sites, employing DFT calculations and microkinetic modeling. Their study revealed that the most favorable pathway involved dehydrogenation at the hydroxyl and methoxy groups of guaiacol, resulting in catechol as the major reaction product in all environments. Despite observing higher hydrodeoxygenation rates in less protic solvents, the persistent lack of deoxygenation activity of Pt terrace sites suggested that Pt(111) is not the active site for guaiacol deoxygenation. Nonetheless, the reported findings are interesting as they offer insights into the reaction chemistry under realistic process scenarios.

By containing the most important functional groups present in lignin-derived bio-oils, namely the hydroxyl, methoxyl, and allyl ones, isoeugenol emerges as a suitable and representative molecular model for atomistic studies of reactions involved in the biomass conversion, hence the reason for its choice in the present work. Isoeugenol [24,25] can be extracted from natural sources (cloves, nutmeg and ylang-ylang, of which it is the main component) or synthesized in laboratory. It is commonly used in food industries as antioxidant and flavoring agent, as well as in medicine as local antiseptic, analgesic, anti-inflammatory and anti-arthritic. It is also the starting material for the synthesis of vanillin and vanillic acid. Several reaction pathways have been proposed in the literature for the HDO of isoeugenol and phenolic derivatives: (i) hydrogenation followed by deoxygenation (HYD), which is based on sequential hydrogenation of the aromatic ring followed by removal of the oxygenated groups [26,27]; (ii) direct deoxygenation (DDO) in which there is first dissociation of the C–O bonds and then hydrogenation of the benzene ring [28,29]; and (iii) tautomerization [30,31]. In our previous study, hencefort indicated as paper I [32], a computational mechanistic analysis of the HDO reaction of isoeugenol on a Pt_10 platinum cluster was carried out following the DDO mechanism mentioned above. In the present study the investigation of the branching reaction pathways that ponder the HYD-type mechanisms is reported, as part of a broader project which has the purpose to completely elucidate the entire reaction path, characterizing the HDO process on a subnanometric platinum catalyst in the presence of molecular hydrogen. The knowledge of the HDO atomistically-detailed mechanism as occurring on the isolated cluster allows one to discriminate the most important elementary steps, thus creating a reference for computational investigations on clusters in the subnanometric size regime. This could pave the way to corresponding, more cumbersome, studies on supported clusters [33–36] under molecular hydrogen. By exploring the most recent literature, it can be considered that the experimental counterpart of the catalytic model employed in the present study could be atomically precise platinum clusters such as the Pt_n (n = 5–13) species obtained on carbon black by Imaoka et al. [37] through low-temperature calcination of platinum organothiolate complexes under hydrogen stream, or those realized by Schmitt et al. [38] by using a continuous-flow approach (commonly applied to organic synthesis) that has both the advantages of being reproducible and providing high yields, thus making it appealing for industrial-scale development. The synthesis of subnanometric Pt clusters proposed by Xiang et al. [39], on the other hand, was performed with solvothermal and deposition-precipitation methods, using H_2PtCl_6 as precursor and $CeFeO_x$ as support; it was followed by catalyst characterization revealing the presence of single Pt atoms on the oxide surface as well as small Pt clusters. Zhang et al. [40], finally, use zeolite with different topologies as support for metal (Pt, Pd, and Rh) clusters. They observed that the introduction of Sn into the zeolite framework generates anchoring sites for the metal clusters, thus preventing sintering during the high-temperature oxidation-reduction treatments.

2. Computational details and models

All the calculations were performed using density functional theory (DFT) as implemented in the Gaussian 16 package [41]. The B3LYP hybrid exchange-correlation functional [42] was used joined with the D3 correction scheme developed by Grimme [43], which allows to empirically correct for the contribution of dispersion interactions. The study of HDO reaction on the platinum cluster was carried out by using the LANL2DZ basis set [44,45]; this employs Dunning's basis set (D95) [46] for light atoms and a double-zeta valence basis set associated to an effective core potential for platinum. Primitive gaussians with the role of polarization functions were added to light atoms in accordance with the following scheme: H (s: 0.049, p: 0.587), C (p: 0.0311, d: 0.587), O (p: 0.0673, d: 0.961). The values of the exponents were taken from the EMSL Basis Set Exchange website [47]. Minima and transition state (TS) species on the reaction pathways were checked by inspection of the harmonic vibrational frequencies. The energetics of the investigated reaction pathways are accordingly reported in terms of vibrational zero-point corrected energies (E_{ZPV}). Desorption energies were corrected for the basis set superposition error (BSSE) by using the counterpoise method of Boys and Bernardi [48]; given that BSSE values were calculated as correction to the SCF energies, they are reported in parentheses together with the uncorrected E_{ZPV} energies.

A regular tetracapped octahedron platinum cluster shaped by ten atoms (considered as a magic number [49]), having T_d symmetry and spin multiplicity equal to 9 was chosen as subnanometric catalyst model. According to DFT calculations reported in the literature [50], this Pt_10 cluster is a global minimum in its potential energy surface. Its structure shows the presence of atoms with different coordination: the four cap atoms actually have coordination number (CN) 3, and the remaining six atoms have CN 6 [18,32]. In passing, it is recalled that, in the work of Imaoka et al. [37], Pt_10 resulted to be the most active catalyst for stirene hydrogenation, supporting the here modeling choice.

Finally, it has to be noted that two assumptions, commonly performed in investigations like the present one, persist: i) the H_2 molecule easily breaks on the cluster with minimal activation energy, allowing atomic hydrogen to diffuse freely and be available where needed; the validity of this assumption for Pt_10 was, in particular, confirmed in paper I, and ii) the barriers for overcoming possible geometric rearrangements of intermediates and fragments on the cluster are lower than the energy barriers related with their transformations.

3. Results and discussion

The HYD mechanism of isoeugenol involves, after the formation of dihydroeugenol by hydrogenation of the double bond on the allyl chain, the complete hydrogenation of the aromatic ring and next the removal of the oxygenated groups. As illustrated in Scheme 1, the sequence of the chemical intermediates from 4-propyl-2-methoxycyclohexan-1-ol indicates four distinct routes for removing the oxygenated groups to obtain propylcyclohexane. These routes are briefly summarized below:

- **HYD-1** involves the removal of the –OCH_3 group as methanol and the subsequent water loss, from 4-propylcyclohexan-1-ol.
- **HYD-2** involves initially the elimination of –OH as water, resulting in 1-methoxy-3-propylcyclohexane, from which methanol is removed to form propylcyclohexane.
- **HYD-3** involves the formation of 3-propylcyclohexan-1-ol by conversion of the OCH_3 fragment to OH due to the elimination of the CH_3 fragment as methane and the hydrogenation of the dangling oxygen in the adsorbed structure.
- **HYD-4** involves the formation of 4-propylcyclohexane-1,2-diol, which leads to propylcyclohexane by subsequent elimination of two water molecules.

The ring saturation follows a Horiuti-Polanyi scheme, involving the
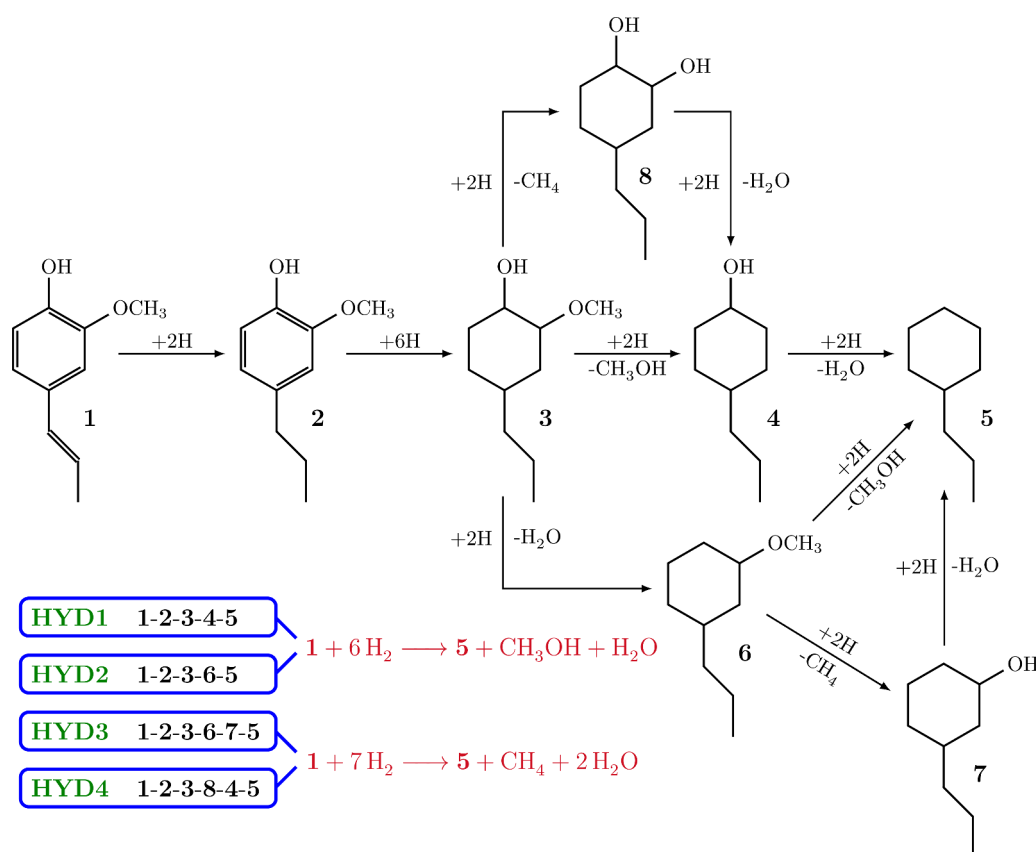
Scheme 1. Isoeugenol conversion to propylcyclohexane according to HYD mechanism: schematic representation of the four reaction pathways.

consecutive addition of hydrogen adatoms [51]. It was observed that, after the first H atom is added, the subsequent addition of atoms always occurs at the *ortho* position to the pre-existing one(s), see Fig. 1. For the addition of the first H atom, all carbon sites in the ring were considered as potentially hydrogenable. The calculated values for the energy barriers and relative stabilities of the intermediates suggest that the first site to undergo hydrogenation is C3; an energy barrier of 105.0 kJ mol^{-1} is required for this process. In agreement with the observation above, the two *ortho* positions at C3 were taken into account for the addition of the second H atom. Following Fig. 1, hydrogenation on C2 appears significantly favored because of a lower energy barrier (57.0 vs. 127 kJ mol^{-1}) and a higher stability of the resulting intermediate **II**, the 6-methoxy-4-propylcyclohexa-1,3-dien-1-ol/Pt$_1$0, species (43.6 vs. 57.0 kJ mol^{-1}). For the latter, a desorption energy from the cluster of 262.5 (BSSE = 31.1) kJ mol^{-1} was calculated. For the addition of the next H atom, the carbon atoms C1 and C4 were considered as reactive centers to originate intermediate III. Hydrogenation on C1 however appeared quite favored by virtue of a larger stability of about 48.0 kJ mol^{-1}. An activation barrier of 71.9 kJ mol^{-1} governs the formation of intermediate **IV** (6-methoxy-4-propylcyclohex-3-en-1-ol/Pt$_1$0), from which by hydrogenation of C4, and crossing an energy barrier of 45.7 kJ mol^{-1}, intermediate **V** is obtained. Finally, the last H atom added on C5 leads to the formation of 2-methoxy-4-propylcyclohexan-1-ol/Pt$_1$0 surface species, which is at an energy of 69.9 kJ mol^{-1} with respect to the species **IV+2H**. It is worth to note that an activation barrier of 39.3 kJ mol^{-1} is required for this last step, which is significantly lower than those calculated for the hydrogenations of the individual carbon atoms of the ring.

In agreement to what is known about substituents effects in aromatic reactions, the ring carbon atoms that preferentially undergo hydrogenation are those at the *ortho* and *para* positions to the oxygenated substituents. By pushing electronic density, these latters make in fact the

ring more reactive to the attack of a hydrogen atom. It is possible to conclude, however, that hydrogenation of dihydroeugenol is disadvantaged if compared to propylbenzene hydrogenation, which has been pursued in DDO mechanisms (paper I). This may be due to greater substrate-cluster interactions when oxygenated groups are present, resulting, among the other effects, also from the high fluxionality of the platinum cluster. Furthermore, another effect contributing to the inhibition of the hydrogenation can be also invoked: in isoeugenol, the *ortho* position with respect to one oxygenated site corresponds to the *meta* position with respect to the other oxygenated one, so partially eliminating the beneficial effect on the fragment reactivity arising from the electron density donation.

3.1. HYD-1

This mechanism (represented in Fig. 2) first implies the removal of methanol determining the production of 4-propylcyclohexan-1-ol followed by the formation of propylcyclohexane caused by the expulsion of one H$_2$O molecule. The first elementary step involves, by crossing an energy barrier of 149.2 kJ mol^{-1}, the cleavage of the C2–O bond in the 2-methoxy-4-propylcyclohexan-1-ol with chemisorption of the OCH$_3$ fragment between the two metal centers of the upper portion of a cluster edge. By comparison, in the loss of OCH$_3$ from dihydroeugenol (paper I), the energy of the transition state is sensibly higher (by *ca.* 40 kJ mol^{-1}) but the reaction is significantly more exothermic (again, by *ca.* 40 kJ mol^{-1}). This could be because, in the case of 2-methoxy-4-propylcyclohexan-1-ol, in the TS there is no stabilization due to the hydrogen bonds interactions, as the OH group is engaged with the metal, while the product is much more stable than the reactant because the O-Pt interaction is replaced by the stronger C-Pt one. The (int1+OCH$_3$)/Pt$_1$0 intermediate, formed following an energy release of 60.5 kJ mol^{-1}, undergoes the fragmentation of a H$_2$ molecule, required to proceed with
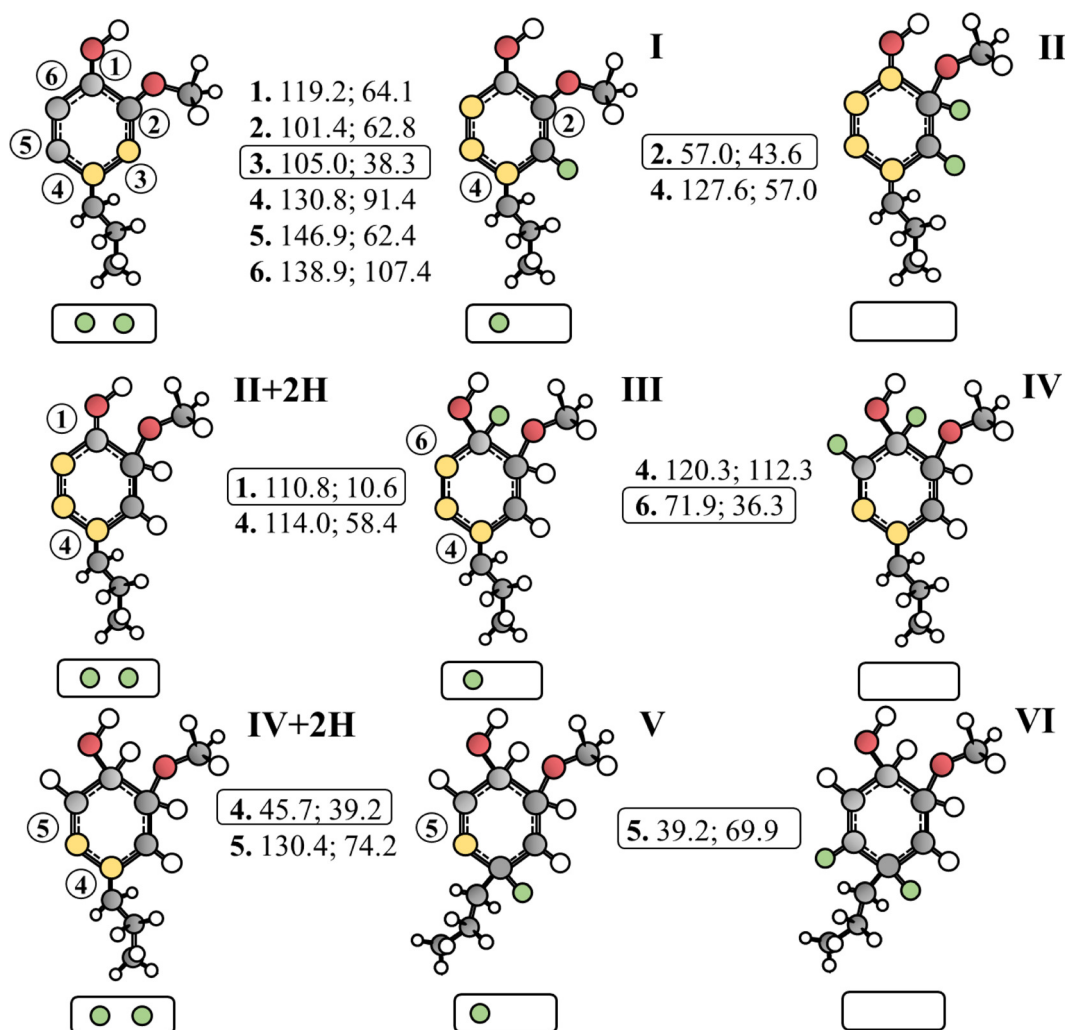
Fig. 1. Schematic depiction of the full saturation of isoeugenol phenyl ring on the $Pt_1 0$ cluster. The latter is represented by the small rectangle below the molecular species; adatoms are shown as green circles within the rectangle, those not-adsorbed are not shown; the yellow circles represent the interaction sites of the molecule with the cluster. In each entry, the first number represents the position where the catalytic hydrogen is added, the second is the energy barrier of the corresponding elementary step, and the third is the energy of the product, always taken with respect to the energy of the reactant with two H atoms still on $Pt_1 0$. All energy values are expressed in kJ mol^{-1}. The first hydrogenation starts from dihydroeugenol, the second from **II+2H** (6-methoxy-4-propylcyclohexa-1,3-dien-1-ol/$Pt_{10}2H$), the last from **IV+2H** (6-methoxy-4-propylcyclohex-3-en-1-ol/$Pt_{10}2H$) and leads to 2-methoxy-4-propylcyclohexan-1-ol/$Pt_1 0$.

the reaction. Thus, in the second elementary step, hydrogenation of the OCH_3 fragment occurs with formation of the CH_3OH molecule, for which a desorption energy of 89.7 (BSSE = 8.9) kJ mol^{-1} was calculated. The int1/$Pt_{10}H$ species, through the hydrogenation on unsaturated C2, leads to the formation of the 4-propylcyclohexan-1-ol, for which the calculated desorption energy is 138.3 kJ mol^{-1} (BSSE = 20.6 kJ mol^{-1}). The latter is lower than the energy barrier of the next stage (178.0 kJ mol^{-1}) that, by C1–OH bond breakage, leads to propylcyclohexane. This would seem to suggest that just a small fraction of molecules should be able to acquire the sufficient energy for proceeding with the reaction. The 178 kJ mol^{-1} barrier is in fact much higher than the one relating to the dehydroxylation of propylphenol (115 kJ mol^{-1}, paper I). This may be due to the fact that, while in the case of propylphenol the molecule was strongly interacting with the cluster by virtue of the presence of the phenyl, in this case, due to the steric hindrance along with the weak interactions between the cyclohexane residue and the cluster — mainly caused by the lack of the anchoring effect owing to the absence of the fragment containing the hydroxyl oxygen — the migration of the –OH group occurs between two terminal fragments well-nigh separated from each other. The resulting (int2+OH)/$Pt_1 0$ species is characterized by the presence of the OH fragment placed between two Pt atoms on an edge of

the cluster, and by int2 interacting only via C1 with the platinum atom at the apical position.

The fragmentation of an additional H_2 molecule enables the desorption of water and the formation of propylcyclohexane. Therefore, an H atom is added to the oxygen atom of the OH fragment (energy barrier of 87.7 kJ mol^{-1}) with an energy release of 12.2 kJ mol^{-1} for the formation of the (int2+H_2O)/$Pt_1 0$ species. From the latter there is desorption of the H_2O molecule, a process whereby the calculated energy is 37.8 kJ mol^{-1} with a BSSE of 5.4 kJ mol^{-1}. The other adatom, by crossing an energy barrier of 47.9 kJ mol^{-1}, is responsible for the formation of propylcyclohexane/$Pt_1 0$; the calculated energy for its desorption was 97.5 (BSSE = 21.1) kJ mol^{-1}.

3.2. HYD-2 and HYD-3

The second reaction pathway involves the elimination of the –OH group as water with the formation of 1-methoxy-3-propylcyclohexane, from which elimination of methanol follows, leading to propylcyclohexane. The first elementary surface transformation, characterized by an energy barrier of 164.0 kJ mol^{-1}, concerns the cleavage of the C1–O bond in the 2-methoxy-4-propylcyclohexane-1-ol and leads, with a
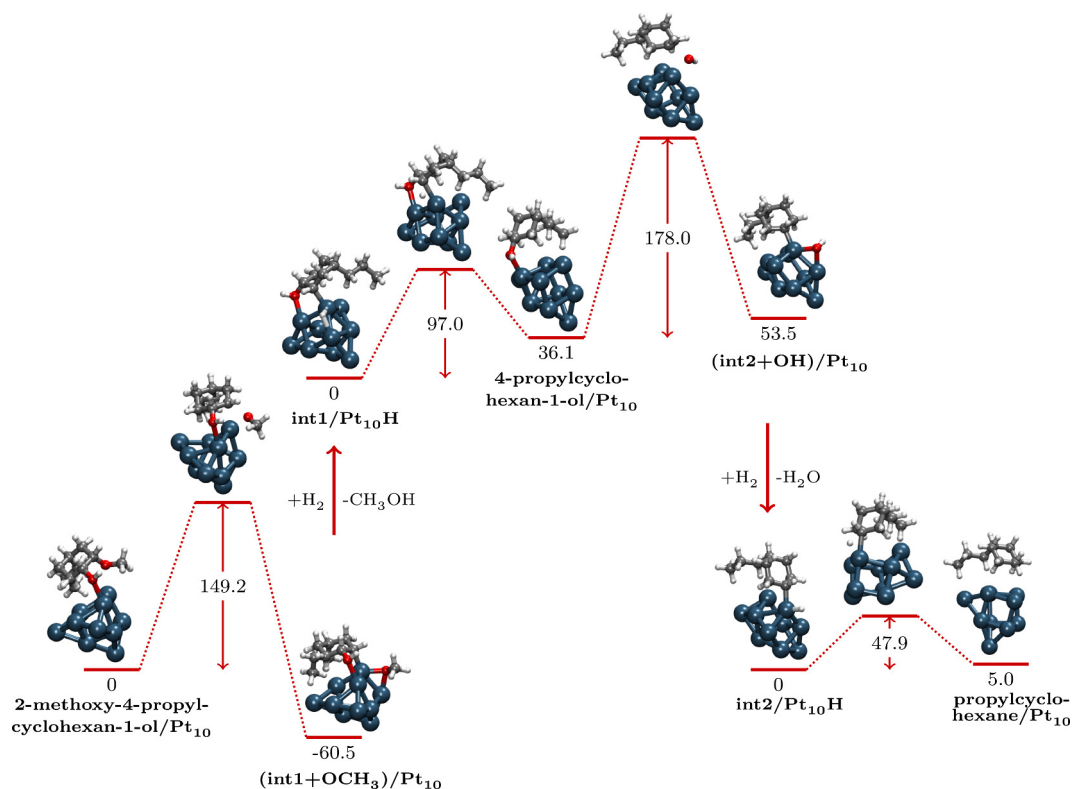
Fig. 2. Reaction profile for HYD-1 mechanism, showing cleavage of the C–OCH$_3$ bond with adsorption of the OCH$_3$ fragment on a side edge of the cluster. After addition of one H$_2$ molecule and desorption of methanol, the formation of 4-propylcyclohexan-1-ol occurs, from which the C–OH bond is broken. The OH fragment, by addition of another H$_2$ molecule, is hydrogenated and desorbed as H$_2$O. Finally, the hydrogenation of the unsaturated carbon, produces propylcyclohexane.

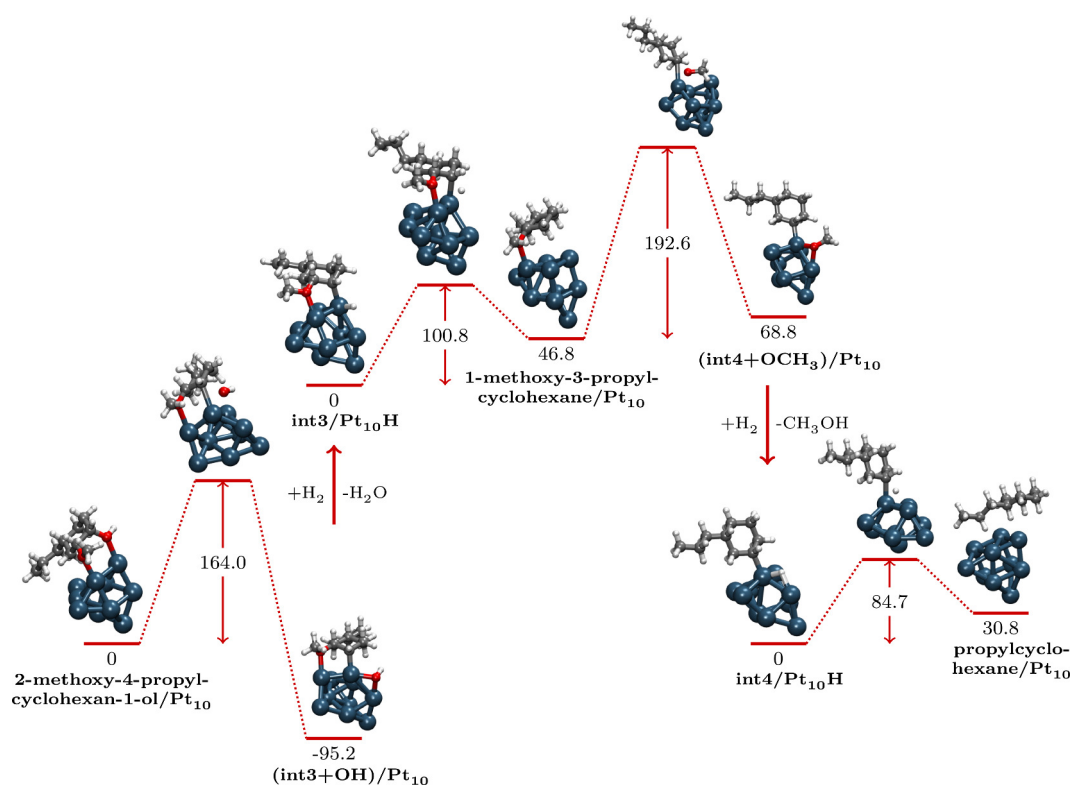**Fig. 3.** Reaction profile corresponding to the HYD-2 mechanism: breakage of the C–OH bond with adsorption of the OH fragment, hydrogenation of the unsaturated carbon with formation of 1-methoxy-3-propylcyclohexane, subsequent cleavage of the C--OCH$_3$ bond and hydrogenation of the unsaturated carbon atom to obtain propylcyclohexane. Fragmentation of two H$_2$ molecules is required for these stages.

considerable energy release of 95.2 kJ mol^{-1}, to the (int3+OH)/Pt$_1$0 species (Fig. 3). On the platinum cluster, in order to proceed with the reaction, a H$_2$ molecule is fragmented. In the next elementary step, there is an H-atom migration from the cluster to the unsaturated C1 (energy barrier of 100.8 kJ mol^{-1}) with formation of the 1-methoxy-3-pro-pylcyclohexane/Pt$_1$0, with the molecular species that can desorb from the cluster clearing an energy barrier of 139.6 (BSSE = 21.9) kJ mol^{-1}.

From the 1-methoxy-3-propylcyclohexane/Pt$_1$0 the removal of the OCH$_3$ fragment might lead to the production of methanol or methane wherein the oxygen atom remains dangling. In the former case there is cleavage of the C--OCH$_3$ bond, characterized by an energy barrier of 192.6 kJ mol^{-1}, with formation of the (int4+OCH$_3$)/Pt$_1$0 species. From this, in turn, by hydrogenation of the OCH$_3$ fragment and subsequent transfer of one H atom to the unsaturated carbon atom, propylcyclo-hexane/Pt$_1$0 is obtained (Fig. 3).

The second case defines the HYD-3 mechanism, reported in Fig. 4, where the cleavage of the O--CH$_3$ bond requires the overcoming of an energy barrier of 180.5 kJ mol^{-1}, leading to the formation of the (int5+CH$_3$)/Pt$_1$0 species. This is less stable than the previous interme-diate by about 52 kJ mol^{-1}. From the species (int5+CH$_3$)/Pt$_1$0 thus the elimination of methane by hydrogenation of the CH$_3$ fragment occurs, followed by the hydrogenation of the dangling oxygen belonging to the int5 species. The next step, which is characterized by an energy barrier of 118.4 kJ mol^{-1}, leads to the formation of 3-propylcyclohexane-1-ol/ Pt$_1$0 from which, chemisorbed propylcyclohexane is generated *via* loss of a H$_2$O molecule and saturation of C1.

3.3. HYD-4

The HYD-4 mechanism considers the removal of methane from 2-methoxy-4-propylcyclohexane-1-ol and the formation of 4-propylcyclo-

hexane-1,2-diol whence, by elimination of two H$_2$O molecules, pro-pylcyclohexane is obtained. The first elementary step involves, through crossing an energy barrier of 164.6 kJ mol^{-1}, the cleavage of the O--CH$_3$ bond with formation of the (int7+CH$_3$)/Pt$_1$0 species (Fig. 4). The latter is characterized by the CH$_3$ fragment adsorbed on the Pt atom at the apical position and the int7 species interacting through the two oxygen atoms with Pt centers showing different coordinations. Methane gen-eration occurs, after fragmentation of a H$_2$ molecule on the cluster, by transfer of a single H atom to the carbon of the CH$_3$ fragment. As a result of *CH$_4$* desorption, the int7/Pt$_{10}$H species marked by the presence of a dangling O atom is obtained. From int7/Pt$_{10}$H there is the hydrogena-tion of oxygen atom to form the 4-propylcyclohexane-1,2-diol/Pt$_1$0 species, for which the calculated desorption energy is 126.2 kJ mol^{-1} with BSSE = 24.3 kJ mol^{-1} (see Fig. 5).

Breakage of the C–OH bond in *para* position with respect to the propyl chain after occurs on the 4-propylcyclohexane-1,2-diol/Pt$_1$0 species, an event for which an energy barrier of 161.0 kJ mol^{-1} must be overcome. The resulting species, (int1+OH)/Pt$_1$0 — being int1 the same residue appearing in the HYD-1 mechanism, Fig. 2, but coadsorbed with OH — is more stable than 4-propylcyclohexane-1,2-diol/Pt$_1$0 by *ca.* 99 kJ mol^{-1}. A new H$_2$ molecule is then fragmented on the cluster in order to remove water thus obtaining propylcyclohexanol.

Hence, after that another hydrogen molecule fragments on the cluster, there is the H atom transfer to the O atom of the OH fragment (energy barrier equal to 106.3 kJ mol^{-1}) with the subsequent H$_2$O for-mation. Following its desorption from the cluster, the remaining int1/ Pt$_{10}$H species connects HYD-4 to the already discussed HYD-1 mecha-nism.

4. Kinetic analysis

In the previous section the four possible routes were discussed, ac-
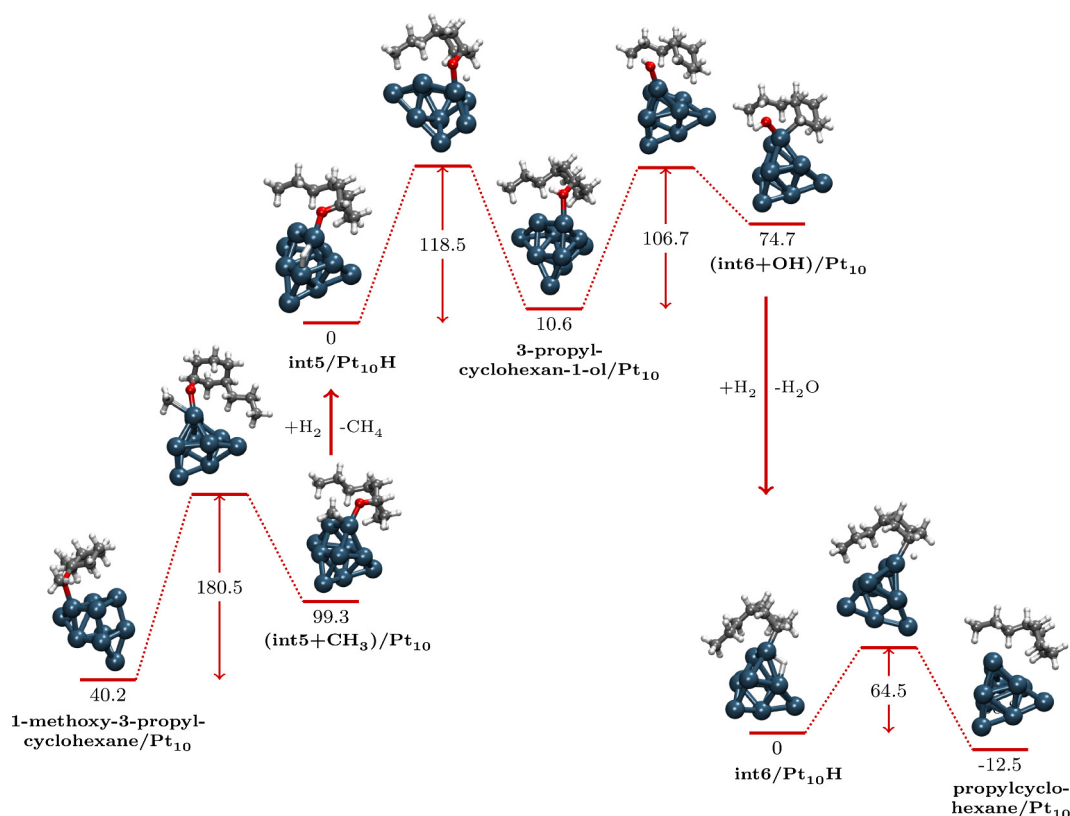
Fig. 4. The reaction profile according with the HYD-3 mechanism, describes: cleavage of the O--CH$_3$ bond from the 1-methoxy-3-propylcyclohexane/Pt$_1$0, hy-drogenation of the CH$_3$ fragment with methane formation, and restoration of the –OH functionality ruling the 3-propylcyclohexanol/Pt$_1$0 formation. From the latter, after the elimination of one water molecule, propylcyclohexane/Pt$_1$0 is formed by hydrogenation of the unsaturated carbon atom.
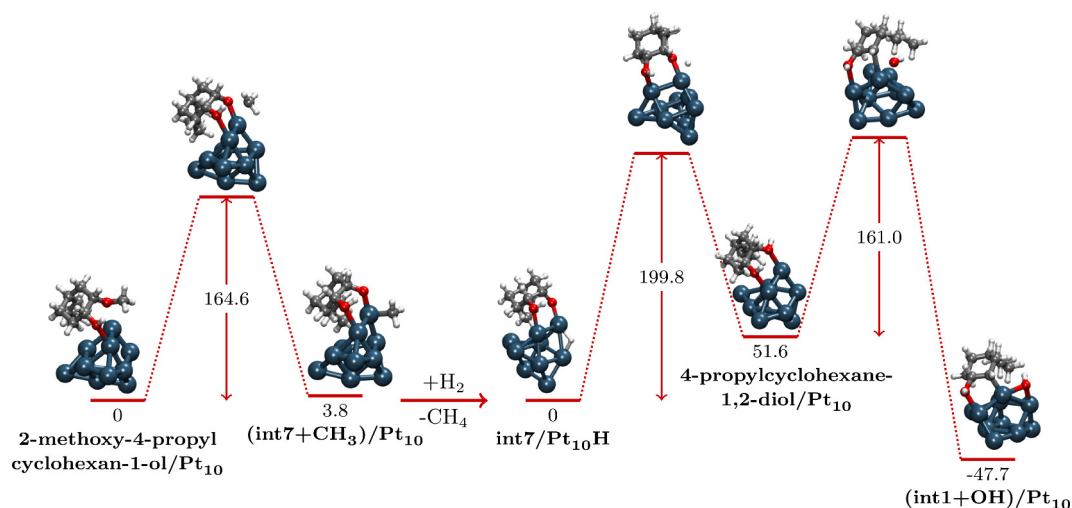
Fig. 5. The reaction profile, which refers to the HYD-4 mechanism, involves the cleavage of the $O-CH_3$ bond in the methoxyl group with adsorption of the CH_3 fragment, which desorbs as methane after hydrogenation; a second H-atom is responsible for restoration of the –OH functionality originating the 4-propylcyclo-hexane-1,2-diol/Pt_10 species; this one evolves to 4-propylcyclohexane-1-ol/Pt_10 as a result of the C–OH bond breaking. The 4-propylcyclohexane-1-ol/Pt_10, as detailed in Fig. 2, leads to propylcyclohexane/Pt_10.

cording to the HYD mechanism, for the conversion of isoeugenol to propylcyclohexane on the Pt_10 cluster. In the first part of the series (paper I), some of the possible routes within the DDO mechanism were detailed [32]. One of these pathways, specifically the DDO-2 route, was further analyzed to ensure comparability and, consequently, discrimination between the two mechanisms, namely DDO and HYD, in terms of both kinetic and thermodynamic aspects. The energetics of the eigth pathways of the two alternative mechanisms, schematized in Fig. 6, suggest, based exclusively on the relative energetics of minima and transition states, that in the early elementary phases following dihydroeugenol formation, hydrogenation of the phenyl ring would appear to be kinetically favored with respect to deoxygenation. Conversely, the latter would seem to be more probable to occur from dihydroeugenol instead of from 4-propyl-2-methoxyclohexan-1-ol, which is the fully hydrogenated product. As a matter of fact, the energy barriers for the elementary steps of deoxygenation in the HYD mechanism are higher by about 40–50 kJ mol^{-1} than the corresponding ones in the DDO mechanism.

However, these inferences do not allow us to identify the path and, on the whole, the fastest mechanism. Therefore, all DFT information was used for an equilibrium microkinetic analysis that employs a new approach, called *Simplified Christiansen Method* (SCM), inspired by Christiansen's algebraic scheme [52], already applied for kinetic analyses of experimental catalytic results [53–56]. Indeed, by using as input the DFT values of the forward and backward energy barriers characterizing the formation of surface species and the desorption energies of reactant and product, the SCM approach returns us the kinetic constants of the different pathways at the selected temperatures.

In order to consider the influence of temperature on reaction rates and desorption processes, the SCM was carried out in terms of Gibbs free energy. The comparison between the data reported in Table 1 — where the Gibbs free energy variations of all the elementary steps occurring on both the HYD and DDO pathways have been collected — and Table 2, shows that the use of Gibbs free energies has a more significant effect on the desorption of stable species than on energy barriers.

The SCM results highlight, as detailed in Table 3, that the pathways
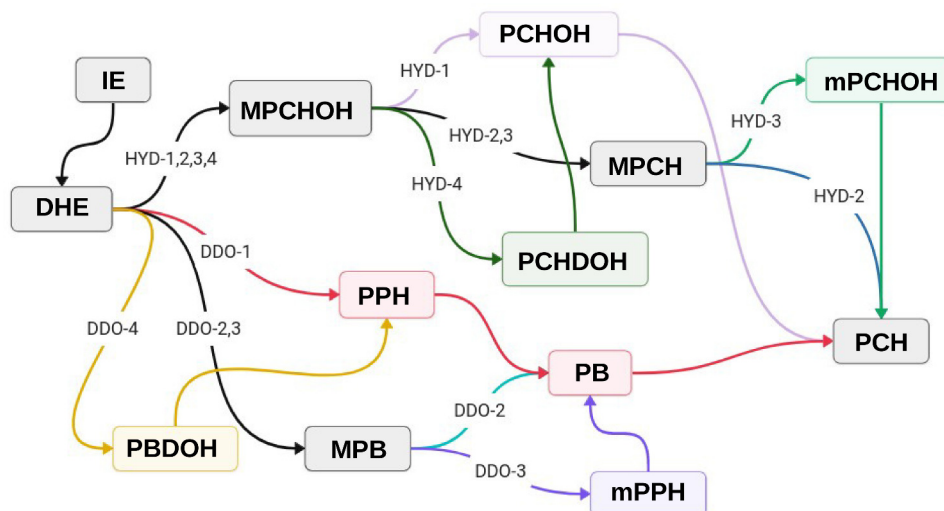
Fig. 6. Visual overview of the eight most important pathways found for the isoeugenol hydrodeoxygenation reaction on Pt_10. The DDO mechanisms are those investigated in paper I. Legend: IE = isoeugenol; DHE = dihydroeugenol; MPCHOH = 2-methoxy-4-propylcyclohexan-1-ol; PCHOH = 4-propylcyclohexan-1-ol; MPCH = 1-methoxy-3-propylcyclohexane; PCHDOH = 4-propylcyclohexan-1,2-diol; mPCHOH = 3-propylcyclohexan-1-ol; PCH = 4-propylcyclohexane; PPH = 4-propylphenol; mPPH = 3-propylphenol; PB = 4-propylbenzene; MPB = 1-methoxy-3-propylbenzene; PBDOH = 4-propylbenzen-1,2-diol.

Table 1

List of the elementary reactions in the HYD and DDO mechanisms with the corresponding standard free energy barriers, $\Delta G^{\#}$, and standard reaction free energies, ΔG, at T = 298.15 K.

	Elementary process[a]	$\Delta G^{\#}$/kJ mol^{-1}	ΔG/kJ mol^{-1}
	HYD pathways		
1	DHE/Pt$_{10}$2H → I	105.7	41.2
2	I → II	60.6	− 12.6
3	II+2H → III	109.4	9.9
4	III → IV	72.0	11.2
5	IV+2H → V	52.4	40.0
6	V → VI	35.6	− 6.7
7	MPCHOH/Pt$_1$0 → (int1+OCH$_3$)/Pt$_1$0	148.3	− 52.8
8	int1/Pt$_{10}$H → PCHOH/Pt$_1$0	99.7	30.3
9	PCHOH/Pt$_1$0 → (int2+OH)/Pt$_1$0	180.3	17.3
10	int2/Pt$_{10}$H → PCH/Pt$_1$0	49.3	7.9
11	MPCHOH/Pt$_1$0 → (int3+OH)/Pt$_1$0	167.5	− 91.9
12	int3/Pt$_{10}$H → MPCH/Pt$_1$0	99.0	40.2
13	MPCH/Pt$_1$0 → (int4+OCH$_3$)/Pt$_1$0	191.3	18.1
14	int4/Pt$_{10}$H → PCH/Pt$_1$0	84.7	30.8
15	MPCH/Pt$_1$0 → (int5+CH$_3$)/Pt$_1$0	180.5	59.1
16	int5/Pt$_{10}$H → mPCHOH/Pt$_1$0	114.6	4.6
17	mPCHOH/Pt$_1$0 → (int6+OH)/Pt$_1$0	168.3	65.3
18	int6/Pt$_{10}$H → PCH/Pt$_1$0	65.0	− 18.4
19	MPCHOH/Pt$_1$0 → (int7+CH$_3$)/Pt$_1$0	167.3	3.9
20	int7/Pt$_{10}$H → PCHDOH/Pt$_1$0	187.1	43.3
21	PCHDOH/Pt$_1$0 → (int1+OH)/Pt$_1$0	167.3	− 4.4
	DDO pathways[b]		
22	IE/Pt$_{10}$2H → int1/Pt$_{10}$H[a]	105.9	88.0
23	int1/Pt$_{10}$H[b] → DHE/Pt$_1$0	119.3	48.6
24	DHE/Pt$_1$0 → (int2+OCH$_3$)/Pt$_1$0	116.9	− 16.7
25	(int3+CH$_3$OH)/Pt$_{10}$2H → (int4+CH$_3$OH)/Pt$_{10}$H	72.4	− 56.6
26	int4/Pt$_{10}$H[b] → PPH/Pt$_1$0	64.1	21.6
27	PPH/Pt$_1$0 → (int5+OH)Pt$_1$0	108.0	− 5.7
28	int6/Pt$_{10}$H → PB/Pt$_1$0	92.7	18.6
29	DHE/Pt$_1$0 → (int2′+CH$_3$)/Pt$_1$0	121.6	− 32.4
30	int2′/Pt$_{10}$H[b] → PBDOH/Pt$_1$0	101.8	68.7
31	PBDOH/Pt$_1$0 → (int3′+OH)/Pt$_1$0	114.4	− 66.6
32	int3′/Pt$_{10}$H[b] → PPH/Pt$_1$0	70.4	− 14.3
33	DHE/Pt$_1$0 → (int7+OH)/Pt$_1$0	123.1[c]	27.1
34	int7/Pt$_{10}$H → MPB/Pt$_1$0	69.5[c]	− 15.3
35	MPB/Pt$_1$0 → (int8+OCH$_3$)/Pt$_1$0	118.9[c]	− 20.4
36	int8/Pt$_{10}$H → PB/Pt$_1$0	80.1[c]	− 10.8
37	MPB/Pt$_1$0 → (int9+CH$_3$)/Pt$_1$0	198.1[c]	− 41.2
38	int9/Pt$_{10}$H → mPPH/Pt$_1$0	164.7[c]	105.8
39	mPPH/Pt$_1$0 → (int10+OH)/Pt$_1$0	156.2[c]	128.0
40	int10/Pt$_{10}$H → PB/Pt$_1$0	53.5[c]	− 1.5
41	PB/Pt$_{10}$2H → I	101.1	53.7
42	I → II	39.2	− 11.6
43	II → III	84.3	36.0
44	III → V	82.4	31.3
45	V → IX	75.6	− 54.9
46	IX → X[d]	110.7	27.6

a See Fig. 6 for the shorthand notation employed for the chemical species.

b The detailed analysis of these pathways is reported in paper I.

c These elementary steps have not been published in paper I, but are reported here for the first time since they were included in the SCM analysis. They correspond to two alternative mechanisms leading to PB. Both are triggered by the C–OH bond breaking, with formation of methoxy-3-propylbenzene (MPB) and water after that one H$_2$ molecule fragments on the cluster. In the first bifurcation, MBP loses its –OCH$_3$ group and a second H$_2$ molecule gives rise to PB and methanol. In the second bifurcation, characterized by very high energy barriers, the O--CH$_3$ bond breaking occurs, leading to methane and 3-prophy-lphenol (mPPH), which then loses the –OH group as water on the way to PB, so requiring one H$_2$ molecule more than the first pathway.

d This corresponds to the PCH/Pt$_1$0 species represented in Scheme 1 of paper I.

Table 2

Standard Gibbs free energies of desorption (T = 298.15 K) for the stable intermediates and products involved in the investigated HYD pathways.

compound[a,d] / ΔG_{des} /kJ mol^{-1}			
IE[b]		130.2	
DHE[b]		85.3	
CP[b]		28.8	
HYD		**DDO**	
MPCHDEOH	190.7	PPH	91.1
MPCHEOH	131.9	PB	77.9
MPCHOH	40.4	MPB	105.9
MPCH	70.4	mPPH	80.1
mPCHOH	54.5	PBDOH	60.8
PCHOH	70.4	PCHDE	176.9
PCHDOH	55.8		
CH$_3$OH[c]	42.5	CH$_3$OH	23.6
H$_2$O	1.4	H$_2$O	50.4
CH$_4$	− 11.8	*CH$_4$*	− 70.9

a See Fig. 6 for the shorthand notation employed for the chemical species; further, in this table the notation MPCHDEOH = 6-methoxy-4-propylcyclohexa-1,3-dien-1-ol; MPCHEOH = 6-methoxy-4-propylcyclohex-3-en-1-ol; PCHDE = 5-propyl-1,3-cyclohexadiene is used. Each molecule is intended adsorbed on the Pt$_1$0 cluster.

b These species are common to all pathways.

c ΔG_{des} of methanol, water and methane are different for HYD and DDO mechanisms because they desorb leaving different species adsorbed on the platinum cluster.

d The desorption process of the A species is $(A + X)/Pt_{10} -> A + X/Pt_{10}$, being X a different species, if any, left adsorbed on the cluster.

Table 3

Reaction rates of the eight isoeugenol HDO mechanisms acording to SCM analysis at various temperature.

	Reaction rate[a]					
	473[b]	573	673	773	873	973
HYD-1	1.1(− 24)	1.8(− 18)	1.9(− 14)	2.0(− 11)	2.3(− 9)	1.5(− 7)
HYD-2	6.6(− 26)	1.2(− 19)	2.5(− 15)	3.3(− 12)	4.4(− 10)	3.3(− 8)
HYD-3	7.5(− 27)	3.3(− 20)	1.1(− 15)	1.9(− 12)	2.9(− 10)	2.4(− 8)
HYD-4	4.5(− 31)	8.8(− 24)	1.1(− 18)	4.6(− 15)	1.6(− 12)	2.6(− 10)
DDO-1	8.1(− 16)	7.2(− 11)	2.0(− 7)	6.5(− 5)	3.1(− 3)	9.6(− 2)
DDO-2	1.6(− 22)	1.0(− 16)	9.9(− 13)	7.8(− 10)	7.7(− 8)	4.2(− 6)
DDO-3	5.4(− 46)	6.2(− 36)	6.3(− 29)	8.2(− 24)	4.2(− 20)	5.1(− 17)
DDO-4	1.7(− 20)	8.6(− 15)	7.4(− 11)	4.9(− 8)	4.2(− 6)	2.1(− 4)

a Reaction rates are expressed in s^{-1}. The power of 10 of scientific notation is given in parenthesis. Gibbs free energies (as a function of temperature, at p = 1 atm) have been considered for the kinetic analysis.

b Temperatures in Kelvin.

and HYD-3 pathways appear to be competitive with each other since, except for the temperature range 673–973 K, they always differ by an order of magnitude. The slowest of the HYD pathways is the fourth, HYD-4, most likely due to the high energy barriers for the formation of 4-propylcyclohexane-1,2-diol and the C–OH bond cleavage from it. This pathway, however, exhibits a faster rate compared to DDO-3, which is the slowest pathway within the DDO mechanism and, consequently, the slowest overall.

At all investigated temperatures, and especially at the higher ones, the HDO reaction of isoeugenol on Pt$_1$0 appears to proceed essentially

in the DDO mechanism are at least two orders of magnitude faster than those in the HYD mechanism. In particular, the HYD-1 pathway, which involves the formation of propylcyclohexane through 4-propylcyclo-hexan-1-ol, is the fastest HYD pathway. On the other hand, the HYD-2

via the first DDO pathway, *i.e.*, the one that runs through the 4-propyl-phenol intermediate in the first deoxygenation step. According to the SCM results, this pathway is about eight orders of magnitude faster than the fastest of the HYD mechanisms. Among the pathways involving the 1-methoxy-3-propylbenzene species, DDO-2, where the breaking of the C–OCH$_3$ bond occurs as an additional deoxygenation step, is significantly favored over DDO-3 which, as already anticipated, is the slowest pathway. The DDO-2 and DDO-4 pathways are somewhat competitive with each other.

The SCM allows to easily analyze the kinetics of the various mechanisms taking into consideration, all at once and in its entirety, the information obtained from the DFT calculations relating to the elementary steps of which the mechanisms are composed and to ultimately express all this information through a single number. Whether this number is comparable to kinetic constants obtained experimentally is a matter of accuracy related to the employed theoretical methods, but what is here important to note is that we can discriminate among different mechanisms on the basis of objective holistic data and not on the basis of mere analyses of the values of the energy barriers, which could lead to hasty conclusions. In particular, considering the research reported in this work and excluding from the analysis the elementary steps common to all DDO-type mechanisms (see Fig. 6 and Table 1), the following analysis could be performed. While it is true that DDO-3 can be excluded by virtue of the very high barriers along the pathway, the evidence that DDO-1 is the preferential mechanism is not directly attributable to the fact that it is characterized by the lowest energy barriers along the corresponding pathway; in fact the highest barriers in DDO-1, DDO-2 and DDO-4 are comparable (116.9, 123.1 and 121.6 kJ mol^{-1}, respectively, for stages 24, 33 and 29 of Table 1). It also does not appear to be due to the fact that DDO-1 has fewer elementary steps, as it actually features one more step than DDO-2 (processes 24-28 for DDO-1, 33-36 for DDO-2). And finally it does not seem to be due to the fact that DDO-1 has the highest backward barrier, as this record belongs to DDO-3 (239.3 kJ mol^{-1}, for step 37) or to DDO-2 (181.0 kJ mol^{-1}, step 31), if DDO-3 is excluded *a priori*. However, the SCM analysis indicates that, taking into account all the forward and backward barriers at a single glance (which are also a reflection of the stability of the intermediates), DDO-1 is undoubtedly the fastest mechanism, followed in order by DDO-4, DDO-2 and DDO-3, being the latter mechanism effectively irrelevant for the whole reaction kinetics.

Incidentally, information similar to that given by the SCM can be obtained considering the differences, Δ_{TEC}, between the total energy content (TEC, i.e. the sum of all the energy barriers encountered along the path [57]) of the forward process and the TEC relating to the backward process for the investigated DDO mechanisms. It is possible to infer that a negative Δ_{TEC} would indicate a favored "flow" in the forward direction (from reactants to products) over the backward one, so the rate of the given mechanism would be higher the more negative the Δ_{TEC} is. In fact, it is easy to show that:

$$\Delta_{\text{TEC}} = \text{RT}\ln\left(\frac{\Pi_B}{\Pi_F}\right)$$

being Π_B and Π_F the products of the occurrence probabilities, at a given temperature T, of all the steps present in the backward and forward paths of each individual reaction mechanism considered, and R the gas constant. Hence $\Delta_{\text{TEC}} < 0$ if $\Pi_b < \Pi_F$, condition corresponding to our assumption, as easily shown by the definition of the event occurence probability [55]. Since Δ_{TEC} is a relative parameter, the steps common to the four mechanisms were eliminated and, using the data of Table 1, the following Δ_{TEC}/kJ mol^{-1} values were obtained: $\Delta_{\text{TEC}}(\text{DDO-1}) = -38.8$, $\Delta_{\text{TEC}}(\text{DDO-2}) = -19.4$, $\Delta_{\text{TEC}}(\text{DDO-3}) = +202.2$ and $\Delta_{\text{TEC}}(\text{DDO-4}) = -31.7$. This set clearly indicates that DDO-3 is an essentially impossible pathway (the backward flow is stronger than the forward one), DDO-1 is the favored mechanism and the DDO-2/DDO-4 pair are arranged in exactly the same order as that indicated by the SCM.

5. Conclusion

In the first paper of this series, we examined Pt$_1$0, a leading platinum cluster in hydrogenation reactions, as a catalyst model. Specifically, we studied its interactions with isoeugenol, its ability to fragment hydrogen molecules and produce atomic hydrogen, and its efficiency in catalyzing the conversion of isoeugenol to propylcyclohexane via the direct deoxygenation, DDO, pathway. In order to provide a comprehensive mapping at the atomistic level of the main mechanisms involved in the HDO process, in the present work the deoxygenation-through-hydrogenation pathway is reported, together with a conclusive systematic comparison between the two alternative mechanisms above.

The detailed energetics of the two studied mechanisms, along with most of their possible routes, enabled us to conduct a Christiansen-like microkinetic analysis which, on the basis of the DFT-calculated forward/backward energy barriers and adsorption/desorption energetics, returned an unbiased guess of the kinetic constants at given temperatures. The kinetic data confirm the thermodynamic hypotheses that the DDO mechanism is the preferred one into the temperature range 473–973 K. In particular, under molecular hydrogen flux the reaction would seem to proceed through the formation of the 4-propylphenol intermediate, by the preferential removal of the methoxy fragment as methanol, to give the final product, propylcyclohexane. The removal of the hydroxyl group, which desorbs as water, also occurs. Further, kinetic data suggest that the route implying the formation of methane could become competitive at higher temperature, while those channels involving 1-methoxy-3-propylbenzene as intermediate could be ruled out, being the one passing through 3-propylphenol the slowest one.

This work provides an almost complete mapping of the HDO mechanism of isoeugenol on a representative subnanometric platinum cluster and can be used as reference for further investigation. In particular, future works mandatorily must be devoted on one side to evaluate the effect of supports and of the employment of different, namely non-noble, metals on the key-point of the reaction, and on another side to ascertain if under molecular hydrogen, hydrodeoxygenation would actually become preferred to the many decomposition modes expected on metals for molecules having several functional groups.

CRediT authorship contribution statement

Chiara Nania: Writing – original draft, Visualization, Investigation, Data curation, Conceptualization. **Francesco Ferrante:** Writing – review & editing, Supervision, Project administration, Conceptualization. **Marco Bertini:** Writing – review & editing, Investigation, Data curation. **Laura Gueci:** Writing – review & editing, Investigation, Data curation. **Dario Duca:** Writing – review & editing, Supervision, Data curation.

Declaration of competing interest

The authors declare that they have no known competing financial interests or personal relationships that could have appeared to influence the work reported in this paper.

Data availability

Data will be made available on request.

Acknowledgements

B53D23005960006.

References

[1] Renewable energy: Power for a sustainable future (3rd ed.), published by Oxford University Press, Oxford in association with The Open University, Milton Keynes2012.

[2] M.N. Uddin, K. Techato, J. Taweekun, M.M. Rahman, M.G. Rasul, T.M. I. Mahlia, S. M. Ashrafur, An overview of recent developments in biomass pyrolysis technologies, Energies 11 (2018), https://doi.org/10.3390/en11113115.

[3] A. Gutierrez, R. Kaila, M. Honkela, R. Slioor, A. Krause, Hydrodeoxygenation of guaiacol on noble metal catalysts, Catal. Today 147 (2009) 239–246, https://doi.org/10.1016/j.cattod.2008.10.037.

[4] J. Chang, T. Danuthai, S. Dewiyanti, C. Wang, A. Borgna, Hydrodeoxygenation of guaiacol over carbon-supported metal catalysts, ChemCatChem 5 (2013) 3041–3049, https://doi.org/10.1002/cctc.201300096.

[5] C.-C. Chiu, A. Genest, A. Borgna, N. Rösch, Hydrodeoxygenation of guaiacol over Ru(0001): a DFT study, ACS Catal. 4 (2014) 4178–4188, https://doi.org/10.1021/cs500911j.

[6] A. Bjelić, M. Grilc, B. Likozar, Catalytic hydrogenation and hydrodeoxygenation of lignin-derived model compound eugenol over Ru/C: intrinsic microkinetics and transport phenomena, Chem. Eng. J. 333 (2018) 240–259, https://doi.org/10.1016/j.cej.2017.09.135.

[7] M. Bertero, G. de la Puente, U. Sedran, Fuels from bio-oils: Bio-oil production from different residual sources, characterization and thermal conditioning, Fuel 95 (2012) 263–271, https://doi.org/10.1016/j.fuel.2011.08.041.

[8] J.A. Maga, I. Katz, Simple phenol and phenolic compounds in food flavor, Crit. Rev. Food Sci. Nutr. 10 (1978) 323–372, https://doi.org/10.1080/10408397809527255.

[9] D. Mohan, C.U. Pittman, P.H. Steele, Pyrolysis of wood-biomass for bio-oil: a critical review, Energy Fuels 20 (2006) 848–889, https://doi.org/10.1021/ef0502397.

[10] G.W. Huber, S. Iborra, A. Corma, Synthesis of transportation fuels from biomass: chemistry, catalysts, and engineering, Chem. Rev. 106 (2006) 4044–4098, https://doi.org/10.1021/cr068360d.

[11] P. Mäki-Arvela, D.Y. Murzin, Hydrodeoxygenation of lignin-derived phenols: From fundamental studies towards industrial applications, Catalysts 7 (2017), https://doi.org/10.3390/catal7090265.

[12] A. Bridgwater, Renewable fuels and chemicals by thermal processing of biomass, Chem. Eng. J. 91 (2003) 87–102, https://doi.org/10.1016/S1385-8947(02)00142-0.

[13] K. Lee, G.H. Gu, C.A. Mullen, A.A. Boateng, D.G. Vlachos, Guaiacol hydrodeoxygenation mechanism on Pt(111): insights from density functional theory and linear free energy relations, ChemSusChem 8 (2015) 315–322, https://doi.org/10.1002/cssc.201402940.

[14] J. Lu, A. Heyden, Theoretical investigation of the reaction mechanism of the hydrodeoxygenation of guaiacol over a Ru(0001) model surface, J. Catal. 321 (2015) 39–50, https://doi.org/10.1016/j.jcat.2014.11.003.

[15] M. Hellinger, H.W. Carvalho, S. Baier, D. Wang, W. Kleist, J.D. Grunwaldt, Catalytic hydrodeoxygenation of guaiacol over platinum supported on metal oxides and zeolites, Appl. Catal. A Gen. 490 (2015) 181–192, https://doi.org/10.1016/j.apcata.2014.10.043.

[16] C. González, P. Mar, F.V. Dez, S. Ordóñez, Gas-phase hydrodeoxygenation of benzaldehyde, benzyl alcohol, phenyl acetate, and anisole over precious metal catalysts, Ind. Eng. Chem. Res. 55 (2016) 2319–2327, https://doi.org/10.1021/acs.iecr.6b00036.

[17] A.R.K. Gollakota, C.-M. Shu, P.K. Sarangi, K.P. Shadangi, S. Rakshit, J.F. Kennedy, V.K. Gupta, M. Sharma, Catalytic hydrodeoxygenation of bio-oil and model compounds – choice of catalysts, and mechanisms, Renew. Sustain. Energy Rev. 187 (2023) 113700, https://doi.org/10.1016/j.rser.2023.113700.

[18] C. Nania, M. Bertini, L. Gueci, F. Ferrante, D. Duca, DFT insights into competing mechanisms of guaiacol hydrodeoxygenation on a platinum cluster, Phys. Chem. Chem. Phys. 25 (2023) 10460–10471, doi:10.1039/D2CP06077A.

[19] H. Guo, X. Lu, Y. Yang, J. Wei, L. Wu, L. Tan, Y. Tang, X. Gu, Harvesting alkyl phenols from lignin monomers via selective hydrodeoxygenation under ambient pressure on Pd/α-MoC catalysts, Mol. Catal. 540 (2023) 113041, https://doi.org/10.1016/j.mcat.2023.113041.

[20] Y. Xu, Z. Liu, B. Liu, B. Dong, Y. Pan, Y. Li, Y. Li, H. Guo, Y. Chai, C. Liu, Regulation of surface hydrophobicity and metal dispersion on Pt-based catalyst for the boosted hydrodeoxygenation of guaiacol into bio-hydrocarbons, Mol. Catal. 553 (2024) 113761, https://doi.org/10.1016/j.mcat.2023.113761.

[21] Z. Li, Z. Li, M. Wu, Z. Qiu, Y. Zhu, R. Zhang, Selective hydrodeoxygenation of lignin-derived eugenol to propylcyclohexane over triazine polymer derived Co/NC-T catalyst, Mol. Catal. 557 (2024) 113987, https://doi.org/10.1016/j.mcat.2024.113987.

[22] C. Zhu, J.-P. Cao, Z. Yang, X.-Y. Zhao, W.-C. Yi, X.-B. Feng, Y.-P. Zhao, H.C. Bai, Study on hydrodeoxygenation mechanism of anisole over Ni(111) by first-principles calculation, Mol. Catal. 523 (2022) 111402, https://doi.org/10.1016/j.mcat.2021.111402.

[23] M. Saleheen, O. Mamun, A. Mohan Verma, D. Sahsah, A. Heyden, Understanding the influence of solvents on the Pt-catalyzed hydrodeoxygenation of guaiacol, J. Catal 425 (2023) 212–232, https://doi.org/10.1016/j.jcat.2023.06.009.

[24] B.Z. Chowdhry, J.P. Ryall, T.J. Dines, A.P. Mendham, Infrared and raman spectroscopy of eugenol, isoeugenol, and methyl eugenol: conformational analysis and vibrational assignments from density functional theory calculations of the anharmonic fundamentals, J. Phys. Chem. A 119 (2015) 11280–11292, https://doi.org/10.1021/acs.jpca.5b07607.

[25] X. Gan, A. Wang, D. Hu, Synthesis of novel antiviral ferulic acid-eugenol and isoeugenol hybrids using various link reactions, J. Agric. Food Chem. 69 (2021) 13724–13733, https://doi.org/10.1021/acs.jafc.1c05521.

[26] A.M. Robinson, J.E. Hensley, J.W. Medlin, Bifunctional catalysts for upgrading of biomass-derived oxygenates: a review, ACS Catal. 6 (2016) 5026–5043, https://doi.org/10.1021/acscatal.6b0092.

[27] W. Jin, L. Pastor-Pérez, D. Shen, A. Sepúlveda-Escribano, S. Gu, T. R. Reina, Catalytic upgrading of biomass model compounds: novel approaches and lessons learnt from traditional hydrodeoxygenation - a review, ChemCatChem 11 (2019) 924, https://doi.org/10.1002/cctc.201801722.

[28] Y. Romero, F. Richard, S. Brunet, Hydrodeoxygenation of 2-ethylphenol as a model compound of bio-crude over sulfided Mo-based catalysts: Promoting effect and reaction mechanism, Appl. Cat. B Env. 98 (2010) 213–223, https://doi.org/10.1016/j.apcatb.2010.05.031.hal-04442216.

[29] Y. Romero, F. Richard, Y. Renème, S. Brunet, Hydrodeoxygenation of benzofuran and its oxygenated derivatives (2,3-dihydrobenzofuran and 2-ethylphenol) over NiMoP/Al₂O₃ catalyst, Appl. Cat. A Gen 353 (2009) 46–53, https://doi.org/10.1016/j.apcata.2008.10.022.

[30] A.M. Barrios, C.A. Teles, P.M. de Souza, R.C. Rabelo-Neto, G. Jacobs, B.H. Davis, L. E. Borges, F.B. Noronha, Hydrodeoxygenation of phenol over niobia supported Pd catalyst, Catal. Today 302 (2018) 115–124, https://doi.org/10.1016/j.cattod.2017.03.034.

[31] C. Zhao, J. He, A.A. Lemonidou, X. Li, J.A. Lercher, Aqueous-phase hydrodeoxygenation of bio-derived phenols to cycloalkanes, J. Catal. 280 (2011) 8–16, https://doi.org/10.1016/j.jcat.2011.02.001.

[32] F. Ferrante, C. Nania, D. Duca, Computational investigation of isoeugenol transformations on a platinum cluster I: Direct deoxygenation to propylcyclohexane, Mol. Catal. 529 (2022) 112541, https://doi.org/10.1016/j.mcat.2022.112541.

[33] V. D'Anna, D. Duca, F. Ferrante, G. La Manna, DFT studies on catalytic properties of isolated and carbon nanotube supported Pd₉ cluster – I: adsorption, fragmentation and diffusion of hydrogen, Phys. Chem. Chem. Phys. 11 (2009) 4077–4083, https://doi.org/10.1039/b820707k.

[34] V. D'Anna, D. Duca, F. Ferrante, G. La Manna, DFT studies on catalytic properties of isolated and carbon nanotube supported Pd₉ cluster: Part II. Hydro-isomerization of butene isomers, Phys. Chem. Chem. Phys. 12 (2010) 1323–1330, https://doi.org/10.1039/b920949m.

[35] R. Schimmenti, R. Cortese, F. Ferrante, A. Prestianni, D. Duca, Growth of sub-nanometric palladium clusters on boron nitride nanotubes: a DFT study, Phys. Chem. Chem. Phys. 18 (2016) 1750–1757, https://doi.org/10.1039/c5cp06625e.

[36] F. Ferrante, A. Prestianni, R. Cortese, R. Schimmenti, D. Duca, Density functional theory investigation on the nucleation of homo- and heteronuclear metal clusters on defective graphene, J. Phys. Chem. C 120 (2016) 12022–12031, https://doi.org/10.1021/acs.jpcc.6b02833.

[37] T. Imaoka, Y. Akanuma, N. Haruta, S. Tsuchiya, K. Ishihara, T. Okayasu, W.-J. Chun, M. Takahashi, K. Yamamoto, Platinum clusters with precise numbers of atoms for preparative-scale catalysis, Nat. Comm. 8 (2017) 1–8, https://doi.org/10.1038/s41467-017-00800-4.

[38] C. Schmitt, N.D. Roit, M. Neumaier, C.B. Maliakkal, D. Wang, T. Henrich, C. Kübel, M. Kappes, S. Behrens, Continuous flow synthesis of atom-precise platinum clusters, Nanoscale Adv. 6 (2024) 2459–24686, https://doi.org/10.1039/D4NA00074A.

[39] G. Xiang, Z. Qiu, H. Fei, Z. Liu, S. Yin, Y. Wu, Synergistic effect of platinum single atoms and nanoclusters for preferential oxidation of carbon monoxide in hydrogen-rich stream, J. Power Sources 591 (2024) 233873.j.jpowsour.2023.233873

[40] K. Zhang, X. Dou, H. Hou, Z. Zhou, M. Lopez-Haro, D.M. Meira, P. Liu, P. He, L. Liu, Generation of subnanometer metal clusters in silicoaluminate zeolites as bifunctional catalysts, JACS Au 3 (2023) 3213–3226, https://doi.org/10.1021/jacsau.3c00548.

[41] M.J. Frisch, G.W. Trucks, H.B. Schlegel, G.E. Scuseria, M.A. Robb, J. R. Cheeseman, G. Scalmani, V. Barone, G.A. Petersson, H. Nakatsuji, X. Li, M. Caricato, A. V. Marenich, J. Bloino, B.G. Janesko, R. Gomperts, B. Mennucci, H.P. Hratchian, J. V. Ortiz, A.F. Izmaylov, J.L. Sonnenberg, D. Williams-Young, F. Ding, F. Lipparini, F. Egidi, J. Goings, B. Peng, A. Petrone, T. Henderson, D. Ranasinghe, V. G. Zakrzewski, J. Gao, N. Rega, G. Zheng, W. Liang, M. Hada, M. Ehara, K. Toyota, R. Fukuda, J. Hasegawa, M. Ishida, T. Nakajima, Y. Honda, O. Kitao, H. Nakai, T. Vreven, K. Throssell, J.A. Montgomery Jr., J.E. Peralta, F. Ogliaro, M. J. Bearpark, J.J. Heyd, E.N. Brothers, K.N. Kudin, V.N. Staroverov, T.A. Keith, R. Kobayashi, J. Normand, K. Raghavachari, A.P. Rendell, J. C. Burant, S. S. Iyengar, J. Tomasi, M. Cossi, J.M. Millam, M. Klene, C. Adamo, R. Cammi, J. W. Ochterski, R.L. Martin, K. Morokuma, O. Farkas, J. B. Foresman, D.J. Fox, Gaussian16 Revision C.01 (2016).

[42] A.D. Becke, A new mixing of Hartree-Fock and local densityfunctional theories, J. Chem. Phys. 98 (1993) 1372–1377, https://doi.org/10.1063/1.464304.

[43] S. Grimme, J. Antony, S. Ehrlich, H. Krieg, A consistent and accurate ab initio parametrization of density functional dispersion correction (DFT-D) for the 94 elements H-Pu, J. Chem. Phys. 132 (2010) 154104, https://doi.org/10.1063/1.3382344.

[44] P.J. Hay, W.R. Wadt, Ab initio effective core potentials for molecular calculations, Potentials for the transition metal atoms Sc to Hg, J. Chem. Phys. 82 (1985) 270–283, https://doi.org/10.1063/1.448799.

[45] P.J. Hay, W.R. Wadt, Ab initio effective core potentials for molecular calculations. Potential for K to Au including the outermost core orbitals, J. Chem. Phys. 82 (1985) 299–310, https://doi.org/10.1063/1.448975.

[46] T.H. Dunning, P.J. Hay, Gaussian basis sets for molecular calculations, in: H. F. Schaefer (Ed.), Modern Theoretical Chemistry, Springer, US, 1977, pp. 1–27, https://doi.org/10.1007/978-1-4757-0887-5-1.Methods of Electronic Structure Theory

[47] B.P. Pritchard, D. Altarawy, B. Didier, T.D. Gibson, T.L. Windus, New basis set exchange: an open, up-to-date resource for the molecular sciences community, J. Chem. Inf. Model. 59 (2019) 4814–4820, https://doi.org/10.1021/acs.jcim.9b00725.

[48] S.F. Boys, F. Bernardi, The calculation of small molecular interactions by the differences of separate total energies. Some procedures with reduced errors, Mol. Phys. 19 (1970) 553–566, https://doi.org/10.1080/00268977000101561.

[49] V. Fung, D.-E. Jang, Exploring structural diversity and fluxionality of Pt_n (n=10-13) clusters from first principles, J. Phys. Chem. C 121 (2017) 10796–10802, https://doi.org/10.1021/acs.jpcc.6b11969.

[50] I. Demiroglu, K. Yao, H.A. Hussein, R.L. Johnston, DFT global optimization of gas-phase subnanometer Ru-Pt clusters, J. Phys. Chem. C 121 (2017) 10773–10780, https://doi.org/10.1021/acs.jpcc.6b11329.

[51] L. Lozano, G.B. Marin, J.W. Thybaut, Analytical rate expressions accounting for the elementary steps in benzene hydrogenation on Pt, Ind. Eng. Chem. Res. 56 (2017) 12953–12962, https://doi.org/10.1021/acs.iecr.7b00742.

[52] J. Christiansen, The Elucidation of Reaction Mechanisms by the Method of Intermediates in Quasi-Stationary Concentrations, Academic Press, 1953, pp. 311–353, https://doi.org/10.1016/S0360-0564(08)60644-6.Vol. 5 of Adv. Catal

[53] L. Gueci, F. Ferrante, A. Prestianni, R. Di Chio, A.F. Patti, D. Duca, F. Arena, DFT insights into the oxygen-assisted selective oxidation of benzyl alcohol on manganese dioxide catalysts, Inorg. Chim. Acta 511 (2020) 119812, https://doi.org/10.1016/j.ica.2020.119812.

[54] L. Gueci, F. Ferrante, A. Prestianni, F. Arena, D. Duca, Benzyl alcohol to benzaldehyde oxidation on MnO_x clusters: Unraveling atomistic features, Mol. Catal. 513 (2021) 111735, https://doi.org/10.1016/j.mcat.2021.111735.

[55] L. Gueci, F. Ferrante, A. Prestianni, F. Arena, D. Duca, Structural, energetic and kinetic database of catalytic reactions: benzyl alcohol to benzaldehyde oxidation on MnO_x clusters, Data Brief 38 (2021) 107369, https://doi.org/10.1016/j.dib.2021.107369.

[56] F. Arena, F. Ferrante, R. DiChio, G. Bonura, F. Frusteri, L. Frusteri, A. Prestianni, S. Morandi, G. Martra, D. Duca, DFT and kinetic evidences of the preferential CO oxidation pattern of manganese dioxide catalysts in hydrogen stream (PROX), Appl. Cat. B Env. 300 (2022) 120715, https://doi.org/10.1016/j.apcatb.2021.120715.

[57] R. Cortese, R. Schimmenti, F. Ferrante, A. Prestianni, D. Decarolis, D. Duca, Graph-based analysis of ethylene glycol decomposition on a palladium cluster, J. Phys. Chem. C 121 (2017) 13606–13616, https://doi.org/10.1021/acs.jpcc.7b00850.

Bibliography

[1] Şerife Elif Can Şener, Julia L. Sharp, and Annick Anctil. Factors impacting diverging paths of renewable energy: A review. *Renewable and Sustainable Energy Reviews*, 81(P2):2335–2342, 2018.

[2] N.L. Panwar, S.C. Kaushik, and Surendra Kothari. Role of renewable energy sources in environmental protection: A review. *Renewable and Sustainable Energy Reviews*, 15(3):1513–1524, 2011.

[3] Siamak Farhad, Majid Saffar-Avval, and Maryam Younessi-Sinaki. Efficient design of feedwater heaters network in steam power plants using pinch technology and exergy analysis. *International Journal of Energy Research*, 32:1 – 11, 01 2008.

[4] Mohsen Khezri, Mohammad Sharif Karimi, Jamal Mamkhezri, Reza Ghazal, and Larry Blank. Assessing the impact of selected determinants on renewable energy sources in the electricity mix: The case of asean countries. *Energies*, 15(13), 2022.

[5] Kamil Makieła, Błażej Mazur, and Jakub Głowacki. The impact of renewable energy supply on economic growth and productivity. *Energies*, 15(13), 2022.

[6] Yong Zhu and Congjia Huo. The impact of agricultural production efficiency on agricultural carbon emissions in china. *Energies*, 15(12), 2022.

[7] Sander Roosjen, Maxim Glushenkov, Alexander Kronberg, and Sascha Kersten. Waste heat recovery systems with isobaric expansion technology using pure and mixed working fluids. *Energies*, 15(14), 2022.

[8] Daishi Shiojiri, Tsutomu Iida, Naomi Hirayama, Yoji Imai, Hiroharu Sugawara, and Jin Kusaka. Recent studies on the environmentally benign

alkaline-earth silicide mg2si for middle-temperature thermoelectric applications. *Energies*, 15(13), 2022.

[9] Carolina Clasen Sousa, Jorge Martins, Óscar Carvalho, Miguel Coelho, Ana Sofia Moita, and Francisco P. Brito. Assessment of an exhaust thermoelectric generator incorporating thermal control applied to a heavy duty vehicle. *Energies*, 15(13), 2022.

[10] Abed Alaswad, Abdelnasir Omran, Jose Ricardo Sodre, Tabbi Wilberforce, Gianmichelle Pignatelli, Michele Dassisti, Ahmad Baroutaji, and Abdul Ghani Olabi. Technical and commercial challenges of proton-exchange membrane (pem) fuel cells. *Energies*, 14(1), 2021.

[11] A.G. Olabi, Tabbi Wilberforce, Enas Taha Sayed, Khaled Elsaid, and Mohammad Ali Abdelkareem. Prospects of fuel cell combined heat and power systems. *Energies*, 13(16), 2020.

[12] Tabbi Wilberforce, Oluwatosin Ijaodola, Ahmad Baroutaji, Emmanuel Ogungbemi, and Abdul Ghani Olabi. Effect of bipolar plate material on proton exchange membrane fuel cell performance. *Energies*, 15(5), 2022.

[13] Md Kashif Gohar Deshmukh, Mohd Sameeroddin, Daud Abdul, and Mohammed Abdul Sattar. Renewable energy in the 21st century: A review. *Materials Today: Proceedings*, 80:1756–1759, 2023.

[14] Nihal Ahmed, Adnan Ahmed Sheikh, Zeeshan Hamid, Piotr Senkus, Ricardo Cosio Borda, Aneta Wysokińska-Senkus, and Waldemar Glabiszewski. Exploring the causal relationship among green taxes, energy intensity, and energy consumption in nordic countries: Dumitrescu and hurlin causality approach. *Energies*, 15(14), 2022.

[15] Galvão Meirinhos, Mariano Malebo, António Cardoso, Rui Silva, and Reiville Rêgo. Information and public knowledge of the potential of alternative energies. *Energies*, 15(13), 2022.

[16] Rabie Said, Muhammad Ishaq Bhatti, and Ahmed Imran Hunjra. Toward understanding renewable energy and sustainable development in developing and developed economies: A review. *Energies*, 15(15), 2022.

[17] Yasutsugu Baba, Andante Hadi Pandyaswargo, and Hiroshi Onoda. An analysis of the current status of woody biomass gasification power generation in japan. *Energies*, 13(18), 2020.

[18] Erika Paola Garduño-Ruiz, Rodolfo Silva, Yandy Rodríguez-Cueto, Alejandro García-Huante, Jorge Olmedo-González, M. Luisa Martínez, Astrid Wojtarowski, Raúl Martell-Dubois, and Sergio Cerdeira-Estrada. Criteria for optimal site selection for ocean thermal energy conversion (otec) plants in mexico. *Energies*, 14(8), 2021.

[19] Jane Marchand, Ajay Shetgaonkar, Jose Luis Rueda Torres, Aleksandra Lekic, and Peter Palensky. Emt real-time simulation model of a 2 gw offshore renewable energy hub integrating electrolysers. *Energies*, 14(24), 2021.

[20] Deepak Jain Veerendra Kumar, Lelia Deville, Kenneth A. Ritter, Johnathan Richard Raush, Farzad Ferdowsi, Raju Gottumukkala, and Terrence Lynn Chambers. Performance evaluation of 1.1 mw grid-connected solar photovoltaic power plant in louisiana. *Energies*, 15(9), 2022.

[21] Sudhakar Reddy and J.P Painuly. Diffusion of renewable energy technologies—barriers and stakeholders' perspectives. *Renewable Energy*, 29(9):1431–1447, 2004.

[22] Divya R. Nair, Manjula G. Nair, and Tripta Thakur. A smart microgrid system with artificial intelligence for power-sharing and power quality improvement. *Energies*, 15(15), 2022.

[23] Hegazy Rezk, Basem Alamri, Mokhtar Aly, Ahmed Fathy, Abdul G. Olabi, Mohammad Ali Abdelkareem, and Hamdy A. Ziedan. Multicriteria decision-making to determine the optimal energy management strategy of hybrid pv–diesel battery-based desalination system. *Sustainability*, 13(8), 2021.

[24] David Martin Alonso, Jesse Q. Bond, and James A. Dumesic. Catalytic conversion of biomass to biofuels. *Green Chem.*, 12:1493–1513, 2010.

[25] Prabir Basu. *Biomass gasification, pyrolysis and torrefaction: practical design and theory*. Academic press, 2018.

[26] Jay Cheng. *Biomass to renewable energy processes*. CRC press, 2017.

[27] Sabzoi Nizamuddin, Humair Ahmed Baloch, G.J. Griffin, N.M. Mubarak, Abdul Waheed Bhutto, Rashid Abro, Shaukat Ali Mazari, and Brahim Si Ali. An overview of effect of process parameters on hydrothermal carbonization of biomass. *Renewable and Sustainable Energy Reviews*, 73(C):1289–1299, 2017.

[28] R.E.H. Sims, A. Hastings, B. Schlamadinger, G. Taylor, and P. Smith. Energy crops: current status and future prospects. *Global Change Biology*, 12(11):2054–2076, 2006.

[29] Yanfang Zhu, Guiyang Xu, Wen Yi Song, Yuzhen Zhao, Zongcheng Miao, Ruijuan Yao, and Jianjing Gao. Catalytic microwave pyrolysis of orange peel: Effects of acid and base catalysts mixture on products distribution. *Journal of The Energy Institute*, 98:172–178, 2021.

[30] G.Sh Tkemaladze and K.A. Makhashvili. Climate changes and photosynthesis. *Annals of Agrarian Science*, 14(2):119–126, 2016.

[31] Staffan Jacobsson and Anna Johnson. The diffusion of renewable energy technology: an analytical framework and key issues for research. *Energy Policy*, 28(9):625–640, 2000.

[32] Peter McKendry. Energy production from biomass (part 1): Overview of biomass. *Bioresource Technology*, 83:37–46, 06 2002.

[33] Kaltschmitt M., Themelis N.J., Bronicki L.Y., Söder L., and Vega L. A. *Renewable Energy from Biomass, Introduction.* Springer New York, 2013.

[34] P. N. R. Vennestrøm, C. M. Osmundsen, C. H. Christensen, and Esben Taarning. Beyond petrochemicals: The renewable chemicals industry. *Angewandte Chemie International Edition*, 50(45):10502–10509, 2011.

[35] Małgorzata Sieradzka, Cezary Kirczuk, Izabela Kalemba-Rec, Agata Mlonka-Medrala, and Aneta Magdziarz. Pyrolysis of biomass wastes into carbon materials. *Energies*, 15(5), 2022.

[36] Daniel Borowiak and Małgorzata Krzywonos. Bioenergy, biofuels, lipids and pigments—research trends in the use of microalgae grown in photobioreactors. *Energies*, 15(15), 2022.

[37] Teuku Azuar Rizal, Khairil, Mahidin, Husni Husin, Ahmadi, Fahrizal Nasution, and Hamdani Umar. The experimental study of pangium edule biodiesel in a high-speed diesel generator for biopower electricity. *Energies*, 15(15), 2022.

[38] H. Chum, A. Faaij, J. Moreira, G. Berndes, P. Dhamija, H. Dong, and et al Gabrielle, B. *Bioenergy*, page 209–332. Cambridge University Press, 2011.

[39] Koray Alper, Kubilay Tekin, Selhan Karagöz, and Arthur J. Ragauskas. Sustainable energy and fuels from biomass: a review focusing on hydrothermal biomass processing. *Sustainable Energy Fuels*, 4:4390–4414, 2020.

[40] Pekka Lauri, Petr Havlík, Georg Kindermann, Nicklas Forsell, Hannes Böttcher, and Michael Obersteiner. Woody biomass energy potential in 2050. *Energy Policy*, 66:19–31, 2014.

[41] Veeranjaneya Reddy Lebaka. Potential bioresources as future sources of biofuels production: An overview. *Biofuel technologies: Recent developments*, pages 223–258, 2013.

[42] Paul Adams, Tony Bridgwater, Amanda Lea-Langton, Andrew Ross, and Ian Watson. Chapter 8 - biomass conversion technologies. In Patricia Thornley and Paul Adams, editors, *Greenhouse Gas Balances of Bioenergy Systems*, pages 107–139. Academic Press, 2018.

[43] James E. Bidlack and William V. Dashek. *Plant cell walls*, chapter 9, pages 209–238. John Wiley & Sons, Ltd, 2017.

[44] Hongzhang Chen. *Biotechnology of Lignocellulose: Theory and Practice*, pages 1–511. Springer Netherlands, 01 2014.

[45] Anna Ottenhall, Jonatan Henschen, Josefin Illergård, and Monica Ek. Cellulose-based water purification using paper filters modified with polyelectrolyte multilayers to remove bacteria from water through electrostatic interactions. *Environ. Sci.: Water Res. Technol.*, 4:2070–2079, 2018.

[46] Zarah Forsberg, Alasdair Mackenzie, Morten Sørlie, Åsmund Røhr Kjendseth, Ronny Helland, Andrew Arvai, Gustav Vaaje-Kolstad, and Vincent Eijsink. Structural and functional characterization of a conserved pair of

bacterial cellulose-oxidizing lytic polysaccharide monooxygenases. *Proceedings of the National Academy of Sciences of the United States of America*, 111, 05 2014.

[47] Hongzhang Chen. *Chemical Composition and Structure of Natural Lignocellulose*, pages 25–71. Springer Netherlands, 01 2014.

[48] Bahareh Azimi, Sima Sepahvand, Saeed Ismaeilimoghadam, Hanieh Kargarzadeh, Alireza Ashori, Mehdi Jonoobi, and Serena Danti. Application of cellulose-based materials as water purification filters; a state-of-the-art review. *Journal of Polymers and the Environment*, 32:1–22, 07 2023.

[49] Liandong Jing, Tianyu Shi, Yulung Chang, Xingliang Meng, Shuai He, Hang Xu, Shengtao Yang, and Jia Liu. Cellulose-based materials in environmental protection: A scientometric and visual analysis review. *Science of The Total Environment*, 929:172576, 2024.

[50] N.C. Joshi, Aroma Joshi, Debasis Mitra, Prateek Gururani, Niraj Kumar, Hemant Joshi, and A. Bhuimali. Removal of heavy metals using cellulose-based materials: A mini-review. *Environmental Nanotechnology Monitoring & Management*, 21:100942, 03 2024.

[51] Arbind Prasad, Ashwani Kumar, and Kishor Gajrani. *Biodegradable Composites for Packaging Application*. CRC Press, 07 2022.

[52] Akshita Kanwar, Parmeshwar Gavande, and Arun Goyal. *Plant-Based Biofuels*, pages 217–246. Springer, Cham, 03 2024.

[53] Daniel Cosgrove. Growth of the plant cell wall. nat rev mol cell bio 6:850-861. *Nature reviews. Molecular cell biology*, 6:850–61, 12 2005.

[54] Badal Saha. Hemicellulose bioconversion. *Journal of industrial microbiology & biotechnology*, 30:279–91, 06 2003.

[55] Florbela Carvalheiro, Luís C. Duarte, and Francisco M. Girio. Hemicellulose biorefineries: a review on biomass pretreatments. *Journal of Scientific & Industrial Research*, 67:849–864, 2008.

[56] Feng Peng, Peng Pai, Feng Xu, and Run-Cang Sun. Fractional purification and bioconversion of hemicelluloses. *Biotechnology advances*, 30:879–903, 01 2012.

[57] Anna Ebringerová and Thomas Heinze. Xylan and xylan derivatives – biopolymers with valuable properties, 1. naturally occurring xylans structures, isolation procedures and properties. *Macromolecular Rapid Communications*, 21(9):542–556, 2000.

[58] Ľudmila Hodásová, Michal Jablonsky, Andrea Butor Skulcova, and Ales Haz. Lignin, potential products and their market value. *Wood research*, 60:973–986, 12 2015.

[59] Mi Li, Yunqiao pu, and Arthur Ragauskas. Current understanding of the correlation of lignin structure with biomass recalcitrance. *Frontiers in Chemistry*, 4, 11 2016.

[60] Mustafa Balat, Havva Balat, and Cahide Öz. Progress in bioethanol processing. *Progress in Energy and Combustion Science*, 34(5):551–573, 2008.

[61] George W. Huber, Sara Iborra, and Avelino Corma. Synthesis of transportation fuels from biomass: chemistry, catalysts, and engineering. *Chemical Reviews*, 106(9):4044–4098, 2006.

[62] Mohammad Taherzadeh and Keikhosro Karimi. Pretreatment of lignocellulosic wastes to improve ethanol and biogas production: A review. *International journal of molecular sciences*, 9:1621–51, 10 2008.

[63] Yan Lin and Shuzo Tanaka. Ethanol fermentation from biomass resources: Current state and prospects. *Applied microbiology and biotechnology*, 69:627–42, 03 2006.

[64] Douglas C. Elliott, Todd R. Hart, Gary G. Neuenschwander, Leslie J. Rotness, Mariefel V. Olarte, Alan H. Zacher, and Yrjö Solantausta. Catalytic hydroprocessing of fast pyrolysis bio-oil from pine sawdust. *Energy & Fuels*, 26(6):3891–3896, 2012.

[65] Eoin Butler, Ger Devlin, Dietrich Meier, and Kevin McDonnell. A review of recent laboratory research and commercial developments in fast pyrolysis

and upgrading. *Renewable and Sustainable Energy Reviews*, 15(8):4171–4186, 2011.

[66] Guanyi Chen, Ruixue Zhang, Wenchao Ma, Bin Liu, Xiangping Li, Beibei Yan, Zhanjun Cheng, and Tiejun Wang. Catalytic cracking of model compounds of bio-oil over hzsm-5 and the catalyst deactivation. *Science of the Total Environment*, 631:1611–1622, 08 2018.

[67] Adetoyese O. Oyedun, Madhumita Patel, Mayank Kumar, and Amit Kumar. *The Upgrading of Bio-Oil via Hydrodeoxygenation*, chapter 2, pages 35–60. John Wiley Sons, Ltd, 2020.

[68] R. Trane, S. Dahl, M.S. Skjøth-Rasmussen, and A.D. Jensen. Catalytic steam reforming of bio-oil. *International Journal of Hydrogen Energy*, 37(8):6447–6472, 2012.

[69] A.A. Lemonidou, P. Kechagiopoulos, E. Heracleous, and S. Voutetakis. Chapter 14 - steam reforming of bio-oils to hydrogen. In Kostas S. Triantafyllidis, Angelos A. Lappas, and Michael Stöcker, editors, *The Role of Catalysis for the Sustainable Production of Bio-fuels and Bio-chemicals*, pages 467–493. Elsevier, 2013.

[70] Anastasia Pafili, Nikolaos D. Charisiou, Savvas L. Douvartzides, Georgios I. Siakavelas, Wen Wang, Guanqing Liu, Vagelis G. Papadakis, and Maria A. Goula. Recent progress in the steam reforming of bio-oil for hydrogen production: A review of operating parameters, catalytic systems and technological innovations. *Catalysts*, 11(12), 2021.

[71] A. Iulianelli, P. Ribeirinha, A. Mendes, and A. Basile. Methanol steam reforming for hydrogen generation via conventional and membrane reactors: A review. *Renewable and Sustainable Energy Reviews*, 29:355–368, 2014.

[72] Chang-Feng Yan, Fei-Fei Cheng, and Rong-Rong Hu. Hydrogen production from catalytic steam reforming of bio-oil aqueous fraction over ni/ceo2–zro2 catalysts. *International Journal of Hydrogen Energy*, 35:11693–11699, 11 2010.

[73] A. Iriondo, V.L Barrio, Jose Cambra, P.L. Arias, M.B. Güemez, Maricruz Sanchez-Sanchez, R.M. Navarro, and J.L.G. Fierro. Glycerol steam reform-

ing over ni catalysts supported on ceria and ceria-promoted alumina. *International Journal of Hydrogen Energy*, 35:11622–11633, 10 2010.

[74] A.V. Bridgwater. Review of fast pyrolysis of biomass and product upgrading. *Biomass and Bioenergy*, 38:68–94, 2012. Overcoming Barriers to Bioenergy: Outcomes of the Bioenergy Network of Excellence 2003 – 2009.

[75] S. Czernik and A. V. Bridgwater. Overview of applications of biomass fast pyrolysis oil. *Energy & Fuels*, 18(2):590–598, 2004.

[76] Juan Antonio Melero, Jose Iglesias, and Alicia Garcia. Biomass as renewable feedstock in standard refinery units. feasibility, opportunities and challenges. *Energy Environ. Sci.*, 5:7393–7420, 2012.

[77] P.M. Mortensen, J.-D. Grunwaldt, P.A. Jensen, K.G. Knudsen, and A.D. Jensen. A review of catalytic upgrading of bio-oil to engine fuels. *Applied Catalysis A: General*, 407(1):1–19, 2011.

[78] Douglas C. Elliott. Historical developments in hydroprocessing bio-oils. *Energy & Fuels*, 21(3):1792–1815, 2007.

[79] Dinesh Mohan, Charles U. Jr. Pittman, and Philip H. Steele. Pyrolysis of wood/biomass for bio-oil: a critical review. *Energy & Fuels*, 20(3):848–889, 2006.

[80] Esben Taarning, Christian M. Osmundsen, Xiaobo Yang, Bodil Voss, Simon I. Andersen, and Claus H. Christensen. Zeolite-catalyzed biomass conversion to fuels and chemicals. *Energy Environ. Sci.*, 4:793–804, 2011.

[81] Torren R. Carlson, Yu-Ting Cheng, Jungho Jae, and George W. Huber. Production of green aromatics and olefins by catalytic fast pyrolysis of wood sawdust. *Energy Environ. Sci.*, 4:145–161, 2011.

[82] Wei Jin, Laura Pastor-Pérez, DeKui Shen, Antonio Sepúlveda-Escribano, Sai Gu, and Tomas Ramirez Reina. Catalytic upgrading of biomass model compounds: Novel approaches and lessons learnt from traditional hydrodeoxygenation – a review. *ChemCatChem*, 11(3):924–960, 2019.

[83] Murtala M. Ambursa, Joon Ching Juan, Y. Yahaya, Y.H. Taufiq-Yap, Yu-Chuan Lin, and Hwei Voon Lee. A review on catalytic hydrodeoxygenation

of lignin to transportation fuels by using nickel-based catalysts. *Renewable and Sustainable Energy Reviews*, 138:110667, 2021.

[84] Rangana Wijayapala, Akila Karunanayake, Damion Proctor, Fei Yu, Charles Pittman, and Todd Mlsna. Hydrodeoxygenation (hdo) of bio-oil model compounds with synthesis gas using a water gas shift catalyst with a mo/co/k catalyst. *Handbook of Climate Change Mitigation and Adaptation, Second Edition*, pages 1903–1935, 10 2017.

[85] Yanfan Yang, Xuan Xu, Haodong He, Dan Huo, Xiaoyun Li, Lin Dai, and Chuanling Si. The catalytic hydrodeoxygenation of bio-oil for upgradation from lignocellulosic biomass. *International Journal of Biological Macromolecules*, 242:124773, 2023.

[86] Anjani R.K. Gollakota, Chi-Min Shu, Prakash Kumar Sarangi, Krushna Prasad Shadangi, Sudip Rakshit, John F. Kennedy, Vijai Kumar Gupta, and Minaxi Sharma. Catalytic hydrodeoxygenation of bio-oil and model compounds - choice of catalysts, and mechanisms. *Renewable and Sustainable Energy Reviews*, 187:113700, 2023.

[87] Louis Bomont, Moldir Alda-Onggar, Vyacheslav Fedorov, Atte Aho, Janne Peltonen, Kari Eränen, Markus Peurla, Narendra Kumar, Johan Wärnå, Vincenzo Russo, Päivi Mäki-Arvela, Henrik Grénman, Marina Lindblad, and Dmitry Yu. Murzin. Production of cycloalkanes in hydrodeoxygenation of isoeugenol over pt- and ir-modified bifunctional catalysts. *European Journal of Inorganic Chemistry*, 2018(24):2841–2854, 2018.

[88] Mark Martínez-Klimov, Päivi Mäki-Arvela, Zuzana Vajglová, Christoph Schmidt, Olha Yevdokimova, Markus Peurla, Narendra Kumar, Kari Eränen, and Dmitry Murzin. Bifunctional pt catalysts supported on a zeolite-binder matrix for the hydrodeoxygenation of isoeugenol for renewable jet fuel production. *Topics in Catalysis*, 66:1–14, 06 2023.

[89] Paul T. Anastas, Mary M. Kirchhoff, and Tracy C. Williamson. Catalysis as a foundational pillar of green chemistry. *Applied Catalysis A: General*, 221(1):3–13, 2001.

[90] Roger A. Sheldon. Atom efficiency and catalysis in organic synthesis. *Pure and Applied Chemistry*, 72(7):1233–1246, 2000.

[91] Paul T. Anastas, Lauren B. Bartlett, Mary M. Kirchhoff, and Tracy C. Williamson. The role of catalysis in the design, development, and implementation of green chemistry. *Catalysis Today*, 55(1):11–22, 2000.

[92] Gadi Rothenberg. *Heterogeneous Catalysis*, chapter 4, pages 127–187. John Wiley & Sons, Ltd, 2008.

[93] Bhavik R. Bakshi, Guy Ziv, and Michael D. Lepech. Techno-ecological synergy: a framework for sustainable engineering. *Environmental science & technology*, 49 3:1752–60, 2015.

[94] Stefanie Hellweg and Llorenç Milà i Canals. Emerging approaches, challenges and opportunities in life cycle assessment. *Science (New York, N.Y.)*, 344:1109–1113, 06 2014.

[95] Fernando Jaramillo and Georgia Destouni. Comment on "planetary boundaries: Guiding human development on a changing planet". *Science (New York, N.Y.)*, 348(6240):1217, June 2015.

[96] James H Clark, Thomas J Farmer, Andrew J Hunt, and James Sherwood. Opportunities for bio-based solvents created as petrochemical and fuel products transition towards renewable resources. *International Journal of Molecular Sciences*, 16(8):17101–17159, jul 2015.

[97] Coby J. Clarke, Wei-Chien Tu, Oliver Levers, Andreas Bröhl, and Jason P. Hallett. Green and sustainable solvents in chemical processes. *Chemical Reviews*, 118(2):747–800, 2018.

[98] Pierre Gallezot. Conversion of biomass to selected chemical products. *Chem. Soc. Rev.*, 41:1538–1558, 2012.

[99] Roger A. Sheldon. Green and sustainable manufacture of chemicals from biomass: state of the art. *Green Chem.*, 16:950–963, 2014.

[100] Roger A. Sheldon. Green chemistry, catalysis and valorization of waste biomass. *Journal of Molecular Catalysis A: Chemical*, 422:3–12, 2016. Contributions of Homogeneous and Heterogeneous Catalysis in Biorefining: Special Issue in Honor of Prof. Ulf Schuchardt.

[101] Amin Talebian-Kiakalaieh, Nor Aishah Saidina Amin, Neda Najaafi, and Sara Tarighi. A review on the catalytic acetalization of bio-renewable glycerol to fuel additives. *Frontiers in Chemistry*, 6, 2018.

[102] Irina P. Beletskaya and Leonid M. Kustov. Catalysis as an important tool of green chemistry. *Russian Chemical Reviews*, 79(6):441–461, aug 2010.

[103] Vivek Polshettiwar and Rajender S. Varma. Green chemistry by nano-catalysis. *Green Chem.*, 12:743–754, 2010.

[104] H. V. Lee, S. B. A. Hamid, and S. K. Zain. Conversion of lignocellulosic biomass to nanocellulose: Structure and chemical process. *The Scientific World Journal*, 2014(1):631013, 2014.

[105] Charles Campbell, Rutger Santen, Michail Stamatakis, Nicola Collis, Hans-Joachim Freund, Craig Plaisance, Joachim Sauer, Bruce Garrett, Elad Gross, Andrzej Kotarba, Bert Weckhuysen, Wataru Ueda, Christian Reece, Richard Catlow, Annette Trunschke, Laure Briquet, Ho Viet Thang, Itai Panas, David Willock, and Jakub Jirkovský. Catalyst design from theory to practice: General discussion. *Faraday discussions*, 188, 06 2016.

[106] Richard Catlow, Matthew Davidson, Christopher Hardacre, and Graham Hutchings. Catalysis making the world a better place. *Philosophical Transactions of the Royal Society A: Mathematical, Physical and Engineering Sciences*, 374:20150089, 02 2016.

[107] Cynthia M. Friend and Bingjun Xu. Heterogeneous catalysis: A central science for a sustainable future. *Accounts of Chemical Research*, 50(3):517–521, 2017.

[108] Nikolay Kornienko, Nina Heidary, Giannantonio Cibin, and Erwin Reisner. Catalysis by design: development of a bifunctional water splitting catalyst through an operando measurement directed optimization cycle. *Chem. Sci.*, 9:5322–5333, 2018.

[109] Jérémie D. A. Pelletier and Jean-Marie Basset. Catalysis by design: Well-defined single-site heterogeneous catalysts. *Accounts of Chemical Research*, 49(4):664–677, 2016.

[110] Ueli Heiz and E. Bullock. Fundamental aspects of catalysis on supported metal clusters. *Cheminform*, 35, 07 2004.

[111] G.A. Somorjai. The flexible surface: new techniques for molecular level studies of time dependent changes in metal surface structure and adsorbate structure during catalytic reactions. *Journal of Molecular Catalysis A: Chemical*, 107(1):39–53, 1996. Proceedings of the 8th International Symposium on the Relations between Homogeneous and Heterogeneous Catalysis.

[112] Bradley J. Holliday. Surface and interfacial organometallic chemistry and catalysis. topics in organometallic chemistry, 16 edited by christophe copéret (laboratoire de chimie organometallique de surface, villeurbanne, france) and bruno chaudret (laboratoire de chimie de coordination du cnrs, toulouse, france). springer: berlin, heidelberg, new york. 2005. x + 291 pp. $259.00. isbn 3-540-26496-5. *Journal of the American Chemical Society*, 129(12):3772–3773, 2007.

[113] Chunyang Dong, Yinlong Li, Danyang Cheng, Mengtao Zhang, Jinjia Liu, Yang-Gang Wang, Dequan Xiao, and Ding Ma. Supported metal clusters: Fabrication and application in heterogeneous catalysis. *ACS Catalysis*, 10(19):11011–11045, 2020.

[114] Huanchen Zhai and Anastassia N. Alexandrova. Fluxionality of catalytic clusters: When it matters and how to address it. *ACS Catalysis*, 7(3):1905–1911, 2017.

[115] Hannu Dr, Stéphane Abbet, Antonio Dr, Ulrich Heiz, and Uzi Landman. Structural, electronic, and impurity-doping effects in nanoscale chemistry: Supported gold nanoclusters. *Angewandte Chemie International Edition*, 42:1297 – 1300, 05 2003.

[116] Sandra Lang and Thorsten Bernhardt. Gas phase metal cluster model systems for heterogeneous catalysis. *Physical chemistry chemical physics : PCCP*, 14:9255–69, 06 2012.

[117] Olaf Hübner and Hans-Jörg Himmel. Metal cluster models for heterogeneous catalysis: A matrix-isolation perspective. *Chemistry – A European Journal*, 24(36):8941–8961, 2018.

[118] Vincenza D'Anna, Dario Duca, Francesco Ferrante, and Gianfranco Manna. Dft studies on catalytic properties of isolated and carbon nanotube supported pd9 cluster-i: Adsorption, fragmentation and diffusion of hydrogen. *Physical chemistry chemical physics : PCCP*, 11:4077–83, 06 2009.

[119] Dario Duca, Francesco Ferrante, and Gianfranco La Manna. Theoretical study of palladium cluster structures on carbonaceous supports. *The Journal of Physical Chemistry C*, 111(14):5402–5408, 2007.

[120] JK Nørskov, T Bligaard, T Bligaard, J Rossmeisl, and CH Christensen. Towards the computational design of solid catalysts. *Nature chemistry*, 1(1):37—46, April 2009.

[121] Danielle Hansgen, Dionisios Vlachos, and Jingguang Chen. Using first principles to predict bimetallic catalysts for the ammonia decomposition reaction. *Nature chemistry*, 2:484–9, 06 2010.

[122] Ajin Rajan, Anoop P. Pushkar, Balaji C. Dharmalingam, and Jithin John Varghese. Iterative multiscale and multi-physics computations for operando catalyst nanostructure elucidation and kinetic modeling. *iScience*, 26(7):107029, 2023.

[123] Pussana Hirunsit, Chuleeporn Luadthong, and Kajornsak Faungnawakij. Effect of alumina hydroxylation on glycerol hydrogenolysis to 1,2-propanediol over cu/al2o3: Combined experiment and dft investigation. *RSC Advances*, 5:11188–11197, 01 2015.

[124] Ambarish Kulkarni, Samira Siahrostami, Anjli Patel, and Jens Nørskov. Understanding catalytic activity trends in the oxygen reduction reaction. *Chemical Reviews*, 118, 02 2018.

[125] Antonio Prestianni, Micaela Crespo-Quesada, Remedios Cortese, Francesco Ferrante, Liubov Kiwi-Minsker, and Dario Duca. Structure sensitivity of 2-methyl-3-butyn-2-ol hydrogenation on pd: Computational and experimental modeling. *The Journal of Physical Chemistry C*, 118(6):3119–3128, 2014.

[126] Veronique Speybroeck, Karen Hemelsoet, Lennart Joos, Michel Waroquier, Robert Bell, and Richard Catlow. Advances in theory and their application within the field of zeolite chemistry. *Chem. Soc. Rev.*, 44, 05 2015.

[127] Jianmin Lu, Sina Behtash, Osman Mamun, and Andreas Heyden. Theoretical investigation of the reaction mechanism of the guaiacol hydrogenation over a pt(111) catalyst. *ACS Catalysis*, 5(4):2423–2435, 2015.

[128] Kyungtae Lee, Geun Ho Gu, Charles A. Mullen, Akwasi A. Boateng, and Dionisios G. Vlachos. Guaiacol hydrodeoxygenation mechanism on Pt(111): Insights from density functional theory and linear free energy relations. *ChemSusChem*, 8:315–322, 2015.

[129] Miroslav Rubeš, Junjie He, Petr Nachtigall, and Ota Bludský. Direct hydrodeoxygenation of phenol over carbon-supported ru catalysts: A computational study. *Journal of Molecular Catalysis A: Chemical*, 423:300–307, 2016.

[130] Omer Elmutasim and Kyriaki Polychronopoulou. Direct deoxygenation reaction of oxygenated model compounds by biomass pyrolysis on the ni5p4(001) surface: a computational study. *Sustainable Energy Fuels*, 7:1415–1432, 2023.

[131] Jiajun Zhang, Beatriz Fidalgo, Dekui Shen, Xiaolei Zhang, and Sai Gu. Mechanism of hydrodeoxygenation (hdo) in anisole decomposition over metal loaded brønsted acid sites: Density functional theory (dft) study. *Molecular Catalysis*, 454:30–37, 2018.

[132] Kushagra Agrawal and Nanda Kishore. Computational study on kinetics of conversion of bio-oil model compound – anisole, to platform chemicals. *Journal of Physics: Conference Series*, 1276:012071, 08 2019.

[133] Nathan Argaman and Guy Makov. Density functional theory: An introduction. *American Journal of Physics*, 68(1):69–79, 2000.

[134] Larry A. Curtiss, Krishnan Raghavachari, Paul C. Redfern, and John A. Pople. Assessment of gaussian-2 and density functional theories for the computation of enthalpies of formation. *The Journal of Chemical Physics*, 106(3):1063–1079, 01 1997.

[135] Larry A. Curtiss, Krishnan Raghavachari, Gary W. Trucks, and John A. Pople. Gaussian-2 theory for molecular energies of first- and second-row compounds. *The Journal of Chemical Physics*, 94(11):7221–7230, 06 1991.

[136] Axel D. Becke. A new mixing of hartree–fock and local density-functional theories. *The Journal of Chemical Physics*, 98(2):1372–1377, 1993.

[137] Christian Tuma and Joachim Sauer. Treating dispersion effects in extended systems by hybrid mp2:dft calculations—protonation of isobutene in zeolite ferrierite. *Phys. Chem. Chem. Phys.*, 8:3955–3965, 2006.

[138] Stefan Grimme, Jens Antony, Stephan Ehrlich, and Helge Krieg. A consistent and accurate ab initio parametrization of density functional dispersion correction (dft-d) for the 94 elements h-pu. *The Journal of Chemical Physics*, 132(15):154104, 2010.

[139] M. J. Frisch, G. W. Trucks, H. B. Schlegel, G. E. Scuseria, M. A. Robb, J. R. Cheeseman, G. Scalmani, V. Barone, G. A. Petersson, H. Nakatsuji, X. Li, M. Caricato, A. V. Marenich, J. Bloino, B. G. Janesko, R. Gomperts, B. Mennucci, H. P. Hratchian, J. V. Ortiz, A. F. Izmaylov, J. L. Sonnenberg, D. Williams-Young, F. Ding, F. Lipparini, F. Egidi, J. Goings, B. Peng, A. Petrone, T. Henderson, D. Ranasinghe, V. G. Zakrzewski, J. Gao, N. Rega, G. Zheng, W. Liang, M. Hada, M. Ehara, K. Toyota, R. Fukuda, J. Hasegawa, M. Ishida, T. Nakajima, Y. Honda, O. Kitao, H. Nakai, T. Vreven, K. Throssell, J. A. Montgomery, Jr., J. E. Peralta, F. Ogliaro, M. J. Bearpark, J. J. Heyd, E. N. Brothers, K. N. Kudin, V. N. Staroverov, T. A. Keith, R. Kobayashi, J. Normand, K. Raghavachari, A. P. Rendell, J. C. Burant, S. S. Iyengar, J. Tomasi, M. Cossi, J. M. Millam, M. Klene, C. Adamo, R. Cammi, J. W. Ochterski, R. L. Martin, K. Morokuma, O. Farkas, J. B. Foresman, and D. J. Fox. Gaussian˜16 Revision C.01, 2016.

[140] Axel D. Becke. A new mixing of Hartree–Fock and local density-functional theories. *J. Chem. Phys.*, 98:1372–1377, 1993.

[141] Stefan Grimme, Jens Antony, Stephan Ehrlich, and Helge Krieg. A consistent and accurate ab initio parametrization of density functional dispersion correction (DFT-D) for the 94 elements H-Pu. *J. Chem. Phys.*, 132:154104, 2010.

[142] P. Jeffrey Hay and Willard R. Wadt. Ab initio effective core potentials for molecular calculations. Potentials for the transition metal atoms Sc to Hg. *J. Chem. Phys.*, 82:270–283, 1985.

[143] P. Jeffrey Hay and Willard R. Wadt. Ab initio effective core potentials for molecular calculations. Potential for K to Au including the outermost core orbitals. *J. Chem. Phys.*, 82:299–310, 1985.

[144] Thom. H. Dunning and P. Jeffrey Hay. Gaussian Basis Sets for Molecular Calculations. In Henry F. Schaefer, editor, *Methods of Electronic Structure Theory*, Modern Theoretical Chemistry, pages 1–27. Springer US, 1977.

[145] Benjamin P. Pritchard, Doaa Altarawy, Brett Didier, Tara D. Gibson, and Theresa L. Windus. New basis set exchange: An open, up-to-date resource for the molecular sciences community. *J. Chem. Inf. Model.*, 59:4814–4820, 2019.

[146] S. F. Boys and F. Bernardi. The calculation of small molecular interactions by the differences of separate total energies. Some procedures with reduced errors. *Mol. Phys.*, 19:553–566, 1970.

[147] José M Soler, Emilio Artacho, Julian D Gale, Alberto García, Javier Junquera, Pablo Ordejón, and Daniel Sánchez-Portal. The siesta method for ab initio order-n materials simulation. *Journal of Physics: Condensed Matter*, 14(11):2745, mar 2002.

[148] John P. Perdew, Kieron Burke, and Yue Wang. Generalized gradient approximation for the exchange-correlation hole of a many-electron system. *Phys. Rev. B*, 54:16533–16539, Dec 1996.

[149] Marco Bertini, Francesco Ferrante, and Dario Duca. Empathes: A general code for nudged elastic band transition states search. *Computer Physics Communications*, 271:108224, 2022.

[150] Ilker Demiroglu, Kezi Yao, Heider A Hussein, and Roy L. Johnston. DFT Global Optimization of Gas-Phase Subnanometer Ru–Pt Clusters. *J. Phys. Chem. C*, 121:10773–10780, 2017.

[151] Matthias Brack. Metal clusters and magic numbers. *Scientific American*, 277(6):50–55, 1997.

[152] Tarit Nimmanwudipong, Ron C. Runnebaum, David E. Block, and Bruce C. Gates. Catalytic conversion of guaiacol catalyzed by platinum supported on alumina: Reaction network including hydrodeoxygenation reactions. *Energy & Fuels*, 25(8):3417–3427, 2011.

[153] Francesco Ferrante, Antonio Prestianni, Marco Bertini, and Dario Duca. H2 transformations on graphene supported palladium cluster: Dft-md simulations and neb calculations. *Catalysts*, 10(11), 2020.

[154] Vincenza D'Anna, Dario Duca, Francesco Ferrante, and Gianfranco La Manna. DFT studies on catalytic properties of isolated and carbon nanotube supported Pd_9 cluster: Part II. Hydro-isomerization of butene isomers. *Phys. Chem. Chem. Phys.*, 12:1323–1330, 2010.

[155] Giampaolo Barone, Dario Duca, Francesco Ferrante, and Gianfranco La Manna. Casscf/caspt2 analysis of the fragmentation of h2 on a pd4 cluster. *International Journal of Quantum Chemistry*, 110(3):55ROL8–562, 2010.

[156] John Immoos. A novel synthesis of isoeugenol, [ring-(u)-14c]. *Journal of labelled compounds radiopharmaceuticals*, 58, 08 2015.

[157] Takao Koeduka, Eyal Fridman, David Gang, Daniel Vassao, Brenda Jackson, Christine Kish, Snejina Spassova, Norman Lewis, Joseph Noel, Thomas Baiga, Natalia Dudareva, and Eran Pichersky. Eugenol and isoeugenol, characteristic aromatic constituents of spices, are biosynthesized via reduction of a coniferyl alcohol ester. *Proceedings of the National Academy of Sciences of the United States of America*, 103:10128–33, 07 2006.

[158] Kishore Dasari and Kannan Srinivasan. Double bond migration of eugenol to isoeugenol over as-synthesized hydrotalcites and their modified forms. *Applied Catalysis a-General*, 270:227–235, 08 2004.

[159] A. Loupy and Lengoc Thach. Base-catalysed isomerization of eugenol: Solvent-free conditions and microwave activation. *Synthetic Communications*, 23(18):2571–2577, 1993.

[160] T Atsumi, Seiichiro Fujisawa, and Keiichi Tonosaki. A comparative study of the antioxidant/prooxidant activities of eugenol and isoeugenol with various

concentrations and oxidation conditions. *Toxicology in vitro : an international journal published in association with BIBRA*, 19:1025–33, 01 2006.

[161] Weihua Li, Ryoko Tsubouchi, Shanlou Qiao, Miyako Haneda, Keiko Murakami, and Masataka Yoshino. Inhibitory action of eugenol compounds on the production of nitric oxide in raw264.7 macrophages. *Biomedical research (Tokyo, Japan)*, 27:69–74, 05 2006.

[162] Gurpreet Kaur and Sarwat Sultana. Evaluation of antiarthritic activity of isoeugenol in adjuvant induced arthritis in murine model. *Food and Chemical Toxicology*, 50(8):2689–2695, 2012.

[163] Morahem Ashengroph and Jahanshir Amini. Bioconversion of isoeugenol to vanillin and vanillic acid using the resting cells of trichosporon asahii. *3 Biotech*, 7:358, 10 2017.

[164] Babur Chowdhry, John Ryall, Trevor Dines, and Andrew Mendham. Infrared and raman spectroscopy of eugenol, isoeugenol and methyl eugenol: Conformational analysis and vibrational assignments from dft calculations of the anharmonic fundamentals. *The journal of physical chemistry. A*, 119, 10 2015.

[165] Joseph A. Maga and Ira Katz. Simple phenol and phenolic compounds in food flavor. *C R C Critical Reviews in Food Science and Nutrition*, 10(4):323–372, 1978.

[166] Kushagra Agrawal, Alberto Roldan, Nanda Kishore, and Andrew J. Logsdail. Hydrodeoxygenation of guaiacol over orthorhombic molybdenum carbide: a dft and microkinetic study†. *Catalysis Science Technology*, 12(3):843–854, 2022.

[167] Danni Gao, Yang Xiao, and Arvind Varma. Guaiacol hydrodeoxygenation over platinum catalyst: Reaction pathways and kinetics. *Industrial Engineering Chemistry Research*, 54:10638–10644, 10 2015.

[168] Rong Kou, Yuyan Shao, Donghai Wang, Mark H Engelhard, Ja Hun Kwak, Jun Wang, Vilayanur V Viswanathan, Chongmin Wang, Yuehe Lin, Yong

Wang, et al. Enhanced activity and stability of pt catalysts on functionalized graphene sheets for electrocatalytic oxygen reduction. *Electrochemistry Communications*, 11(5):954–957, 2009.

[169] Lifeng Dong, Raghavendar Reddy Sanganna Gari, Zhou Li, Michael M Craig, and Shifeng Hou. Graphene-supported platinum and platinum–ruthenium nanoparticles with high electrocatalytic activity for methanol and ethanol oxidation. *Carbon*, 48(3):781–787, 2010.

[170] Farnosh Tavakoli and Masoud Salavati-Niasari. A facile synthesis of cui-graphene nanocomposite by glucose as a green capping agent and reductant. *Journal of Industrial and Engineering Chemistry*, 20(5):3170–3174, 2014.

[171] EM Crabb, MK Ravikumar, Y Qian, AE Russell, S Maniguet, Jun Yao, D Thompsett, M Hurford, and SC Ball. Controlled modification of carbon supported platinum electrocatalysts by mo. *Electrochemical and solid-state letters*, 5(1):A5, 2001.

[172] B An, F Huang, L Li, SF Xu, and X Geng. Electrocatalytical performance of the activated and the nitrogen-doped carbon layer coated carbon nanotubes loaded with platinum. *Functional Materials*, 23:3435–3438, 2013.

[173] Hongtao Wang, Qiong Feng, Yingchun Cheng, Yingbang Yao, Qingxiao Wang, Kun Li, Udo Schwingenschlögl, Xi Xiang Zhang, and Wei Yang. Atomic bonding between metal and graphene. *The Journal of Physical Chemistry C*, 117(9):4632–4638, 2013.

[174] Zheng Fang, Yurong Gao, Nanthi Bolan, Sabry M. Shaheen, Song Xu, Xiaolian Wu, Xiaoya Xu, Haiyao Hu, Jinhao Lin, Fangbin Zhang, Jianhua Li, Jörg Rinklebe, and Hailong Wang. Conversion of biological solid waste to graphene-containing biochar for water remediation: A critical review. *Chemical Engineering Journal*, 390:124611, 2020.

[175] Dmitry Yu. Murzin. On the topological representation of catalytic cycles with nonlinear steps. *Reaction Kinetics and Catalysis Letters*, 90:225–232, 2007.

[176] Graeme Henkelman, Blas P. Uberuaga, and Hannes Jónsson. A climbing image nudged elastic band method for finding saddle points and minimum energy paths. *The Journal of Chemical Physics*, 113(22):9901–9904, 12 2000.

[177] Hongli Liu, Ruiqi Fang, Zhong Li, and Yingwei Li. Solventless hydrogenation of benzene to cyclohexane over a heterogeneous ru–pt bimetallic catalyst. *Chemical Engineering Science*, 122:350–359, 2015.

[178] Mark Saeys, M.-F. Reyniers, M. Neurock, and G. B. Marin. Ab initio reaction path analysis of benzene hydrogenation to cyclohexane on Pt(111). *J. Phys. Chem. B*, 109(6):2064–2073, 2005.

[179] J.A. Christiansen. The elucidation of reaction mechanisms by the method of intermediates in quasi-stationary concentrations. volume 5 of *Adv. Catal.*, pages 311–353. Academic Press, 1953.

[180] Laura Gueci, Francesco Ferrante, Antonio Prestianni, Francesco Arena, and Dario Duca. Benzyl alcohol to benzaldehyde oxidation on MnO_x clusters: Unraveling atomistic features. *Mol. Catal.*, 513:111735, 2021.

[181] F Arena, F Ferrante, R Di Chio, G Bonura, F Frusteri, L Frusteri, A Prestianni, S Morandi, G Martra, and D Duca. DFT and kinetic evidences of the preferential CO oxidation pattern of manganese dioxide catalysts in hydrogen stream (PROX). *Appl. Cat. B Env.*, 300:120715, 2022.

[182] Laura Gueci, Francesco Ferrante, Antonio Prestianni, Roberto Di Chio, Antonio Patti, Dario Duca, and Francesco Arena. Dft insights into the oxygen-assisted selective oxidation of benzyl alcohol on manganese dioxide catalysts. *Inorganica Chimica Acta*, 511:119812, 06 2020.

[183] Laura Gueci, Francesco Ferrante, Antonio Prestianni, Francesco Arena, and Dario Duca. Structural, energetic and kinetic database of catalytic reactions: benzyl alcohol to benzaldehyde oxidation on MnO_x clusters. *Data in Brief*, 38:107369, 2021.

[184] G. Luchini, J. V. Alegre-Requena, I. Funes-Ardoiz, and R. S. Paton. Goodvibes: Automated thermochemistry for heterogeneous computational chemistry data. *F1000Research*, 9:291, 2020.

[185] S. Grimme. Supramolecular binding thermodynamics by dispersion-corrected density functional theory. *Chem. Eur. J.*, 18:9955–9964, 2012.

[186] Tapan Bera, Joris W. Thybaut, and Guy B. Marin. Single-Event MicroKinetics of Aromatics Hydrogenation on Pt/H-ZSM22. *Ind. Eng. Chem. Res.*, 50(23):12933–12945, 2011.

[187] Luis Lozano, Guy B. Marin, and Joris W. Thybaut. Analytical rate expressions accounting for the elementary steps in benzene hydrogenation on Pt. *Ind. Eng. Chem. Res.*, 56:12953–12962, 2017.

[188] Francesco Ferrante, Chiara Nania, and Dario Duca. Computational investigation of isoeugenol transformations on a platinum cluster – I: Direct deoxygenation to propylcyclohexane. *Mol. Catal.*, 529:112541, 2022.

[189] Romain Réocreux, Cherif A. Ould Hamou, Carine Michel, Javier B. Giorgi, and Philippe Sautet. Decomposition mechanism of anisole on pt(111): Combining single-crystal experiments and first-principles calculations. *ACS Catalysis*, 6(12):8166–8178, 2016.

[190] Päivi Mäki-Arvela and Dmitry Yu. Murzin. Hydrodeoxygenation of lignin-derived phenols: From fundamental studies towards industrial applications. *Catalysts*, 7, 2017.

[191] Yayun Zhang and Xiaolu Huang. Study of guaiacol pyrolysis mechanism based on density function theory. *Fuel Processing Technology*, 123:159–165, 07 2014.

[192] Anand Mohan Verma and Nanda Kishore. Dft analyses of reaction pathways and temperature effects on various guaiacol conversion reactions in gas phase environment. *ChemistrySelect*, 1(19):6196–6205, 2016.

[193] Cheng-Chau Chiu, Alexander Genest, Armando Borgna, and Notker Rösch. Hydrodeoxygenation of guaiacol over Ru(0001): A DFT study. *ACS Catalysis*, 4:4178–4188, 2014.

[194] Kyungtae Lee, Geun Ho Gu, Charles A. Mullen, Akwasi A. Boateng, and Dionisios G. Vlachos. Guaiacol hydrodeoxygenation mechanism on Pt(111): Insights from density functional theory and linear free energy relations. *ChemSusChem*, 8:315–322, 2015.

[195] Jianmin Lu, Sina Behtash, Osman Mamun, and Andreas Heyden. Theoretical investigation of the reaction mechanism of the guaiacol hydrogenation over a Pt(111) catalyst. *ACS Catal.*, 5:2423–2435, 2015.

[196] Emanuel V. Scoullos, Michelle S. Hofman, Yiteng Zheng, Denis V. Potapenko, Ziyu Tang, Simon G. Podkolzin, and Bruce E. Koel. Guaiacol adsorption and decomposition on platinum. *J. Phys. Chem. C*, 122:29180–29189, 2018.

[197] T Imaoka, Y Akanuma, N Haruta, S Tsuchiya, K Ishihara, T Okayasu, W.-J. Chun, M Takahashi, and K Yamamoto. Platinum clusters with precise numbers of atoms for preparative-scale catalysis. *Nat. Comm.*, 8:1–8, 2017.

[198] Christian Schmitt, Nicola Da Roit, Marco Neumaier, Carina B. Maliakkal, Di Wang, Thilo Henrich, Christian Kübel, Manfred Kappes, and Silke Behrens. Continuous flow synthesis of atom-precise platinum clusters. *Nanoscale Adv.*, 6:2459–2468, 2024.

[199] Ganghua Xiang, Zhihuan Qiu, Huilong Fei, Zhigang Liu, Shuangfeng Yin, and Yuen Wu. Synergistic effect of platinum single atoms and nanoclusters for preferential oxidation of carbon monoxide in hydrogen-rich stream. *Journal of power sources*, 591:233873–, 2024.

[200] V. P. Babar, S Jaiswal, and V. Kumar. Interaction of a carbon atom on small platinum clusters and its effects on hydrogen binding. *Chem. Phys. Lett.*, 560:41–48, 2013.

[201] D. J. Harding, C. Kerpal, G. Meijer, and A. Fielicke. Unusual bonding in platinum carbido cluster. *J. Phys. Chem. Lett.*, 4:892–896, 2013.

[202] Chiara Nania, Marco Bertini, Laura Gueci, Francesco Ferrante, and Dario Duca. DFT insights into competing mechanisms of guaiacol hydrodeoxygenation on a platinum cluster. *Phys. Chem. Chem. Phys.*, 25:10460–10471, 2023.

[203] Chiara Nania, Francesco Ferrante, Marco Bertini, Laura Gueci, and Dario Duca. Computational investigation of isoeugenol transformations on a platinum cluster – II: Deoxygenation through hydrogenation to propylcyclohexane. *Molecular Catalysis*, 564:114298, 2024.

223

[204] National Research Council. *Catalysis Looks to the Future.* The National Academies Press, 1992.

[205] Debra R Rolison. Catalytic nanoarchitectures–the importance of nothing and the unimportance of periodicity. *Science*, 299(5613):1698–1701, 2003.

[206] Marc Armbrüster, Kirill Kovnir, Matthias Friedrich, Detre Teschner, Gregor Wowsnick, Michael Hahne, Peter Gille, Lászlo Szentmiklósi, Michael Feuerbacher, Marc Heggen, et al. Al13fe4 as a low-cost alternative for palladium in heterogeneous hydrogenation. *Nature Materials*, 11(8):690–693, 2012.

[207] MH Valkenberg, C DeCastro, and WF Hölderich. Immobilisation of ionic liquids on solid supports. *Green Chemistry*, 4(2):88–93, 2002.

[208] Ilkeun Lee, Manuel A Albiter, Qiao Zhang, Jianping Ge, Yadong Yin, and Francisco Zaera. New nanostructured heterogeneous catalysts with increased selectivity and stability. *Physical Chemistry Chemical Physics*, 13(7):2449–2456, 2011.

[209] Tsutomu Ioroi, Kazuaki Yasuda, Zyun Siroma, Naoko Fujiwara, and Yoshinori Miyazaki. Enhanced co-tolerance of carbon-supported platinum and molybdenum oxide anode catalyst. *Journal of the Electrochemical Society*, 150(9):A1225, 2003.

[210] Xiulei Ji, Kyu Tae Lee, Reanne Holden, Lei Zhang, Jiujun Zhang, Gianluigi A Botton, Martin Couillard, and Linda F Nazar. Nanocrystalline intermetallics on mesoporous carbon for direct formic acid fuel cell anodes. *Nature chemistry*, 2(4):286–293, 2010.

[211] Sumant Upadhyay, Samira Bagheri, and Sharifah Bee Abd Hamid. Enhanced photoelectrochemical response of reduced-graphene oxide/zn1- xagxo nanocomposite in visible-light region. *International journal of hydrogen energy*, 39(21):11027–11034, 2014.

[212] Duck Hyun Lee, Ji Eun Kim, Tae Hee Han, Jae Won Hwang, Seokwoo Jeon, Sung-Yool Choi, Soon Hyung Hong, Won Jong Lee, Rodney S. Ruoff, and Sang Ouk Kim. Versatile carbon hybrid films composed of vertical carbon nanotubes grown on mechanically compliant graphene films. *Advanced Materials*, 22(11):1247–1252, 2010.

[213] Alexander A. Balandin, Suchismita Ghosh, Wenzhong Bao, Irene Calizo, Desalegne Teweldebrhan, Feng Miao, and Chun Ning Lau. Superior thermal conductivity of single-layer graphene. *Nano Letters*, 8(3):902–907, 2008.

[214] Liming Dai. Functionalization of graphene for efficient energy conversion and storage. *Accounts of chemical research*, 46(1):31–42, 2013.

[215] Changgu Lee, Xiaoding Wei, Jeffrey W. Kysar, and James Hone. Measurement of the elastic properties and intrinsic strength of monolayer graphene. *Science*, 321(5887):385–388, 2008.

[216] Martin Pumera. Graphene-based nanomaterials and their electrochemistry. *Chemical Society Reviews*, 39(11):4146–4157, 2010.

[217] Shaojun Guo and Shaojun Dong. Graphene nanosheet: synthesis, molecular engineering, thin film, hybrids, and energy and analytical applications. *Chemical Society Reviews*, 40(5):2644–2672, 2011.

[218] Xiao Huang, Xiaoying Qi, Freddy Boey, and Hua Zhang. Graphene-based composites. *Chemical Society Reviews*, 41(2):666–686, 2012.

[219] Siegmar Roth and Hye Jin Park. Nanocarbonic transparent conductive films. *Chemical Society Reviews*, 39(7):2477–2483, 2010.

[220] J.A.S. Bett, K. Kinoshita, and P. Stonehart. Crystallite growth of platinum dispersed on graphitized carbon black: Ii. effect of liquid environment. *Journal of Catalysis*, 41(1):124–133, 1976.

[221] Dacheng Wei, Bin Wu, Yunlong Guo, Gui Yu, and Yunqi Liu. Controllable chemical vapor deposition growth of few layer graphene for electronic devices. *Accounts of chemical research*, 46(1):106–115, 2013.

[222] Frank Schwierz. Graphene transistors. *Nature nanotechnology*, 5(7):487–496, 2010.

[223] Xiangjian Wan, Yi Huang, and Yongsheng Chen. Focusing on energy and optoelectronic applications: a journey for graphene and graphene oxide at large scale. *Accounts of chemical research*, 45(4):598–607, 2012.

[224] Z. H. Ni, L. A. Ponomarenko, R. R. Nair, R. Yang, S. Anissimova, I. V. Grigorieva, F. Schedin, P. Blake, Z. X. Shen, E. H. Hill, K. S. Novoselov, and A. K. Geim. On resonant scatterers as a factor limiting carrier mobility in graphene. *Nano Letters*, 10(10):3868–3872, 2010.

[225] Kai Yang, Liangzhu Feng, Xiaoze Shi, and Zhuang Liu. Nano-graphene in biomedicine: theranostic applications. *Chemical Society Reviews*, 42(2):530–547, 2013.

[226] MJ Allen, VC Tung, and RB Kaner. Multi-scale approach for statistical broad absorption and emission spectra of organic compounds and biologic objects. *Chem. Rev.*, 110:132–145, 2010.

[227] P Avouris, ZH Chen, and V Perebeinos. Fine structure constant defines visual transparency of graphene. *Nat. Nanotechnol*, 2:605–615, 2007.

[228] Kinam Kim, Jae-Young Choi, Taek Kim, Seong-Ho Cho, and Hyun-Jong Chung. A role for graphene in silicon-based semiconductor devices. *Nature*, 479(7373):338–344, 2011.

[229] Dale AC Brownson, Dimitrios K Kampouris, and Craig E Banks. Graphene electrochemistry: fundamental concepts through to prominent applications. *Chemical Society Reviews*, 41(21):6944–6976, 2012.

[230] Da Chen, Longhua Tang, and Jinghong Li. Graphene-based materials in electrochemistry. *Chemical Society Reviews*, 39(8):3157–3180, 2010.

[231] Minmin Liu, Ruizhong Zhang, and Wei Chen. Graphene-supported nanoelectrocatalysts for fuel cells: synthesis, properties, and applications. *Chemical reviews*, 114(10):5117–5160, 2014.

[232] Young Hee Lee, Seong Gon Kim, and David Tománek. Catalytic growth of single-wall carbon nanotubes: an ab initio study. *Physical Review Letters*, 78(12):2393, 1997.

[233] Isabella Gierz, Christian Riedl, Ulrich Starke, Christian R Ast, and Klaus Kern. Atomic hole doping of graphene. *Nano letters*, 8(12):4603–4607, 2008.

[234] Harman Johll, Hway Chuan Kang, and Eng Soon Tok. Density functional theory study of fe, co, and ni adatoms and dimers adsorbed on

226

graphene. *Physical Review B—Condensed Matter and Materials Physics*, 79(24):245416, 2009.

[235] AV Krasheninnikov, PO Lehtinen, Adam S Foster, Pekka Pyykkö, and Risto M Nieminen. Embedding transition-metal atoms in graphene: structure, bonding, and magnetism. *Physical review letters*, 102(12):126807, 2009.

[236] Kevin T. Chan, J. B. Neaton, and Marvin L. Cohen. First-principles study of metal adatom adsorption on graphene. *Phys. Rev. B*, 77:235430, Jun 2008.

[237] Alejandro Lugo-Solis and Igor Vasiliev. Ab initio study of k adsorption on graphene and carbon nanotubes: Role of long-range ionic forces. *Phys. Rev. B*, 76:235431, Dec 2007.

[238] Xiaojie Liu, C. Z. Wang, Y. X. Yao, W. C. Lu, M. Hupalo, M. C. Tringides, and K. M. Ho. Bonding and charge transfer by metal adatom adsorption on graphene. *Phys. Rev. B*, 83:235411, Jun 2011.

[239] H. Sevinçli, M. Topsakal, E. Durgun, and S. Ciraci. Electronic and magnetic properties of $3d$ transition-metal atom adsorbed graphene and graphene nanoribbons. *Phys. Rev. B*, 77:195434, May 2008.

[240] Qiang Sun, Qian Wang, Puru Jena, and Yoshiyuki Kawazoe. Clustering of ti on a c60 surface and its effect on hydrogen storage. *Journal of the American Chemical Society*, 127(42):14582–14583, 2005.

[241] Bing Ding and Xiaoliang Wu. Transition metal oxides anchored on graphene/carbon nanotubes conductive network as both the negative and positive electrodes for asymmetric supercapacitor. *Journal of Alloys and Compounds*, 842:155838, 2020.

[242] Jie Chang, Tanate Danuthai, Silvia Dewiyanti, Chuan Wang, and Armando Borgna. Hydrodeoxygenation of guaiacol over carbon-supported metal catalysts. *ChemCatChem*, 5:3041–3049, 2013.

[243] M. M. Ugeda, I. Brihuega, F. Guinea, and J. M. Gómez-Rodríguez. Missing atom as a source of carbon magnetism. *Phys. Rev. Lett.*, 104:096804, Mar 2010.

[244] Yanjie Gan, Litao Sun, and Florian Banhart. One- and two-dimensional diffusion of metal atoms in graphene. *Small*, 4(5):587–591, 2008.

[245] Julio A. Rodríguez-Manzo, Ovidiu Cretu, and Florian Banhart. Trapping of metal atoms in vacancies of carbon nanotubes and graphene. *ACS Nano*, 4(6):3422–3428, 2010.

[246] Sami Malola, Hannu Häkkinen, and Pekka Koskinen. Gold in graphene: In-plane adsorption and diffusion. *Applied Physics Letters*, 94:043106, 2008.

[247] María J. López, Iván Cabria, and Julio A. Alonso. Palladium clusters anchored on graphene vacancies and their effect on the reversible adsorption of hydrogen. *The Journal of Physical Chemistry C*, 118(10):5081–5090, 2014.

[248] I. Cabria, M. J. López, S. Fraile, and J. A. Alonso. Adsorption and dissociation of molecular hydrogen on palladium clusters supported on graphene. *The Journal of Physical Chemistry C*, 116(40):21179–21189, 2012.

[249] Florian Banhart, Jani Kotakoski, and Arkady V. Krasheninnikov. Structural defects in graphene. *ACS Nano*, 5(1):26–41, 2011.

[250] C.M. Ramos-Castillo, J.U. Reveles, R.R. Zope, and R. de Coss. Palladium clusters supported on graphene monovacancies for hydrogen storage. *The Journal of Physical Chemistry C*, 119(15):8402–8409, 2015.